Feasibility study of performing high precision gamma spectroscopy of $\Lambda\Lambda$ hypernuclei in the $\overline{\mathsf{P}}\mathsf{ANDA}$ experiment

Doktorarbeit
von
Alicia Sanchez-Lorente
geboren in Murcia (Spanien)

Institut für Kernphysik
Johannes Gutenberg-Universität Mainz
August 2010

Erster Berichterstatter:	
Zweiter Berichterstatter:	
Dekan des Fachbereichs Physik:	
Datum der mündlichen Prüfung:	30. September 2010

Contents

Introduction

Quantum Chromo Dynamics (QCD) is the theory of the force responsible for the confinement of quarks and gluons in hadrons, but it is also responsible for the binding of nucleons in nuclei and thus of the appearances of ordinary matter in our universe. While the internal structure of hadrons and the spectra of their excited states are important aspects of QCD, it is also important to understand the origin of the nuclear force in a more rigorous way out of QCD and how nuclear structures - nuclei on the small scale and dense stellar objects on the large scale - are formed [1].

Furthemore, strangeness has played important roles in nuclear physics. Introducing strangeness into nuclei extends our understanding of matter as hadronic many-body systems, rather than nucleon many-body systems, and provides new clues to their nature that can hardly be understood directly through QCD. Indeed, a hyperon bound in a nucleus offers a selective probe of the hadronic many-body problem as it is not restricted by the Pauli principle in populating all possible nuclear states, in contrast to neutrons and protons. On one hand a strange baryon embedded in a nuclear system may serve as a sensitive probe for the nuclear structure and its possible modification due to the presence of the hyperon. On the other hand properties of hyperons may change dramatically if implanted inside of a nucleus. Therefore a nucleus may serve as a laboratory offering a unique possibility to study basic properties of hyperons and strange exotic objects. Thus, hypernuclear physics represents an interdisciplinary science linking many fields of particle, nuclear and many-body physics.

Detailed information on hyperon–nucleon and hyperon–hyperon interactions is indispensable to the present understanding of high-density nuclear matter inside neutron stars, where hyperons are possibly mixed and play crucial roles(*e.g.* ref. [2]). Indeed, when the strangeness number increases, strangeness hadronic matter made of equal numbers of protons, neutrons, Λs, Ξ^-s and Ξ^0s with neutral charge is expected to be stable [3]. It is argued that in the core of neutron stars, where hyperons appear due to the large Fermi energy of neutrons, the fractions of various baryons as a function of density are very sensitive to the hyperon-nucleon (YN) and hyperon-hyperon (YY) interactions, of which realistic data have partly been obtained from hypernuclear studies in recent years as reviewed in Ref. [4].

Furthemore, it is also clear that a detailed and consistent understanding of the quark aspect of the baryon-baryon forces in the SU(3) space will not be possible as long as experimental information on the hyperon-hyperon channel is not available.

Since scattering experiments between two hyperons are impractical, the precise spectroscopy of multi-strange hypernuclei will provide a unique approach to explore the hyperon-hyperon interaction. Nuclei with strangeness

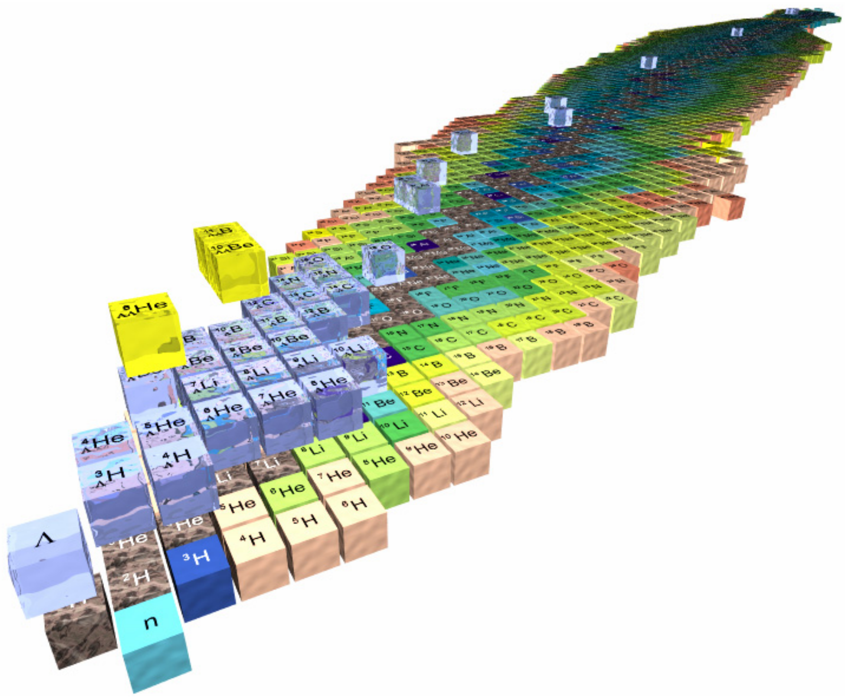

Figure 1: Present knowledge on hypernuclei. Experimental data are limited to only 39 Λ hypernuclei in the S = 1 plane (blue) and only very few individual events of double hypernuclei (yellow) have been detected and identified so far [5].

can be plotted in the three-dimensional nuclear chart, where the strangeness number (S) increases along the third axis. Experimental data are limited to only 39 Λ hypernuclei in the S = 1 plane (blue) and a few ΛΛ hypernuclei (yellow) in the S = 2 plane (Fig. 1).

A common difficulty to all theoretical investigations of multi-strange hypernuclei (*e.g* double–Λ hypernuclei) is the lack of high–resolution and systematic data on multi–hypernuclei and their level structure. Although the analysis of emulsion stacks by automated means (*e.g*, by scanning the film with a CCD camera) has been found possible in some circumstances, these studies cannot provide high production rates. Furthermore, whether particle unstable states (whose decay photons are not detected) are populated, or whether neutrons are being emitted, this method gives ambiguous results. The possibility to trigger via kaon detection on potentially interesting events clearly calls for experiments based on electronic detectors. Moreover, since the kinetic energies of the nuclear fragments are very low, these experiments have to rely on specific decay channels.

Hypernuclear research will be one of the main topics addressed by the $\overline{\text{P}}$ANDA experiment [6] at the planned Facility for Antiproton and Ion Research FAIR [7]. The FAIR complex will include the High Energy Storage Ring (HESR) to store antiprotons between 0.8 and 14.4 MeV energy. Intense and high quality beams with luminosities up to $10^{32}\,\text{cm}^{-2}\text{s}^{-1}$ and momentum resolutions down to 10^{-5} are expected. The $\overline{\text{P}}$ANDA hypernuclear programme shall reveal the strength of Λ–Λ interaction via the high resolution γ spectroscopy of double Λ hypernuclei. Contrary to past hypernuclear experiments, where only a few double hypernuclei events were found, the challenge of the $\overline{\text{P}}$ANDA experiment will be to produce statistics of five orders of magnitude larger. The reason resides in the fact that germanium detectors have presently an efficiency of only a few percent.

Nevertheless, in combination with high luminosity of the antiproton beam at HESR, a high production rate of single and double hypernuclei under unique experimental conditions will be possible for the first time.

The production of low momentum Ξ^- hyperons and their capture in atomic levels is therefore essential for the experiment. Initially hyperons, in particular $\Xi^- + \bar{\bar{\Xi}}$, are produced on a primary nuclear target via the following reactions,

$$\overline{p} + p \rightarrow \Xi^-\overline{\Xi}^+ \tag{1}$$

$$\overline{p} + n \rightarrow \Xi^-\overline{\Xi}^0 \tag{2}$$

The slowing down of the Ξ proceeds through a sequence of nuclear elastic scattering (rescattering) processes inside the residual nucleus in which the antiproton annihilation has occurred, and by energy loss during the passage through an active absorber. If decelerated to rest before decaying, the particle can be captured in a nucleus, eventually releasing two Λ hyperons and forming a double hypernucleus via the strong interaction $\Xi^- + p \rightarrow \Lambda\Lambda + 28\,\text{MeV}$. This process leaves the system in an high excited intermediate state which can lead to the emission of slightly excited nuclear or hypernuclear fragments. In the next stage, those hyperfragments which are in a excited nuclear level decay first to the ground state via electromagnetic transitions, and then via the weak decay (mesonic and non–mesonic decay modes). The identification of double hypernuclei will be performed by using the information obtained from the electromagnetic transitions, and from the detection of weak decay charged products. Additionally, the associated antihyperons $\overline{\Xi}$ (or even positive kaons) produced as a result of their annihilation with nucleons of the target nucleus, can be used for tagging the double hypernuclei production over the background reactions.

In the present work the feasibilty of performing γ spectroscopy of double Λ hypernuclei at the $\overline{\textsf{P}}$ANDA experiment will be investigated by means of a Monte Carlo simulation.

The major challenges that the simulation has to deal with are on the one hand the optimization of a dedicated detector layout for accurate measurements in a high rate environment and on the other hand, to provide effective analysis strategies for the hypernuclei spectroscopy. These two major items will be treated separately in the present work. Indeed, it must show that excited double hypernuclei can be produced significantly in order to perform high resolution gamma spectroscopy with germanium detectors. In addition, analysis strategies must also be optimized to ensure a unique identification of the single and double hypernuclei produced.

Accordingly, the structure of the present work will be introduced in the next paragraph. In Chapters 1 and 2, the general aspects of hypernuclear physics will be treated in detail, giving an overview of the single and double Λ hypernuclei production mechanism, and of the experimental developments of the last decades. These two first chapters will serve as motivation to introduce the hypernuclear physics program at the $\overline{\textsf{P}}$ANDA experiment. The main parts of the $\overline{\textsf{P}}$ANDA detector will be presented in Chapter 3. However, due to the complexity of the hypernuclear production mechanism, the $\overline{\textsf{P}}$ANDA detector will need to be extended to accomodate a devoted detector setup for the hypernuclear project. This devoted detector setup consisting of a primary nuclear target, a secondary active target and a germanium array detector, will be introduced in Chapter 4. In addition, the requirements of these three components will be studied to optimize the first step of the hypernuclear production process, which comprises of the production of $\Xi^- + \bar{\Xi}$ pairs in the primary target, the deceleration and capture of Ξ^- in the secondary active target, and the evaluation of possible radiation damage on the germanium detectors due to the hadronic background interactions. In Chapter 5, the second step of the hypernuclear production mechanism will be studied. This is related to the production of excited double Λ hypernuclei via a statistical decay model. In this chapter, the population of particles stable excited states in double hypernuclei after the capture of a Ξ^- will be investigated. This new technique offers the possibility of studying the feasibility to perform gamma spectroscopy of double hypernuclei at $\overline{\textsf{P}}$ANDA. Accordingly a full hypernuclear event will be simulated. The different steps of this simulation will be presented in Chapter 6. The analysis of this event will be performed by using a strategy which consists of using the photons emitted from the electromagnetic deexcitations of the produced double hypernuclei, and the momenta correlation of the negative pions from their sequential mesonic decay. With this technique, some of the electromagnetic transitions can be uniquely assigned to the corresponding hypernuclide species. The background contribution has also been studied. Moreover, a method based on the time measurement has been developed for background rejection. Due to the vicinity of the germanium array detectors to the $\overline{\mathsf{P}}\mathsf{ANDA}$ spectrometer, its energy resolution can be affected. As a consequence, an exhaustive study has been performed in order to evaluate the possible damage under these conditions. The description of this measurement and the results of its analysis can be found in Chapter 8. Furthemore, a method to correct possible distortion of the energy resolution will be presented. To conclude, the results of the present work will be summarized and briefly discussed in Chapter 9, followed by an insight into further improvements.

Chapter 1

Topics on hypernuclear physics

1.1 Motivation

While it is difficult to study nucleons deeply bound in ordinary nuclei, a Λ hyperon not suffering from Pauli blocking can form deeply bound hypernuclear states which are directly accessible in experiments. In turn, the presence of a hyperon inside the nuclear medium may give rise to new nuclear structures which cannot be seen in normal nuclei consisting only of nucleons. Furthermore, a comparison of ordinary nuclei and hypernuclei may reveal new insights in key questions in nuclear physics like for example the origin of the nuclear spin-orbit force [8].

An important scope is to measure the level spectra and decay properties of hypernuclei in order to check the energy spectra and wave functions predicted by microscopic structure models. Indeed recent calculations of light nuclei based on modern nucleon-nucleon potentials, which also incorporate multi-nucleon interactions, are able to describe the excitation spectra of light nuclei with a very high precision of 1-2% [9, 10, 11, 12]. A challenging new approach to hyperon interactions and structure of hypernuclei is the relativistic density functional theory. This is a full quantum field theory enabling an *ab initio* description of strongly interacting many-body system in terms of mesons and baryons by deriving the in-medium baryon-baryon interactions from free space interactions by means of Dirac-Brueckner theory [13, 14]. The field theoretical approach is also the appropriate starting point for the connection to QCD-inspired descriptions based for example on chiral effective field theory (χEFT) [15, 16]. At present, χEFT is well understood for low-energy meson-meson [17] and meson-baryon dynamics in the vacuum [18] and infinite nuclear matter[19, 20]. A task left for the future is to obtain the same degree of understanding for processes in a finite nuclear environment. Present nuclear structure calculations of the light nuclei in χEFT [12, 21, 22, 23] signal significant progress.

It is this progress made in our theoretical understanding of nuclei which nurtures the hope that detailed information on excitation spectra of hypernuclei and their structure will provide unique information on the hyperon-nucleon and - in case of double hypernuclei – on the hyperon-hyperon interactions.

In this chapter the main topics on hypernuclear physics, which have been studied during the last decade, will be reviewed. In particular, a description of the main mechanisms which contribute to the production of Λ hypernuclei will be presented. In addition, an overview of the the present status of the spectroscopy of Λ hypernuclei will be given.

1.2 General Aspects on Λ–Hypernuclei

A hypernucleus is a nucleus in which one or more nucleons have been replaced by hyperons (Λ, Σ, Ξ). Hypernuclei are denoted with the following notation ${}^{A+Y}_{Y}Z$, where Z accounts for the number of protons, A represents the total numbers of nucleons(protons and neutrons) and Y is the number of hyperons. A Λ–nucleons bound state is very different from an ordinary nucleus ${}^{A}Z$. When a Λ hyperon replaces one of the nucleons, the original nuclear structure changes to a system composed by the hyperon and the core ${}^{A-1}Z$ of the remaining nucleons. The Λ–core system is rearranged in order to generate a bound state, maximizing the binding energy (B_Λ). The ground state of a hypernucleus is defined as the state in which the nuclear core lies in its ground state and the Λ hyperon occupies the lowest energy state. All the other possible configurations correspond to excited states. As a consequence, the binding energy of a Λ hyperon at the ground state can be deduced as,

$$\mathrm{B}_\Lambda = m_{core} + m_\Lambda - m_{Hyp} \tag{1.1}$$

where

1. $m_{core} = m({}^{A-1}Z)$: mass of the nuclear core.

2. m_Λ : Λ hyperon mass.

3. $m_{Hyp} = m({}^{A}_{\Lambda}Z)$: measured mass of hypernucleus.

Here m_{core} and m_Λ are known, additionally one has to calculate the hypernucleus mass m_{Hyp} from the momentum of the incident and reaction particles since the hypernucleus production is just a two-body kinematic process.

Once a Λ–core bound state occurs, the Λ is not subjected to Pauli–Principle, due to the the strangeness of the hyperon, which gives it one degree of freedom more and makes it distinguishable from the nucleons. As a consequence, it will be able to move in the nuclear medium interacting weakly with rest of nucleons. This property leads to think of the possibility to describe the Λ hyperon as single–particle objects moving in a mean field in a similar way as it is described by the shell model. In fact, the appearance of the first hypernuclear spectra corroborated this idea, and it helped to conclude that the well defined binding energies of the observed low–lying hypernuclear states could be described by the single–particle formalism. Moreover, this description is without the complications encountered in ordinary nuclei, like for example pairing interactions. Thus, the hyperon, in general, inside a hypernucleus can be used as a probe for the inspection of the nuclear medium.

The ΛN interaction is the first step toward the unified understanding of general baryon–baryon interactions beyond the well–known NN interaction. Since the ΛN interaction contains new information on the baryon–baryon interactions even at the limit of flavour SU(3) symmetry, the knowledge of the elementary hyperon–nucleon (YN) and hyperon–hyperon (YY) interaction is crucial to describe the structure of these strange systems.

In this respect, an interesting question to be answered is whether the ΛN interaction can be represented by meson exchange models in a consistent way with the NN interaction or one has to consider the quark–gluon degree of freedom. Furthermore, the ΛN interaction is the most fundamental subject in the study of hypernuclei as the NN interaction in the study of ordinary nuclei.

1.2.1 The Spin–dependent ΛN interaction

The elementary interaction of a Λ with a nucleon are poorly known, mainly due to the short lifetime of hyperons, which makes practically impossible the experimental determination of the Λ–N interaction through Λ scattering.

However, hypernuclear physics allows the study of the baryon–baryon interaction at a normal nuclear densities since as discussed before, an effective Λ–N potential can be extracted from hypernuclear spectra. Furthermore, the hypernucleus can be described by a set of single–particle basis states assuming that a nuclear Λ can be well represented by a superposition of a few single–particle states, interacting via an effective ΛN potential within the nuclear medium. This single–particle field can be constructed either phenomenologically from the experimental data on Λ binding energies or from the elementary ΛN interaction in a reduction scheme as e.g., the many–body hadronic problem. Furthermore, the decomposition of ΛN interaction into the different spin-dependent contributions may be analyzed. For these contributions, significantly different predictions exist for example from meson exchange-current and quark models.

According to that, the effective two-body ΛN in a Λ–hypernuclei can be expressed in the form;

$$\begin{aligned} V_{\Lambda N}(r) &= V_0(r)+V_\sigma(r)\sigma_N\cdot\sigma_\Lambda+V_\Lambda(r)l_{\Lambda N}\sigma_\Lambda+V_N(r)l_{\Lambda N}\sigma_N \\ &\quad +V_T(r)\{\frac{3(\sigma_N r)(\sigma_\Lambda r)}{r^2}-\sigma_N\sigma_\Lambda\} \end{aligned} \tag{1.2}$$

It consist of central force (V_0(r)) and four spin–dependent terms, spin–spin force ($V_\sigma(r)\sigma_N\cdot\sigma_\Lambda$), Λ–spin–dependent spin–orbit force ($V_\Lambda(r)l_{\Lambda N}$), and tensor force ($V_T(r)\{\frac{3(\sigma_N r)(\sigma_\Lambda r)}{r^2}-\sigma_N\sigma_\Lambda\}$). In the above equation, $l_{\Lambda N}$ and $\vec{r}$ are the Λ–N relative orbital angular momentum and position respectively, σ denotes the spin of each particle. Additionally, the potential contains both symmetric and anti–symmetric whose combination is expressed as $\frac{1}{2}(S_N \pm S_Y)$, where (S_N) and (S_Y) are the nucleon and hyperon spin operators. For p–shell hypernuclei, the radial integral of the spin–dependent terms over the shell model wavefunctions are often expressed as Δ, S_Λ, S_N and T. The definition of Δ is given by

$$\Delta=\int \phi^*_{\Lambda N}(\vec{r})V_\sigma\phi^*_{\Lambda N}(\vec{r})d\vec{r} \tag{1.3}$$

where ($\phi^*_{\Lambda N}(\vec{r})$ is the ΛN relative spatial wavefunction for $p_N s_\Lambda$ state. Similarly, the other are defined from V_Λ, V_N, and V_T. They can be treated as parameters which are to be determined phenomenologically by fitting the data of p–shell hypernuclear level energies. It is also known that the behaviour of the Λ–N interaction is much different from the NN interaction. From Λ–hypernuclear binding energies, the depth of the potential for a Λ particle in nuclear matter has been derived to be 28 MeV [24] with the assumption of Wood–Saxon potential, representing a 2/3 of that for a nucleon. This weakness comes from the fact that one–pion exchange is forbidden due to isospin conservation. Moreover, spin–dependent components of the Λ–N effective interaction are expected to be much smaller than those of the NN interaction. Additionally, the antisymmetric spin orbit term vanishes for the N–N potential due to the Pauli principle. The "hypernuclear fine structure", namely, the level splittings due the spin–dependent Λ–N effective interaction between a Λ and a core nucleus, are known to be as small as an order 100 keV or less, which represents a big challenge for their measurement.

1.2.2 Specific production reactions

Hypernuclei can be produced by using strong processes in which a particle (generally a pion or a kaon) hits a nucleus. Since strangeness has to be conserved, one can use the following production reactions:

- Process with strangeness exchange:

$$\begin{aligned} K^- n &\longrightarrow \Lambda\pi^- \\ K^- p &\longrightarrow \Lambda\pi^0, \end{aligned} \tag{1.4}$$

- Processes with associated production of strange hadrons:

$$\begin{array}{rcll} \pi^- n & \longrightarrow & \Lambda K^+, & \text{pion} - \text{induced} \\ pN & \longrightarrow & \Lambda K^+ N & \text{proton} - \text{induced} \\ \gamma p & \longrightarrow & \Lambda K^+, & \text{photoproduction} \\ e^- p & \longrightarrow & e^- \Lambda K^+, & \text{electroproduction} \end{array}$$

- Reactions in which strangeness exchange and associated production of strangeness are combined (used for the production of S = -2, -3 hypernuclei):

$$\begin{array}{rcl} K^- p & \longrightarrow & \Xi^- K^+, \\ & & \Xi^0 K^0, \\ & & K^+ K^0 \Omega^-, \\ K^- n & \longrightarrow & \Xi^- K^0, \\ pp & \longrightarrow & \Xi^0 K^+ K^+ n, \\ p\overline{p} & \longrightarrow & \Xi^- \overline{\Xi} \end{array}$$

In general, the hypernuclei production is basically based on the production of hyperons within the nuclear medium via the following process,

$$aN \rightarrow Yb \tag{1.5}$$

where a is the projectile interacting with a nucleon N to produce a hyperon Y and a residual particle b.

The above considered reactions have different characteristics depending on their kinematics. Since these reactions require stable target nuclei, hypernuclei accessible by these reactions are limited. Fig. 1.1 displays the regions of the hypernuclear chart with proton number up to Z = 18 which can be explored by this technique. The drip-lines for single Lambda hypernuclei were predicted by [24]. The different colors indicate n→ Λ, p→ Λ and pp→ Λn reactions. For Z $<$ 16 the reactions populate distinct regions of hypernuclei without overlap. This nicely illustrates the complementarity of the various production mechanisms and the need to study single hypernuclei with different reactions.

In order to produce a hypernucleus, the hyperon emerging from the reaction has to remain inside the nuclear system. The formation probability of a hypernucleus depends on the energy transferred in the production. When the momentum transferred to the hyperon,q_Y is much larger than the nuclear Fermi momentum k_F, the hyperon has a very small sticking probability and it leaves the nucleus. Instead, when $q_Y \lesssim k_F$, the hyperon is created with high probability in a bound state. In Fig. 1.2 the momenta transferred to the

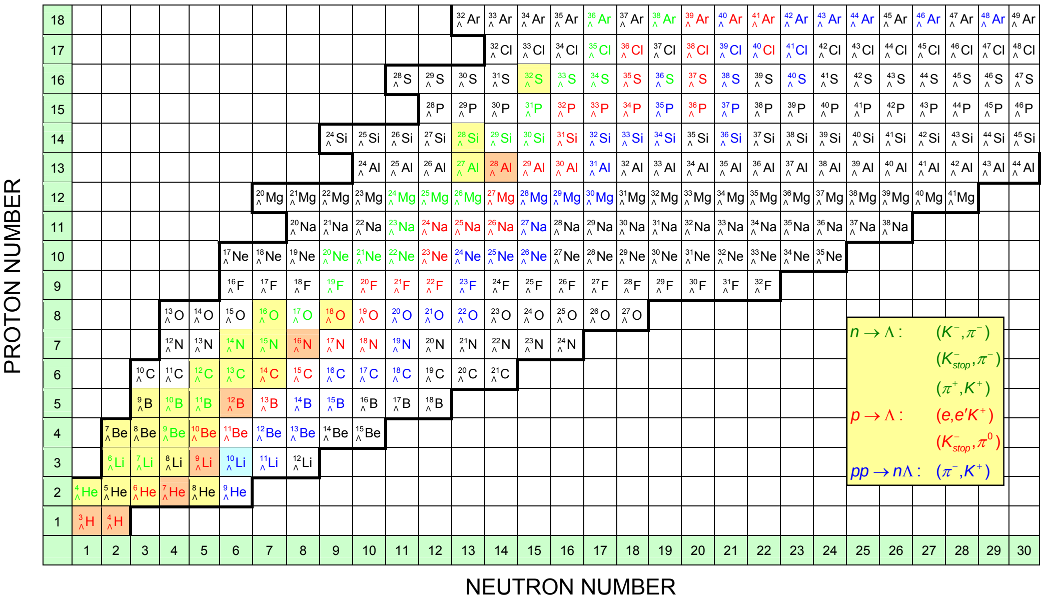

Figure 1.1: Hypernuclei accessible by reaction spectroscopy. The boundaries at the neutron- and proton rich side mark drip-lines predicted by [24].

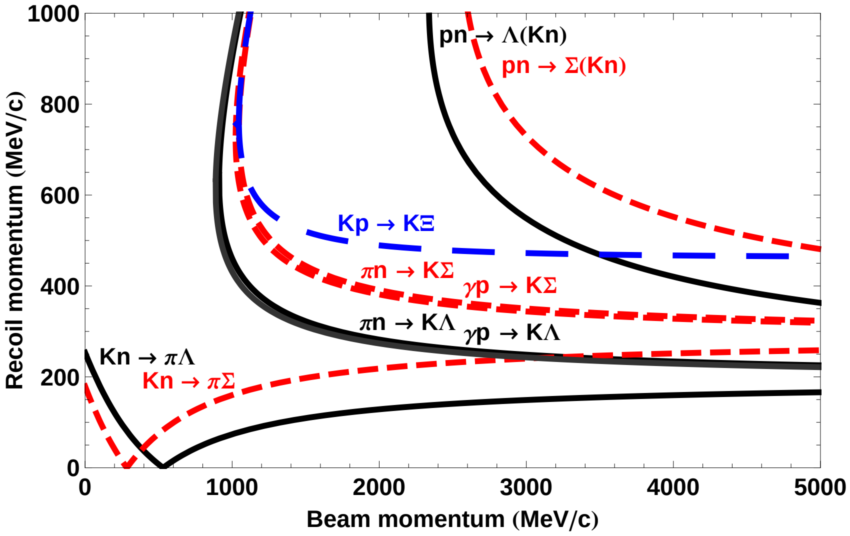

Figure 1.2: Momentum q_Y transferred to the Y hyperon [26] as a function of the projectile momentum p_{Lab} in the laboratory frame for the reaction $aN \rightarrow Yb$ at the laboratory angle $\theta_{b,Lab} = 0°$.

hyperon Y in the reaction $N(a,b)Y$ are shown as a function of the projectile momentum p_a at $\theta = 0°$ in the laboratory frame. With the exception of the

$(K^-, \pi^\pm)$ reactions, in the other ones reported in the figure the hyperon cannot be produce at rest since q_Y decreases with increasing projectile momentum but it remains finite for high p_a. In this situation the hyperon is produced with a non-negligible probability above its emission threshold, namely with a non–zero binding energy B_Λ (quasi–free production). Some hypernuclear states in the continuum may be quasi–bound states, where nucleons and/or cluster of nucleons are emitted instead of hyperons.

1.2.2.1 The $(K^-, \pi^\pm)$ strangeness exchange reactions

Depending on the momentum of the incident kaon one can have In–flight production or the production with K^- at rest. These two processes differ both in branching ratio for hyperon production and in kinematics. In the $(K^-, \pi^\pm)$ reactions the incident K^- transforms the struck neutron (proton) into a Λ and a $\pi^\pm$ is emitted with an energy spectrum which is directly related to the populated hypernuclear level. The reaction $n(K^-, \pi^-\Lambda)$, (used for the first time at CERN [27] and BNL [28] to produce Λ) can create the hyperon at rest ($q_Y = 0$). By considering, as an approximation, the initial neutron in $n(K^-, \pi^\pm\Lambda)$ at rest, the transferred momentum is zero $\vec{p}_K = \vec{p}_\pi \equiv \vec{p}$, and the pion is emitted at $\theta = 0°$ in the laboratory frame. Thus, from energy–momentum conservation:

$$\sqrt{\vec{p}^2 + m_K^2} + m_N = m_\Lambda + \sqrt{\vec{p}^2 + m_\pi^2} \tag{1.6}$$

and the momentum for the production of the recoilless Λ (called magic momentum) can be derived as follows:

$$E_K \equiv \sqrt{\vec{p}^2 + m_K^2} = \frac{m_K^2 - m_\pi^2 + (m_\Lambda - m_N)^2}{2(m_\Lambda - m_N)} \Rightarrow p \simeq 530\, MeV. \tag{1.7}$$

Since both the initial K^- and the final pion are strongly absorbed in the nucleus, the kaon induced reactions preferentially populate less bound single particle Λ–levels and they have been only employed for s- and p-shell hypernuclear studies. Moreover, the low intensity and poor resolution of the kaon beams hinder the use of the $(K^-, \pi^\pm)$ reactions. By using the strangeness exchange reaction at $\theta = 0°$, the hyperon is predominantly produced in a state with the same quantum numbers of the struck nucleon, namely the neutron hole and the Λ are coupled to $J^P = 0^+$ and the $\Delta l = 0$(substitutional reaction). By increasing θ the relative importance of $\Delta l = 1{,}2$, etc. transitions increases, and hypernuclear states with higher spin can be produced. From measures at both $\theta \simeq 0°$ and $\theta > 10 - 15°$ it has been possible to study a large part of the level structure of light hypernuclei [29, 28]. In the last 20 years the strangeness exchange reaction has been used at BNL [30, 31] for production and decay studies of hypernuclei from ${}^4_\Lambda H$ to ${}^{12}_\Lambda C$. However, because of the small momentum transfer and the large background coming from in-fight kaon decays, the measurement could not be extended to heavy hypernuclei.

The (stopped K^-, π^-) reaction has been used at KEK [32, 33, 34], and at DaΦne [198], the Frascati Φ–factory. Moreover, this process was the standard method to produce Λ–hypernuclei in emulsion and in bubble chambers experiments during the 1960s. When the K^- is stopped in the target, it is captured into an atomic level and then, after cascade down to inner levels, it is absorbed in the nuclear surface, converting a nucleon into a Λ. The momentum transferred to the produced Λ is closed to k_F (for 0^0 scattering angle, $q_\Lambda \simeq 250\,MeV$). The process with absorption of a kaon at rest in nuclei has the good feature of a large production yields and a large number of hypernuclear states is accessible. Moreover, differently from the in–flight reaction, it allows a clean separation of the quasi–free hypernuclear production (because of the larger transferred momentum), resulting in a better determination of the weak decay rates, especially in light systems.

1.2.2.2 The n$(\pi^+, K^+)\Lambda$ strangeness exchange reactions

When a π^- hits a neutron, by the creation of a $s\overline{s}$ quark pair one has the associated production of two strange hadrons in the final state: the s–quark becomes a constituent of Λ and the $\overline{s}$ is transferred to the meson, which becomes a K^+. The n$(\pi^+, K^+)\Lambda$ reaction is complementary to the n$(K^-, \pi^-)\Lambda$ one, and it preferentially populates bound states with high spin configurations. It produces almost background free spectra and it has the advantages of using good quality and large intensity pion beams. Since the mass of the final hadrons pair is sizeable larger than the mass of the initial particles, the n$(\pi^+, K^+)\Lambda$ reaction takes place with a quite large momentum transferred to the hyperon: ($q_\Lambda \simeq 300 - 400\,\mathrm{MeV}$) at 0^0 scattering angle.

The associated production reaction has been used for the first time at BNL [35, 36] for ${}^{12}_{\Lambda}$C and at KEK [37, 38, 39]. Moreover, (π^+, K^+) spectroscopy experiments at KEK [37, 40] observed double-peak structures in ${}^{12}_{\Lambda}$C, ${}^{16}_{\Lambda}$O, ${}^{51}_{\Lambda}$V and ${}^{89}_{\Lambda}$Y, interpretable as Λ spin–orbit splittings. The magnitude of the shifts suggests a Λ–nucleus spin–orbit interaction stronger than the one extracted from (K^-, π^-) experiments.

1.2.2.3 The p$(e, e'K^+)\Lambda$ reaction

In the electroproduction reaction a virtual photon is produced by the interaction between the incident e^- and the target nucleus, and can be absorbed by a quark of a nucleon, giving rise to an $s\overline{s}$ quark pair; then the latter can combine with the quarks initially contained in the nucleon generating a ΛK^+ pair. The electroproduction reaction is also characterized by a large momentum transfer and by the dominance of the spin–flip amplitudes in the elementary process p$(\gamma, K^+)\Lambda$. This reaction could complement our knowledge of hypernuclear spectroscopy derived from studies performed with mesons beams. Indeed, the high precision of electron beams can considerably improve the quality of experimental data. Moreover, the meson induced reactions hardly produce ground states and deep–hole states in heavy hypernuclei, because of the strong pion and kaon absorption in the nuclear medium. Spectroscopic studies with high resolution have already been started at TJNAF laboratories [41] and are planned at MAMIC [42] in the next future.

1.2.2.4 Λ–Hypernuclei formed in heavy–ion collisions

Hypernuclear production via heavy ion collision was first studied by Kerman and Weiss [43]. In high energy heavy ion collisions the participant–spectator model explains the general feature of the reaction. The overlapped region between the two nuclei (participants) participates in the collision, while the nucleons in the off–overlapping region (spectators) pass by each other without being much influenced. Hyperons such as Λ are produced in the participants region at around the mid–rapidity. Due to their wide rapidity distribution, hypernuclei may be produced with a coalescence of hyperon(s) in the projectile fragments, what leaves the hypernuclei with a velocity closed to the one of the projectile. As a consequence the effective lifetime of the produced hyperon is longer than at rest because of the large Lorentz factor, what makes possible the study of hypernuclei decays in–flight. In the late 80s, hypernuclear production with heavy ions was performed in JINR [44, 45]. Recently they have been also produced and identified by BNL AGS–E864 experiment [46]. Futures experiments with heavy ion beams at relativistic energies with associated kaon production are planned at the future facility of GSI [47].

1.2.3 Decay modes of Λ–Hypernuclei

In the production of hypernuclei, the populated state may be highly excited, above one or more threshold energies for particle decays. These states are unstable with respect to the emission of the hyperon, of photons and nucleons. The spectroscopic studies of strong and electromagnetic de–excitations give information on the hypernuclear structure which is complementary to that one can extract from excitation functions and angular distribution studies. Once a hypernucleus is stable respect to electromagnetic and strong processes, it has reached its ground state, with the hyperon in the 1 s level, and it can only decay via a strangeness-changing weak process through the disappearance of the hyperon.

1.2.3.1 Electromagnetic decay of Λ–Hypernuclei

In the weak–coupling picture for a Λ hyperon and a core nucleus, γ transitions in hypernuclei are classified into three types:

1. core transitions,
2. Λ spin–flip transitions,
3. and Λ inter–shell transitions.

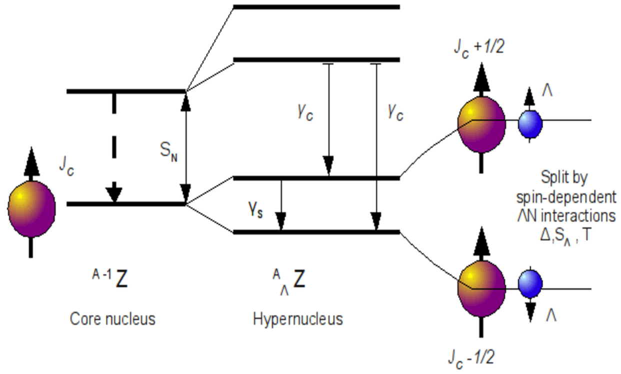

Figure 1.3: schematic view of low–lying levels of a Λ hypernucleus and their γ transitions. γ_C and γ_S are referred to as the "core transition" and "Λ spin–flip transition", respectively.

Fig. 1.3 illustrates schematically the low–lying levels of a hypernucleus. Each state of the core nucleus with non–zero spin (J_C) is split into a doublet ($J_C + 1/2,\ J_C - 1/2$) by the spin coupling between the Λ hyperon and the core nucleus. A transition connecting different doublets (γ_C in Fig. 1.3 is called "core transition". It is induced by a transition in the core nucleus itself (shown with a dashed arrow in Fig. 1.3). This type of transition was first observed for $^{7}_{\Lambda}Li$ ($5/2^+ \rightarrow 1/2^+$) and $^{9}_{\Lambda}Be(5/2^+, 3/2^+ \rightarrow 1/2^+)$. A transition from the upper to the lower member of the same doublet (γ_S in Fig. 1.3) is a M1 transition caused by a flip of the Λ spin. It is called "Λ spin–flip transition". When the doublet spacing energy is less than $\simeq 100\,\mathrm{keV}$, the Λ spin–flip rate is generally smaller than the weak decay rate, and the γ transition is not to be observed. The other type of hypernuclear γ transition is a E1 transition in which the Λ hyperon changes the major shell orbit from p_Λ to s_Λ ("Λ inter–shell transition"). This transitions are not expected to be seen often in light p–shell hypernuclei because the transition energy is usually higher than the nucleon separation energies. On the contrary, Λ inter–shell transitions are expected to be observed in medium and heavy hypernuclei.

1.2.3.2 Weak Decay of Λ–Hypernuclei

In this section the various weak decay modes of Λ–Hypernuclei are described: indeed in a nucleus Λ can decay by emitting a nucleon and a pion (*mesonic mode*) as it happens in free space, but its (weak) interaction with the nucleons opens new channels, customary indicated as *non–mesonic decay modes*. These are dominant decay channels of heavy nuclei, where the mesonic decay is disfavoured by the Pauli blocking principle. In particular, one can distinguish between one–body and two–body–induced decays, according whether the hyperon interacts with a single nucleon or with a pair of correlated nucleons. Furthermore, an interesting rule for the amount of isospin violation ($\Delta I = 1/2$) is strongly suggested by the mesonic decay of free Λ's, whose branching ratios are almost in the proportion 2 to 1, according to whether π^-p or π^0n are emitted. This totally empirical rule has been generally adopted in most of the models proposed for the evaluation of the Λ–hypernuclei widths.

Mesonic decay mode The mesonic mode is the main decay channel of a Λ in free space:

$$\begin{aligned}\Lambda \;\rightarrow\; & \pi^- p \qquad \text{B.R.} = 63.9 \times 10^{-2} \\ & \pi^0 n \qquad \text{B.R.} = 35.8 \times 10^{-2}\end{aligned}$$

with a lifetime $\tau_\Lambda^{\text{free}} \equiv \hbar/\Gamma_\Lambda^{\text{free}} = 2.632 \times 10^{-10}$ s.

The Λ hyperon is an isospin singlet ($I_\Lambda = 0$), while the πN system can be either in $I_\Lambda = 1/2$ or $I_\Lambda = 3/2$ isospin states. The customary angular–momentum coupling implies

$$|\pi^- p\rangle = \sqrt{\frac{1}{3}}|\frac{3}{2}, -\frac{1}{2}\rangle - \sqrt{\frac{2}{3}}|\frac{1}{2}, -\frac{1}{2}\rangle \tag{1.8}$$

$$|\pi^0 n\rangle = \sqrt{\frac{2}{3}}|\frac{3}{2}, -\frac{1}{2}\rangle - \sqrt{\frac{1}{3}}|\frac{1}{2}, -\frac{1}{2}\rangle \tag{1.9}$$

Hence the ratio of amplitudes for $\Delta I = 1/2$ transition yields

$$\frac{\Gamma^{\text{free}}_{\Lambda\to\pi^- p}}{\Gamma^{\text{free}}_{\Lambda\to\pi^0 n}} \simeq \frac{|\langle\pi^- p|T_{1/2,-1/2}|\Lambda|^2}{|\langle\pi^0 n|T_{1/2,-1/2}|\Lambda|^2} = |\frac{\sqrt{2/3}}{\sqrt{1/3}}|^2 = 2, \tag{1.10}$$

while a $\Delta I = 3/2$ process should give

$$\frac{\Gamma^{\text{free}}_{\Lambda\to\pi^- p}}{\Gamma^{\text{free}}_{\Lambda\to\pi^0 n}} \simeq \frac{|\langle\pi^- p|T_{3/2,-1/2}|\Lambda|^2}{|\langle\pi^0 n|T_{3/2,-1/2}|\Lambda|^2} = |\frac{\sqrt{2/3}}{\sqrt{1/3}}|^2 = \frac{1}{2}. \tag{1.11}$$

Experimentally the above ratio turns out to be

$$\{\frac{\Gamma^{\rm free}_{\Lambda\to\pi^- p}}{\Gamma^{\rm free}_{\Lambda\to\pi^0 n}}\}^{\rm Exp} \simeq 1.78, \qquad (1.12)$$

which is very close to 2 and strongly suggests the $\Delta I = 1/2$ rule on the isospin change. From the above considerations and from analysis of the Λ polarization observables it follows that the measured ratio between $\Delta I = 1/2$ and $\Delta I = 3/2$ transition amplitudes is very large, so around 30. The $\Delta I = 1/2$ rule is based on experimental observations but its dynamical origin is not yet understood on theoretical grounds. Actually the rule is slightly violated in the Λ free decay, and it is not clear whether it is a universal characteristic of all non–leptonic processes with $\Delta S \neq 0$. The Λ free decay in the standard model can occur through both $\Delta I = 1/2$ and $\Delta I = 3/2$ transitions, with comparable strengths: an s quark converts into a u quark through the exchange of a W boson. Moreover, the effective 4–quark weak interaction derived from the Standard Model including QCD corrections gives too small $|A_{1/2}/A_{3/2}|$ ratios, $\simeq$ 3-4, as a calculated at the hadronic scale of about 1 GeV by using renormalization group techniques [48, 49]. Therefore, non–perturbative QCD effects at low energy (such as hadron structure and reaction mechanisms), which are more difficult to handle, and/or final–state interactions could be responsible for the enhancement of $\Delta I = 1/2$ amplitude and/or the suppression of the $\Delta I = 3/2$ amplitude. The Q–value for free–Λ mesonic decay at rest is $\mathrm{Q}_\Lambda \simeq m_\Lambda - m_N - m_\pi \simeq 40\,MeV$. Then taking into account energy–momentum conservation, $\mathrm{m}_\Lambda \simeq \sqrt{\vec{p}^2 + m_\pi^2} + \sqrt{\vec{p}^2 + m_N^2}$ in the center of mass system and the momentum of the final nucleon turns out to be $p \simeq$100 MeV. Inside a hypernucleus, the binding energies of the recoil nucleon ($\mathrm{B}_N \simeq -8\,MeV$ and the Λ ($\mathrm{B}_\Lambda \simeq -27\,MeV$ tend to further decrease Q_Λ ($\mathrm{Q}_{\Lambda,\mathrm{bound}} = Q_\Lambda + B_\Lambda - B_N$) and hence p. As a consequence, in nuclei the Λ mesonic decay is disfavoured by the Pauli principle, particularly in heavy systems. It is strictly forbidden in normal nuclear matter (where the fermi momentum is $\mathrm{k}_F^0 \simeq$270 MeV), while in finite nuclei (Ref. [56]) it can occur because of three important effects:

1. In nuclei the hyperon has a momentum distribution (being confined in a limited spatial region) that allows larger momenta to be available to the final nucleon.

2. The final pion is attracted by the medium such that for fixed momentum $\vec{q}$ it has an energy smaller than the free one, and consequently, due to energy conservation, the final nucleon again has more chance to come out above the Fermi surface. Indeed, it has been shown that the pion distortion increases the mesonic width by one or two orders of magnitude for very heavy hypernuclei (A$\simeq$200) with respect to the value obtained without the medium distortion.

3. At the nuclear surface the local Fermi momentum is considerably smaller than k_F^0, and the Pauli blocking is less effective in forbidding the decay.

In any case the mesonic width decreases rapidly as the nuclear mass number A of the hypernucleus increases.

Non–mesonic decay mode In hypernuclei the weak decay can occur through processes which involve a weak interaction of the Λ with one or more nucleons. Sticking to the weak hadronic vertex $\Lambda \to \pi N$, when the emitted pion is virtual, then it will be absorbed by the nuclear medium, resulting in a non–mesonic process of the following type:

1. $\Lambda n \to nn \qquad (\Gamma_n)$,
2. $\Lambda p \to np \qquad (\Gamma_p)$,
3. $\Lambda NN \to nNN \qquad (\Gamma_2)$

The total weak decay rate of a Λ hypernucleus is then

$$\Gamma_T = \Gamma_M + \Gamma_{NM},$$

where

$$\Gamma_M = \Gamma_{\pi_-} + \Gamma_{\pi_0}, \qquad \Gamma_{NM} = \Gamma_1 + \Gamma_2 \Gamma_1 = \Gamma_n + \Gamma_p,$$

and the lifetime is $\tau = \hbar/\Gamma_T$. Channel 3. can be interpreted assuming that the pion is absorbed by a pair of nucleons, correlated by the strong interaction. Obviously, the non–mesonic processes can also be mediated by the exchange of more massive mesons than the pion(see Fig. 1.4). The non–mesonic mode is *only possible in nuclei* and, nowadays, the systematic study of the hypernuclear decay is the only practical way to get information on the weak process $\Lambda N \to NN$ (which provides the first extension of the weak $\Delta S = 0$ $NN \to NN$ interaction to strange baryons), specially on its parity–conserving part, which is masked by the strong interaction in the weak $NN \to NN$ reaction. The final nucleons in the non–mesonic processes emerge with large momenta: disregarding the Λ and nucleon binding energies and assuming the available energy $Q = m_\Lambda - m_N \simeq 176\,\mathrm{MeV}$ to be equally splitted among the final nucleons, it turns out that $p_N \simeq 420\dot{\mathrm{M}}\mathrm{eV}$ for the one–nucleon–induced channels 1. and 2. and $p_N \simeq 340\,\mathrm{MeV}$ in the case of two–nucleon–induced mechanism (channel 3). Therefore, the non mesonic mechanism dominates over the mesonic mode for all but the s–shell hypernuclei. Only for very light systems the two decay modes are competitive(see Fig. 1.5).

Since the non–mesonic channel is characterized by large momentum transfer, the details of the hypernuclear structure do not have a substantial influence. On the other hand, NN and ΛN short–range correlations turn out to be very important. It is interesting to observe that there is an anticorrelation between mesonic and non–mesonic decay modes such that the experimental lifetime is quite stable from light to heavy hypernuclei [50, 51]. Since the mesonic width is less than 1% of the total width for A > 100, the above consideration implies that the non–mesonic rate is rather constant in the region of heavy hypernuclei.

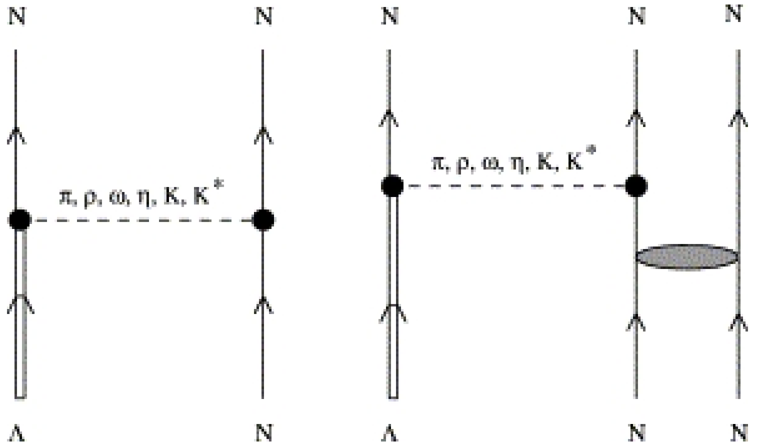

Figure 1.4: Left: one–nucleon– and right: two–nucleon–induced Λ decay in nuclei.

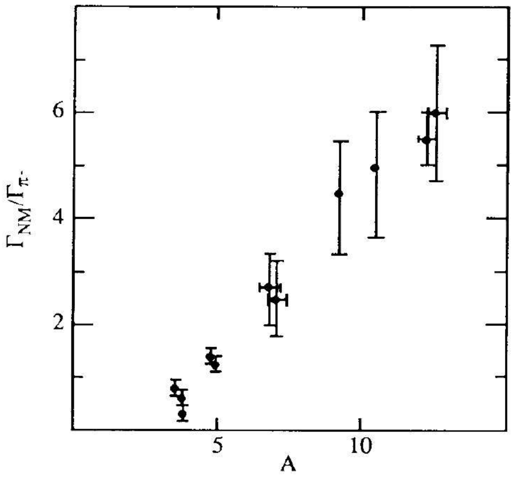

Figure 1.5: Measured ratio of nonmesonic ($\Lambda N \to NN$) to mesonic ($\Lambda \to N\pi$) hypernuclear decay widths as a function of the nuclear mass [52].

1.3 Spectroscopy of Λ Hypernuclei

Nuclear physics has been very successful in interpreting low–lying excited nuclear states. But very little is known about the relationship between the fundamental interactions of quasiparticles in nuclei. The comparison between the effective Λ-nucleus, the nucleon–nucleus interaction and their fundamental interaction should give additional constraints, which would be of great help in solving this hinterto almost completely neglected problem of nuclear physics. As it was remarked in Sec. 1.2.3, hypernuclei may be produced, in a situation where populated states may be highly excited. As a consequence, it will generally lead to rearrangements of the structure after the production. The energy released in these rearrangements can be removed by gamma rays or Auger–like neutron emission. In a hypernucleus the neutron emission threshold can be lower than the one corresponding to the Λ emission, and at any event, nucleon or small fragments emission can occur even from unbound Λ states. Thus, the final hypernuclear species may differ from the one initially produced. Indeed the hypernuclear system may fragmentate, producing hypernuclei much lower in mass. Therefore, hypernuclei can be studied either by

- production mechanisms where the reaction is constrained by measuring the reaction products; or by

- decay mechanisms where the production processes may be not well determined, but measurement of the decay products is sufficient to determine a specific hypernucleus. In many cases, the measurement of the electromagnetic transitions, of intermediate hypernuclear states (γ–ray spectroscopy) should be accomplished using coincidence between a formation reaction and the emission of photons. That will help to unambiguously identify hypernucleus or even a hypernuclear transition.

In the case of production spectroscopy, hypernuclear states can be directly populated, revealing the level structure in the Λ bound region and can even have access to the observation of excited states between the nucleon emission thresholds and the Λ emission threshold. It provides information on the Λ hypernuclear structure and ΛN interaction through the determination of hypernuclear masses, reaction cross sections, angular distributions, etc. In contrast, γ–ray spectroscopy, can have access only to hypernuclear states below nucleon emission thresholds, but it achieves very high resolution(typically a few keV). It is therefore a powerful spectroscopic tool for the investigation, for example, of spin–dependent ΛN interactions, which requires information on the precise level structure of hypernuclei.

Additionally, if the hypernucleus is to be studied through its production mechanism, the momenta of both the beam and the reaction particles are normally measured using magnetic spectrometers. In order to measure a hypernuclear spectrum one needs to determine the excitation energy or bindings energies of the recoiling hypernuclear system with sufficient resolution to separate states of an MeV or so a apart. Moreover, while energy resolution using spectrometers and meson beams is presently limited to no better than a few MeV, the energy of electromagnetic transitions between states can be measured to a few keV.

1.3.1 Historical background

Hypernuclear investigations has already undergone three stages of development since the first discovery of the hypernucleus in 1953 (see Fig.1.6), was observed through their decays [53]. This observation came shortly after the discovery of the strange particles in bubble chambers [54]. The picture of the event [53] observed by Danysz and Pniewski is shown on the bottom part of Fig. 1.6), where one can see an incoming high energy proton from the top, which collides with

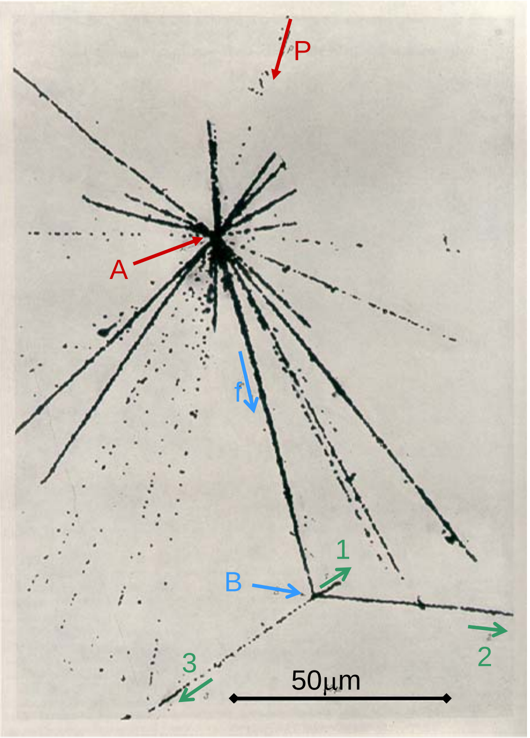

Figure 1.6: First hyperfragment event. This picture shows the event discovered by Danysz and Pniewski [53] where an incident cosmic ray P interacts at A with a heavy nucleus in the nuclear emulsion. A produced hyperfragment f decays at B into three charged particles.

one of the nuclei of the emulsion breaking it into different nuclear fragments (star shape produced in point "A" in the picture). These fragments, after a short path, eventually stops in the emulsion, but one disintegrates into three more particles(point "B " in the figure), revealing the presence of a unstable particle stuck among the nucleons. This event can be interpreted as the weak decay of a light fragment containing a hyperon. In the 1950's the production of hypernuclear states was possible only breaking the target nucleus, due to the high energy of used projectiles. The hyperon was produced by the interaction between the projectile and one of the nucleon of the target nucleus. These particular bound states were named "hyperfragments". Over the years, the production of hypernuclei was limited to the cosmic–ray interactions in emulsion (first stage). The produced system could then be detected in nuclear emulsion by studying the incident and decay tracks created in the reaction.

As time passed new techniques of hyperon production were developed and the hyperon production inside a nucleus without fragmentation became possible, allowing to design experiments focused on the study of selected hypernuclei. Although cosmic rays were then by the time replaced by protons from terrestrial accelerators, emulsions or liquid –bubble chambers coupled with stopping K$^-$ beams remained the detectors and beams of choice (the second stage). This essentially spallation interactions with emulsion atoms limited the production to light hypernuclei where sufficient recoil momentum could be observed and measured. While emulsion provided good energy and position resolution and complete kinematic reconstruction of a hypernuclear decay, scanning was tedious, atomic species limited to those produced from emulsion (or bubble chamber) targets, and statistics were poor. Still the masses of many s– and p–shell hypernuclei were determined by this technique.

The (K$^-_{stop}$, π^-) reaction was for instance the reaction used in the very beginning, where both the kaon and the target are at rest. In this process, hypernuclei masses m_{hyp} were obtained by applying the energy and momentum conservation :

$$m_{target} + m_{K^-} = \sqrt{\vec{p}^{\,2}_{hyp} + m^2_{hyp}} + \sqrt{\vec{p}^{\,2}_{\pi^-} + m^2_{\pi^-}} \tag{1.13}$$

where $m_{target} = m(^AZ)$ is the mass of the target nucleus and $p_{hyp} = p(^{A-1}_{\Lambda}Z)$ is the momentum transferred to the produced hypernucleus. Applying momentum conservation $p_{hyp} = p_{\pi^-}$, then:

$$m^2_{target} + m^2_{K^-} + 2m_{target}m_{K^-} = m^2_{hyp} + \vec{p}^{\,2}_{\pi^-} + m^2_{\pi^-} \tag{1.14}$$

Then the hypernucleus mass m_{hyp} can be evaluated directly from the π^- momentum:

$$m_{hyp} = \sqrt{(m_{target} + m_{K^-})^2 - 2\vec{p}^{\,2}_{\pi^-} + m^2_{\pi^-}} \tag{1.15}$$

In the 1970s, the so–called recoilless method was utilized in a series of experiments at CERN with the in–flight (K$^-$, π^-) reaction. The spectroscopic information was obtained with the missing mass method. The hypernucleus mass m_{hyp} can be then obtained by measuring both the incident K^- momentum p_{K^-} and the outgoing π^- momentum as follows:

$$m_{hyp} = \sqrt{(E_{\pi^-} - E_{target} - E_{K^-})^2 - (p_{\pi^-} + p_{K^-})^2} \tag{1.16}$$

where the pion energy E_{π^-} is calculated as $\sqrt{\vec{p}^{\,2}_{\pi^-} + m^2_{\pi^-}}$. Moreover, additional information on p–shell hypernuclear excited states (small spin–orbit splittings) was extracted for the first time. Nevertheless, the new development of counter experiments have opened a new phase of hypernuclear physics. In fact, the old experiments in the 1960s practically only measured the hyperons bindings energies. Through counter techniques, the experiments have discovered new and interesting features of the hypernuclear structure, although several questions still remain unsolved.

The third stage, which features the use of the (π^+,K$^+$) reaction, began in the mid-1980's at the alternating gradient synchrotron (AGS) of the Brookhaven National Laboratory (BNL), USA and was extended dramatically when the new experimental facilities became available at the 12 GeV proton synchrotron of KEK, Japan. In particular, the superconducting kaon spectrometer (SKS) played a key role in exploring Λ hypernuclear spectroscopy by the (π^+,K$^+$) reaction. From high–quality (π^+,K$^+$) spectra with a energy resolution better than 2 MeV (FWHM), it became possible to study the unique structure of Λ hypernuclei and the nature of the Λ–N interaction quantitatively. Analog to the (K$^-$, π^-) reaction, the spectroscopy information is determined by using the missing mass technique. An example of the good resolution provided by the (π^+,K$^+$) reaction can be seen in Fig. 1.7 and Fig. 1.8, showing the missing mass spectra for the $^{12}_{\Lambda}C$ and $^{89}_{\Lambda}Y$ respectively. On one hand, the two prominent peaks exhibited in both spectra by Fig. 1.7, correspond to $^{12}_{\Lambda}C$ states with Λ hyperons in the s and p orbits. Comparing the SKS [37] spectrum of 1.45 MeV (FWHM) resolution with the BNL [55] spectrum of 3 MeV (FWHM) resolution, the improvement of the spectrum in the region between the two prominent peaks makes possible to disentangle structure such as excited states corresponding to core excitations.

On the other hand, the series of bumps observed in the spectrum in Fig. 1.8 reflects the coupling of a Λ hyperon with a neutron hole state of the $^{88}_{\Lambda}Y$ core. The widths of the states corresponding to the p, d, and f orbits were significantly broader in comparison to the ground state. This effect might reveal a complicated levels structure what becomes more complicated as the hypernuclear mass number increases.

Recently, binding energies of a Λ single–particle orbit for a given l have been derived experimentally as a function of hypernuclear mass number for heavy hypernuclei up to $^{208}_{\Lambda}Pb$ [38]. In Fig. 1.9 the particle hole structure for the wide mass region of is clearly evident. Taking the positions of the major

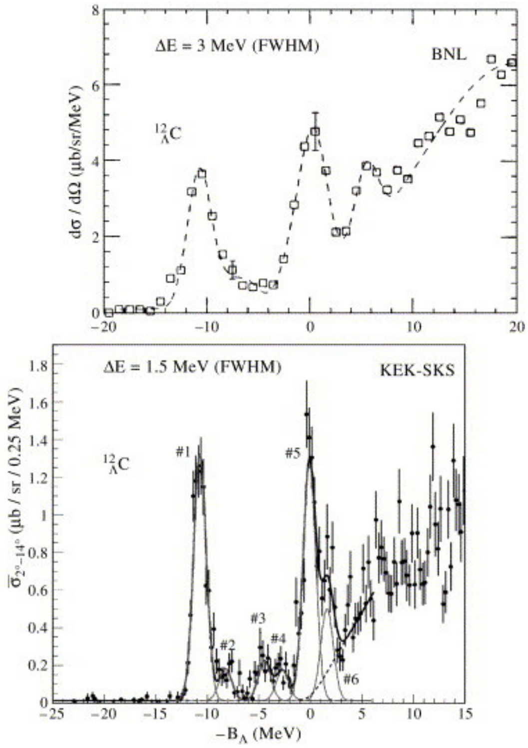

Figure 1.7: Missing mass spectra of the ${}^{12}_{\Lambda}C$ reaction measured at the BNL–AGS [55] with 3 MeV FWHM resolution(top) and at the KEK 12 GeV PS using SKS spectrometer with 1.45 MeV FWHM resolution (bottom) [37].

shells, a set of curves of shell energies against the mass number A provides a classic confirmation that in good approximation, Λ can be considered as an identifiable, distinguishable particle when embedded in a nucleus.

In the last decade, new experimental techniques have been developed. One of these is the use of the (e,e'K^+) reaction for hypernuclear spectroscopy. The high–quality and high–intensity electron beams available at Thomas Jefferson National Laboratory(JLab), USA, permitted the first successful (e,e'K^+) measurement, with a energy resolution of $\sim$0.7 MeV.

In Fig. 1.10 excitation spectra for the three hypernuclear production reaction on a ${}^{12}C$ target are compared schematically. As seen in the figure, the in-flight (K^-, π^-) reaction preferentially populates substitutional hypernuclear states with small total angular momenta near the nucleon emission threshold. On the other hand, the (π^+,K^+) reaction and the (e,e'K^+) reaction efficiently populate bound hypernuclear states. Additionally, the (e,e'K^+) reaction has the feature of exciting spin-flip states.

Another development is hypernuclear γ–ray spectroscopy. The observation of hypernuclear γ rays was first reported in 1978 [57]. This experiment is

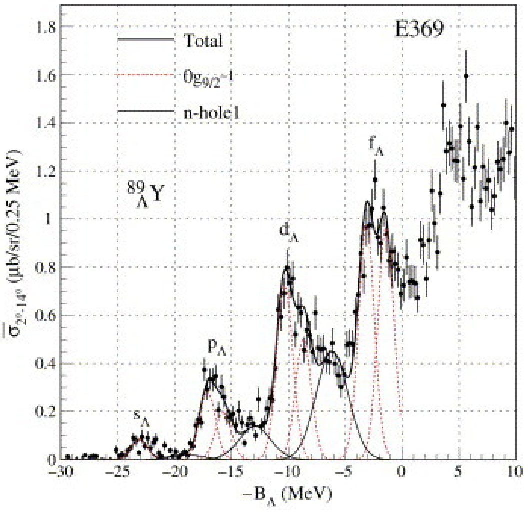

Figure 1.8: Missing mass spectrum of $^{89}_{\Lambda}Y$ (KEK E369) [37] produced by using the (π^+,K$^+$) reaction.

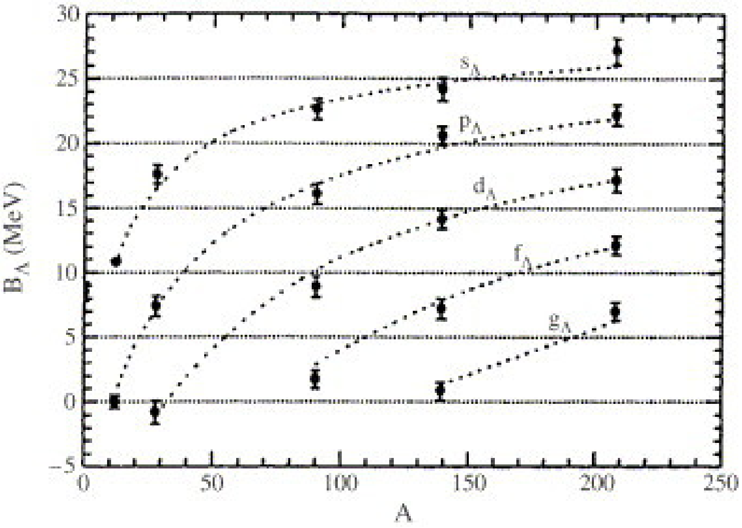

Figure 1.9: Hypernuclear mass dependence of Λ hyperon binding energy in various orbits [38].

the first counting experiment for hypernuclei, and was carried out even before hypernuclear reaction spectroscopy with magnetic spectrometers began.

The inclusive γ–ray spectrum from stopped K^- absorption on a ^{7}Li target exhibited an unknown γ–ray peak at 1.09 MeV. It was assigned to the γ–rays from $1^+ \rightarrow 0^+$ transitions of A = 4 hypernuclei($^4_\Lambda H$ and $^4_\Lambda He$), since these are the only γ transitions expected from hyperfragments with mass numbers

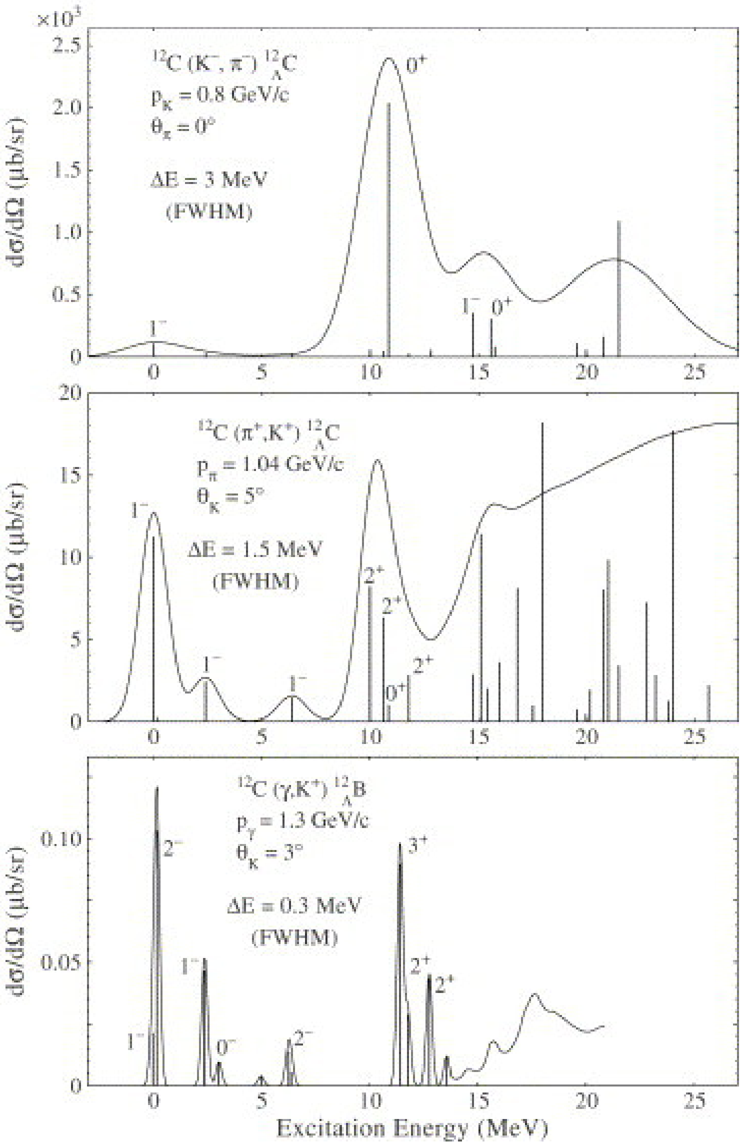

Figure 1.10: Comparison of the excitation functions to be observed in the (K$^-$, π^-), (π^+,K$^+$) and (e,e'K^+) reactions on a ^{12}C target. [56]

smaller than 6. Later, by measuring coincidences between these γ rays and pions that have energies corresponding to the weak decay of $^4_\Lambda H \rightarrow ^4 He + \pi^-$ and $^4_\Lambda He \rightarrow ^4 He + \pi^0$, the $1^+ \rightarrow 0^+$ transition of $^4_\Lambda H$ and $^4_\Lambda He$ were separately identified [58]. In 1985, the observation of γ rays from well –identified Λ hypernuclei produced by the (K$^-$, π^-) direct reaction at BNL–AGS [28] experiment was first reported. Later, in a similar method, another BNL experiment succeeded in observing both inter–shell transitions of $^{13}_\Lambda C$, E1($1/2^- \rightarrow 1/2^+$ and $3/2^- \rightarrow 1/2^+$).

In all of the experiments described above, NaI(Tl) crystals were employed as γ–ray detectors, which limited the energy resolution to $\simeq$0.1 MeV (FWHM) at 1 MeV. Although high–precision γ–ray spectroscopy using germanium(Ge) detectors with a few keV resolution has played a remarkably important role in the development of nuclear physics, use of Ge detectors for hypernuclei has been quite difficult because of small experimental yields, huge backgrounds and, in particular, technical problems in operating Ge detectors under conditions of very high count rates. Hypernuclear experiments with Ge detectors were first attempted in 1979 and then in 1990 at BNL–AGS [59]. In 1998, a large acceptance Ge detector array dedicated to hypernuclear γ–ray spectroscopy (Hyperball) was constructed. The experimental problems due to high counting rates and huge backgrounds were solved by special readout electronics and background suppression counters. Hyperball established a new technique for hypernuclear study, “high–precision hypernuclear γ–ray spectroscopy”, which have been revealed detailed level schemes of various p–shell hypernuclei.

The excellent energy precision of a few keV (FWHM) achieved by Ge detectors is most useful in resolving the spin doublet in hypernuclei that is called “hypernuclear fine structure” because this structure has a small energy spacing, of the order of 10–100 keV. Even if the spacing is so small ($<$ 100 keV) than the Λ spin–flip transition is overwhelmed by weak decay, the spacing can be obtained by separately observing the two core transitions going to the two members of the doublet as illustrated fig. 1.3. The spacing of such a doublet provide information on the spin–dependent components of the ΛN interaction (see eq. 1.2).

Modifications of nuclear properties such as size, shape, symmetry, cluster shell structure and collective motions may be induced by “impurity” of a Λ hyperon in the nucleus. Such effects can be investigated experimentally by measuring detailed levels scheme and transitions probabilities such as the ones corresponding to the electric quadrupole radiation B(E2). These values can be derived from the lifetimes of the excited states of hypernuclei which are measured using the Doppler shift attenuation method [56]. Also the magnetic dipole transition probability B(M1) can be measured with the same method mentioned above and the coincidence between the γ emission and the weak decay products.

Chapter 2

S = -2 System and Double Λ hypernuclei

2.1 Overview

While the nucleon-nucleon scattering was extensively studied since the 50's, direct experimental investigations for the hyperon–hyperon interactions are still very sparse. Because of their short lifetimes, hyperon targets are not available. Low-momentum hyperons are very difficult to produce and hyperon-proton scattering is only feasible via the double-scattering technique [60, 61]. There are only a few hundreds low-momentum Λ-N and $\Sigma^{\pm}$-N scattering events available and there is essentially no data on Ξ-N or Ω-N scattering.

It is interesting to note that the different S=-2 systems, Ξ^--atoms and single Ξ^--hypernuclei on the one hand and double $\Lambda\Lambda$ hypernuclei on the other hand, provide complementary information on the baryon–baryon force: on the one-meson exchange level strange mesons with I=1/2 do not contribute to the Ξ-N interaction. On the other hand, only strange mesons act in the ΞN-$\Lambda\Lambda$ coupling while only non-strange mesons contribute in the Λ-Λ interaction [62, 63]. Indeed, hyperatoms created during the capture process of the hyperon will supply additional information on the hyperon-nucleus interaction. X- rays from π^-, K^-, $\overline{p}$ and Σ^- atoms have already been studied in several experiments in the past. At J-PARC first precise studies of Ξ-atoms are planned [64]. At $\overline{\mathsf{P}}$ANDA not only Ξ^- atoms but also Ω^- atoms can be studied for the first time thus providing unique information on the nuclear optical potential of Ω^- baryons. The Ω hyperon is particularly interesting because due to its long lifetime and its spin of 3/2 it is the only 'elementary' baryon with a non-vanishing spectroscopic quadrupole moment. Since the quadrupole moment of the Ω is mainly determined by the one-gluon exchange contribution to the quark-quark interaction [65, 66] its measurement represents a unique benchmark for our understanding of the quark-quark interaction.

Furthermore, the claimed observation of pentaquark states places also the question for other exotic quark states on the agenda. Thus the possible existence of an S=-2 six quark (uuddss) H-dibaryon [67, 68] represents another challenging topic of ΛΛ hypernuclear physics. Because of their long lifetimes double Λ hypernuclei may serve as 'breeder' for the H-particle. Although some theories predict the H-dibaryon to be stable ([69] and references therein), the observation of several double hypernuclei makes the existence of a strongly bound free H-dibaryon unlikely. However, since the mass of the H-particle might drop inside a nucleus [69] and due to hyperon mixing [70, 71, 72, 73] it might be possible to observe traces of a H-dibaryon even if it is unbound in free space by a detailed study of the energy levels in double hypernuclei.

In the following, the principles for the formation of double Λ hypernuclei will be in Sec. 2.2 introduced. Additionally, the decay mechanism of this systems will be explained in Sec. 2.2.1. In contrast to single hypernuclei,the double hypernuclei formation is not based on a two–body process, and therefore different spectroscopic techniques have to be used. In Sec. 2.2.2, the concepts to perform double hypernuclei spectroscopy will be described. This chapter concludes with an historical background of the spectroscopy of Λ hypernuclei during the last decades since their discovery (Sec. 2.2.3).

2.2 Principles of Double–Λ–Hypernuclei Formation

In analogy with Λ hypernuclei, a double Λ hypernucleus is considered as the bound state of a core nucleus and two Λ particles. However, the simultaneous production and implementation of two Λ particles into a nucleus is not easy feasible. There is a possibility to produce multi-strange hypernuclei in heavy ion collisions as discussed for example in ref. [74]. However, a probability of this process is expected to be very small and high resolution spectroscopy of excited states will not be feasible. The optimal way to produce double hypernuclei is the conversion of a Ξ^- and a proton into two Λ particles. This process releases – ignoring binding energy effects – only 28 MeV/c^2. Accordingly, there is a chance of typically a few percent that both Λ hyperons stick to the same nucleus [75, 76, 77]. Unfortunately Ξ^- hyperons produced in reactions with *stable* hadron beams typically have rather high momenta. Therefore, the capture of the Ξ^- in the nucleus is rather unlikely and it proceeds usually in two or even more steps. Using the $p(K^-K^+)\Xi^-$ double strangeness exchange reaction, Ξ^- hyperons are produced with typical momenta of 500 MeV/c at a beam momenta of 1.8 GeV/c [78, 79].

One can consider two production mechanisms, the *direct formation* and the *indirect formation.* In the direct formation, a few percent of the produced

Ξ is captured in the nucleus where the (K^-, K^+) takes place. However, as a consequence of the large momentum transfer the probability to form bound Ξ^- states directly is rather small on the level of $\sim 1\%$ and the production of quasi–free Ξ^- dominates. Still the Ξ^- hyperons in the quasi–free region may be absorbed into the target nucleus via a rescattering process on a nucleon which itself is knocked out of the target nucleus. This two step process is predicted to exceed the direct capture by more than a factor of 6 [75]. The advantage of this production process is that the outgoing K^+ can be used as a tag for the reaction. A drawback is the low kaon beam intensity because of the short kaon lifetime and hence the need for thick primary targets.

On the other hand most ($\sim 80\%$) hyperons escape from the primary target nucleus in (K^-, K^+) reactions. However, in a second step, these Ξ^- hyperons can be slowed down in a dense, solid material (e.g. a nuclear emulsion) and form Ξ^- atoms [80] after an atomic cascade, the Ξ^- particle is eventually captured by a secondary target nucleus and converted via the strong interaction $\Xi^- + p \longrightarrow \Lambda\Lambda$ into two Λ hyperons (*indirect formation*). Then, the double–Λ sticking intermediate state *double–Λ compound nucleus*) is formed, and fragmentates resulting in small slightly excited hyperfragments. Fig. 2.1 shows an schematic view of the formation of double hypernuclei via $p(K^-, K^+)\Xi^-$ reaction.

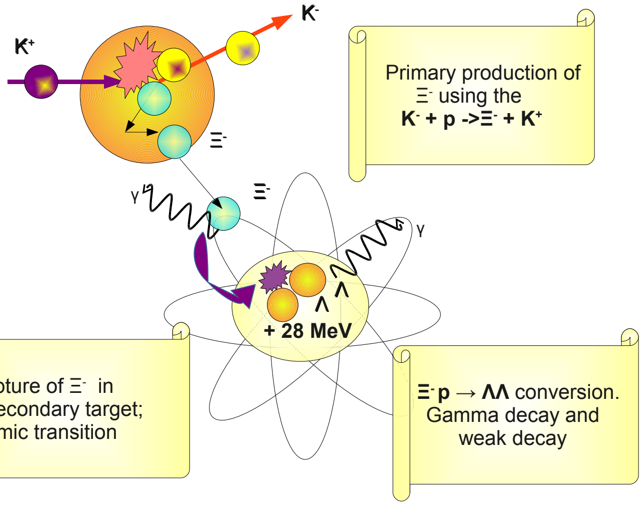

Figure 2.1: schematic view of the formation steps of double hypernuclei via $p(K^-, K^+)\Xi^-$ reaction.

The Ξ^+ was discovered in antiproton–proton interactions at 3 GeV/c [81] (See Fig. 2.2). This discovery opened the possibility to produce low–momentum Ξ^- by using the $\overline{p} + p \longrightarrow \Xi^-\overline{\Xi}$ reaction as an alternative to $p(K^-, K^+)\Xi^-$ re-

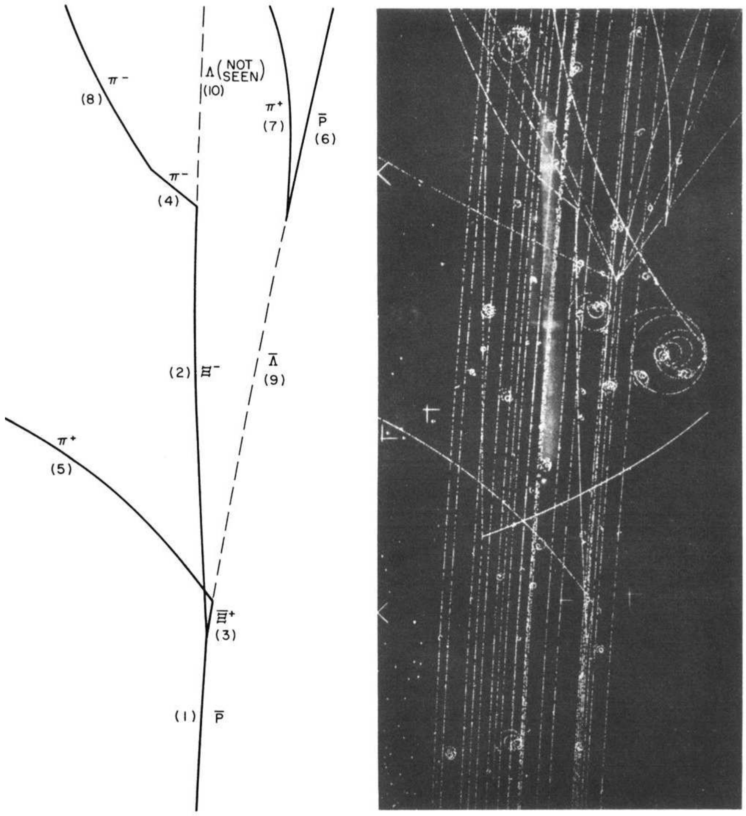

Figure 2.2: A print of the event $\overline{p} + p \rightarrow \Xi^-\overline{\Xi}$ as photographed in the BNL 20-in. liquid hydrogen bubble chamber is shown [81]. The sketch of the event as shown is labeled according to the most likely mass interpretation for each observed track.

action . Also in this case, double hypernuclei will be produced as a result of a multi–stage process. In the first stage a Ξ^- (together with its associated strange particle) is produced in a primary target. The $\overline{\Xi}$ will undergo scattering or (in most cases) annihilation inside the residual nucleus. Strangeness is conserved in the strong interaction and the annihilation products contain at least two anti-kaons that can be used as a tag for the reaction.

In a second stage, the Ξ^- is slowed down in a dense, solid material (e.g. a nuclear emulsion) and forms a Ξ^- atom [80]. After an atomic cascade, the hyperon is finally captured by a secondary target nucleus. If the momentum of the hyperon is too high its stopping time will exceed the lifetime and hence the Ξ^- will decay prior to the atomic capture with high probability. In order to reach a high capture probability it is mandatory to keep the primary momentum of the produced Ξ^- as low as possible.

The energy release of about 28 MeV during the conversion of the Ξ into two Λ hyperons may give rise to the emission of particles from the nucleus (*double*

Λ *compound nucleus*), where the conversion took place. As a consequence, a variety of double, single or twin hypernuclei as well as ordinary nuclei may be produced in excited states. The main advantage compared to the kaon–induced reaction is the fact that the antiproton is stable and can thus be retained in a storage ring. This allows to achieve rather high luminosities even with very thin primary targets.

2.2.1 Decay of double Λ Hypernuclei

In line with the decay of single hypernuclei, a double hypernucleus can decay in three ways due to the different combinations of mesonic and non mesonic decay:

1. both mesonic,
2. both non mesonic and
3. mixed mesonic and non mesonic decay.

Moreover, in double hypernuclei hyperon induced non-mesonic weak decays $\Lambda\Lambda \rightarrow \Lambda N$ and $\Lambda\Lambda \rightarrow \Sigma N$ are possible [83, 84, 85] giving unique access to the $\Lambda\Lambda K$ coupling. Studying this decay will be complementary to the study of double hypernuclei spectra for understanding the general baryon-baryon interaction. For example, the $\Lambda\Lambda \rightarrow \Lambda \mathrm{n}$ channel is especially intriguing since the dominant pion exchange is forbidden, thus forcing this reaction to proceed mostly via kaon exchange. One would therefore gain access to the weak $\Lambda\Lambda K$ and $\Lambda\Sigma K$ vertices.

This decay has already been searched for by the Collaboration E373 at KEK [86] in the channel $\Lambda\Lambda \rightarrow \Sigma^-\mathrm{p}$ and an upper limit of 3 % for the double hypernucleus production from the Ξ capture at rest times the $\Sigma^-\mathrm{p}$ decay branching ratio has been determined. Predictions for the partial decay rates expressed in units of Γ_Λ are in the range of a few times 10^{-3}, unless the H-di-baryon is formed inside the nucleus instead of the double hypernucleus.

2.2.2 Spectroscopy of double Lambda Hypernuclei

In section 2.2, it was shown that double hypernuclei production proceeds as a multi–stage mechanism. As a consequence, spectroscopic studies, based on the analysis of two-body reactions like in single hypernuclei reactions, cannot be performed. Spectroscopic information on double hypernuclei can only be obtained via their decays. One can distinguish several steps of the decay process:

1. γ-rays emitted via the sequential decay of an excited double hypernucleus can provide information on the level structure with rather high resolution.

2. Once the ground-state is reached, the weak decay of the hyperon(s) will initiate the emission of several particles. Here, the determination of the ground-state mass requires the knowledge of all masses of the various decay products and their kinetic energies. Hence, unique identification of the final particles and precise determination of their kinetic energies is mandatory. Nuclear emulsions are presently the only technique which meets all requirements for these measurements of ground-state masses. However, it is impossible to detect neutrons or γ-rays from intermediate, particle-unstable fragments with this method. As a consequence, the determination of the ground-state masses of double hypernuclei is limited to those light nuclei which decay exclusively into charged particles.

3. Furthermore, the kinetic energies of weak decay products are sensitive to the binding energies of the two Λ hyperons. However, the unique identification of hypernuclei ground states via their pion decay is usually hampered by the limited resolution (see ref. [87]), even though it can be used as an effective experimental filter to reduce the background as it will be shown in Sec. 6 of the present work. Instead, γ-rays emitted via the sequential decay of excited double hypernuclei may provide precise information on the level structure.

2.2.3 Status of identified ΛΛ–hypernuclei

The observation of double Λ hypernuclei gives important information about the $\Lambda\Lambda$ interaction symbolized by $\Delta B_{\Lambda\Lambda}$. The binding energy of two Λ hyperons, $B_{\Lambda\Lambda}$ and the $\Lambda\Lambda$ interaction energy $\Delta B_{\Lambda\Lambda}$, can be obtained from the measurement of the masses of double Λ hypernuclei, where $B_{\Lambda\Lambda}$ and $\Delta B_{\Lambda\Lambda}$ are defined by

$$\begin{aligned} B_{\Lambda\Lambda}({}^{A}_{\Lambda\Lambda}Z) &= M({}^{A-2}Z) + 2M(\Lambda) - M({}^{A}_{\Lambda\Lambda}Z) \\ \Delta B_{\Lambda\Lambda}({}^{A}_{\Lambda\Lambda}Z) &= B_{\Lambda}({}^{A}_{\Lambda\Lambda}Z) - B_{\Lambda}({}^{A-1}_{\Lambda}Z) \end{aligned} \tag{2.1}$$

Here $M({}^{A-2}Z)$ represents the mass of the core nucleus, $M(\Lambda)$ the Λ mass, $B_{\Lambda}({}^{A-1}_{\Lambda}Z)$ and $B_{\Lambda}({}^{A}_{\Lambda\Lambda}Z)$ are the binding energy of a single and double hypernucleus, respectively. Evidently, $\Delta B_{\Lambda\Lambda}$ only represents the net $\Lambda\Lambda$ binding assuming that the core is not distorted by adding one Λ after the other and that the core spin is zero. The determination of $\Delta B_{\Lambda\Lambda}({}^{A}_{\Lambda\Lambda}Z)$ requires the knowledge of all masses of the various decay products and their kinetic energies. The deduced values are also sensitive to the population of γ–unstable excited states in the primary $\Lambda\Lambda$ nucleus or its decay products. The world supply of data on $\Lambda\Lambda$ hypernuclei is very limited. Up to now only few candidates for double hypernuclei were observed via their sequential pionic decay [88, 91, 89, 90].

Over four decades ago, Danysz *et al.* reported the sequential weak decay of a double hypernucleus produced from a Ξ^- hyperon capture at rest in emul-

Figure 2.3: The first low energy K^-–beam for hypernuclear physics was build at CERN. In order to achieve a pathlength of 10 meter pions and kaons depending on their stopping power in a fluid absorber were partially separated in the middle of the chicane

sion (see Fig. 2.3 and Fig. 2.4). The event suggested two interpretations on the nuclide, ${}^{10}_{\Lambda\Lambda}$Be or ${}^{11}_{\Lambda\Lambda}$Be, but later reanalysis indicated the production of ${}^{10}_{\Lambda\Lambda}$Be, which leads to $\Delta B_{\Lambda\Lambda} = 4.3\pm0.4\,\mathrm{MeV}$. However, there still exits the possibility of the decay to the single hypernucleus in excited states, which gives the different value of $\Delta B_{\Lambda\Lambda}$. For instance, assuming an excitation energy of 3 MeV, the new value of $\Delta B_{\Lambda\Lambda}$ is reduced to 1.3 MeV. It should be noticed that it was found in a emulsion exposed to about 10^4 K^- mesons, and the expected number of stopped Ξ^- hyperons was no more than four.

Another example of double hypernucleus was presented by D. J. Prowse in 1960s. It was identified as ${}^{6}_{\Lambda\Lambda}$He, and the value of $\Delta B_{\Lambda\Lambda}$ was obtained to be $4.6\pm0.5\,\mathrm{MeV}$. However, only a schematic drawing of the event was reported, and measured angles were not presented. Its authenticity was therefore considered doubtful.

About twenty years ago, a hybrid–emulsion experiment, E176, was carried out at KEK 12 GeV proton synchrotron (Fig. 2.5). An event accompanied with sequential decay of a double hypernucleus was found among 80 Ξ^- hyperons captures at rest in nuclear emulsion. The most probable interpretation was the production of ${}^{13}_{\Lambda\Lambda}$B leading to $\Delta B_{\Lambda\Lambda} = 0.6\pm0.8\,\mathrm{MeV}$. The event also contemplated the possibility of the decay to the single hypernucleus in excited states. In addition, Aoki et al. presented evidence for the production and subsequent weak decay of three heavy double hypernuclei [92], but their nuclides could not be identified.

In 2001 the AGS–E885/E906 collaboration published the first “ mass pro-

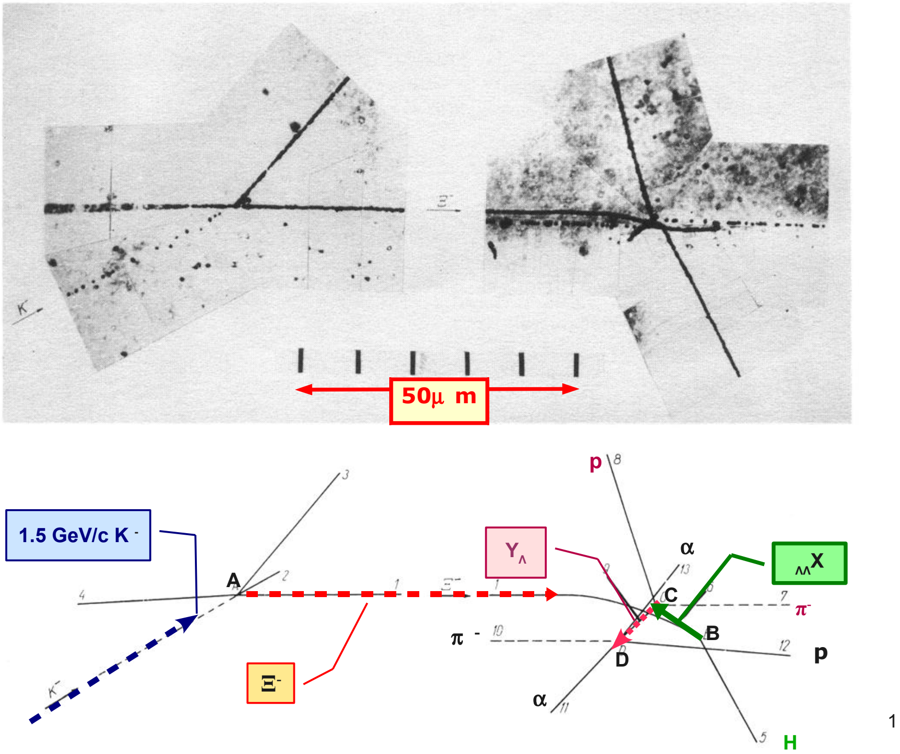

Figure 2.4: Study of hyperfragment production by K$^-$ mesons of momenta 1.3 GeV/c and 1.5 GeV/c in emulsions irradiated in the separated K$^-$ meson beam at CERN 2.3. A Photomicrograph (a) and a schematic drawing (b) of the production of a Ξ^- hyperon in the interaction at A of a K$^-$ meson of momentum 1.5 GeV/c followed by capture at rest of the Ξ^- hyperon at B with the emission of a double hyperfragment decaying in cascade at C and D. The double hyperfragment decays at C into a π^- meson, a singly charged particle and an ordinary hyperfragment. This hyperfragment in turn decays at D into a π^- meson and three other charged particles. [88]

duction " of about 30 ${}^{4}_{\Lambda\Lambda}$H events based on $\sim 10^4$ stopped Ξ^- [93]. The ΛΛ are identified through the sequential weak decay via π^- emission which dominates in light nuclei (see Fig. 2.6). Since the pion kinetic energies are proportional to $\Delta B_{\Lambda\Lambda}$, coincidences between two pions help to trace the decay of the ΛΛ nucleus. While the first spectrometer experiment could not determine the binding energies of ${}^{4}_{\Lambda\Lambda}$H, the number of observed events shows that the production process of double hypernuclei is reasonably well understood. A later reanalysis [87] has shown that of the AGS–E906 data could be represented without the inclusion of ${}^{4}_{\Lambda\Lambda}$H decay. It was more likely that the decay of ${}^{7}_{\Lambda\Lambda}$H was observed in this experiment. This result illustrates that the existence of

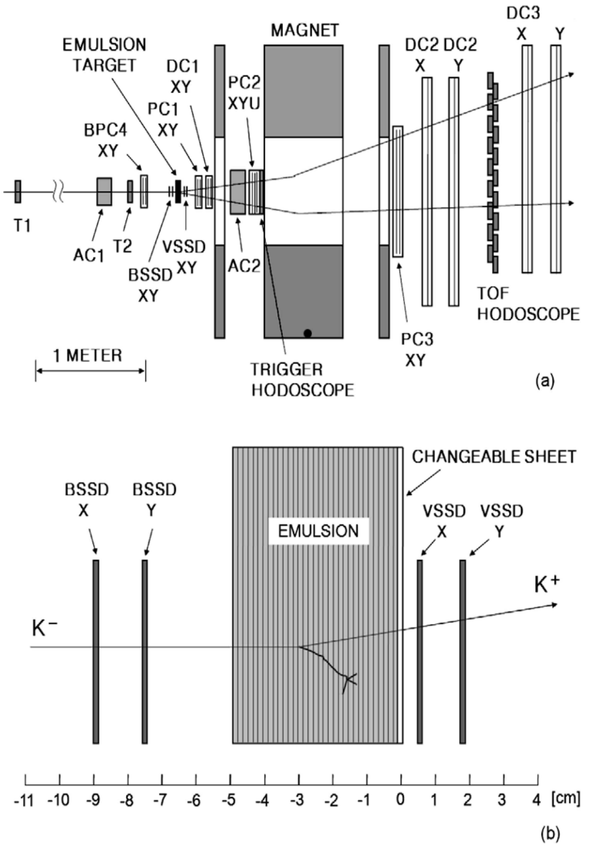

Figure 2.5: (a) Experimental setup for the emulsion–counter hybrid experiment (KEK E176) using a 1.66 GeV/c separated K^- beam [92]. The emulsion–counter hybrid detector consisted of a K^+–spectrometer and an emulsion target. The (K^-,K^+) reactions from nuclei in the emulsion were identified with K^+–spectrometer. The Xi^- hyperons produced in the quasifree reaction were studied in the emulsion. The incident K^- and scattered K^+ mesons are identified with aerogel Cherenkov counters(AC1 and AC2) and time–of–flight measurements (T2–T1 and TOF hodoscope–T2). The PC1–3 are MWPC's and DC1–3 are MWDC's. (b) Emulsion target and its location relative to the SSD's (BSSd and VSSD).

$^{4}_{\Lambda\Lambda}$H as a bound system remains an open question since its formation and decay were not needed for the explanation of these data. Furthermore, this analysis is consistent with the assignment of a weak value for $\Delta B_{\Lambda\Lambda}$, and for $^{7}_{\Lambda\Lambda}$H, this is $\simeq$1 MeV. On the other hand, excitation energy spectra from the E885 experiment 2.7 indicated the existence of Ξ^- hypernuclei and agreed with the theoretical calculation assuming the depth of the Ξ^--nucleus potential with the Woods–Saxon shape to be 14 MeV or less.

Only lately four additional events were found from the Ξ^- at rest in KEK–

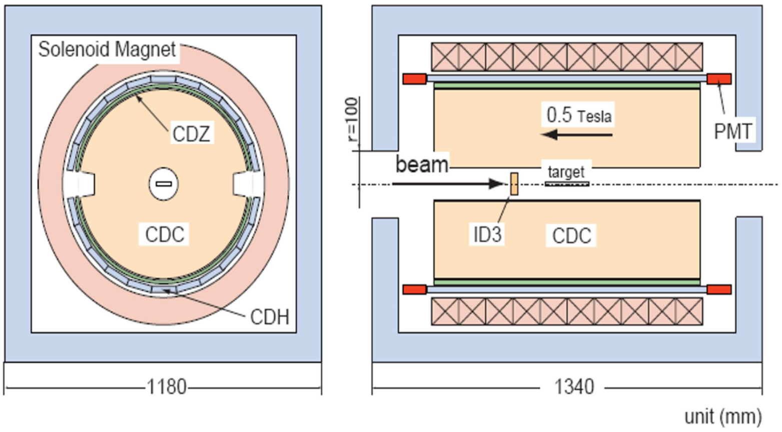

Figure 2.6: The AGS–E906 experiment was carried out at AGS D6 line, using the beamline and its associated spectrometer to momentum analyze the incoming K^- and outgoing K^+, respectively. The setup with exception of the target region, is identical to that previously employed in several double strangeness experiments. Pions emitted from the sequential weak decay of the double Λ hypernuclei in (K^-,K^+) reaction on ^{9}Be are tracked in the cylindrical detector system(CDS) comprised of cylindrical drift chambers in a solenoidal magnetic field(0.5 T) surrounding a beryllium target.[93]

E373(emusion–counter hybrid experiment), which collected $\simeq$ 1000 stopped Ξ^- [94]. One of the double hypernuclei was uniquely identified as the ${}^{6}_{\Lambda\Lambda}$He (NAGARA event, Fig. 2.8 and Fig. 2.2.3). The mass was measured, and the binding energy of the two ΛΛ, and the ΛΛ interaction energy, were determined by the first time without the ambiguities arising from the possibilities of excited states. The value of $\Delta B_{\Lambda\Lambda}$ was to be 0.67±0.17 MeV, where the Ξ^- binding energy of an atomic 3D state of ^{12}C, 0.13 MeV is used as the most probable value. It established that the ΛΛ interaction energy is attractive but considerably smaller than previously estimated experimentally.

In addition, the MIKAGE , the DEMACHIYANAGI events were also interpreted as the production of ${}^{6}_{\Lambda\Lambda}$He, ${}^{10}_{\Lambda\Lambda}$Be, respectively . The HIDA event allowed two interpretations, namely the production of ${}^{12}_{\Lambda\Lambda}$Be and ${}^{11}_{\Lambda\Lambda}$Be respectively. However, the value of $\Delta B_{\Lambda\Lambda}$ for ${}^{12}_{\Lambda\Lambda}$Be could not be calculated. The values of $\Delta B_{\Lambda\Lambda}({}^{A}_{\Lambda\Lambda}Z)$. for MIKAGE , the DEMACHIYANAGI and the HIDA events are found in Table I.

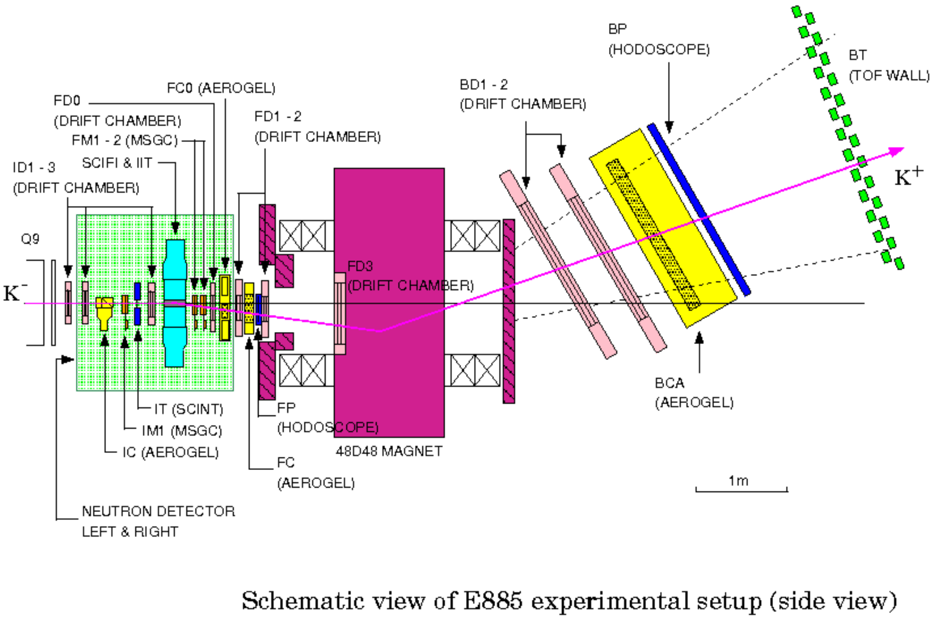

Figure 2.7: Side view of the E885 detector apparatus. The 1.8 GeV/c K$^-$ beam at the AGS was used to create strange (S = -2) systems in E885 via the $^{12}C(K^-, K^+)X$ reaction. The beam was focused in the vertical direction by the last beam line quadrupole magnet onto a synthetic diamond target. The momentum of the incident particle was measured using information from a scintillator hodoscope, MP, and information from 3 drift chambers (ID1-3). The amplitude in the IC Cherenkov counter, along with the measured particle momentum and the beam line time-of-flight, were used to suppress triggers from pions. The momentum of the outgoing K$^+$ was measured in the 1.4 T 48D48 magnetic spectrometer. The amplitude in the FC Cherenkov counter, along with the measured momentum and IT-BT time-of-flight, was used to select kaons. To reduce the hardware trigger rate, an aerogel Cherenkov counter, FC0, was used to suppress background protons.

Table I summarizes our present knowledge on $\Delta B_{\Lambda\Lambda}(^{A}_{\Lambda\Lambda}Z)$. The value of $\Delta B_{\Lambda\Lambda}$ obtained from the three emulsion measurements illustrates the ΛΛ interaction is attractive, while $\Delta B_{\Lambda\Lambda}$ = -1.52 MeV presented by E373 indicates the repulsive ΛΛ interaction. Moreover, two of the measurements considered the possibility of the decay to the single hypernucleus in excited states. Indeed, the

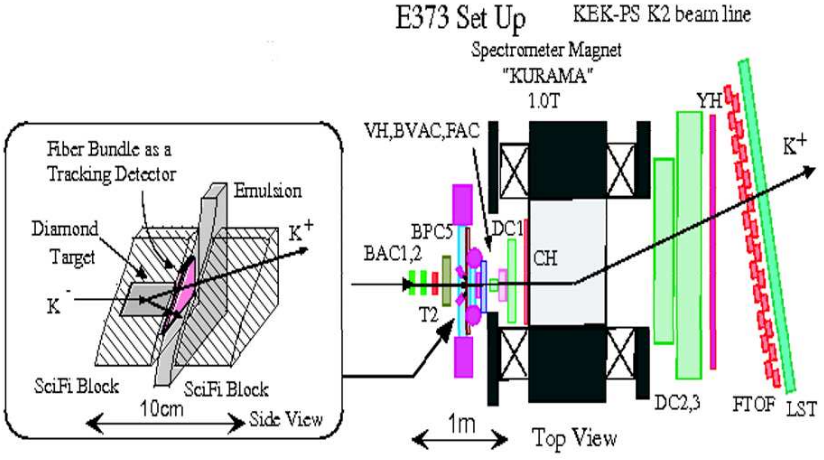

Figure 2.8: Schematic view of the emulsion/scintillating – fiber hybrid (E373) experimental setup. The E373 experiment was carried out at the KEK proton synchrotron using a 1.66 GeV/c separated K^- bean. The incident K^- meson beam was focused on a 3 cm long diamond target. Ξ^- hyperons were produced via the quasifree (K^-,K^+) reaction in a diamond target and brought to rest in emulsion. The (K^-,K^+) reactions were tagged by a spectrometer system. In order to measure the position and angle of entry of the Ξ^- hyperons at the emulsion stack a high resolution tracking detector consisting of coherent bundles of scintillator micro fibers were used. The tracks of Ξ^- hyperons were scanned and traced in the emulsion by a newly developed automatic track scanning system. [94]

differences of $\Delta B_{\Lambda\Lambda}$ between the DEMACHIYANAGI and the Danysz event may indicate the excitation energy of ${}^{10}_{\Lambda\Lambda}Be^*$ nucleus to be 2.8±0.4 MeV. Hence, the ΛΛ interaction energy has not been determined yet. Evidently, even if the high precision of the emulsion data does not allow an unequivocal interpretation of the deduced values for ΛΛ binding energy in terms of the strength of the ΛΛ interaction. This difficulty is due to several effects:

- the dynamical change of the core nucleus[95]
- the non–zero spin of the core
- $\Lambda\Lambda - \Xi N$ coupling effects and

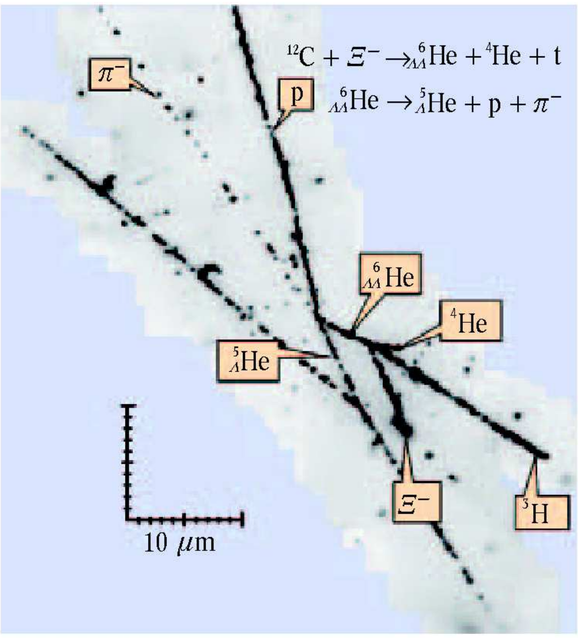

Figure 2.9: Photograph and schematic drawing of NAGARA event. A Ξ^- hyperon comes to rest, and three charged particles are emitted. One of them decayed into a π^- meson and two other charged particles. [94]

Table 2.1: Presently available information on the effective binding energy $\Delta B_{\Lambda\Lambda}({}^{A}_{\Lambda\Lambda}Z)$ between two Λ particles. Note that each case (except for the Prowse event) resulted from the capture reaction of a Ξ^- hyperon in a 3D atomic level for each target nucleus.

event	Hypernucleus	$\Delta B_{\Lambda\Lambda}({}^{A}_{\Lambda\Lambda}Z)$	Ref.
Prowse	${}^{6}_{\Lambda\Lambda}He$	4.7±0.6	[91]
NAGARA	${}^{6}_{\Lambda\Lambda}He$	0.67 ± 0.17	E373 [92, 94]
MIKAGE	${}^{6}_{\Lambda\Lambda}He$	3.82 ± 1.72	E373 [92, 94]
DEMACHIYANAGI	${}^{10}_{\Lambda\Lambda}Be$	-1.52 ± 0.15	E373 [92, 94]
HIDA	${}^{11}_{\Lambda\Lambda}Be$	2.27± 1.23	E373 [92, 94]
Danysz	${}^{10}_{\Lambda\Lambda}Be({}^{9}_{\Lambda\Lambda}Be^*)$	1.3 ± 0.4	[88]
E176	${}^{13}_{\Lambda\Lambda}B$	0.6 ± 0.8	E176 [92, 94]

- the possible production in γ–unstable excited states or the emission of the emission of undetected neutrons[95]

In the future, thanks to novel experiments as for instance the $\overline{\mathsf{P}}\mathsf{ANDA}$ experiment planned at FAIR in Darmstadt [7], which aims at the high resolution γ spectroscopy of double Λ hypernuclei, the strength of the $\Lambda\Lambda$ interaction will be determined for the first time without the ambiguities of past experiments. In the following, the physics program and the subdetectors of the $\overline{\mathsf{P}}\mathsf{ANDA}$ experiment will be introduced as well as the challenging strategy to measure and produce double Λ hypernuclei.

Chapter 3

The PANDA experiment at FAIR

In the present chapter a description of the $\overline{\mathsf{P}}$ANDA physics program as well as its detector system will be given.

3.1 Physics program of PANDA

The $\overline{\mathsf{P}}$ANDA experiment will use the antiproton beam from the HESR colliding with an internal proton target and a general purpose spectrometer to carry out a rich and diversified hadron physics program. The HESR will be part of a large scale construction of an accelerator complex for antiproton and ion beams

The experiment is being designed to fully exploit the extraordinary physics potential arising from the availability of high-intensity, cooled antiproton beams. The aim of the rich experimental program is to improve our knowledge of the strong interaction and of hadron structure. Significant progress beyond the present understanding of the field is expected thanks to improvements in statistics and precision of the data.

Many experiments are foreseen in $\overline{\mathsf{P}}$ANDA.

- The study of **QCD bound states** is of fundamental importance for a better, quantitative understanding of QCD. Particle spectra can be computed within the framework of non-relativistic potential models, effective field theories and Lattice QCD. Precision measurements are needed to distinguish between the different approaches and identify the relevant degrees of freedom. The measurements to be carried out in $\overline{\mathsf{P}}$ANDA include charmonium, D meson and baryon spectroscopy. In addition to that $\overline{\mathsf{P}}$ANDA will look for exotic states such as gluonic hadrons (hybrids and glueballs), multiquark and molecular states.

- **Non-perturbative QCD Dynamics.**

  In the quark picture hyperon pair production either involves the creation of a quark-antiquark pair or the knock out of such pairs out of the nucleon sea. Hence, the creation mechanism of quark-antiquark pairs and their arrangement to hadrons can be studied by measuring the reactions of the type $\overline{p}p \rightarrow \overline{Y}Y$, where Y denotes a hyperon. By comparing several reactions involving different quark flavours the OZI rule, and its possible violation, can be tested for different levels of disconnected quark-line diagrams separately.

- **Study of hadrons in nuclear matter.** The study of medium modifications of hadrons embedded in hadronic matter is aimed at understanding the origin of hadron masses in the context of spontaneous chiral symmetry breaking in QCD and its partial restoration in a hadronic environment. So far experiments have been focussed on the light quark sector. The high-intensity $\overline{\mathrm{p}}$ beam of up to 15 GeV/c will allow an extension of this program to the charm sector both for hadrons with hidden and open charm. The in-medium masses of these states are expected to be affected primarily by the gluon condensate.

- **Hypernuclear physics.** Hypernuclei are systems in which up or down quarks are replaced by strange quarks. In this way a new quantum number, strangeness, is introduced into the nucleus. Although single and double Λ-hypernuclei were discovered many decades ago, only 6 double Λ-hypernuclei are presently known. The availability of $\overline{\mathrm{p}}$ beams at FAIR will allow efficient production of hypernuclei with more than one strange hadron, making $\overline{\mathsf{P}}\mathsf{ANDA}$ competitive with experiments planned at J-PARC. This will open new perspectives for nuclear structure spectroscopy and for studying the forces between hyperons and nucleons.

- **Electromagnetic Processes.** In addition to the spectroscopic studies described above $\overline{\mathsf{P}}\mathsf{ANDA}$ will be able to investigate the structure of the nucleon using electromagnetic processes, such as Deeply Virtual Compton Scattering (DCVS) and the process $\overline{\mathrm{p}}\mathrm{p} \rightarrow e^+e^-$, which will allow the determination of the electromagnetic form factors of the proton in the timelike region over an extended q^2 region.

- **Electroweak Physics.**

  With the high-intensity antiproton beam available at HESR a large number of D-mesons can be produced. This gives the possibility to observe rare weak decays of these mesons allowing to study electroweak physics by probing predictions of the Standard Model and searching for enhancements introduced by processes beyond the Standard Model.

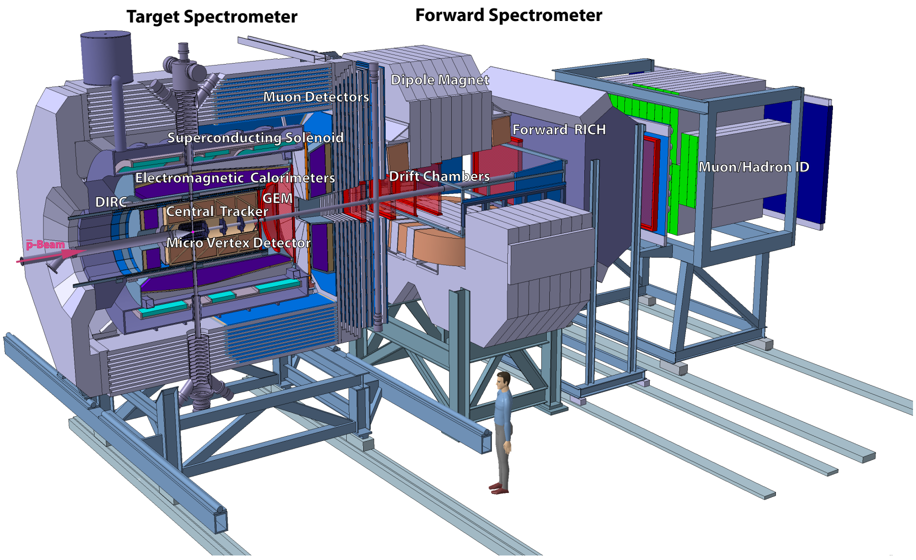

Figure 3.1: Artistic view of the $\overline{\text{P}}$ANDA Detector

3.2 Detector Overview

The main objectives of the design of the $\overline{\text{P}}$ANDA experiment pictured in Fig. 3.1 are to achieve 4π acceptance, high resolution for tracking, particle identification and calorimetry, high rate capabilities and a versatile readout and event selection. To obtain a good momentum resolution the detector is split into a *target spectrometer* based on a superconducting solenoid magnet surrounding the interaction point and measuring at high angles and a *forward spectrometer* based on a dipole magnet for small angle tracks. A silicon vertex detector surrounds the interaction point. In both spectrometer parts tracking, charged particle identification, electromagnetic calorimetry and muon identification are available to allow to detect the complete spectrum of final states relevant for the $\overline{\text{P}}$ANDA physics objectives.

In the following paragraphs the components of all detector subsystems are briefly described.

3.2.1 Target Spectrometer

The target spectrometer surrounds the interaction point and measures charged tracks in a solenoidal field of 2 T. It consists of detector layers arranged in an onion shell configuration. Pipes for the injection of target material have to cross the spectrometer perpendicular to the beam pipe.

The target spectrometer is arranged in a barrel part for angles larger than 22° and an end-cap part for the forward range down to 5° in the vertical and

10° in the horizontal plane. A side view of the target spectrometer is shown in Fig. 3.2.

One of the main design requirements is compactness to avoid a too large and a too costly magnet and crystal calorimeter. The primary interaction region, defined by the cross point of the beam and the hydrogen target, will be surrounded by the inner tracking detector, the Micro Vertex Detector (MVD). This detector component is composed of silicon pixel and strip detectors for high precision track and vertex reconstruction. The outer tracking system follows directly behind the MVD. At present, there are two options for the realization of this device, either a Time Projection Chamber (TPC), or a Straw

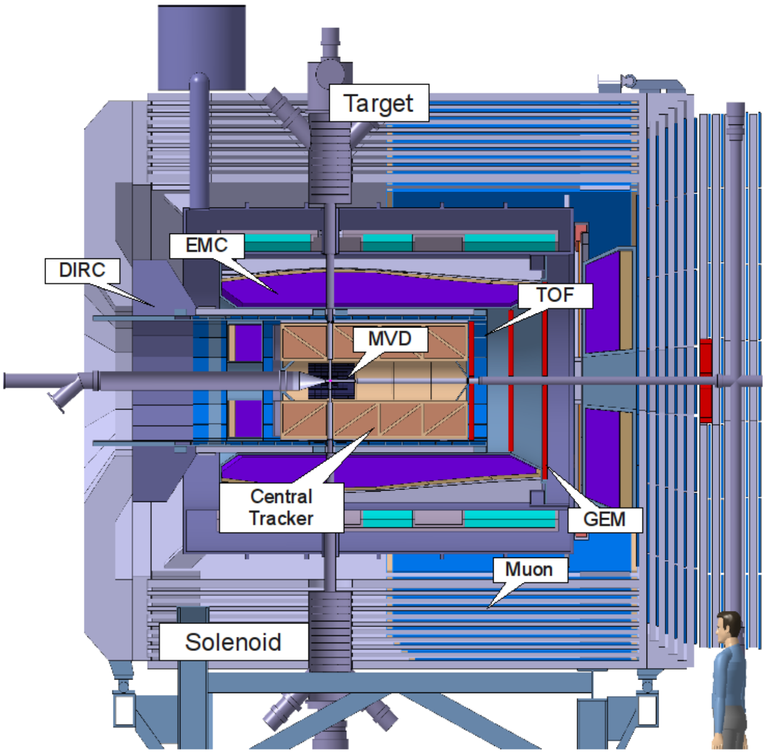

Figure 3.2: Side view of the target spectrometer

Tube Tracker (STT). After the tracking detectors other components for particle identifications are fore- seen. A Direct Imaging Ring Cherenkov (DIRC) detector provides information about different particle species via its different amount of produced Cherenkov light at the same incident momentum. The Electromagnetic Calorimeter (EMC) is designed to reconstruct the shape of an electromagnetic shower produced in the optical sensitive crystals. The shape and amount of the collected light delivers information about the energy and direction of mainly photons and leptons. These detector components are placed inside a super-conducting solenoid, which provides a magnetic field parallel to the beam direction of maximal 2 T. The iron return yoke of the solenoid will be instrumented with Muon Counters (MUO). Additional to the barrel-shaped structure of the target spectrometer two endcap structures close the gap to the forward spectrometer and in addition in upstream beam direction. The backward hemisphere is mainly covered by the backward EMC and the readout of the barrel DIRC, whereas in forward direction additional tracking stations and an endcap Cherenkov detector, as well as a forward EMC endcap, complete the target spectrometer setup. The barrel section of the target spectrometer will mainly measure lower energetic particles. If the momentum is larger than 800 MeV/c, the barrel DIRC and endcap Cherenkov detectors are able to identify the nature of a particular trajectory. To provide particle identification for slower particles, the tracking detectors, in particular the central tracker, can deliver energy loss information of the reconstructed trajectory. Furthermore a time-of-flight system is currently under investigation in the barrel section which can contribute in the low momentum region.

3.2.1.1 Target

Two basically different hydrogen target options are under investigation for use in PANDA. A cluster jet target and a pellet target. The luminosity can be expressed in terms of the number of stored antiprotons $N_{\overline{p}}$, the revolution frecuence of the beam in storage ring f_{rev} and the effective target density $\frac{\langle N \rangle}{A}$:

$$L = f_{rev} N_{\overline{p}} \frac{\langle N \rangle}{A} \tag{3.1}$$

With $\mathrm{N}_{\overline{p}} = 10^{11}$ antiprotons in the ring a luminosity of larger than $L = 10^{32}\,\mathrm{cm}^{-2}\,\mathrm{s}^{-1}$ at medium antiproton beam momentum can only be reached with a target density of at least $\langle N \rangle/\mathrm{A} = 4{\cdot}10^{15}$ atoms per cm^{-2} . Both target options would be able to fulfill this requirement, but under different circumstances. Both alternatives would fit into the compact design of the central part of the $\overline{\mathsf{P}}\mathsf{ANDA}$ detector and show specific advantages and disadvantages, which will be briefly discussed.

Cluster-Jet Target Cold hydrogen gas is ejected through a nozzle which leads to the formation of a homogeneous stream of hydrogen clusters. The size of the clusters can be adjusted by the gas pressure and varies between $\cdot 10^3$ and $\cdot 10^6$ molecules per cluster. The main advantage of this target type is the homogeneity of the cluster stream at the interaction point and over the interaction time with the circulating antiproton beam. Over the beam spill [1], where almost the complete antiproton beam will be consumed, the density of the cluster jet can be adjusted to keep the luminosity as large as possible while the number of antiprotons decreases over time. Currently there are some applications running with an internal cluster jet target, e.g. the ANKE [99] experiment located as an internal experiment at the COSY beam facility. For the use in $\overline{\text{P}}$ANDA the distance between target nozzle and interaction point has to be increased to 2 m compared to 60 cm in case of the ANKE target. A disadvantage of this target type will be the large uncertainty of the beam-target interaction zone due to the lateral spread of the cluster jet. The uncertainty in beam direction will be in the order of a few millimeter. The interaction point (IP) will be defined in the transverse plane reasonable well by the emittance of the beam of, which can be adjusted to be smaller than < 1 mm mrad. The reconstruction of the longitudinal component of the IP has to rely on the precision of the tracking system.

Pellet Target This target type provides a stream of frozen hydrogen droplets, the so-called pellets, with dimensions between 25 - 40 μm. The distance between individual pellets can be adjusted that only one pellet at once will interact with the antiproton beam. The lateral spread of the pellet stream will be in the order of one millimeter and therefor reduced to the cluster jet target alternative. Furthermore, the interaction time with the beam is long enough to reconstruct the position of each individual pellet. This would result in a very good knowledge of the primary interaction point not only in transverse direction, which will be predominantly defined by the beam emittance. A major disadvantage will be the non-uniform luminosity over the interaction time of an individual pellet with the beam. Since the $\overline{\text{P}}$ANDA experiment will be a high luminosity an use a continuous beam, the readout of the individual detector components has to be fast and continuously. A strong variation of the luminosity would result in an additional challenge to cope with high data rates. Currently a pellet target is in operation at the WASA at COSY experiment [96] located in Jülich, which can provide the needed target thickness of 10^{15}-10^{16} atoms per cm^{-2} [98], but with larger pellet sizes than aspired for the use in $\overline{\text{P}}$ANDA. Further more, the distance between the target nozzle and the IP will

---

[1] A Spill is the time of operation of an experiment with only one filling of the HESR ring with antiprotons. The length of this time period depends mainly on the antiproton loss rate due to beam target interactions, the beam cooling and the production rate of antiprotons

be much larger, which would increase the lateral spread of the pellets. To track the pellets individually, a optical tracking system for the use in $\overline{\mathsf{P}}$ANDA is under development. With such a device an absolute position determination of 50 μm could be reached.

Other Targets are under consideration for the hyper-nuclear studies where a separate target station upstream will comprise primary and secondary target and detectors. Details will be presented in sec. 4 of this thesis. Moreover, current R&D is undertaken for the development of a liquid helium target and a polarized ^{3}He target. A wire target may be employed to study antiproton-nucleus interactions.

3.2.1.2 Solenoid Magnet

The magnetic field in the target spectrometer is provided by a superconducting solenoid coil with an inner radius of 90 cm and a length of 2.8 m. The maximum magnetic field is 2 T. The field homogeneity is foreseen to be better than 2 % over the volume of the vertex detector and central tracker. In addition the transverse component of the solenoid field should be as small as possible, in order to allow a uniform drift of charges in the time projection chamber. This is expressed by a limit of $\int B_r/B_z dz < 2\,\text{mm}$ for the normalized integral of the radial field component.

In order to minimize the amount of material in front of the electromagnetic calorimeter, the latter is placed inside the magnetic coil. The tracking devices in the solenoid cover angles down to 5°/10° where momentum resolution is still acceptable. The dipole magnet with a gap height of 1.4 m provides a continuation of the angular coverage to smaller polar angles.

The cryostat for the solenoid coils has two warm bores of 100 mm diameter, one above and one below the target position, to allow for insertion of internal targets.

3.2.1.3 Microvertex Detector

The design of the micro-vertex detector (MVD) for the target spectrometer is optimized for the detection of secondary vertices from D and hyperon decays and maximum acceptance close to the interaction point. It will also strongly improve the transverse momentum resolution. The setup is depicted in Fig. 3.3.

The concept of the MVD is based on radiation hard silicon pixel detectors with fast individual pixel readout circuits and silicon strip detectors. The layout foresees a four layer barrel detector with an inner radius of 2.5 cm and an outer radius of 13 cm. The two innermost layers will consist of pixel detectors while the outer two layers are considered to consist of double sided silicon strip detectors.

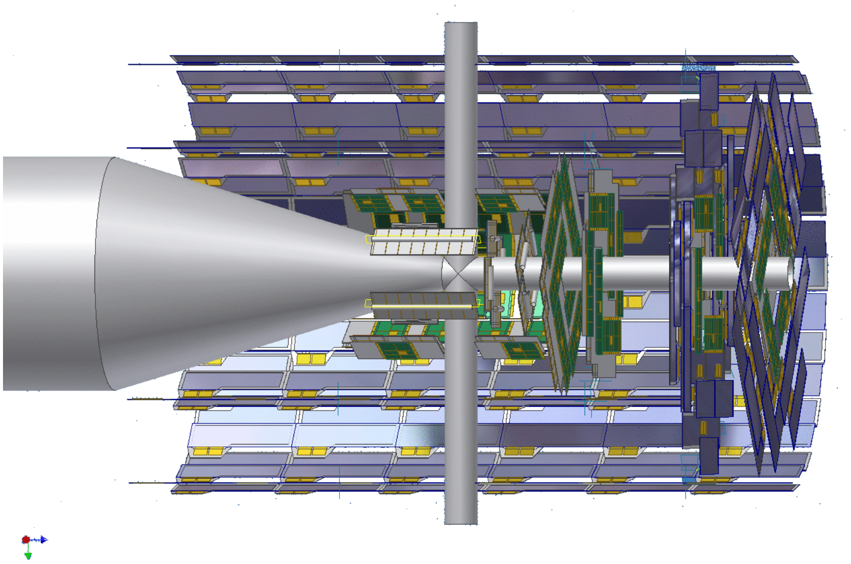

Figure 3.3: The Micro-vertex detector of $\overline{\text{P}}$ANDA

Eight detector wheels arranged perpendicular to the beam will achieve the best acceptance for the forward part of the particle spectrum. Here again, the inner two layers are made entirely of pixel detectors, the following four are a combination of strip detectors on the outer radius and pixel detectors closer to the beam pipe. Finally the last two wheels, made entirely of silicon strip detectors, are placed further downstream to achieve a better acceptance of hyperon cascades.

The present design of the pixel detectors comprises detector wafers which are $200\,\mu$m thick ($0.25\%\,X_0$). The readout via bump-bonded wafers with ASICs as it is used in ATLAS and CMS [100, 101] is foreseen as the default solution. It is highly parallelised and allows zero suppression as well as the transfer of analog information at the same time. The readout wafer has a thickness of 300 μm ($0.37\%\,X_0$). A pixel readout chip based on a $0.13\,\mu$m CMOS technology is under development for $\overline{\text{P}}$ANDA. This chip allows smaller pixels, lower power consumption and a continuously sampling readout without external trigger.

3.2.1.4 Central Tracker

The charged particle tracking devices must handle the high particle fluxes that are anticipated for a luminosity of up to several $10^{32}\,\text{cm}^{-2}\text{s}^{-1}$. The momentum resolution $\delta p/p$ has to be on the percent level. The detectors should have good detection efficiency for secondary vertices which can occur outside the inner vertex detector (e.g. K_S^0 or Λ). This is achieved by the combination of the silicon vertex detectors close to the interaction point (MVD) with two outer systems. One system is covering a large area and is designed as a barrel around the MVD. This will be either a stack of straw tubes (STT) or a time-projection chamber (TPC). The forward angles will be covered using three sets of GEM trackers similar to those developed for the COMPASS experiment [102] at CERN. The two options for the central tracker are explained briefly in the following.

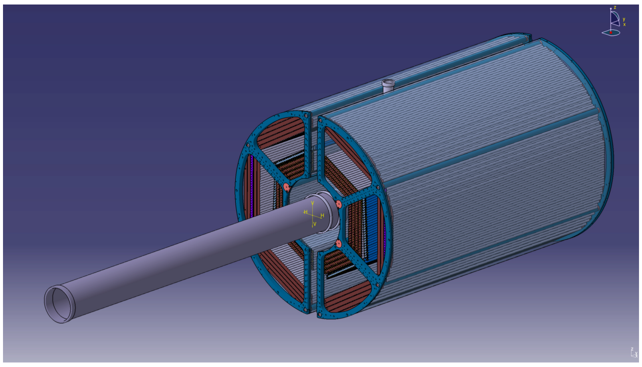

Figure 3.4: Straw Tube Tracker in the Target Spectrometer.

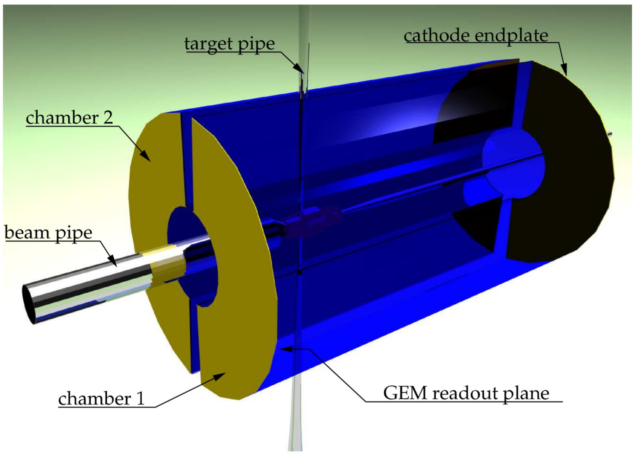

Figure 3.5: GEM Time Projection Chamber in the Target Spectrometer.

Straw Tube Tracker (STT) This detector consists of aluminized mylar tubes called *straws*, which are self supporting by the operation at 1 bar over-pressure. The straws are arranged in planar layers which are mounted in a hexagonal shape around the MVD as shown in Fig. 3.4. In total there are 24 layers of which the 8 central ones are tilted to achieve an acceptable resolution of 3 mm also in z (parallel to the beam). The gap to the surrounding detectors is filled with further individual straws. In total there are 4200 straws around the beam pipe at radial distances between 15 cm and 42 cm with an overall length of 150 cm. All straws have a diameter of 10 mm. A thin and light space frame will hold the straws in place, the force of the wire however is kept solely by the straw itself. The mylar foil is 30 μm thick, the wire is made of 20 μm thick gold plated tungsten. This design results in a material budget of 1.3 % of a radiation length.

The gas mixture used will be Argon based with CO_2 as quencher. It is foreseen to have a gas gain no greater than 10^5 in order to warrant long term operation. With these parameters, a resolution in x and y coordinates of about 150 μm is expected.

Time Projection Chamber (TPC) A challenging but advantageous alternative to the STT is a TPC, which would combine superior track resolution with a low material budget and additional particle identification capabilities through energy loss measurements.

The TPC depicted in a schematic view in Fig. 3.5 consists of two large gas-filled half-cylinders enclosing the target and beam pipe and surrounding the MVD. An electric field along the cylinder axis separates positive gas ions from electrons created by ionizing particles traversing the gas volume. The electrons drift with constant velocity towards the anode at the upstream end face and create an avalanche detected by a pad readout plane yielding information on two coordinates. The third coordinate of the track comes from the measurement of the drift time of each primary electron cluster. In common TPCs the amplification stage typically occurs in multi-wire proportional chambers. These are gated by an external trigger to avoid a continuous backflow of ions in the drift volume which would distort the electric drift field and jeopardize the principle of operation.

In $\overline{\mathsf{P}}\mathsf{ANDA}$ the interaction rate is too high and there is no fast external trigger to allow such an operation. Therefore a novel readout scheme is employed which is based on GEM foils as amplification stage. These foils have a strong suppression of ion backflow, since the ions produced in the avalanches within the holes are mostly caught on the backside of the foil. Nevertheless about two ions per primary electron are drifting back into the ionisation volume even at moderate gains. The deformation of the drift field can be measured by a laser calibration system and the resulting drift can be corrected accordingly. In addition a very good homogeneity of the solenoid field with a low radial component is required.

A further challenge is the large number of tracks accmulating in the drift volume because of the high rate and slow drift. While the TPC is capable of storing a lot of tracks at the same time, their assignment to specific interactions has to be done by time correlations with other detectors in the target spectrometer. To achieve this, first a tracklet reconstruction has to take place. The tracklets are then matched against other detector signals or are pointed to the interaction. This requires either high computing power close to the readout electronics or a very high bandwidth at the full interaction rate.

Forward GEM Detectors Particles emitted at angles below 22° which are not covered fully by the Straw Tube Tracker or TPC will be tracked by three stations of GEM detectors placed 1.1 m, 1.4 m and 1.9 m downstream of the target. The chambers have to sustain a high counting rate of particles peaked at the most forward angles due to the relativistic boost of the reaction products as well as due to the small angle $\overline{\mathrm{p}}\mathrm{p}$ elastic scattering. With the envisaged luminosity, the expected particle flux in the first chamber in the vicinity of the 5 cm diameter beam pipe is about $3{\cdot}10^4\,\mathrm{cm}^{-2}\mathrm{s}^{-1}$. In addition it is required that the chambers work in the 2 T magnetic field produced by the solenoid. Drift chambers cannot fulfil the requirements here since they would suffer from aging and the occupancy would be too high. Therefore gaseous micropattern detectors based on GEM foils as amplification stages are chosen. These detectors have rate capabilities three orders of magnitude higher than drift chambers.

In the current layout there are three double planes with two projections per plane. The readout plane is subdivided in an outer ring with longer and an inner ring with shorter strips. The strips are arranged in two orthogonal projections per readout plane. Owing to the charge sharing between strip layers a strong correlation between the orthogonal strips can be found giving an almost 2D information rather than just two projections.

The readout is performed by the same front-end chips as are used for the silicon microstrips. The first chamber has a diameter of 90 cm, the last one of 150 cm. The readout boards carrying the ASICs are placed at the outer rim of the detectors.

3.2.1.5 Cherenkov Detectors and Time-of-Flight

Charged particle identification of hadrons and leptons over a large range of angles and momenta is an essential requirement for meeting the physics objectives of $\overline{\mathsf{P}}$ANDA. There will be several dedicated systems which, complementary to the other detectors, will provide means to identify particles. The main part of the momentum spectrum above 1 GeV/*c* will be covered by Cherenkov detectors. Below the Cherenkov threshold of kaons several other processes have to be employed for particle identification: The tracking detectors are able to provide energy loss measurements. Here in particular the TPC with its large number of measurements along each track excels. In addition a time-of-flight barrel can identify slow particles.

Barrel DIRC Charged particles in a medium with index of refraction n, propagating with velocity $\beta c < 1/n$, emit radiation at an angle $\Theta_C = \arccos(1/n\beta)$. Thus, the mass of the detected particle can be determined by combining the velocity information determined from Θ_C with the momentum information from the tracking detectors.

A very good choice as radiator material for these detectors is fused silica (*i.e.* artificial quartz) with a refractive index of 1.47. This provides pion-kaon-separation from rather low momenta of 800 MeV/c up to about 5 GeV/c and fits well to the compact design of the target spectrometer. In this way the loss of photons converting in the radiator material can be reduced by placing the conversion point as close as possible to the electromagnetic calorimeter.

At polar angles between 22° and 140°, particle identification will be performed by the detection of internally reflected Cherenkov (DIRC) light as realized in the BaBar detector [103]. It will consist of 1.7 cm thick quartz slabs surrounding the beam line at a radial distance of 45 - 54 cm. At BaBar the light was imaged across a large stand-off volume filled with water onto 11 000 photomultiplier tubes. At $\overline{\text{P}}$ANDA, it is intended to focus the images by lenses onto micro-channel plate photomultiplier tubes (MCP PMTs) which are insensitive to magnetic fields. This fast light detector type allows a more compact design and the readout of two spatial coordinates. In addition MCP PMTs provide good time resolution to measure the time of light propagation for dispersion correction and background suppression.

Forward Endcap DIRC A similar concept can be employed in the forward direction for particles between 5° and 22°. The same radiator, fused silica, is to be employed however in shape of a disk. At the rim around the disk focussing will be done by mirroring quartz elements reflecting onto MCP PMTs. Once again two spatial coordinates plus the propagation time for corrections will be read. The disk will be 2 cm thick and will have a radius of 110 cm. It will be placed directly upstream of the forward end-cap calorimeter.

Barrel Time-of-Flight For slow particles at large polar angles particle identification will be provided by a time-of-flight detector. In the target spectrometer the flight path is only of the order of 50 - 100 cm. Therefore the detector must have a very good time resolution between 50 and 100 ps.

Implementing an additional start detector would introduce too much material close to the interaction point deteriorating considerably the resolution of the electromagnetic crystal calorimeter. In the absence of a start detector relative timing of a minimum of two particles has to be employed.

As detector candidates scintillator bars and strips or pads of multi-gap resistive plate chambers are considered. In both cases a compromise between time resolution and material budget has to be found. The detectors will cover angles between 22° and 140° using a barrel arrangement around the STT/TPC at 42 - 45 cm radial distance.

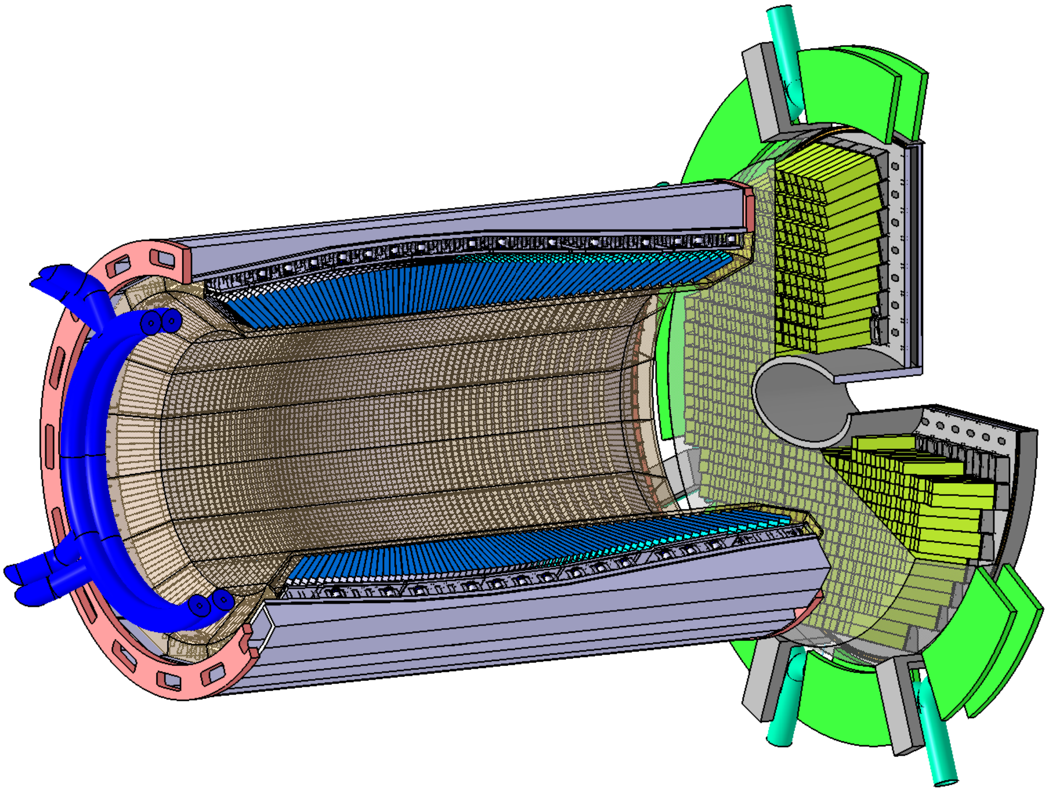

Figure 3.6: The $\overline{\text{P}}$ANDA barrel and forward end-cap EMC

3.2.1.6 Electromagnetic Calorimeters

Expected high count rates and a geometrically compact design of the target spectrometer require a fast scintillator material with a short radiation length and Molière radius for the construction of the electromagnetic calorimeter (EMC). Lead tungstate ($PbWO_4$) is a high density inorganic scintillator with sufficient energy and time resolution for photon, electron, and hadron detection even at intermediate energies [104, 105, 106]. For high energy physics $PbWO_4$ has been chosen by the CMS and ALICE collaborations at CERN [107, 108] and optimized for large scale production. Apart from a short decay time of less than 10 ns good radiation hardness has been achieved [109]. Recent developments indicate a significant increase of light yield due to crystal perfection and appropriate doping to enable photon detection down to a few MeV with sufficient resolution. The light yield can be increased by a factor of about 4 compared to room temperature by cooling the crystals down to -25°C.

The crystals will be 20 cm long, *i.e.* approximately 22 X_0, in order to achieve an energy resolution below 2 % at 1 GeV [104, 105, 106] at a tolerable energy loss due to longitudinal leakage of the shower. Tapered crystals with a front size of $2.1 \times 2.1\,\mathrm{cm}^2$ will be mounted with an inner radius of 57 cm. This implies 11 360 crystals for the barrel part of the calorimeter. The forward end-cap calorimeter will have 3600 tapered crystals, the backward end-cap calorimeter 592. The readout of the crystals will be accomplished by large area avalanche photo diodes in the barrel and vacuum photo-triodes in the forward and backward endcaps.

The barrel part and the forward endcap of the target spectrometer EMC are depicted in Fig. 3.6.

3.2.1.7 Muon Detectors

Muons are an important probe for, among others, J/ψ decays, semi-leptonic D-meson decays and the Drell-Yan process. The strongest background are pions and their decay daughter muons. However at the low momenta of $\overline{\mathsf{P}}$ANDA the signature is less clean than in high energy physics experiments. To allow nevertheless a proper separation of primary muons from pions and decay muons a range tracking system will be implemented in the yoke of the solenoid magnet. Here a fine segmentation of the yoke as absorber with interleaved tracking detectors allows the distinction of energy loss processes of muons and pions and kinks from pion decays. Only in this way a high separation of primary muons from the background can be achieved.

In the barrel region the yoke is segmented in a first layer of 6 cm iron followed by 12 layers of 3 cm thickness. The gaps for the detectors are 3 cm wide. This is enough material for the absorption of pions in the momentum range in $\overline{\mathsf{P}}$ANDA at these angles. In the forward end-cap more material is needed. Since the downstream door of the return yoke has to fulfil constraints for space and accessibility, the muon system is split in several layers. Six detection layers are placed around five iron layers of 6 cm each within the door, and a removable muon filter with additional five layers of 6 cm iron is located in the space between the solenoid and the dipole. This filter has to provide cut-outs for forward detectors and pump lines and has to be built in a way that it can be removed with few crane operations to allow easy access to these parts.

As detector within the absorber layers rectangular aluminium drift tubes are used as they were constructed for the COMPASS muon detection system [110]. They are essentially drift tubes with additional capacitively coupled strips read out on both ends to obtain the longitudinal coordinate.

3.2.2 Forward Spectrometer

3.2.2.1 Dipole Magnet

A dipole magnet with a window frame, a 1 m gap, and more than 2 m aperture will be used for the momentum analysis of charged particles in the forward spectrometer. In the current planning, the magnet yoke will occupy about 2.5 m in beam direction starting from 3.5 m downstream of the target. Thus, it covers the entire angular acceptance of the forward spectrometer of ±10° and ±5° in the horizontal and in the vertical direction, respectively. The maximum bending power of the magnet will be 2 Tm and the resulting deflection of the antiproton beam at the maximum momentum of 15 GeV/*c* will be 2.2°. The design acceptance for charged particles covers a dynamic range of a factor 15 with the detectors downstream of the magnet. For particles with lower momenta, detectors will be placed inside the yoke opening. The beam deflection will be compensated by two correcting dipole magnets, placed around the $\overline{\text{P}}$ANDA detection system.

3.2.2.2 Forward Trackers

The deflection of particle trajectories in the field of the dipole magnet will be measured with a set of wire chambers (either small cell size drift chambers or straw tubes), two placed in front, two within and two behind the dipole magnet. This will allow to track particles with highest momenta as well as very low momentum particles where tracks will curl up inside the magnetic field.

The chambers will contain drift cells of 1 cm width. Each chamber will contain three pairs of detection planes, one pair with vertical wires and two pairs with wires inclined by +10° and -10°. This configuration will allow to reconstruct tracks in each chamber separately, also in case of multi-track events. The beam pipe will pass through central holes in the chambers. The most central wires will be separately mounted on insulating rings surrounding the beam pipe. The expected momentum resolution of the system for 3 GeV/*c* protons is $\delta p/p = 0.2\,\%$ and is limited by the small angle scattering on the chamber wires and gas.

3.2.2.3 Forward Particle Identification

RICH Detector To enable the π/K and K/p separation also at the very highest momenta a RICH detector is proposed. The favoured design is a dual radiator RICH detector similar to the one used at Hermes [111]. Using two radiators, silica aerogel and C_4F_{10} gas, provides π/K/p separation in a broad momentum range from 2–15 GeV/*c*. The two different indices of refraction are 1.0304 and 1.00137, respectively. The total thickness of the detector is reduced to the freon gas radiator (5 % X_0), the aerogel radiator (2.8 % X_0), and the aluminium window (3 % X_0) by using a lightweight mirror focusing the Cherenkov light on an array of photo tubes placed outside the active volume. It has been studied to reuse components of the HERMES RICH.

Time-of-Flight Wall A wall of slabs made of plastic scintillator and read out on both ends by fast photo tubes will serve as time-of-flight stop counter placed at about 7 m from the target. In addition, similar detectors will be placed inside the dipole magnet opening, to detect low momentum particles which do not exit the dipole magnet. The relative time of flight between two charged tracks reaching any of the time-of-flight detectors in the experiment (including the barrel TOF) will be measured. The wall in front of the forward spectrometer EMC will consist of vertical strips varying in width from 5 to 10 cm to account for the differences in count rate. With the expected time resolution of $\sigma = 50\,\text{ps}$ π-K and K/p separation on a $3\,\sigma$ level will be possible up to momenta of 2.8 GeV/c and 4.7 GeV/c, respectively.

3.2.2.4 Forward Electromagnetic Calorimeter

For the detection of photons and electrons a Shashlyk-type calorimeter with high resolution and efficiency will be employed. The detection is based on lead-scintillator sandwiches read out with wave-length shifting fibres passing through the block and coupled to photomultipliers. The technique has already been successfully used in the E865 experiment [112]. It has been adopted for various other experiments [113, 114, 115, 116, 117, 118]. An energy resolution of $4\,\%/\sqrt{E}$ [116] has been achieved. To cover the forward acceptance, 26 rows and 54 columns are required with a cell size of 55 mm, *i.e.* 1404 modules in total, which will be placed at a distance of 7–8 m from the target.

3.2.2.5 Forward Muon Detectors

For the very forward part of the muon spectrum a further range tracking system consisting of interleaved absorber layers and rectangular aluminium drift-tubes is being designed, similar to the muon system of the target spectrometer, but laid out for higher momenta. The system allows discrimination of pions from muons, detection of pion decays and, with moderate resolution, also the energy determination of neutrons and anti-neutrons.

3.2.3 Data adquisition

In many contemporary experiments the trigger and data acquisition (DAQ) system is based on a two layer hierarchical approach. A subset of specially instrumented detectors is used to evaluate a first level trigger condition. For the accepted events, the full information of all detectors is then transported to the next higher trigger level or to storage. The available time for the first level decision is usually limited by the buffering capabilities of the front-end electronics. Furthermore, the hard-wired detector connectivity severely constrains both the complexity and the flexibility of the possible trigger schemes.

In $\overline{\text{P}}$ANDA, a data acquisition concept is being developed which is better matched to the high data rates, to the complexity of the experiment and the diversity of physics objectives and the rate capability of at least $2 \cdot 10^7$ events/s.

In our approach, every sub-detector system is a self-triggering entity. Signals are detected autonomously by the sub-systems and are preprocessed. Only the physically relevant information is extracted and transmitted. This requires hit-detection, noise-suppression and clustering at the readout level. The data related to a particle hit, with a substantially reduced rate in the preprocessing step, is marked by a precise time stamp and buffered for further processing. The trigger selection finally occurs in computing nodes which access the buffers via a high-bandwidth network fabric. The new concept provides a high degree of flexibility in the choice of trigger algorithms. It makes trigger conditions available which are outside the capabilities of the standard approach. One obvious example is displaced vertex triggering.

In this scheme, sub-detectors can contribute to the trigger decision on the same footing without restrictions due to hard-wired connectivity. Different physics can be accessed either in parallel or via software reconfiguration of the system.

High speed serial (10 Gb/s per link and beyond) and high-density FPGA (field programmable gate arrays) with large numbers of programmable gates as well as more advanced embedded features are key technologies to be exploited within the DAQ framework.

The basic building blocks of the hardware infrastructure which can be combined in a flexible way to cope with varying demands, are the following:

- Intelligent front-end modules capable of autonomous hit detection and data preprocessing (e.g. clustering, hit time reconstruction, and pattern recognition) are needed.

- A precise time distribution system is mandatory to provide a clock norm from which all time stamps can be derived. Without this, data from subsystems cannot be correlated.

- Data concentrators provide point-to-point communication, typically via optical links, buffering and online data manipulation.

- Compute nodes aggregate large amounts of computing power in a specialized architecture rather than through commodity PC hardware. They

> may employ fast FPGAs (Fast Programmable Gate Arrays), DSPs (Digital Signal Processors), or other computing units. The nodes have to deal with feature extraction, association of data fragments to events, and, finally, event selection.

A major component providing the link for all building blocks is the network fabric. Here, special emphasis is put on embedded switches which can be cascaded and reconfigured to reroute traffic for different physics selection topologies. Alternatively, with an even higher aggregate bandwidth of the network, which according to projections of network speed evolution will be available by the time the experiment will start, a flat network topology where all data is transferred directly to processing nodes may be feasible as well. This requires a higher total bandwidth but would have a simpler architecture and allow event selection in a single environment. The bandwidth required in this case would be at least 200 GB/s. After event selection in the order of 100-200 MB/s will be saved to mass storage.

An important requirement for this scheme is that all detectors perform a continuous online calibration with data. The normal data taking is interleaved with special calibration runs. For the monitoring of the quality of data, calibration constants and event selection a small fraction of unfiltered raw data is transmitted to mass storage.

To facilitate the association of data fragments to events the beam structure of the accelerator is exploited: Every $1.8\,\mu$s there is a gap of about $400\,$ns needed for the compensation of energy loss with a bucket barrier cavity. This gap provides a clean division between consistent data blocks which can be processed coherently by one processing unit.

Chapter 4

The Hypernuclear Detector Setup at $\overline{\mathsf{P}}$ANDA

As mentioned before, the production of hypernuclei at the $\overline{\mathsf{P}}$ANDA experiment proceeds as a multi–stage process (See Fig. 4.1).

One can deduce from this scheme that the major difficulty to perform hypernuclear physics at the $\overline{\mathsf{P}}$ANDA experiment resides in the multi–step production mechanism (see Fig. 4.1) and as a consequence, a successful achievement of this goal will require major additions to the experimental $\overline{\mathsf{P}}$ANDA setup (Fig. 4.2 in Sec. 3.2) as well as in the simulation package Pandaroot.

In this context, this chapter is devoted to study the requirements of the detector setup envisaged for the hypernuclei project at $\overline{\mathsf{P}}$ANDA. This study will be performed by a Monte Carlo simulation. Therefore, the first part of this chapter (Sec. 4.1) will be dedicated to give a brief description of the software components which has been used for the Monte Carlo calculations. In Sec. 4.2 the requirements of the main components of the hypernuclear setup will be studied separately. In particular, these studies are focused on the optimization of a primary target, a secondary active target and a germanium detector array. In addition, the concept of a time of flight system consisting of a scintillator fiber array detector and the TOF detector of $\overline{\mathsf{P}}$ANDA will be also studied as a possible setup for background rejection.

4.1 The $\overline{\mathsf{P}}$ANDA Simulation Framework

In the following, the aim of this section will be dedicated to introduce the simulation framework components of Pandaroot. Additionaly, the general issues to describe the physics environment of the $\overline{\mathsf{P}}$ANDA experiment within a montecarlo simulation also will be fully addressed. A large variety of tools for the detector simulation and offline analysis are provided by the FAIRroot framework [119], which is based on the object-oriented data analysis framework,

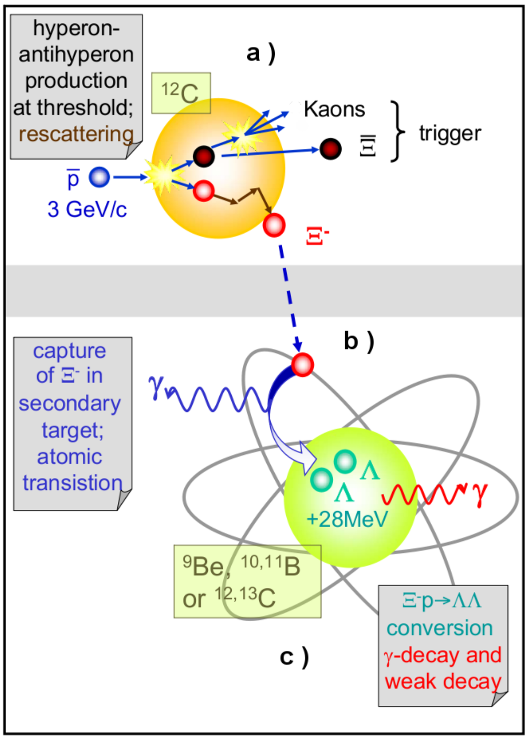

Figure 4.1: Various steps of the double hypernucleus production in $\overline{\text{P}}$ANDA. These steps are labeled by a) hyperon-antihyperon production at threshold; rescattering in a primary a target. b) indicates the atomic capture of the hyperon in a secondary target, with the subsequent electromagnetic emission. c) Nuclear capture of the hyperon and conversion into two Λ's, leading to the eventual formation of a highly excited double Λ hypernucleus. The system can eventually fragmentate creating hyperfragments lower in mass and in slightly excited states.

ROOT [120], and the Virtual Monte-Carlo (VMC) interface [121]. In general, Monte Carlo simulations of a complex detector system as for instance, the $\overline{\text{P}}$ANDA detector, can be separated into well defined steps: event generation, detector simulation(geometry and response to particle interaction), digitization, event reconstruction and the physics analysis.

In the following, the general aspects of the event generation as well as the detector simulation procedure within the Pandaroot will be introduced. The last three points will be treated in a dedicated chapter emphasizing its application to hypernuclear case.

Event Generation The simulation of primary collisions(interaction of probe and target) and generation of the emerging particles, represented in form of four-vectors and production vertices. The primary interactions are simulated via event generators, which produce a set of particles with their four–momenta.

The event generators available in the PANDAroot framework are

- The EvtGen Generator([123]). It is controlled by means of a decay table, which lists all possible decay processes, their branching ratios and the decay model. A user decay table can be written to override the default table and, thereby, exclude unwanted processes.
- The Dual Parton Model based generator([124]), DPM, for the simulation of the generic annihilation background, is used in the case of $\overline{\text{p}}\text{p}$.
- The Ultra-relativistic Quantum Molecular Dynamic model (UrQMD) [125, 126] is a microscopic model based on a phase space description of nuclear reactions($\overline{\text{p}}$N.)
- The Box Generator allows to generate particles of the same type within a uniform distribution in a given range, such as momentum, angular variables, rapidity and so on.
- The Ascii Generator is an interface to a user–defined particle distribution. The input for this interface are ascii files with a predefined format.

Detector Simulation In this part, the general aspects concerning the simulation of the detector response to the particles interacting within its volume will be introduced following the PANDAroot guidelines.

In PANDAroot, the main actions managed at each step of the simulation run are:

- construction and initialization of the geometry
- storage of primary track in an external stack container
- pre–tracking action. (Actions at the beginning of the track)
- stepping action and dispatching the hit processing to individual sensitive detectors.
- post–tracking action. Actions at the end of the track.

These issues will be performed along a so–called *Event*. An event is intended as an interaction between the beam particle and the target, namely primary interaction. On the first stage the information about the subsystem geometry is read from the input file during the *Initialization* step and transfer this information to the *Construction* procedure for its implementation into the whole detector setup. On the next stage particles generated by one of the event generators are filled in a external stack container.The concrete Montecarlo Engine(Geant4) is selected at run time to perform the transport of the particles through the detector modules(*sensitive volumes*). Presently there are three possible transport models Geant3 [127], Geant4 [128], and Fluka [129]) The transport engine takes care of the electromagnetic and hadronic processes undergone by the particle along its trayectory depending on the particle type(hadron, lepton, photons etc) and its energy. The propagation prodedure starts looping over all particles from the stack container. The particle is then traced step by step through all the volumes material until they exit, stop or dissapear(by decay or annihilation). At each step, the probability of a certain physical process to occur is calculated, to simulate the interaction of the particle with the matter. If an interaction takes place, the energy lost by the particle is again computed and subtracted from its kinetic energy. After each step the particle range is calculated and if it is zero, the particle stops, otherwise a new step is performed. Information such as interaction position, energy loss of the particle, momentum, etc after each particle interaction with the sensitive material of the detector is registered in a so called*Hit*. The storage of all information collected by different sensitive detectors is done event by event basis. All registered hits are then collected into dedicated lists. Finally, the various hit collections are organized in an ROOT file output which can be later handled to model the electronic signal associated with a certain front-end-electronic device(*Digitization*).

Reconstruction The reconstruction process comprises two stages, the *track finding* and the *track fitting*. During the track finding the reconstructed detector hits are sorted out, building track candidates which are associated to particle trayectories. In the $\overline{\text{P}}$ANDA Framework, the track finding specially in the target spectrometer region is accomplished by algorithms based on conformal mapping [130] or extended Riemann [131] techniques. In most cases, these algorithms are also used as pre-fit within a more complex tracking chain. The *track fitting* consist in extracting kinematic information from the track such as momentum, trayectory length and so on. This information is obtained within a minimation procedure or fit where the particle trayectories are parametrized by means of mathematical curves. An overwiew of the mentioned procedure can be found in section(A.1). In the *Analysis* stage, the efficiency of the physics channel of interest is determined from the processing of the various information obtained during the reconstruction.

4.2 Hypernuclear Detector Setup Requirements

In particular, the aim of this section will be to evaluate the hypernuclear detector requirements based on the production of $\Xi^- + \overline{\Xi}^+$ pairs, which represents the first stage in the hypernuclei production. In the following the main parts of the hypernuclei detector setup will be introduced. This is mainly characterized by,

- A primary carbon target at the entrance to the central tracking detector of $\overline{\mathsf{P}}$ANDA. To avoid unnecessary radiation damage to the micro vertex detectors surrounding the nominal target region, these detectors will be removed during the hypernucleus runs.
- A small secondary active sandwich target composed of silicon detectors and ^{9}Be, ^{10,11}B or ^{12,13}C absorbers to slow down and stop the Ξ^- and to identify the weak decay products.
- To detect the γ-rays from the excited double hypernuclei an array of 15 n-type Germanium triple Cluster-arrays will be added. To maximize the detection efficiency the γ-detectors must be arranged as close as possible to the target. Hereby the main limitation is the load of particles from $\overline{p}$-nucleus reactions. Since the γ-rays from the slowly moving hypernuclei is emitted nearly isotropic the Ge-detectors will be arranged at backward angles.

The hypernuclei study will make use of the modular structure of the $\overline{\mathsf{P}}$ANDA detector. Removing the backward end-cap calorimeter will allow to add a dedicated nuclear target station and the required additional detectors for γ spectroscopy (see Fig. 4.2) close to the entrance of $\overline{\mathsf{P}}$ANDA. While the detection of anti-hyperons and low momentum K^+ can be ensured by the universal detector and its Particle Identification system, a specific target system and a γ-detector are additional components required for the hypernuclear studies. The micro vertex detector (MVD) and the associated beam pipe will be replaced by a dedicated beam line in order to avoid damage to the main vertex detector by forward scattered particles.

4.2.1 Choice of the primary target

The task of the primary (production) target is the production of $\Xi + \bar{\Xi}$ pairs and the rescattering of the Ξ hyperon towards larger laboratory angles and smaller momenta. Moreover, the target geometry needs to be considered since the average luminosity may vary during the machine filling. In addition, also the generation of background and possible radiation damages in the detectors have to be taken into account.

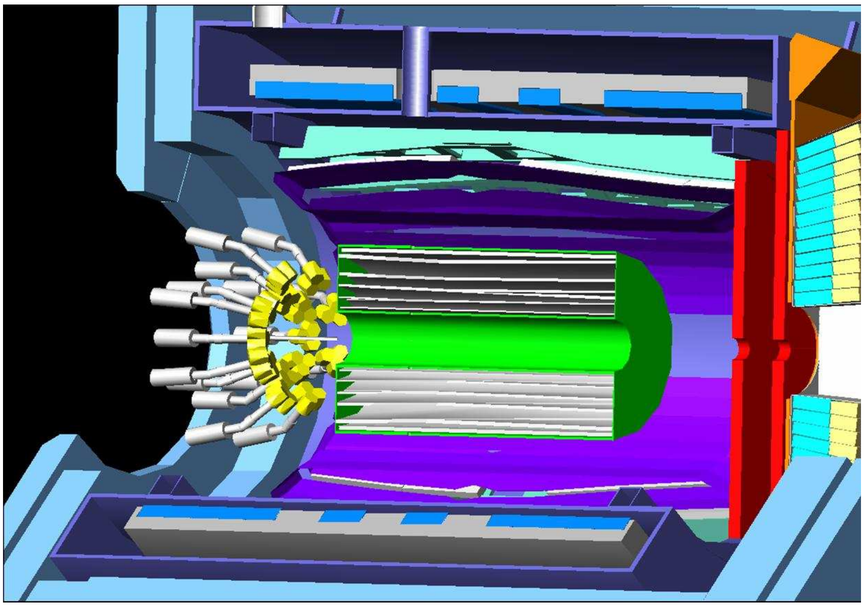

Figure 4.2: Integration of the secondary target and the germanium Cluster–array in the $\overline{\text{P}}$ANDA detector, with the beam entering from left.

At a $\overline{\text{p}}$ momentum of 3 GeV/c the $\bar{p}p \rightarrow \Xi^{-}\bar{\Xi}^{+}$ production cross section is about $2\,\mu$b [81], to be compared to the elastic cross section $\sigma_e(\overline{\text{p}}\text{p} \rightarrow \overline{\text{p}}\text{p}) \approx 23.7$ mb and the annihilation cross section of $\sigma_a(\overline{\text{p}}\text{p} \rightarrow X) \approx 26$ mb. Since no information on the mass dependence of the $\Xi^{-,0}\,\bar{\Xi}^{+}$ production cross section is available, a $A^{2/3}$ dependence was assumed in all considerations shown below.

At present the production of hyperon-antihyperon pairs in antiproton-nucleus can be performed within two models:

- The Intra Nuclear Cascade model. An event generator [132] based on an Intra Nuclear Cascade model is used considering as a main ingredient the rescattering of the antihyperons and hyperons in the target nucleus into account. Starting point of the simulations was the two-body reaction $\overline{\text{p}}\text{p} \rightarrow \Xi\bar{\Xi}$. Unfortunately, the statistics produced by this event generator is limited to one sample, and high statistics are not long affordable.

- For the contrary, full microscopic transport calculations using an extension of UrRQMD [126] (UrQMD+SMM) for the production of strangeness allow to produce high statistics.

In both of these event generators the rescattering mechanism plays an important role in the production of low momenta Ξ^{-} below 500 MeV/c. This feature is essential for the experiment, since Ξ^{-} with a momenta below 500 MeV/c can be captured and converted within a nucleus most likely than those with larger momenta which decay prior to their capture.

In addition, both models produce Ξ^- hyperons with momenta ranging from a few hundred MeV/c to 2 GeV/c. On the other hand, some differences can be observed by comparing the maximum of both momentum distributions. Contrary to the INC model, the UrQMD offers a more optimistic result, producing a number larger of Ξ^- below 500 MeV/c. Nevertheless, in the present work both models will be used as starting point of the hypernuclei production in the present Monte Carlo simulation. It will be shown later, that both points of view by means of Ξ^- production will lead to an successful result of the realization of the hypernuclear experiment at $\overline{\text{P}}$ANDA.

In the following, the performance of the hypernuclear detector setup will be studied using the INC generator interface for the production of $\Xi^-\overline{\Xi}$ in $\overline{p}$+^{12}C reaction. Since Ξ^- largest than 500 MeV/c are unlikely to form double hypernuclei, the present $\Xi^-\overline{\Xi}$ calculations have been performed considering those events where Ξ^- below 500 MeV/c are produced (See Fig. 4.3).

The relevant quantity for the optimization of the target system is the rate of the stopped Ξ^- over the produced Ξ^-. The rate depends on several parameters: production rate, distance between the production and the hypernuclear targets, beam pipe diameter, materials of the targets and their sizes and shapes.

To explore the role of the primary target independently a detailed study of the dependence of the Ξ^- production rate on the mass number of the primary target has been performed [132]. The nuclear targets used for this study were ^{12}C, ^{27}Al, ^{57}Ni, ^{108}Ag, ^{137}Ba and ^{197}Au. As expected, the production rate rises with the mass number A by a factor 3.5 going from carbon to gold. Considering only the Ξ^- production rate, a heavy target would be preferable. However, another point which needs to be taken into account is the neutron background (See Fig. 4.4) at backward angles, where the Germanium detectors are located. For lighter targets the neutrons are mainly forward focused in the laboratory frame, thus reducing significantly the number of neutron hits in the Germanium detectors. The use of a target for example, in the Nickel mass region ($Z \approx 30$) allows a stable operation over a sufficiently long measuring period.

Target nuclei with larger mass are more efficient for rescattering of the produced primary particles and hence for the emission of low momentum Ξ^- hyperons. However, heavier targets increase the neutron and X-ray background in the germanium detectors, as it can be observed in Fig. 4.4. Furthermore, Coulomb scattering in heavy primary targets leads to significant losses of antiprotons. It is preferable to avoid this difficulty by using a target with atomic number below $Z \approx 30$. The thickness of the primary target is constrained by small angular scattering causing beam heating as well as the possible interaction rate ($10^7\,\mathrm{s}^{-1}$). However, a precise determination of the primary interaction point is not required and the interaction rate can be adjusted by the quality of the beam focus and by steering an appropriate fraction of the beam onto the target. For a hydrogen target a thickness of 50 μm seems acceptable, heavy

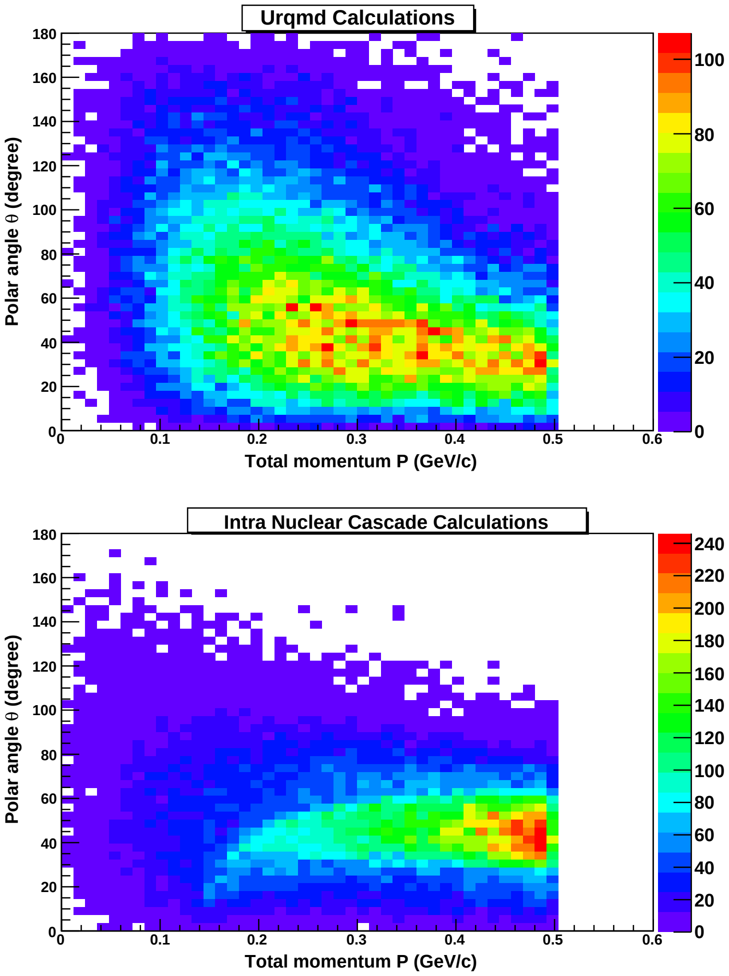

Figure 4.3: Production of $\Xi^-\overline{\Xi}$ in $\overline{p}+^{12}$C reaction within a Intra nuclear cascade based model and a UrQMD based model respectively. Both models produces Ξ^- in the momentum range of 100 MeV/c to about 2 GeV/c. Unlike the INC model, high statistics of Ξ^- below 500 MeV/c are produced by using an extension code of the UrQMD model.

targets require significantly lower area densities. Presently, two scenarios are being explored: self-supporting wires of thickness in the order of 10 μm are readily available. However, such a thickness is only acceptable for light elements like e.g. Beryllium. For heavier elements thin metal sheets – as being used at the internal target of the ANKE experiment at COSY [99] – with a thickness of the order of $< 1\,\mu$m can be used. For example, self-supporting filaments attached to a frame could be produced by etching techniques as being used in the production of micro wire detectors. Therefore it is foreseen to use thin carbon micro-ribbons [133] as a primary target in the HESR ring.

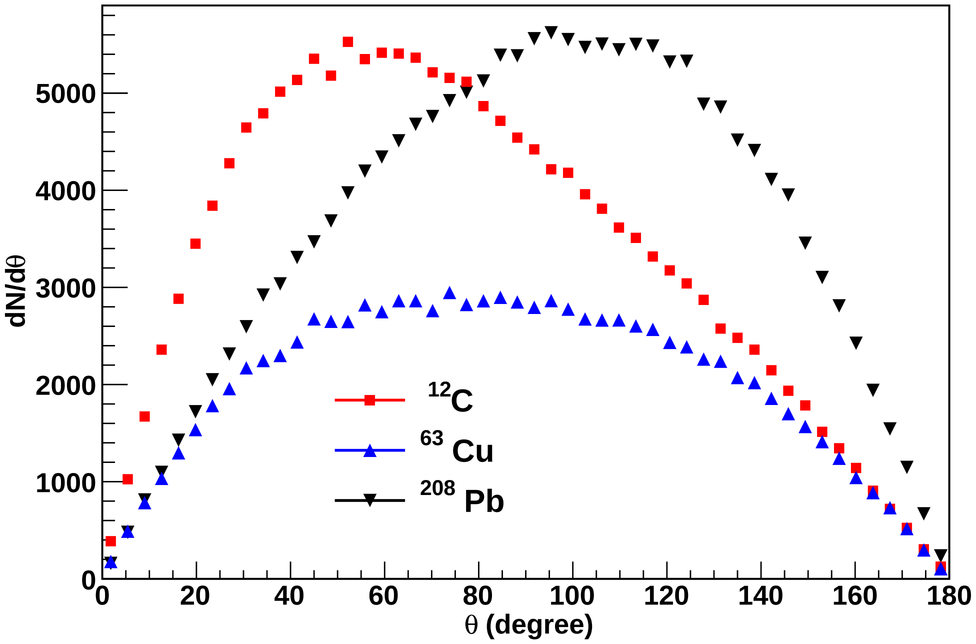

Figure 4.4: Angular distributions of neutrons produced as a result of the interaction of $\overline{p}$ on ^{12}C, ^{68}Cu and ^{208}Pb respectively. For lighter targets (^{12}C) the neutrons are more forward focused in the laboratory frame, thus reducing significantly the number of neutron hits in the Germanium detectors.

The feasibility of using this kind of targets has been evaluated considering the possible beam losses caused by the interaction of antiprotons on a carbon target.

Beam losses are the main restriction for high luminosities, since the antiproton production rate is limited. The main contributions of beam-target interaction are the hadronic interaction, single Coulomb scattering and energy straggling of the circulating beam in the target. However, for the present calculations, only the hadronic interaction has been considered. The influence of these beam losses depend on the fraction of the beam onto the target, the target diameter and the average antiproton luminosity. Large beam losses may cause an increment of the temperature of the target and in the worse case, may lead the target to melt. Accordingly, the relative beam loss rate (τ^{-1}) for total cross section σ_0 is defined as a function of the reference particle's revolution frequency f_0 and the target thickness n_t as follows,

$$\left(\tau^{-1}\right) = n_t \sigma_0 f_0 \tag{4.1}$$

being τ the beam lifetime. In order to evaluate the hadronic cross section of antiprotons with nuclear targets geometrical considerations can be considered. For instance, starting from the antiproton-proton hadronic cross section $\sigma_H^{\bar{p}p}$ for 3 GeV/c,

$$\sigma_H^{\bar{p}p} \approx 50\,\text{mbarn} := \pi r^2 \tag{4.2}$$

with the proton radius $r = 0.9\,\text{fm}$, the antiproton-nucleus hadronic cross section can be deduced as

$$\sigma_H^{\bar{p}A} = \pi \left(R_A + r\right)^2 \tag{4.3}$$

being R_A and A, the radius of a spherical nucleus and the mass number respectively. Up to recently, the accumulation of antiprotons at the FAIR facility was expected to be performed by the RESR [7], achieving in this way an antiprotons rate of approximately 10^{11} per second. However, recent modifications of the setup has been done [7] removing the RESR from the setup. As a consequence, the HESR will have to be accordingly modified to perform the task previously performed by the RESR. As a consequence, the number of antiprotons accumulated will be, after a machine cycle of 1000 s, approximately 10^{10} particles per second (See Fig. 4.5). The variation of the beam lifetime with the thickness d of a ^{12}C target is illustrated in panel a) of Fig. 4.6. In the following, the antiprotons rate and beam lifetime behaviour for two different target thickness (0.02 μm(green line) and 0.04 μm (red line)) will be presented.

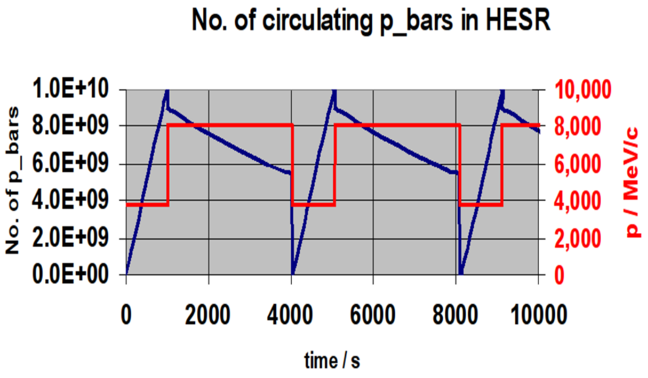

Figure 4.5: A typical cycle in HESR. After a machine cycle of 1000 s the number of antiprotons accumulated will be approximately 10^{10} particles

.

Assuming a ^{12}C target with a 0.02 μm thickness and and a beam fraction [1] of $\simeq$ 0.005, the expected beam lifetime is around 3200 s (one hour), what

---

[1] beam fraction defined as $\frac{AreaBeam}{AreaTarget}$

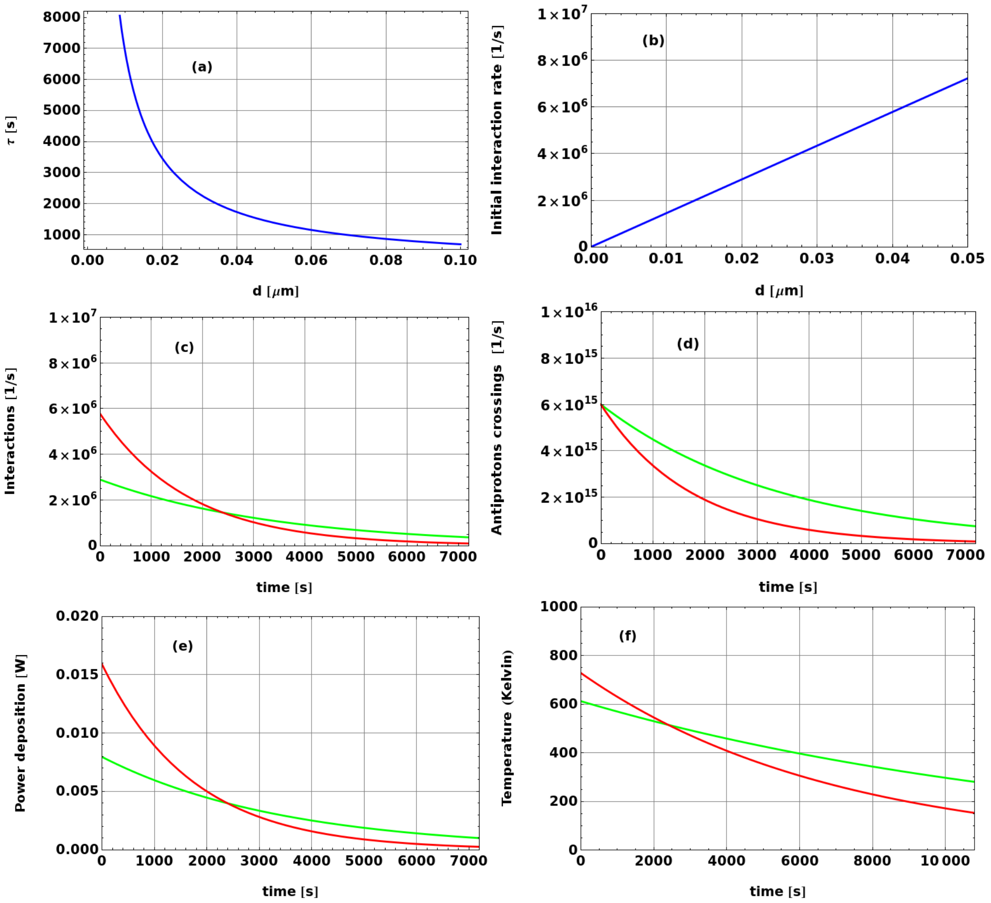

Figure 4.6: Luminosity and beam lifetime considerations for a ^{12}C target with a thickness of 0.02 μm (green line) and 0.04 μm (red line). a) Dependence of the beam lifetime on the target thickness. b) Initial antiprotons rate as a function of the target thickness. c) Variation of the antiprotons rate with time. d)Fraction of antiprotons rate crossing the a target thickness of 0.02 μm (green line) and 0.04 μm (red line), respectively. e) Calculated power as a function of the time. f) Thermal load on a target thickness of 0.02 μm (green line) and 0.04 μm (red line), respectively.

is a reasonable value since beam lifetimes below half an hour cannot be compensated by the antiproton production rate (See panel a. of Fig. 4.6).

The initial interaction rate produced after the interaction with a ^{12}C target is shown in panel b. of Fig. 4.6 as a function of the target thickness. It can be observed that for a 0.02 μm target thickness, the expected initial antiprotons rate is about $3{\times}10^6\,\overline{p}$/s. Moreover, the time variation of the antiproton rate under the above conditions can also be observed in panel c. of Fig. 4.6.

Furthermore, the fraction of antiprotons crossing (See panel d. of Fig. 4.6) the target may lead to an increment of the temperature. To evaluate this influence, the energy lost by the antiprotons crossing the target can be calculated assuming a minimum energy loss of 1.8 MeV/g cm^2. Panel e. of Fig. 4.6 shows the variation of energy deposit per unit time (Power) as a function of the time. Moreover, one can assume that the target behaves as a black body, and as a consequence a temperature can be deduced applying the Stefan-Boltzmann law [2] for a target area of 1 mm^2. As a result, panel f. of Fig. 4.6 shows the dependence of the target temperature on the target diameter and the beam lifetime.

For a diameter of 0.02 μm, and a beam fraction of $\simeq$0.005, the beam lifetime is approximately one hour, what lead to a temperature increment of 500 Kelvin, what is much less than the target melting point (3820 K Diamond, 3948 K Graphite, 3948 K Amorphous). In addition, considering that the instantaneous luminosity must not vary more than a factor 2, the maximum running time could be expected to be about five hours with the above conditions.

Nevertheless, further investigations including the influence of single coulomb scattering are needed as well as reliable cooling system estimates.

4.2.2 Active Secondary Target

The main purpose of the secondary, or hypernuclear, target is the stopping and absorption of the produced Ξ hyperon and the identification of the secondary reaction vertex by tracking of the incident Ξ and charged decay products from the weak decay of the $\Lambda\Lambda$ hypernuclei. Even with a moderate spatial resolution, this information will help to reduce the background in the offline analysis significantly.

The energy release of about 28 MeV during the conversion of the Ξ into two Λ hyperons may give rise to the emission of particles from the secondary target nucleus. As a consequence, a variety of double, single or twin hypernuclei as well as ordinary nuclei may be produced in excited states.

In order to limit the number of possible transitions and thus to increase the possible signal to background ratio, the experiment will focus on light secondary target nuclei with mass number $A_0 \leq 13$. Since the identification of the double hypernuclei has to rely on the unique assignment of the detected γ-transitions, different isotopically enriched light absorbers (^{9}Be, ^{10,11}B, ^{12,13}C) will be used. In addition, the interactions in the material of the silicon detector can be studied. At the same time, the light elements help minimizing the absorption of γ-rays emitted by the excited hypernuclei.

---

[2] The total energy radiated per unit surface area of a black body per unit time or irradiance, is directly proportional to the fourth power of the black body's thermodynamic temperature T (also called absolute temperature)

4.2.2.1 Optimization of the Secondary Target setup

The geometry of this secondary target is essentially determined by the short mean life of the Ξ^- of only 0.164 ns and its stopping time in solid material. The separation between the primary target and the secondary target has to be optimized so that low momentum Ξ^- (approximately below 500 MeV/c) do not decay prior to stopping. As a consequence, the required thickness of the active secondary target is limited to a few cm. The stopping probability of a Ξ^- hyperon with a momentum range between 100 MeV/c and 750 MeV/c depends mainly on the probability of traveling a certain distance comparable with the beam pipe radius d and on the energy losses along its passage through the absorber material. Fig. 4.7 shows the stopping probability calculated numerically as a function of the Ξ^- hyperon momenta for different beam pipe radii and 1 cm carbon absorber. As the figure indicates the maximum probability is reached for a momentum around 250 MeV/c and for a beam pipe diameter of about 2 mm. In addition, for a safe operation of HESR, the beam spot must not be smaller than 0.3 mm. Therefore, a beam pipe with a radius of 7.5 mm corresponding to a beam spot of approximately 2.5 mm is foreseen. The range estimates of Ξ^- hyperon with momentum below 1 GeV/c in a carbon absorber (see Fig. 4.8) lead also to similar conclusions as those deduced from Fig. 4.7. However, in order to determine more in detail the required sensitive region of the secondary target, the distribution of the stopping points of the Ξ^- entering the secondary target has been investigated by using the Pandaroot simulation framework. Initially, the geometry of the secondary target was modeled for simplicity by a solid box (50 cm×50 cm×50 cm) made of carbon with a cylindrical hole of 15 mm diameter representing the beam pipe. The preliminary secondary target setup was placed at a distance of 70 cm upstream from the center of the $\overline{\text{P}}$ANDA solenoid. The generation of 10^6 $\Xi^-\overline{\Xi}$ pairs was accomplished by using the Intra Nuclear Cascade data Sample as input for the Ascii Generator. Under a magnetic field of 2 T, the Ξ^- were traced within the secondary target material. Fig. 4.9 shows the stopping points of Ξ^- hyperons, where the horizontal axis represents the beam direction and the vertical axis is the radial distance from the beam axis. The origin marks the primary target point. Consistent with the schematic calculations shown in Fig. 4.7 and Fig. 4.8 the stopping points are concentrated in an angular range from 40° to 90° and a radial thickness of about 20 mm. The free angular range between 0° and 40° is sufficiently large for the detection of the associated kaons emitted mainly in the forward region (see Fig. 4.10).

In order to track the Ξ^- (and the charged fragments resulting from the decay of the produced hypernuclei), it is planned to sandwich the secondary absorber with layers of silicon detectors. Outside of the beam pipe we projected in a first design a multi-layered structure of 1. mm thick carbon absorbers surrounded by 300 μm thick silicon layers.

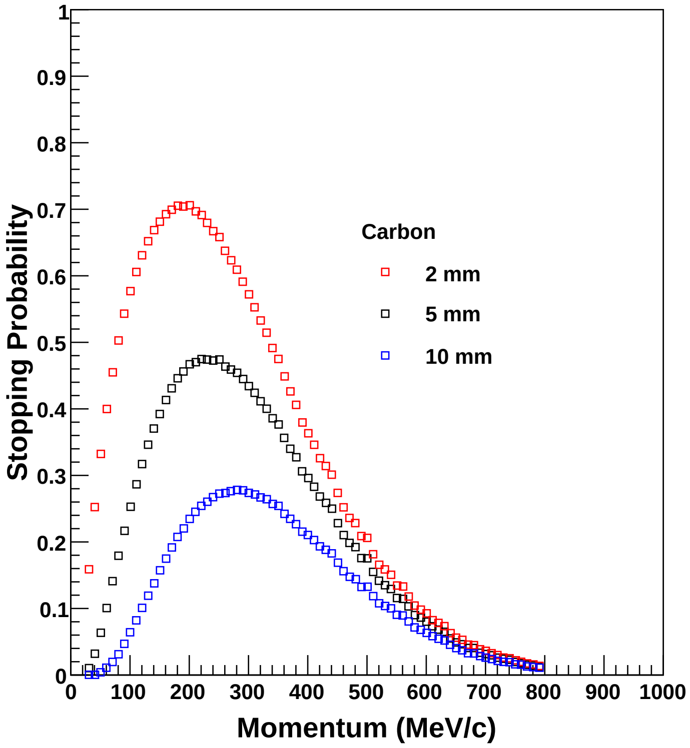

Figure 4.7: Stopping probability calculated numerically as a function of the Ξ^- hyperon momenta for different beam pipe radii and 1 cm carbon absorber.

The number of silicon detectors and the thickness of the absorber is a compromise between the necessary number of readout channels and the corresponding costs on one hand and a large stopping probability on the other hand. Furthermore, in order to keep the γ-ray absorption low, the overall thickness should be kept as low as possible. The γ-rays emitted from the hypernuclei will traverse a typical distance of 2 cm in the secondary target. Therefore, γ-rays with energies of 0.1, 1 and 10 MeV will reach the Germanium detectors with 60, 80 and 93 % probability, respectively. Front-end electronics and upstream cable connections may cause additional losses in the order of 10 %.

For the choice of the silicon detectors two options are being considered:

(i) A pixel detector based e.g. on the ATLAS pixel chip. This solution would guarantee broad compatibility with the main vertex detector. However, major disadvantages are the small size of the present ATLAS chips and the space needed for the supporting structure onto which the chips are glued. The small size of the chips does not allow a geometry where the readout cables are concentrated in the upstream region. The additional support structures

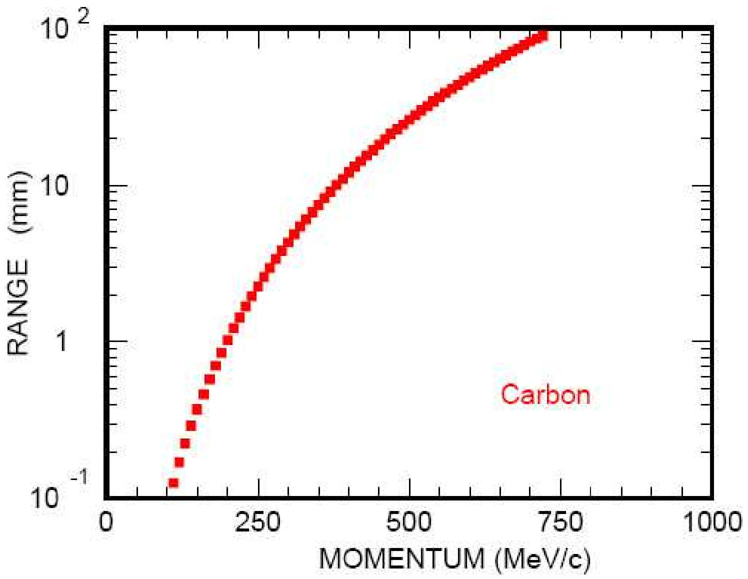

Figure 4.8: Range of Ξ^- hyperon with momentum below 1 GeV/c in a carbon absorber.

would result in major empty or inactive regions between the main secondary absorber material, thus reducing the stopping and capture probability.

(ii) A silicon strip detector. For a possible readout scheme we plan to follow the developments for the SCT barrel module of ATLAS. A thickness of the readout board of less than 1.5 mm has been achieved by the ATLAS collaboration for e.g. the ABCD chip. Thus, a dense sandwich structure with about 1.5 mm absorber material enclosed by detector layers is feasible. Since in the region of the silicon sensors no additional components are located, this well known technology leads to the required compact configuration of the secondary target.

An optimal coverage of the region between 40° and 90° would require silicon sensors of different sizes (see upper and lower part of Fig. 4.11). The size of the detector closest to the beam is about $15 \times 9\,\mathrm{mm}^2$, the largest of the order of $55 \times 33\,\mathrm{mm}^2$. While such a solution is not impractical we are now exploring also different geometries with sensors allowing identical front-end electronics. One example is shown in the upper part of Fig. 4.11.

4.2.3 Germanium Array

An existing germanium-array with refurbished readout is planned to be used for the γ-spectroscopy of the nuclear decay cascades of hypernuclei. The main limitation will be the load due to neutral or charged particles traversing the germanium detectors. Therefore, readout schemes and tracking algorithms are

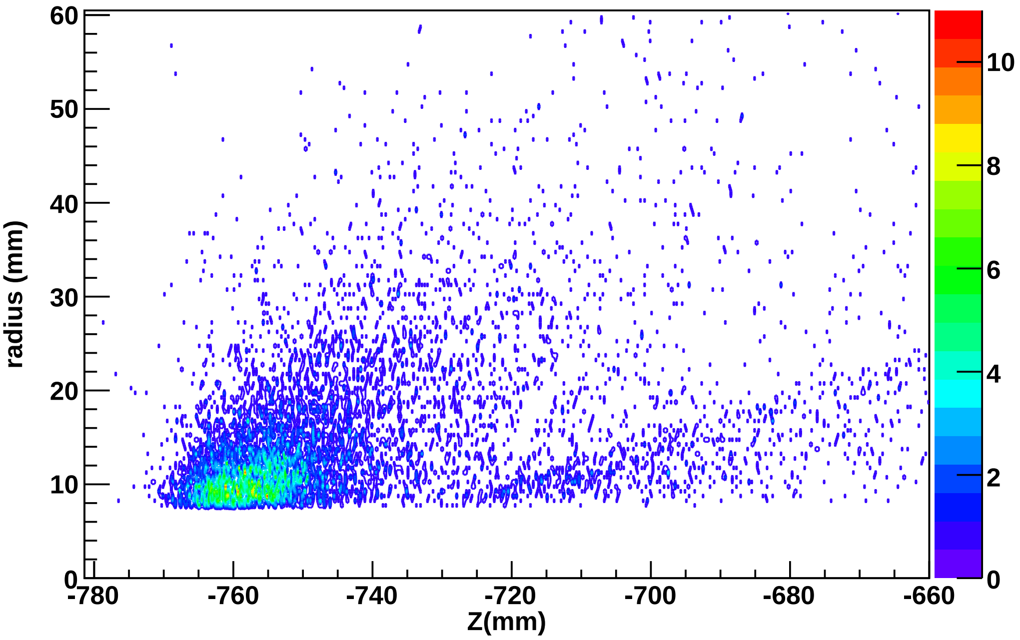

Figure 4.9: Stopping points of Ξ^- hyperons produced in $\overline{\mathrm{p}} + X$ interactions at 3 GeV/c within an INC calculation. The primary target was placed at distance of -76.5 cm to the center of the P̄ANDA spectrometer.

presently being developed which will enable high resolution γ-spectroscopy in an environment of high particle flux. The germanium-array crystals will be grouped asymmetrically by forming triple clusters. Each cluster consists of three encapsulated n–type Germanium crystals of the Euroball type. The total γ–array set-up consists of 15 triple Germanium clusters positioned at backward axial angle around the target region as shown in Fig. 4.12.

4.2.3.1 Required modifications of the Germanium detectors

Standard electronic readout systems are hardly capable of dealing with particle rates exceeding 10 kHz. However, the fully digital electronic system currently developed for the new generation of Germanium arrays like Vega [135] will – in connection with fast preamplifiers – allow the load of background particles at rates higher than 100 kHz for each detector element. Arranging several cluster detectors – each cluster contains in its present configuration 3 independent detector elements – and taking into account that most of the produced particles are emitted into the forward region not covered by the Germanium array an interaction rate of $10^7\,\mathrm{s}^{-1}$ seems to be manageable.

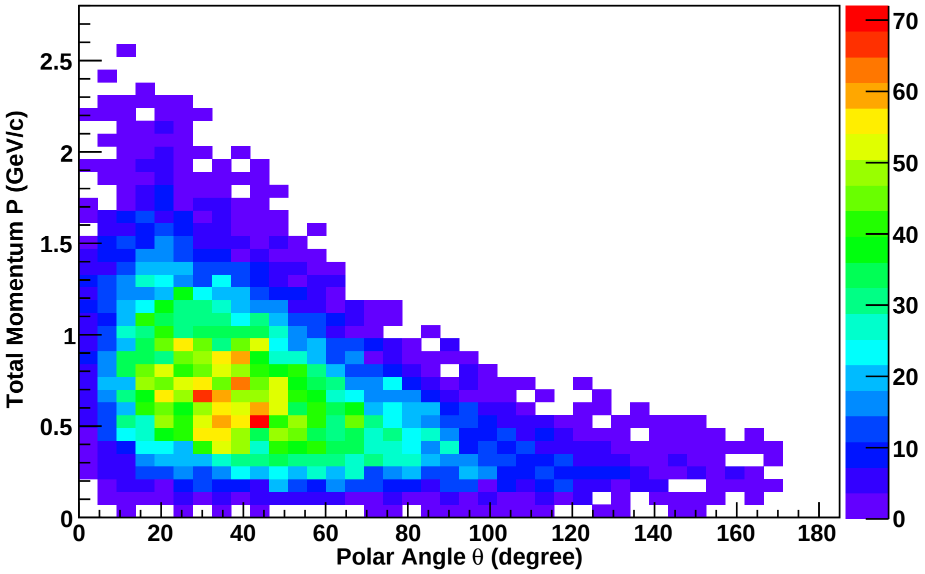

Figure 4.10: Distribution of positive kaons produced as a result of the annihilation of of $\bar{\Xi}^{-}$ hyperons in the primary carbon target.

Close to the $\overline{\mathsf{P}}$ANDA main detectors the available space in radial direction is limited to the diameter of the tracking detector. Therefore, a practical mounting of the Germanium detectors inside the tracking detector is not feasible when including the present dewar into the setup. It is planned to replace the bulky storage tanks for liquid Nitrogen by a more compact cooling system. Presently one possible solution is being explored consisting of a mechanical cooling system based on the Stirling thermal cycle, like e.g. the X-COOLER II by ORTEC [136]. These systems have a good cooling power, however, acoustic noise and vibrations present a serious problem. Although, when using a fully digital readout system based on flash ADCs it might be possible to correct for these (periodic) distortions.

4.2.4 Time of Flight System

The $\bar{p}p \rightarrow \Xi^{-}\bar{\Xi}$ cross section of 2μb is about a factor 25000 smaller than the total $p\bar{p}$ cross section of 50 mb at 3 GeV/c. As a consequence an strategy must be performed to enable an efficient background signal suppression. As it was remarked before, associated antihyperons annihilates with a large probability ($\simeq 80\%$) within the primary target nucleus releasing at least two positive kaons which can be used to tag the hypernuclei production. Kaons produced in this way are emitted in the forward direction (beam direction) and with a momen-

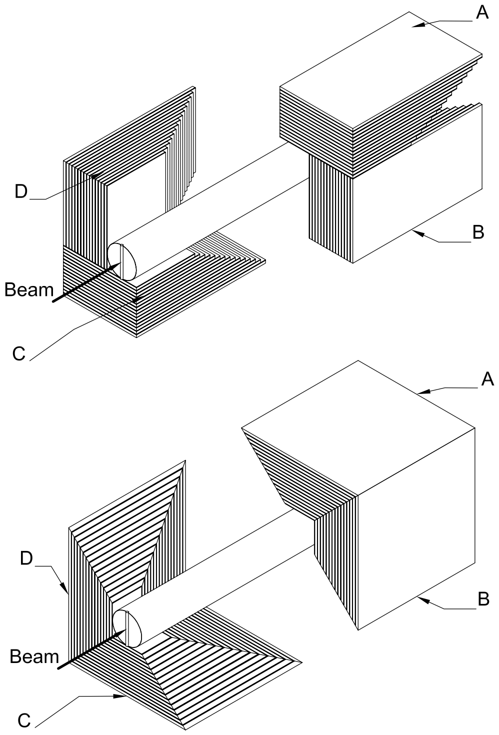

Figure 4.11: Possible geometries of the secondary target showing the four sectors. For the geometry shown on the bottom, front-end boards of different sizes are needed, the geometry on top allows the usage of equally sized front-end electronics. Two sections are displaced for clarity.

tum range around 500 MeV/c. Here the difficulty resides in finding a proper detector system to identify efficiently positive kaons. In the current $\overline{\textsf{P}}$ANDA design, particle identification for slow particles may be provided at large polar angles by a TOF detector in combination with the Time Projection Chamber (TPC). As candidates for this detector scintillator bars and strips or alternatively multi-gap resistive plate chambers are considered. In the absence of a start detector the relative timing of multiple particle hits has to be employed. A small fiber barrel read-out by Silicon Photo Multipliers (SiPM) has been discussed as an option for a start detector. Such a detector might also be used as a time reference for the DIRC detector or for track deconvolution of the time projection chamber. The SiPM is intrinsically a very fast detector and its single photoelectron time resolution is about 100 ps (FWHM). When coupled to thin and short scintillating fibers the timing properties are fully dominated by the scintillation time constants and depend only on the average number of detected photons. For such a sub-detector system the achievable time resolution at minimum detector mass is a main issue. In measurements

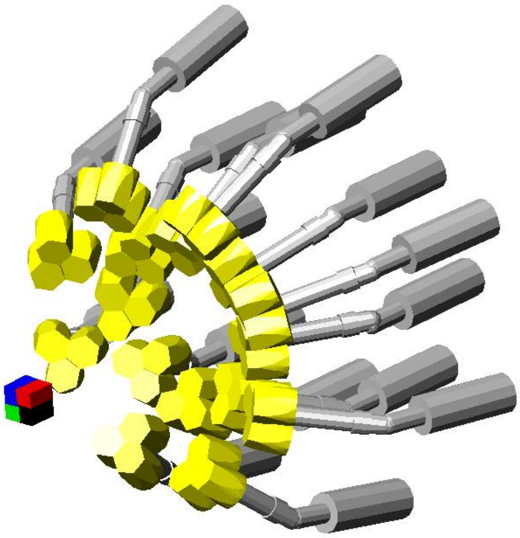

Figure 4.12: Design of the γ–ray spectroscopy setup with 15 germanium cluster detector, each comprising 3 germanium crystals.

using the electromagnetic calorimeter the additional material will deteriorate considerably its resolution.

The setup of the proposed start detector consist of 1200 scintillating fibers placed placed parallel to the beam axis in two rings around the secondary active target. The first ring contains 500 fibers located at a distance of 70 mm from the primary interaction point. In the second ring, a number of 750 fibers are displaced at a distance of 99 mm from the primary interaction point. All the fibers have a diameter of 0.83 mm and a length of 1800 mm.

Particles traveling through the target spectrometer (TPC and TOF) describe a path length varying from 0.5 m to 1 m. Using the principle that particles with different masses (m_1 and m_2) and same momentum p travel a path L in different times, particle separation can be performed. The momentum range over which particle separation is possible depends crucially on the timing resolution σ_t. For a path length L between two counters the time of flight T is inversely proportional to its velocity $\beta = v/c$, being c the speed of light, and v the particle linear velocity:

$$T = \frac{L}{c\beta} \tag{4.4}$$

Moreover, the particle separation capability or separation power N_{σ_t} can be expressed in terms of time resolution σ_t units as,

$$N_{\sigma_t} = \frac{\Delta T}{c\sigma_t} \tag{4.5}$$

where ΔT^3 is the difference in time. Fig. 4.13 shows the separation power of

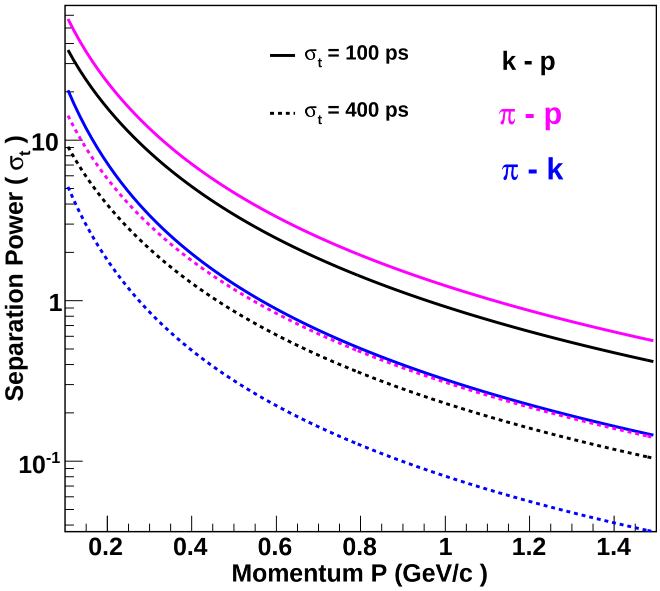

Figure 4.13: Separation power in standard deviation units for protons, pions and kaons by using the timing and the tracking information (momentum, track length, etc). The solid and dashed curves reprent the separation by assuming a time resolution of 100 ps and 400 ps respectively.

protons, pions and kaons by using the timing and tracking information (e.g. momentum, track length and charge). For a path length of 1 m approximately, the separation power increases with increasing time resolution but at the same time decreases as the particle momentum rises up. For instance, the dashed and the solid curves represent the separation power at the time resolution values of 400 ps and 100 ps respectively.

This calculation also reveals that for low and moderate momentum kaon identification the stop detector must provide a time resolution of about 100 ps, whereas the fiber detector has to provide the start time with a minimum resolution of 400 ps. It seems challenging to achieve these values with the geometries and photon detection devices described so far. One improvement is made by using a large area SiPM/fiber combination, and it was concluded that SiPM with 3×3 mm^2 active area can be used in combination with scintillator or radiator strips of this cross-section for fast time response measurements [137]. Only recently, lutetium aluminum garnet (LuAG, chemical formula $Al_5Lu_3O_{12}$)

---

[3] $\Delta T = T_1 - T_2 = \frac{L}{c}\left(\sqrt{1+\frac{m_1^2}{p^2}} - \sqrt{1+\frac{m_2^2}{p^2}}\right)$

activated by cerium became available as possible fiber material. Its density of 6.73 g/cm^3 and decay time of 70 ns brings some advantages for time dependent and coincidence measurements. Primarily, the higher density compared to organic fibers results in a higher light output from the fibers. The wavelength of the emission spectrum is at 535 nm which is ideal for avalanche diode or SiPM readout. The photon yield is 20000 Photons/MeV and crystals can be grown 1 mm in diameter and up to 500 mm length. Further investigations on prototypes such as fiber bundles indicates that these devices could be used as a possible TOF start detector.

CVD Diamond detectors can be also used as alternative to the scintillation fibers detector. It can provide a time resolution close to the 100 ps and are radiation hard. Further investigations about its applications as start detectors have been already performed at GSI. The results present this technology as a promising alternative to be used for timing measurements [139]. A possible detector setup will be a CVD diamond plate segmented placed downstream of the secondary active target.

Chapter 5

Performance of the Hypernuclei production mechanism

In this chapter the second stage of the hypernuclei production mechanism (see Fig. 4.1 in chap. 4) will be introduced. An important issue to be studied is the population of particle stable, excited states in double hypernuclei after the capture of a Ξ^- within a statistical decay model. This study will be relevant for the performance of gamma spectroscopy at the $\overline{\mathsf{P}}\mathsf{ANDA}$ experiment. In the present Monte Carlo simulation, the use of this model will be used as basis for the implementation of hypernuclei event generation.

According to that, the principles of the statistical model used for the hypernuclei production in the present work will be introduced in Sec. 5.1. In Sec. 5.1.2 the production yields of different double hypernuclei will be performed using different assumptions. The results of these calculations will be compared in Sec. 5.1.3 with the present results of the AGS-E906 experiment. The last sections of this chapter are focused on the procedure for implementing the hypernuclei event generation in the simulation code.

5.1 Production of excited double hypernuclei via a statistical decay model

In Sec. 1.3, it has been discussed about the importance of using the gamma–spectroscopy of single hypernuclei to obtain direct information about the hyperon–nucleon. In analogy with single Λ hypernuclei, the identification of double Λ hypernuclei can benefit from the observation of their corresponding excitation spectra (See Sec. 2.2.2). In particular, information on the Λ-Λ interaction will be directly obtained using this technique without the ambiguities of past experiments.

Unfortunaly, for double hypernuclei the experimental information is restricted to a few cases only [140, 91, 92, 93, 94]. Except for the ${}^{6}_{\Lambda\Lambda}\mathrm{He}$ nucleus reported in Ref. [94], the interpretation of the observed events is however not unique [88, 89, 90, 95, 87]. Furthermore no direct experimental information on possible excited states is at hand (see e.g. discussion in Ref. [95]).

In the following the population of particle stable, excited states in double hypernuclei after the capture of a Ξ^- will be therefore studied within a statistical decay model. Since the identification of the double hypernuclei has to rely on the unique assignment of the detected γ-transitions, we will perform these calculations for different target nuclei which are experimentally feasible.

5.1.1 The double Λ compound nucleus model

The deep inelastic interaction of fast hadrons and heavy ions with nuclei may result in the formation of intermediate nuclear systems in states far from the nuclear ground state. The evolution of these systems proceed in general into several stages:

- the formation of an intermediate highly excited nuclear system,
- the expansion of the system and its disassembly into individual fragments,
- the de–excitation of hot primary fragments.

Schematically this process is shown in Fig. 5.1. Despite of simplicity, the statistical approach makes possible a full description of the highly excited system of hadrons and nucleon clusters, but the price for this simplicity is the assumption of statistical equilibrium. At present there exist several versions of the statistical model of nuclear multifragmentation. They differ in the statistical ensembles considered (macrocanonical, canonical or microcanonical), in the way of describing individual fragments and in the calculational procedures. Nevertheless, all models presuppose that before disintegrating a hot nuclear matter system gets into partial or complete thermodynamical equilibrium with respect to some or all of its degrees of freedom.

One step beyond, is the generalization of this model to describe the evolution of hypermatter (highly excited nuclear systems containing Λ hyperons) produced in peripheral collisions of relativistic heavy ions (see Sec. 1.2.2.4).

In the following an extension [141] of the grand–canonical version of the statistical multifragmentation model (SMM) [142] will be used to describe the formation of double and single hypernuclei. This model also provides the possibility to study the population of particle stable, excited states in double hypernuclei which is relevant for the performance of γ spectroscopy at $\overline{\text{P}}$ANDA. In analogy with the compound nucleus model of Sano and co–workers [143, 144] the production of excited states in double hypernuclei is studied following the break–up of an excited double hypernucleus after the absorption and conversion of a stopped Ξ^-.

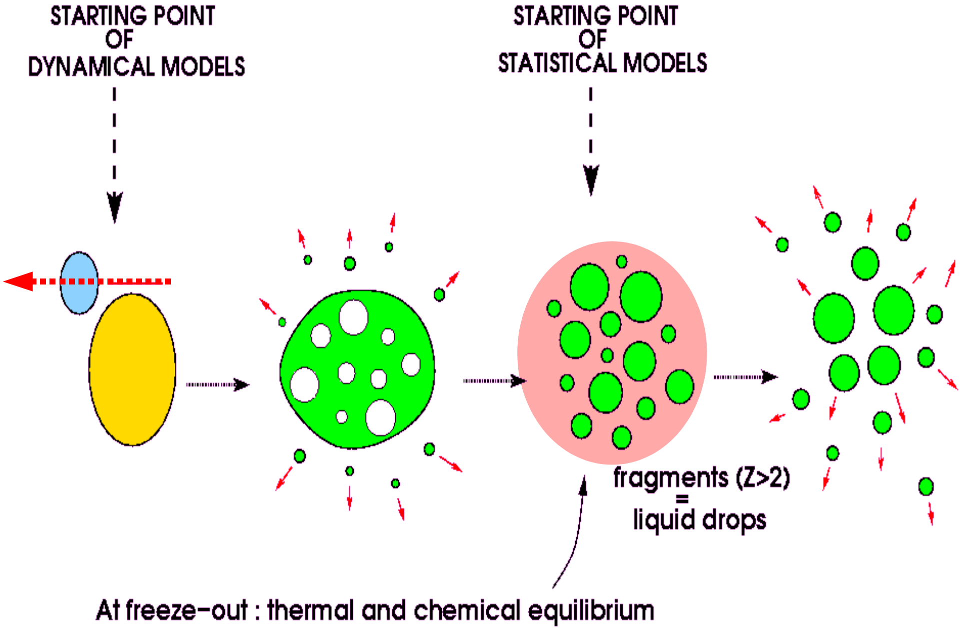

Figure 5.1: Schematic view of the fragmentation process: a) formation of highly-excited system with initial fluctuations; b) formation of fragments during the expansion stage; c) propagation and deexcitation of fragments after the break-up of the composite system.

According with the model, for light nuclei even a relatively small excitation energy may be comparable with their binding energy. In this case it is assumed that the principal mechanism of de-excitation is the explosive decay of the excited nucleus into several smaller clusters. The description of this break-up process is given by the model in a similar way as it is established by the famous Fermi model for particle production in nuclear reactions [145]. Moreover, it is assumed that the nucleus with mass numbers A_0, charge Z_0, and the number of Λ hyperons Λ H_0 (here H_0=2) break-ups simultaneously into cold and slightly excited fragments, which have a lifetime longer than the decay time, estimated as an order of 100-300 fm/c. This break-up takes place in some freeze-out volume V, where the produced fragments moves in the phase space determined by the free volume V_f. This free volume is smaller than the freeze-out volume, at least, by the proper volume of the fragments. The "excluded volume" approximation is used for this parametrization:

$$V_f = \kappa V_0 \tag{5.1}$$

where $V_0 = 4/3\pi r_0^3 A_0$ is the initial volume of the nucleus, $r_0 \approx 1.3$ fm the nucleon radius, and $V = V_f + V_0$. In the following the parameter κ=2 is considered which is consistent with many description of the data of normal nuclei [142].

In the case of production of conventional nuclear fragments in a break-up channel, their experimental masses in ground states and their excited states are considered, which are stable respective to emission of nucleons (ref. [146]). For hypernuclei with single Λ particle, the experimental masses and excited states are used, which were collected in various reviews [147, 56] and some theoretical predictions [148] (see table. A.7)).

In the case of double hypernuclei, theoretical predictions of bound and exited states of double hypernuclei by Hiyama and co-workers [95] were used in the present model calculation for nuclei with mass number 6$\leq A_0 \leq$10. The masses of ${}^{8}_{\Lambda\Lambda}$He and ${}^{9}_{\Lambda\Lambda}$He were calculated from the known single hypernuclear masses and assuming $\Delta B_{\Lambda\Lambda}$=1 MeV. For the mirror nuclei ${}^{5}_{\Lambda\Lambda}$H and ${}^{5}_{\Lambda\Lambda}$He there seems to be a consensus that these nuclei are indeed bound [71, 73, 149, 150, 151]. In view of the theoretical uncertainties, these calculations assume a value for the Λ-Λ bond energy $\Delta B_{\Lambda\Lambda}$ of 1 MeV for both nuclei. In case of ${}^{4}_{\Lambda\Lambda}$H the experimental situation is ambiguous [93, 87] and also the various model calculations predict an unbound [152] or only slightly bound nucleus [153, 154, 151].

For nuclei with mass number $A \geq$11 the masses of ground states were taken from ref. [75] which correspond to $\Delta B_{\Lambda\Lambda}$ values between 2.0 and 4.6 MeV. Also for these heavy nuclei several particle stable excited states are expected [75]. Furthermore, the calculations of Hiyama and co-workers [95] signal that in the mass range relevant for this work the level structure of particle stable double hypernuclei(${}^{A}Z_{\Lambda\Lambda}$) resembles the level scheme of the corresponding core nucleus(${}^{A-2}Z$).

In order to explore the role of possible additional states the set of double hypernuclei with $A \geq$11 has been extended by the excited states of the corresponding core nucleus. Only states below the lowest particle decay threshold were considered. In the present calculations $1s_\Lambda 1p_\Lambda$ states have been ignored though these states may possibly contribute at high excitation energies in heavy nuclei [155]. As a consequence, it is considered that the two Λ particles are coupled to ${}^1S_0$ wave (spin S=0 and isospin T=0), and therefore the spins and parities are the same as those of its nuclear core.

In case of ${}^{11}_{\Lambda\Lambda}$Be, ${}^{11}_{\Lambda\Lambda}$B, ${}^{12}_{\Lambda\Lambda}$Be and ${}^{12}_{\Lambda\Lambda}$B this procedure results in 9, 3, 7 and 24 excited states, respectively (For more details see tables. A.10). Furthermore, it has been observed that by considering a subset of the whole excited states, (e.g the 3–4 lowest states) the final result does not change significantly. Following the microcanonical approach, all possible break-up channels are considered, which satisfy the mass number, hyperon number (i.e. strangeness), charge, energy and momenta conservations, and the competition between these channels is also taken into account.

The model considers that the probability of each break-up channel ch is proportional to the occupied phase space [142, 156, 157]. The statistical weight of the channel containing n particles with masses m_i $(i = 1, \cdots, n)$ can be calculated within the microcanonical approximation :

$$W_{ch}^{mic} \propto \frac{S}{G} \left(\frac{V_f}{(2\pi\hbar)^3} \right)^{n-1} \left(\frac{\prod_{i=1}^{n} m_i}{m_0} \right)^{3/2} \frac{(2\pi)^{\frac{3}{2}(n-1)}}{\Gamma(\frac{3}{2}(n-1))} \cdot \left(E_{kin} - U_{ch}^{C} \right)^{\frac{3}{2}n - \frac{5}{2}}, \tag{5.2}$$

where $m_0 = \sum_{i=1}^{n} m_i$ is the summed mass of the particles, $S = \prod_{i=1}^{n}(2s_i + 1)$ is the spin degeneracy factor (s_i is the i-th particle spin), $G = \prod_{j=1}^{k} n_j!$ is the particle identity factor (n_j is the number of particles of kind j). E_{kin} is the total kinetic energy of particles at infinity which is related to the nucleus excitation energy $E_{A_0}^{*}$ as

$$E_{kin} = (M(\Xi^-) + M_{target})c^2 - B_{\Xi^-} - \sum_{i=1}^{n} m_i c^2. \tag{5.3}$$

Here B_{Ξ^-} is the binding energy of the converted Ξ^- and $E_{max} = (M(\Xi^-) + M_{target})c^2$ represents the maximum available excitation energy ignoring the binding energy B_{Ξ^-}, U_{ch}^{C} is the Coulomb interaction energy between fragments given in the Wigner-Seitz approximation [142]:

$$U_{ch}^{C} = \frac{3}{5} \frac{e^2}{r_0} (V/V_0)^{-1/3} \left(\frac{Z_0^2}{A_0^{1/3}} - \sum_{i=1}^{n} \frac{Z_i{}^2}{A_i{}^{1/3}} \right), \tag{5.4}$$

where A_i, Z_i are mass numbers and charges of produced particles. The masses of fragments in excited states are calculated by adding the corresponding excitation energy to their ground state masses.

5.1.2 Population of Excited States in Double Hypernuclei

Unfortunately, still very little is established experimentally on the interaction of Ξ hyperons with nuclei. Various data(see e.g. [158, 159]) suggest a nuclear potential well depth around 20 MeV. Calculations of light Ξ atoms [80] predict that the conversion of the captured Ξ^- from excited states with correspondingly small binding energies dominates. In a nuclear emulsion experiment a Ξ^- capture at rest with two single hyperfragments has been observed [160] which was interpreted as $\Xi^- + C \rightarrow^4_\Lambda H +^9_\Lambda Be$ reaction. The deduced binding energy of the Ξ^- varied between 0.62 MeV and 3.70 MeV, depending whether only one out of the two hyperfragments or both fragments were produced in an excited particle stable state.

Model calculations [161, 162, 63] suggest that the width for the conversion of a Ξ^- and a proton into two Λ's is around 1 MeV, i.e. the conversion is rather fast and takes less than 200 fm/c. Moreover this conversion may happen at different energy levels, and a part of the released energy may be lost. Therefore, in order to take into account the uncertainties of the excitation energy of the converted Ξ^--states, the calculations have been performed for a range of energies $0 \leq B_{\Xi}^- \leq E_{max}$, constructing in this way the excitation functions for production of hypernuclei.

In the following, in order to limit the number of possible electromagnetic transitions and thus to increase the possible signal to background ratio, light target nuclei with mass number $A_0 \leq 13$ will be considered. Moreover, for this mass range significant experimental information on bound single hypernuclei states exists already [56] and can be used as an ingredient in the model calculations. Therefore, calculations were done for all stable secondary targets (^9Be, ^{10}B, ^{11}B, ^{12}C and ^{13}C) which lead to the production of excited states in double hypernuclei.

The Fermi break-up events were generated by comparing probabilities of all possible channels with Monte–Carlo method. For instance, there are included 993 channels for the reaction induced by absorption of Ξ^- on ^{13}C nucleus, and this number decreases for smaller target nuclei. The Coulomb expansion stage was not considered explicitly for such light systems. The momentum distributions of the final break-up products were obtained by the random generation over the whole accessible phase space, determined by the total kinetic energy (5.3), taking into account exact energy and momentum conservation laws. For this purpose a very effective algorithm proposed by G.I. Kopylov [163] has been applied.

Previously, this model was applied rather successfully for description of break-up of conventional light nuclei in nuclear reactions initiated by protons, pions, antiprotons, and ions [164, 165, 166, 167]. In comparison with experimental yields of different fragments the maximum deviation was about 20–50%. This precision seems to be sufficient for the present analysis of hypernucleus decay, since the main uncertainty is in unknown masses and energy levels of produced hyperfragments. The estimation of their yields within this model is extremely helpful for planning future experiments for searching double hypernuclei.

Fig. 5.2 shows as an example the production of ground (g.s.) and excited (ex.s.) states of single + one free Λ (SHP), twin (THP) and double (DHP) hypernuclei in case of a ^{12}C target as a function of the assumed Ξ^- binding energy. With increasing Ξ^- binding energy the excitation energy of the excited primary $^{13}_{\Lambda\Lambda}B^*$ decreases from left to right from 40 MeV to 15 MeV. For all excitation energies above 20 MeV the production of *excited* double hypernuclei dominates (green triangles).

This can be caused by the opening of several thresholds for various excited double hypernuclei already at moderate excitation energies (see e.g. Fig. 5.3 in ref. [75]). Only for small binding energies and hence large excitation energies the production of single and twin hypernuclei becomes of significant importance (10%). The non–monotonic behaviour for single hypernucleus + free Λ production reflects the fact that the various lowest thresholds are relative high and widely separated, e.g. ${}^{12}_{\Lambda}B+\Lambda$ at $B_{\Xi}=23.9\,\text{MeV}$ followed by ${}^{11}_{\Lambda}B+n+\Lambda$ at 11.3 MeV.

Twin–hypernuclei (both in the ground in excited states(g.s.), exactly one in the ground state or both in excited states) are only produced for Ξ^- binding energies below the threshold for ${}^{8}_{\Lambda}Li + 5_{\Lambda}He$ with $B_{\Xi} = 13.6$. As discussed above the observation of twin–hypernuclei [160, 168, 169, 170, 171, 172] denotes a conversion from a Ξ^- state with moderate binding energy. In this range of B_{Ξ} the production probability of double hypernuclei is comparable to previous estimates within a canonical statistical model [75].

It is important to stress that these numbers do not include a possible pre–equilibrium emission of hyperons during the capture and conversion stage. With respect to the number of stopped Ξ^- hyperons, pre-equilibrium processes will decrease the yield of double hypernuclei(see e.g. [173]). For these calculations a joint capture×conversion probability of 5% will be assumed to mimic the pre–equilibrium stage. Taking this factor into account the probability for the various channels is compatible with the present scarce experimental information [76, 77, 173].

Fig. 5.4 shows the population of the four lowest lying, particle stable states in double hypernuclei. The ${}^{12}_{\Lambda}\text{Be}$+p and ${}^{12}_{\Lambda}\text{B}$+n have the lowest thresholds [75] and dominate at large binding energies and hence small excitation energies. At smaller and more realistic binding energies the lighter double hypernuclei ${}^{11}_{\Lambda\Lambda}\text{Be}$, ${}^{10}_{\Lambda\Lambda}\text{Be}$ and ${}^{9}_{\Lambda\Lambda}\text{Li}$ prevail. Due to higher spin degeneracy factor the population of excited states can exceed those of ground states significantly at low binding energies. The dominant population of excited states in e.g. ${}^{10}_{\Lambda\Lambda}\text{Be}$ is consistent with the conjecture of Hiyama and co–workers [95] that the Demachi–Yanagi [94, 174] event can be interpreted most probably as the observation of 2^+ excited state in ${}^{10}_{\Lambda\Lambda}\text{Be}$.

These calculations also indicate that by studying relative probabilities of some excited states one may obtain additional information on the binding energy of the of the captured Ξ^- hyperons. Additionally to that, the corresponding population for the rest of target nuclei(${}^{9}Be$, ${}^{10}B$, ${}^{11}B$, and ${}^{13}C$) considered in these calculations can be found in Appendix A.5.

In order to check the behaviour of the relative population at small values of the binding energy, a value for the Ξ^- binding energy of 0.5 MeV is now adopted for the various Ξ^--absorbing stable target nuclei (${}^{9}Be$, ${}^{10}B$, ${}^{11}B$, ${}^{12}C$ and ${}^{13}C$). The summed population of the excited states in all double produced hypernuclei with this new value of B_{Ξ} is shown in Fig. 5.5.

As can be seen from Fig. 5.2 this choice should not be crucial for the main trend. However, as discussed above, the relative population of specific excited levels can depend on the binding energy. In Fig. 5.5 one can observe that the relative yield is proportional to the rectangles area. For each target the area for the most probable hypernucleus is normalized to the unity. For each of the five targets different double hypernuclei dominate.

Thus combining the information of Fig. 5.5 with the measurement of two pion momenta from the subsequent weak decays a unique assignment of various newly observed γ-transitions to specific double hypernuclei seems possible as intended by the $\overline{\text{P}}$ANDA collaboration [7].

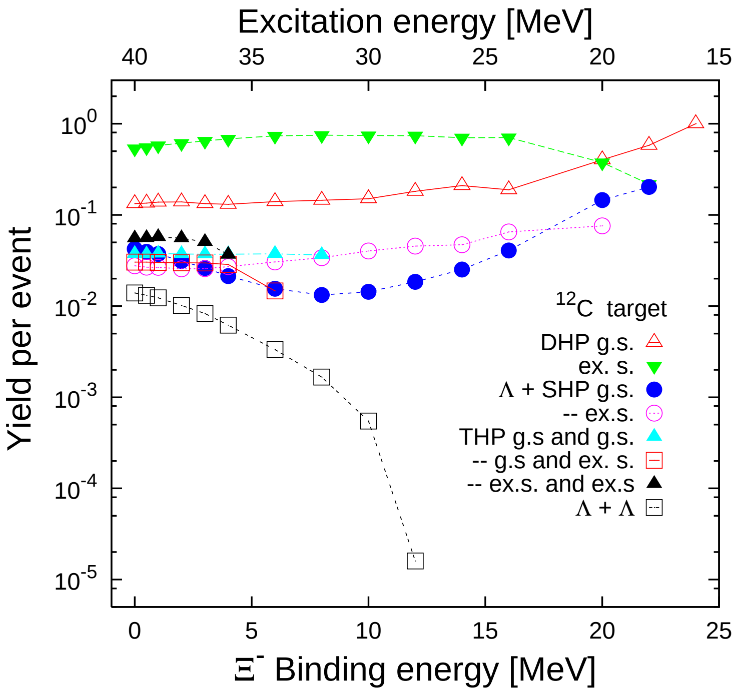

Figure 5.2: Production probability of ground (g.s.) and excited states (ex.s.) in conventional nuclear fragments and in one single (SHP), twin (THP) and double hypernuclei (DHP) after the capture of a Ξ^- in a ^{12}C nucleus and its conversion into two Λ hyperons predicted by a statistical decay model.

5.1.3 Comparison of the present calculations with the E906 experimental results

In 2001 the BNL experiment E906 reported the observation of the $^{4}_{\Lambda\Lambda}H$ hypernucleus by measuring the sequential pionic decays after a (K ,K^{+}) reaction deposited two units of strangeness in a ^{9}Be target [93].

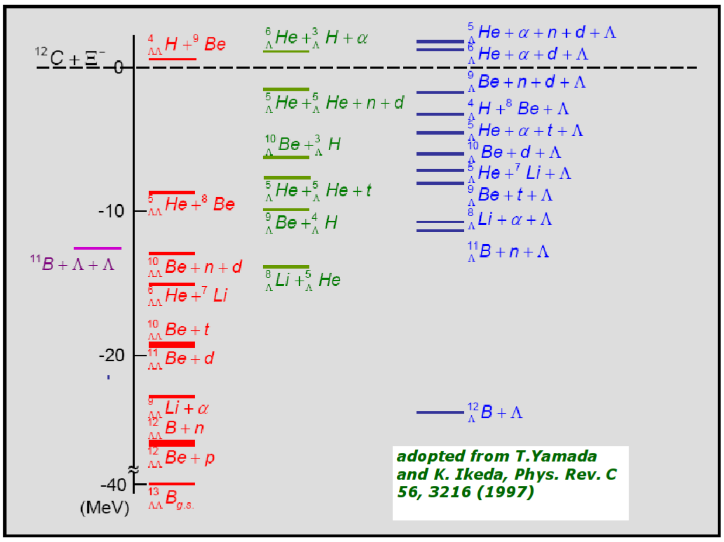

adopted from T.Yamada and K. Ikeda, Phys. Rev. C 56, 3216 (1997)

Figure 5.3: Various thresholds for double-Λ and single-Λ hypernuclear production channels in the ^{12}C + Ξ^- system. The energy is measured from the ^{12}C + Ξ^- threshold.

Two dominant structures in the correlated pion momenta at (114,104) MeV/c and at (133,114) MeV/c were observed. The first structure was interpreted as the production of $^{3}_{\Lambda}$H+$^{4}_{\Lambda}$H twins while the bump at (114,104) MeV/c was attributed to pionic decays of the double hypernucleus $^{4}_{\Lambda\Lambda}$H.

However, as it was pointed out by Kumagai-Fuse and Okabe also twin Λ-hypernuclear decays of $^{3}_{\Lambda}$H and $^{6}_{\Lambda}$He are a possible candidate to form this peak if excited resonance states of ^{6}Li are considered [176]. More recently Randeniya and Hungerford showed that the published E906 data can be reproduced without the inclusion of $^{4}_{\Lambda\Lambda}H$ decay and that it is more likely that the decay of $^{7}_{\Lambda\Lambda}He$ was observed in this experiment [87].

In their analysis this double hypernucleus was accompanied by a background of coincident decays of pairs of the single hypernuclear fragments $^{3}_{\Lambda}H$ with $^{4}_{\Lambda}H$, $^{3}_{\Lambda}H$ with $^{3}_{\Lambda}H$, and $^{4}_{\Lambda}H$ with $^{4}_{\Lambda}H$. Here the first twin pair dominated. and the production ratio $^{7}_{\Lambda\Lambda}He$ to coincident $^{3}_{\Lambda}H$ + $^{4}_{\Lambda}H$ pairs was estimated to be in the range of 7.7 to 12. In order to reproduce the E906 observation our model is used to predict the relative probabilities for the production of particle stable twin and double hypernuclei, the results are summarized in Tab. 5.1. In the second column the associated pion momenta is listed for orientation, assuming a $\Lambda\Lambda$ bond energy of $B_{\Lambda\Lambda} = 1\,$MeV and purely subsequent pionic two-body decays from the excited or groundstate to the corresponding groundstate.

For orientation an increase of $\Delta B_{\Lambda\Lambda}$ to e.g. 4 MeV decreases the first mo-

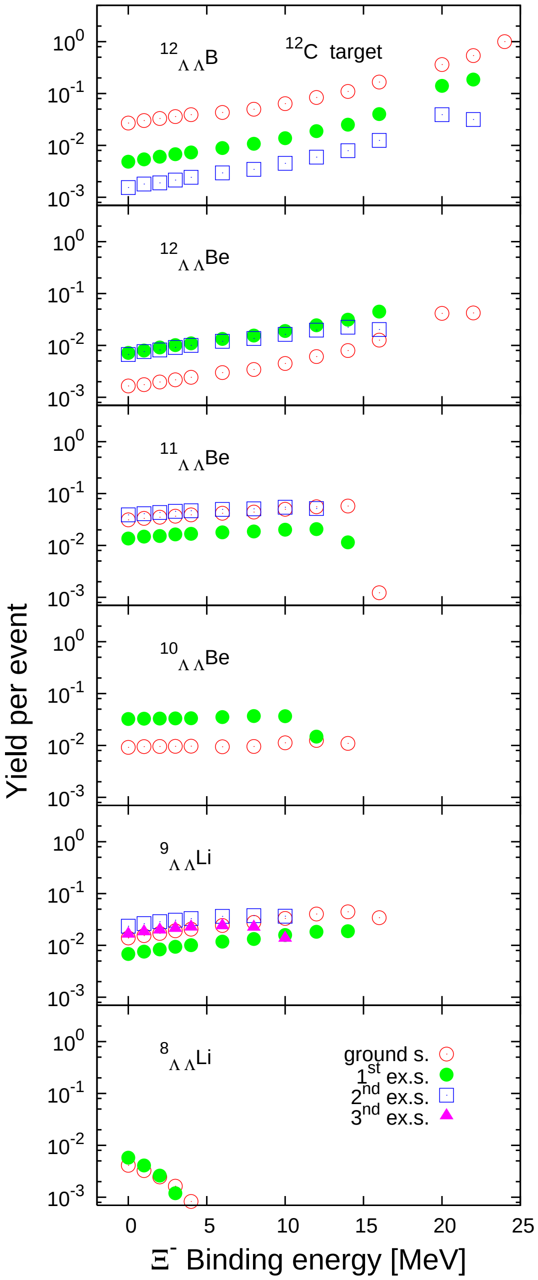

Figure 5.4: Production probability of ground and excited states of accessible double hypernuclei after the capture of a Ξ^- in a ^{12}C nucleus and the Ξ^- conversion into two Λ hyperons. Excited states in $^{11}_{\Lambda\Lambda}$Be, $^{10}_{\Lambda\Lambda}$Be and $^{9}_{\Lambda\Lambda}$Li dominate over a wide range of the Ξ^- binding energy.

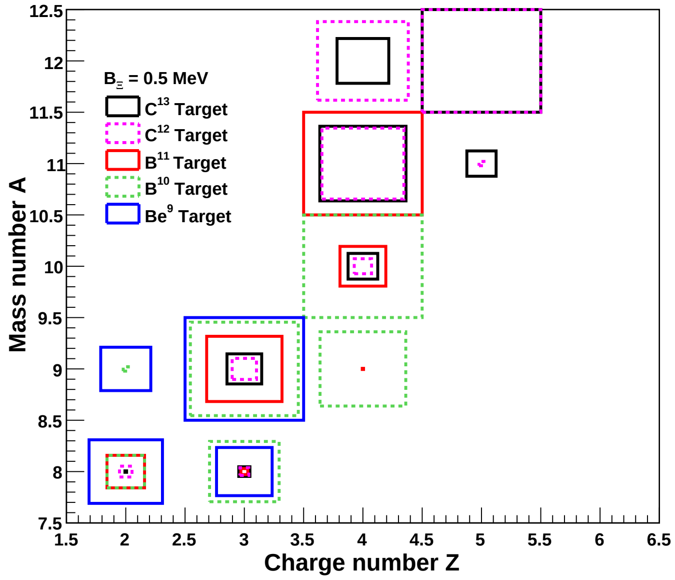

Figure 5.5: Relative population of the all excited states in all produced double hypernuclei for various Ξ^--absorbing stable target nuclei (^{9}Be, ^{10}B, ^{11}B, ^{12}C and ^{13}C).

menta given in the second column for $\Lambda\Lambda$ hypernuclei by about 5 MeV/c. Moreover, lower pion momenta may also arise from multibody decays or the decay into excited intermediate nuclei. Excited states which will deexcite prior to the weak decay will eventually also result in lower pion momenta. Comparing to experimental data one also has to keep in mind that starting from pion pairs with rather similar or equal pion momenta, a finite momentum resolution will result in a more asymmetric peak structure due to the sorting of the momenta. In case of the ${}^{7}_{\Lambda\Lambda}He$ decays a momentum resolution like in the E906 experiment of σ_{rms}=4 MeV/c will shift the peak from (109,108) MeV/c to (111,106) MeV/c.

In the third column of Tab. 5.1 the production probabilities after the capture and conversion of a stopped Ξ^- in a secondary ^{9}Be target are listed. As mentioned above, the microcanonical model consider the $\Xi^- + {}^{9}Be$ capture reaction for the production of the *compound hypernucleus* ${}^{10}_{\Lambda\Lambda}Li^*$, instead of the (K ,K$^+$) reaction followed by a knock–out process with a excitation energy of 33 MeV.

In our case a Ξ binding energy of 0.5 MeV was assumed. For comparison, column 4 shows the result of the canonical calculations of ref. [175] provided in their Table 5. Those calculations use a somewhat higher excitation energy of 35 MeV. Inspecting the excitation functions for double and twin hypernuclei

Table 5.1: Total production probability of particle stable twin and double hypernuclei after the capture of a Ξ^- by a ^{9}Be target and the conversion into an excited $^{10}_{\Lambda\Lambda}\mathrm{Li}^*$ hypernucleus (third and forth [175] column). The four last columns are the results assuming the production of excited $^{8}_{\Lambda\Lambda}\mathrm{He}^*$ and $^{8}_{\Lambda\Lambda}\mathrm{H}^*$ nuclei after a knock-out process with an excitation energy of 33 MeV [75]. Here columns 5 and 6 are results of the present work, the last two columns are again from Ref. [175]. A – indicates that this particular channel cannot be reached or was not considered.

decay channel	π pair momenta (MeV/c)		decaying system and probability					
			$^{10}_{\Lambda\Lambda}\mathrm{Li}^*$	$^{10}_{\Lambda\Lambda}\mathrm{Li}^*$ [175]	$^{8}_{\Lambda\Lambda}\mathrm{He}^*$	$^{8}_{\Lambda\Lambda}\mathrm{H}^*$	$^{8}_{\Lambda\Lambda}\mathrm{He}^*$ [175]	$^{8}_{\Lambda\Lambda}\mathrm{H}^*$ [175]
$^{3}_{\Lambda}\mathrm{H}+^{3}_{\Lambda}\mathrm{H}$	114	114	–	0	0	–	0	–
$^{3}_{\Lambda}\mathrm{H}+^{4}_{\Lambda}\mathrm{H}_{gs}$	114	133	–	0	0.008	–	0.018	–
$^{3}_{\Lambda}\mathrm{H}+^{4}_{\Lambda}\mathrm{H}_{1.05}$	114	134	–	–	0.014	–	–	–
$^{3}_{\Lambda}\mathrm{H}+^{5}_{\Lambda}\mathrm{He}$	114	99	0.0001	0.011	–	–	–	–
$^{3}_{\Lambda}\mathrm{H}+^{6}_{\Lambda}\mathrm{He}$	114	108	0.004	0.012	–	–	–	–
$^{3}_{\Lambda}\mathrm{H}+^{7}_{\Lambda}\mathrm{He}_{gs}$	114	115	0.026	0.018	–	–	–	–
$^{3}_{\Lambda}\mathrm{H}+^{7}_{\Lambda}\mathrm{He}_{1.66}$	114	118	0.046	0.018	–	–	–	–
$^{3}_{\Lambda}\mathrm{H}+^{7}_{\Lambda}\mathrm{He}_{1.74}$	114	118	0.068	0.018	–	–	–	–
$^{4}_{\Lambda}\mathrm{H}_{gs}+^{4}_{\Lambda}\mathrm{H}_{gs}$	133	133	–	0.005	0.017	–	0.055	–
$^{4}_{\Lambda}\mathrm{H}_{gs}+^{4}_{\Lambda}\mathrm{H}_{1.05}$	133	134	–	–	0.096	–	–	–
$^{4}_{\Lambda}\mathrm{H}_{1.05}+^{4}_{\Lambda}\mathrm{H}_{1.05}$	134	134	–	–	0.137	–	–	–
$^{4}_{\Lambda}\mathrm{H}_{gs}+^{5}_{\Lambda}\mathrm{He}$	133	99	0.022	0.045	–	–	–	–
$^{4}_{\Lambda}\mathrm{H}_{1.05}+^{5}_{\Lambda}\mathrm{He}$	134	99	0.055	–	–	–	–	–
$^{4}_{\Lambda}\mathrm{H}_{gs}+^{6}_{\Lambda}\mathrm{He}$	133	108	0.031	0.049	–	–	–	–
$^{4}_{\Lambda}\mathrm{H}_{1.05}+^{6}_{\Lambda}\mathrm{He}$	134	108	0.088	–	–	–	–	–
$^{4}_{\Lambda\Lambda}\mathrm{H}$	117	98	0.0006	0.026	0.003	0.0002	0.026	0
$^{5}_{\Lambda\Lambda}\mathrm{H}$	134	99	0.007	0.139	0.069	0.635	0.108	0.877
$^{5}_{\Lambda\Lambda}\mathrm{He}$	–	–	–	0.0	0	–	0.009	–
$^{6}_{\Lambda\Lambda}\mathrm{He}$	100	99	0.028	0.147	0.051	–	0.128	–
$^{7}_{\Lambda\Lambda}\mathrm{He}$	109	108	0.117	0.133	0.116	–	0.157	–
$^{8}_{\Lambda\Lambda}\mathrm{He}_{gs}$	116	124	0.022	small	–	–	–	–
$^{8}_{\Lambda\Lambda}\mathrm{He}_{ex}$	119	124	0.096	–	–	–	–	–
$^{9}_{\Lambda\Lambda}\mathrm{He}_{gs}$	117	121	0.021	0.025	–	–	–	–
$^{9}_{\Lambda\Lambda}\mathrm{He}_{ex}$	122	121	0.027	–	–	–	–	–
$^{7}_{\Lambda\Lambda}\mathrm{Li}$	101	96	0.0001	0.008	–	–	–	–
$^{8}_{\Lambda\Lambda}\mathrm{Li}_{gs}$	109	97	0.012	0.028	–	–	–	–
$^{8}_{\Lambda\Lambda}\mathrm{Li}_{ex}$	111-117	97	0.028	–	–	–	–	–
$^{9}_{\Lambda\Lambda}\mathrm{Li}_{gs}$	123	97	0.028	0.026	–	–	–	–
$^{9}_{\Lambda\Lambda}\mathrm{Li}_{ex}$	124-131	97	0.098	–	–	–	–	–

we have verified that this difference is not crucial.

While for most channels both calculations agree qualitatively, there are also important differences. The most striking difference is seen in the production of the ${}^{4}_{\Lambda\Lambda}$H and ${}^{5}_{\Lambda\Lambda}$H double hypernuclei where the calculations differ by a factor of 4 and more than an order of magnitude, respectively. Furthermore the total produced yield for ${}^{9}_{\Lambda\Lambda}$Li is about a factor of 5 higher in the present model which is mainly related to the presence of excited states. It can be also noted, that the production of ${}^{4}_{\Lambda}$H+${}^{4}_{\Lambda}$H twins is even at an excitation energy of 35 MeV energetically not possible and does therefore not occur in the micro-canonical model.

As an alternative production scheme the quasi-free/rescattering picture of Yamamoto *et al.* [175] is also considered, resulting in the production of excited ${}^{8}_{\Lambda\Lambda}$He or ${}^{8}_{\Lambda\Lambda}$H nuclei. As in ref. [175] the excitation energy of the initial ${}^{8}_{\Lambda\Lambda}$He and ${}^{8}_{\Lambda\Lambda}$H nuclei was fixed to 33 MeV. The last columns of Tab.5.1 show the results from Ref. [175] while Columns 5 and 6 contain the values predicted by our micro-canonical model at the same excitation energy for this scenario. In both models the production of ${}^{5}_{\Lambda\Lambda}$H, ${}^{6}_{\Lambda\Lambda}$He and ${}^{7}_{\Lambda\Lambda}$He as well as the ${}^{4}_{\Lambda}$H+${}^{4}_{\Lambda}$H twins dominate. Due to the higher spin factor, the production of excited states of ${}^{4}_{\Lambda}$H is enhanced over the direct ground state production in the present model.

In the following, the structure at (114,104)MeV/c which has been attributed to double hypernuclei decays will be discussed. Generally the production of double hypernuclei is energetically favored over the production of twins: all channels with twin–production lie significantly above the thresholds for ${}^{9}_{\Lambda\Lambda}$Li, ${}^{7}_{\Lambda\Lambda}He$ and ${}^{6}_{\Lambda\Lambda}He$ production in case of the ${}^{10}_{\Lambda\Lambda}$Li compound picture.

Correspondingly the production of ${}^{3}_{\Lambda}H$ and ${}^{6}_{\Lambda}He$ twins which has been suggested [176] as a possible source of the peak structure around (114,104)MeV/c is in our model by a factor of 30 and in the model of Ref. [175] by a factor of 10 lower than the ${}^{7}_{\Lambda\Lambda}$He production probability. Unlike in ref. [175] the ${}^{7}_{\Lambda\Lambda}He$ production exceeds the one of a ${}^{4}_{\Lambda\Lambda}H$ by more than two orders of magnitude (see Tab. 5.1 column 3) and the production of ${}^{5}_{\Lambda\Lambda}$H by a factor of about 17 in our model.

Similarly, also within the quasi-free/rescattering picture the ${}^{7}_{\Lambda\Lambda}$He nucleus is the most probable channel. Of course, a direct comparison with the E906 data requires a detailed consideration of the branching ratios for pionic two-body decays many of which are not known so far. Keeping that caveat in mind our microcanonical model supports independent on the assumed production scheme the interpretation of the E906 observation by Randeniya and Hungerford [87] in terms of ${}^{7}_{\Lambda\Lambda}$He decays. Decays from the ground or even exited states of ${}^{8}_{\Lambda\Lambda}$Li or ${}^{9}_{\Lambda\Lambda}$Li can possibly contribute some background to the structure at (114,104)MeV/c.

In order to describe the (133,114)MeV/c structure of the E906 experiment, the production of ${}^{3}_{\Lambda}$H+${}^{4}_{\Lambda}$H twins seems mandatory [93]. However, the ${}^{3}_{\Lambda}$H+${}^{4}_{\Lambda}$H+t mass lies above the initial mass $m_0 = m(\Xi^-) + m({}^9Be)$ and can therefore not be produced in the Ξ^-+^{9}Be compound production scheme. With an energy of 12.6 MeV below m_0, the channel $^4_\Lambda$H+$^6_\Lambda$He is the most likely twin in the present scenario, followed by the $^4_\Lambda$H+$^5_\Lambda$He+n decay. Given however the experimental precision of about 1 MeV/c for the momentum calibration in E906 [93], neither the decays of $^4_\Lambda$H+$^6_\Lambda$He with (133,108)MeV/c nor decays of $^4_\Lambda$H+$^5_\Lambda$He pairs with (133,99)MeV/c seem to explain the structure around (133,114)MeV/c. Of course particularly the first one could contribute to this enhancement in the tail region.

As can be seen from the last four columns of Tab.5.1 also in the quasi-free/rescattering picture the production of $^3_\Lambda$H+$^4_\Lambda$H twins plays only a minor role and none of the dominant decay channels can account for the observed structure at (133,114)MeV/c even though the yield ratio for $^7_{\Lambda\Lambda}$He to $^3_\Lambda$H+$^4_\Lambda$H twin production of about 8.7 in ref. [175] resp. 5.2 in our model are still compatible with the estimated ratio mentioned above. More intriguing is however the fact that both statistical models predict a strong production of $^4_\Lambda$H+$^4_\Lambda$H twins exceeding the $^3_\Lambda$H+$^4_\Lambda$H production. Considering furthermore the branching ratios for two-body π^- decays of $\Gamma_{\pi^-+^3He}/\Gamma_{total} \approx 0.26$ [177] and $\Gamma_{\pi^-+^4He}/\Gamma_{total} \approx 0.5$ [178] the absence of a bump which could be attributed to $^4_\Lambda$H+$^4_\Lambda$H is particularly puzzling.

At first sight it seems that an alternative production process than the ones discussed so far is required to explain the singular structure at (133,114)MeV/c in terms of $^3_\Lambda$H+$^4_\Lambda$H twins. Note however that in the initial analysis of the E906 data the bump at (133,114)MeV/c served as a calibration point for the pion momenta, taking the decay of $^3_\Lambda$H+$^4_\Lambda$H twins as granted [93, 179]. If that structure were indeed caused by $^4_\Lambda$H+$^6_\Lambda$He twins with (133,108)MeV/c, it would of course influence the momentum scale in the region of the (114,104)MeV/c bump. This bump would then be shifted to approximately (108,97)MeV/c. Considering the uncertainty of $\Delta B_{\Lambda\Lambda}$ also such a momentum scale would be compatible with the decay of $^7_{\Lambda\Lambda}$He and $^8_{\Lambda\Lambda}$Li or a mixture of both. The absence of $^9_{\Lambda\Lambda}$Li nuclei may be related to the decreasing pionic decay probability with increasing nuclear mass. Clearly, the present statistical decay model needs to be complemented by quantitative weak decay calculations (see e.g. [180]) to further corroborate our conjecture.

In summary we have presented a micro-canonical decay model to describe the break-up of an excited double hypernucleus after the absorption and conversion of a stopped Ξ^- hyperon. Generally the formation of excited states dominates in our model. For different Ξ^- absorbing target nuclei, different produced double hypernuclei dominate. Once combined with a weak decay model these calculations will enable more reliable estimates of the γ-ray yields for the double hypernucleus measurements envisaged by the $\overline{\text{P}}$ANDA collaboration [181] and a definite interpretation of the E906 data. In future studies we also plan to extend the present model to the production of bound $\Xi\Lambda$ or triple Λ hypernuclei after the conversion of a Ω^- into an excited $\Xi\Lambda$ nucleus.

5.2 Simulation of hypernuclei production

The aim of this section will be to explain the principles of the simulation of hypernuclei production mechanism within the simulation code. Hypernuclei are not defined by default within the software package and therefore further modifications of the latter are needed to this respect. The implementation of hypernuclei production consists of the definition of hypernuclei as particle within the software by means of mass, charge, number of hyperons(strangeness), spin, lifetime. and decay modes.

In general, one should also provide the physical processes associated with its production. These processes are mainly characterized by an atomic and nuclear capture of Ξ^- hyperon by the target nucleus (See Fig. 4.1 in chap. 4) followed by the conversion of the absorbed Ξ^- hyperon into two Λs. The final state is the described by the formation and subsequent statistical decay of an highly excited compound system into small fragments.

However, due to the complexity of its implementation, the production of hypernuclei will regard only the statistical decay after the capture of a Ξ^-. This process will be accomplished by a devoted event generator.

Once the particle is defined, it is ready to be transported by the simulation engine via the event generator interface. Depending on its energy it will be transported within the detector material according to their associated physical processes.

5.2.1 Hypernuclei event generator

The hypernuclei production has been implemented within the simulation code via a dedicated event generator procedure. This event generator is based on the statistical decay of a Ξ^- hypernuclei, whose principles have been explained in the previous section.

The starting point of the hypernuclei generation consists in providing some input information, such as mass number A and charge Z of the nucleus target as well as the binding energy of the absorbed Ξ^- hyperon. In the present work, a Ξ^- binding energy of 3 MeV has been considered. Previously, the several hypernuclei species available for production as well as the possible decay modes have to be implemented in the particle database of the software.

The output of the event generation will be the statistical decay of the selected excited Ξ^- hypernucleus in form of single and double hypernuclei, eventually in excited states. Among hypernuclei species, light and heavy nuclide can be formed. In the following, the procedure to define hypernuclei within the software will be introduced.

5.2.2 Hypernuclei Definition

Contrary to elementary particle (mesons, leptons, baryons and light and heavy) hypernuclei are not default particle and therefore they must be implemented externally by the user. Hypernuclei will be treated by the transport engine as heavy ions and its implementation will be accomplished by using an extended version of the simulation framework P andaroot. The main modification consists in defining a general particle by giving properties such as mass, charge, spin, strangeness and lifetime to characterize them.

If the user defined particle is unstable, the possible decay modes must be also provided. Hypernuclei will be distinguished from other particles by means of the particle identification number which provides information about the mass number A, the charge Z and the number of hyperons S. (For more details see Appendix A.5.1).

5.2.3 Decay modes of Hypernuclei

As it has been remarked before, hypernuclei have been defined as unstable particle. According with Sec. 1.2.3, hypernuclei decay mainly via the emission of photons from particle stable states and via the weak decay (mesonic and non–mesonic).

In general, electromagnetic transitions are much faster that the weak decay, therefore it can be considered that hypernuclei occupying excited levels will decay first electromagnetically to the ground state, and then the weak decay will takes place. Of course, that is true unless for the case of isomer states, where the weak decay can also occur from a excited energy level.

Electromagnetic decay In analogy with nuclear matter, the probability of a electromagnetic transition between two states to occur is governed by the electromagnetic radiation multipole [183].

In the present work, only electromagnetic transitions (See Tab. A.7 and A.10) from hypernuclear excited states to the corresponding ground states have been considered. The emission of a photon from a excited hypernucleus is first treated as a two body decay in the center of mass and later the momenta of emitted photon as well as the residual hypernucleus are boosted with the initial momentum of the hypernucleus.

In comparison with the weak decay, the electromagnetic transition is fast. As a consequence, the electromagnetic decay mode will be handled by the event generator after the hypernucleus production. Fig. 5.2.1 illustrates the energy spectra corresponding to electromagnetic deexcitations of nuclei, single and double hypernuclei which have been produced after the statistical decay of an excited compound hypernucleus (${}^{13}_{\Lambda\Lambda}\mathrm{B}^*$).

For these calculations a Ξ^- binding energy of 0.5 MeV and a ^{12}C target have been considered. In future, further modifications of the present code regarding all possible electromagnetic hypernuclear transitions will be performed.

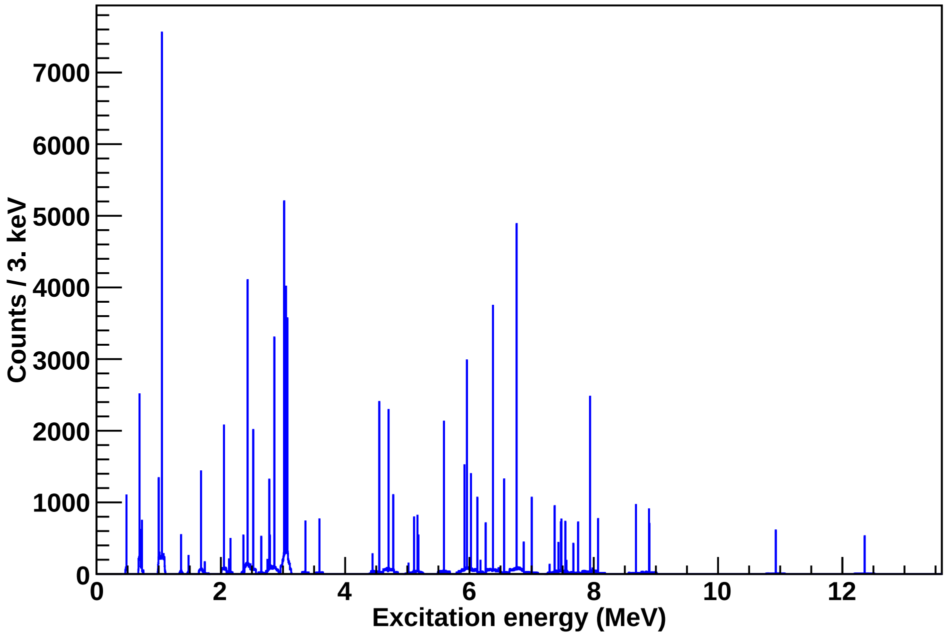

Figure 5.6: Energy spectra corresponding to electromagnetic transitions of nuclei, single, double hypernuclei produced after the statistical decay of an excited compound hypernucleus ($^{13}_{\Lambda\Lambda}$B*)

Mesonic weak decay For light hypernuclei, the non-mesonic and mesonic decays are of similar importance (See Fig. 1.5 in Sec.1.2.3). A formal implementation of the hypernuclear weak decay widths requires the knowledge of the dynamics as well as the kinematics of the process in nuclear matter.

In the present work, a simplistic approach of the mesonic weak decay process has been considered. This approach considers only the kinematic point of view of the two or three body mesonic decay of hypernuclei (See Tab. A.8 and A.6) and the decay final states are sampled according to the phase–space. For instance, for the case of double hypernuclei, two subsequent mesonic weak decays are taking into account. This decay chain is performed as follows,

$$\begin{aligned} {}^{A}_{\Lambda\Lambda}Z &\rightarrow \pi_1 + ^{A}_{\Lambda}(Z+1) \\ {}^{A}_{\Lambda}(Z+1) &\rightarrow \pi_2 + ^{A}(Z+2) \end{aligned} \tag{5.5}$$

where ${}^{A}_{\Lambda\Lambda}Z$, ${}^{A}_{\Lambda}(Z+1)$ and ${}^{A}(Z+2)$ denote the initial double Λ hypernucleus, the single Λ hypernucleus and the ion respectively. The two pions emitted during this process are denoted by π_1 and π_2.

Additionally, according to some theoretical estimates the lifetime of a hypernucleus at its ground state has been fixed to 200 ps. Pions with monoenergetic momenta will be emitted as a result of a two or three body decay. The momenta range achieved by these particles vary from 70 MeV/c to 133 MeV/c.

Furthermore, the momenta of the two pions are strongly correlated and their coincident measurement provides an effective method to tag the production of a double hypernucleus. An improvement of the present implementation of the weak decay, by including the non mesonic weak decay modes with the corresponding branching ratios, is also foreseen in the near future.

Chapter 6

Hypernuclear Event Simulation

6.1 Overview

Up to now, the detector setup requirements for the performance of the hypernuclear physics at the $\overline{\text{P}}$ANDA experiment have been studied based on the $\overline{p} + p \rightarrow \Xi^{-}\overline{\Xi}^{+}$ reaction which corresponds to the first stage of the hypernuclei production mechanism. Additionally, a statistical decay model has been introduced as main tool for the production of hypernuclei at excited levels. Moreover, the electromagnetic decay as well as the weak mesonic decay have been considered as the most probable hypernuclei decay modes. Based on these features, a new event generator based on these assumptions has been implemented to be used in the software.

In the present chapter, the simulation of a full hypernuclear event will be addressed following the simulation chain procedure explained in Sec. 4.1: event generation, detector signal simulation, reconstruction and analysis. The reason for that is to give a complete overview of the possibility to perform hypernuclear physics not only from the detector point of view but also from the point of view of the analysis procedure. In particular, the analysis of a full hypernuclear event is of big interest since the success of the project will depend on the capability of identifying uniquely double hypernuclei.

The structure of this chapter is divided as follows: In Sec. 6.2, the different steps which has been performed to simulate the hypernuclei production mechanism will be explained. For that the devoted detector concept which have been studied in Chap. 4, will be here included.

In Sec. 6.3, the Monte Carlo information stored as result of the interaction of the above produced particles with the detector materials will be modeled accordingly to obtain the corresponding electronic detector signals. In Sec. 6.4, the different detectors electronic signals are reconstructed to build particles trajectories, whose momenta can be extracted by using a devoted tracking algorithm. The assignment of particles trajectories to a certain particle type, takes place in Sec. 6.4.2, where the energy loss and the timing measurements together with the tracking information is used to calculate particle hypotheses. In Sec. 6.5, a novel strategy will be presented to identify uniquely double hypernuclei. This technique uses the electromagnetic deexcitations of excited double hypernuclei in coincidence with negative pions from sequential mesonic decays. The contribution of possible background sources will be studied by using the same technique in Sec. 6.5.1 In addition, the efficiency of a method for the background rejection based on positive kaon identification will be in Sec. 6.5.3 evaluated. To finalize, in Sec. 6.5.4 the possible radiation damages due to $\overline{p}$Nucleus reaction in the germanium array detector and in the scintillating fiber array detector will be evaluated.

6.2 Event Generation

The simulation of a full hypernuclear event should reproduce the multi–stage production mechanism described in Sec. 4. For simplicity, it will be performed in different steps.

The first part involves the generation of $\Xi^-+\overline{\Xi}^+$ pairs in the $\overline{p}$+^{12}C reaction within the primary target, their interaction with the secondary target detector and the other detectors of the experimental setup. Special emphasis will be given to the deceleration process of Ξ^- within the secondary target absorber material.

As in Sec. 4.2, where this process was used to optimize the detector setup, the INC and UrQMD model will also be used as primary generators. For the present simulation, the devoted detector setup discussed in sec. 4 is considered. The secondary active target is located upstream at a distance of -75.6 cm from the center of the $\overline{\text{P}}$ANDA spectrometer. The corresponding simulated setup is based on the design presented in the upper part of Fig. 4.11 in Sec. 4.2.2.

Fig. 6.1 shows a compact structure of 26 mm thickness, consisting of 20 layers of silicon strip detectors with alternating layers of absorber material. The active silicon layers must provide also tracking information on the emitted weak decay products of the produced hypernuclei. The case of ^{12}C absorbers in all four quadrants of the secondary target have been considered in the present simulation.

The two rings of the scintillator fibers array, whose geometry corresponds to the one given in Sec. 4.2.4, are placed covering the primary interaction point at outer radii of 7 cm and 9.9 cm, respectively. The HPGe array geometry implemented here, is the one shown by Fig. 4.12 of Sec. 4.2.3. It is located upstream at a distance of 30 cm from the primary interaction point (See Fig. 6.2).

Furthermore, the time projection chamber (TPC) and the Time–of–Flight (TOF) scintillator barrel are also implemented as part of the hypernuclei setup, and their geometry description corresponds to the one given in the general

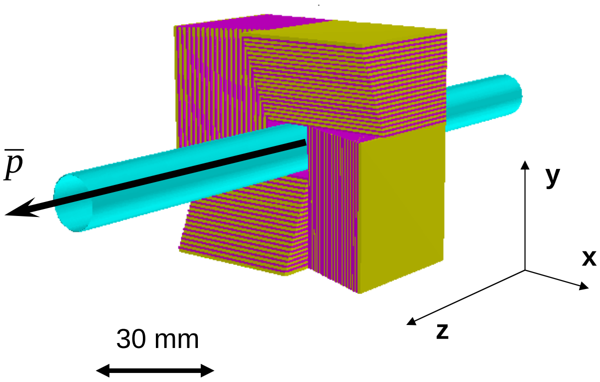

Figure 6.1: The active silicon layers provide also tracking information on the emitted weak decay products of the produced hypernuclei.

$\overline{\mathrm{P}}$ANDA detector setup in Sec. 3.2. Particularly, these detectors together with the scintillator fibers array form part of the TOF system used for the background signal suppression (See Fig. 6.3).

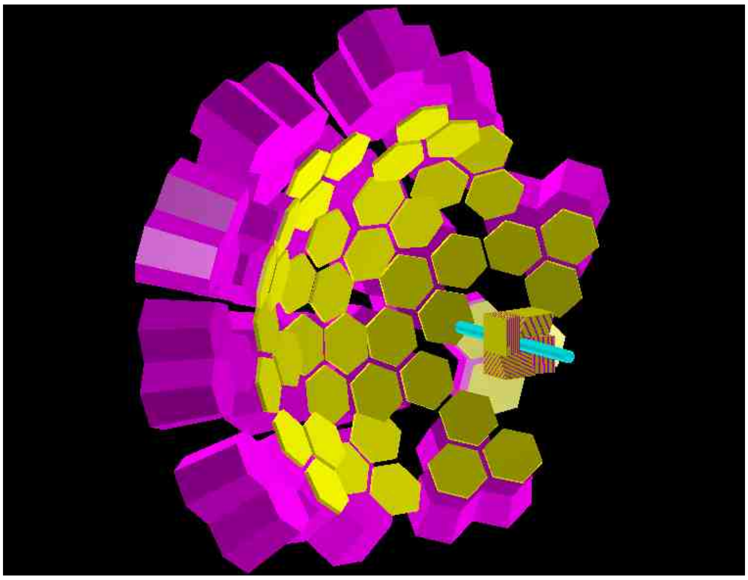

Figure 6.2: The germanium array geometry implemented here is located upstream at a distance of 30 cm from the primary interaction point. In the picture, the beam goes from the left to the right.

Additionally, all physics processes undergone by the passage of the generated particles through the detector materials are also taken into account. Particularly, within the secondary target two kind of hits information will be

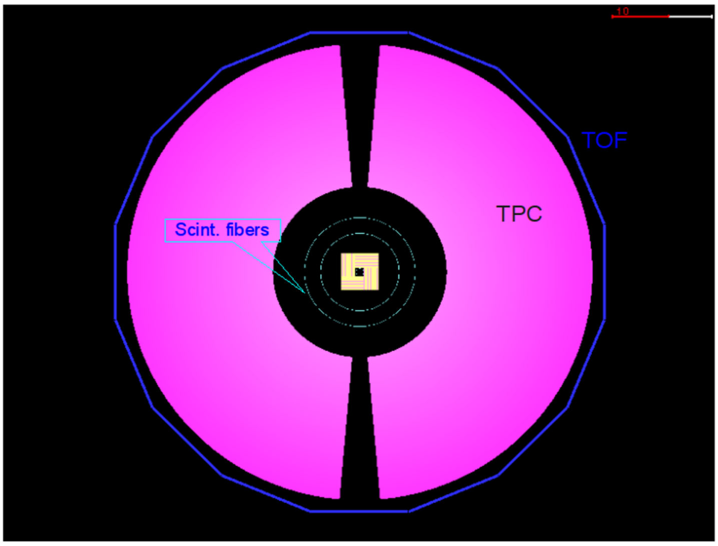

Figure 6.3: Detector setup showing the secondary target, surrounded by the scintillator fibers, TOF and TPC. Particularly, the TPC and TOF together with the scintillator fibers array form part of the TOF system used for the background signal suppression.

collected during the simulation. One is related to the hits produced by all produced charged particles within the silicon layers and the other one regards the hit production by Ξ^- hyperons stopping in the absorber layers. In particular, this absorber hits collection contain information about position of stopping vertexes and momentum of the Ξ^- hyperons before and after the deceleration process. This part is specially important, since it will serve as input for the generation of hypernuclei. In addition to the information storage on the secondary active target, hit collections produced by the interaction of the generated particles with others detectors such as the germanium array, the time of flight system and the TPC will be also stored.

In the following, results related to the INC primary generator and a the magnetic field intensity of 2 T will be presented. From 50505 produced $\Xi^-\overline{\Xi}$ events, which contained Ξ^- hyperons with a laboratory momentum lower than 500 MeV/c, 7396 hyperons are stopped within the secondary target.

Recently Yamada and co-workers studied within the framework of the doorway double-Λ hypernuclear picture [184] the production of double-Λ hypernuclei for stopped Ξ^- particles in ^{12}C [75]. Per stopped Ξ^- they predict a total double-Λ hypernucleus production probability of 4.7%. An even larger probability of 11.1% was recently obtained by Hirata *et al.* within the Antisymmetrized Molecular Dynamics approach [76, 77].

Since the present studies concentrate on the production of double hypernu-

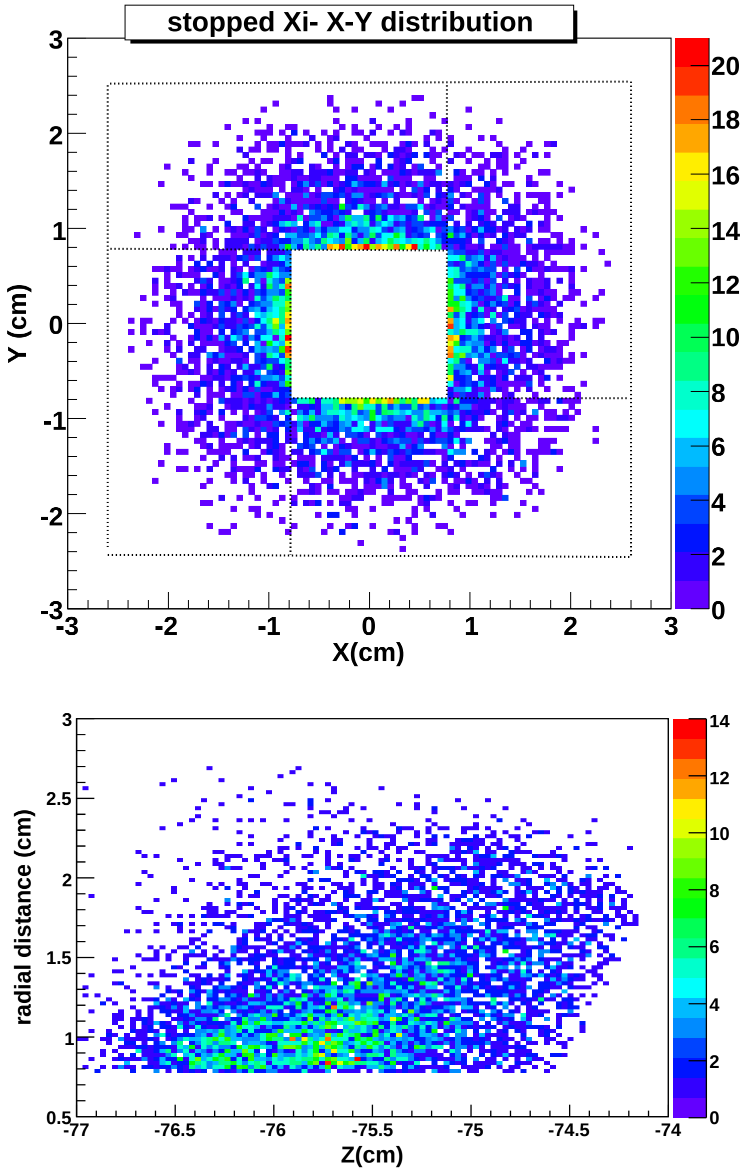

Figure 6.4: Setup of the secondary sandwich target used in the present simulations. The figure marks the stopping points of the Ξ^- hyperons within the target in the X-Y plane, transverse to the beam direction (Z axis) and in the R-Z plane. Where R is the radial distance from beam direction. The rectangles indicate the outlines of the four target segments. All four segments are equipped with ^{12}C absorbers.

clei, a full microscopic simulation of the atomic cascade and capture of the Ξ^- hyperons has not been performed. For the final rate the $\Xi^- p \rightarrow \Lambda\Lambda$ conversion probability is estimated to be only 5%. However, in the present simulation it will be assumed that all stopped Ξ^- lead to hypernuclei production, namely a

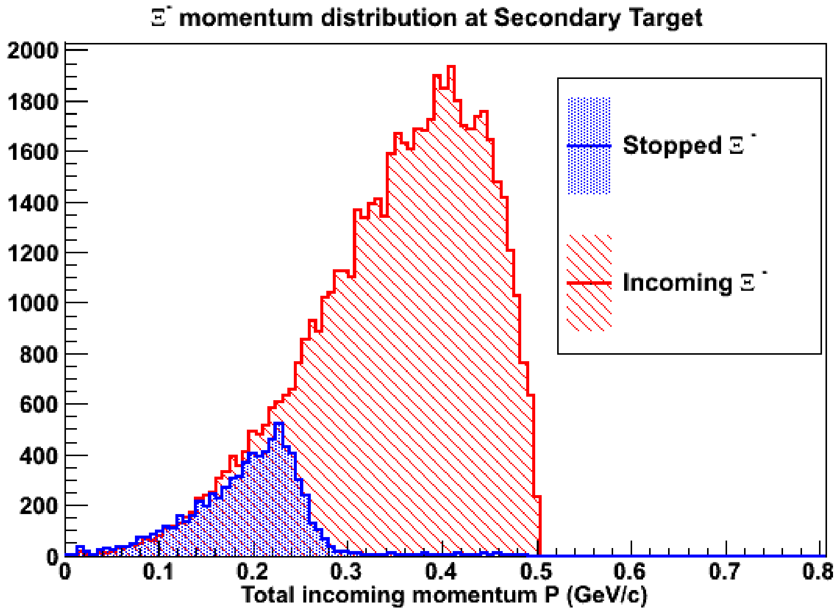

Figure 6.5: Momentum distribution of Ξ^- entering the secondary target volume and of those Ξ^- which stop in the absorber material labelled in red and in blue respectively.

100% conversion probability is assumed.

From the point of view of the detector acceptance, one can observe that the majority of the hyperons are stopped in the most inner layers of the sandwich structure (Fig. 6.4). The typical momenta of these stopped Ξ^- are around 200 MeV/c (see Fig. 6.5 and Fig. 6.6).

The second part of the simulation regards the production of excited Λ hypernuclei (double and single). As discussed in Chap. 5, the hypernuclei generation will be accomplished by a devoted event generator based on a statistical decay model. The input for this event generator interface is the position of the stopping vertexes of the Ξ^- in the interior of the absorber material and a list of hyperfragments, heavy and light ions, and photons produced as a result of the statistical decay of a compound hypernuclei (See chap. 5).

This list is generated during the first part of the simulation at the time a Ξ^- hyperon stops in the absorber material of the secondary active target. During the simulation several hits collections are produced after the interaction of these particles with the detectors.

In particular, heavy and charged particle produced during this stage are characterized for having low momentum, and therefore they will mainly stop in the interior of the absorber material of the secondary target. On the contrary, photons, neutrons and charged decay products (pions, protons) with moderate

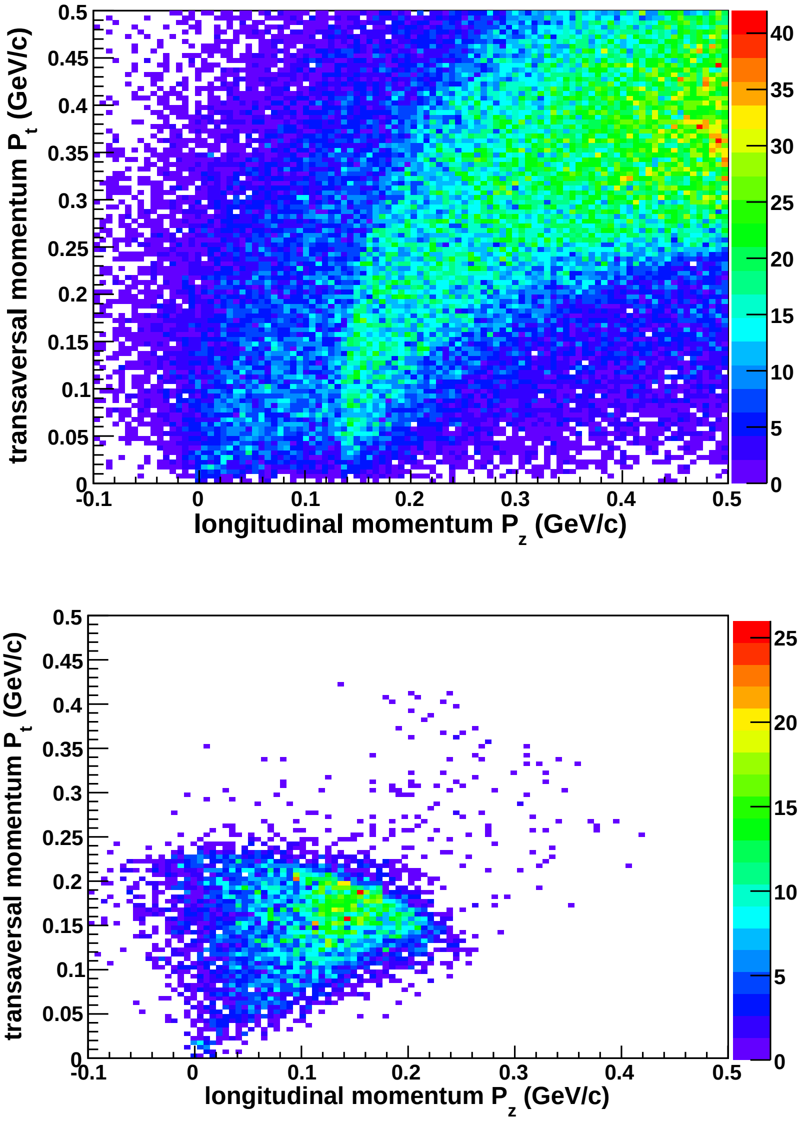

Figure 6.6: Transverse vs. longitudinal momentum distribution of Ξ^- generated with momenta less than 500 MeV/c (upper part) and those stopped within the secondary target (lower part).

momenta will be able to reach other detectors. Thus, the detector hits collections considered as a result of the hypernuclei (with their decay products) simulation are those produced in the secondary target, scintillation fibers array and the germanium array.

As an example, Fig. 6.7 displays (X-Y and Y-Z views) the production of ^{3}H + $^{10}_{\Lambda\Lambda}$Be as a result of the statistical decay of the compound hypernuclei $^{13}_{\Lambda\Lambda}$B*.

The light ion ^{3}H and the excited double hypernuclei ${}^{10}_{\Lambda\Lambda}$Be stop immediately after their production due to their low momentum. In both pictures it can also be observed the two pions tracks produced in the sequential mesonic decay of ${}^{10}_{\Lambda\Lambda}$Be. The decay chain is in the following shown as,

$$\begin{aligned} {}^{10}_{\Lambda\Lambda}Be &\longrightarrow {}^{10}_{\Lambda}B + \pi^{-} \\ {}^{10}_{\Lambda}B &\longrightarrow {}^{10}C + \pi^{-} \end{aligned}$$

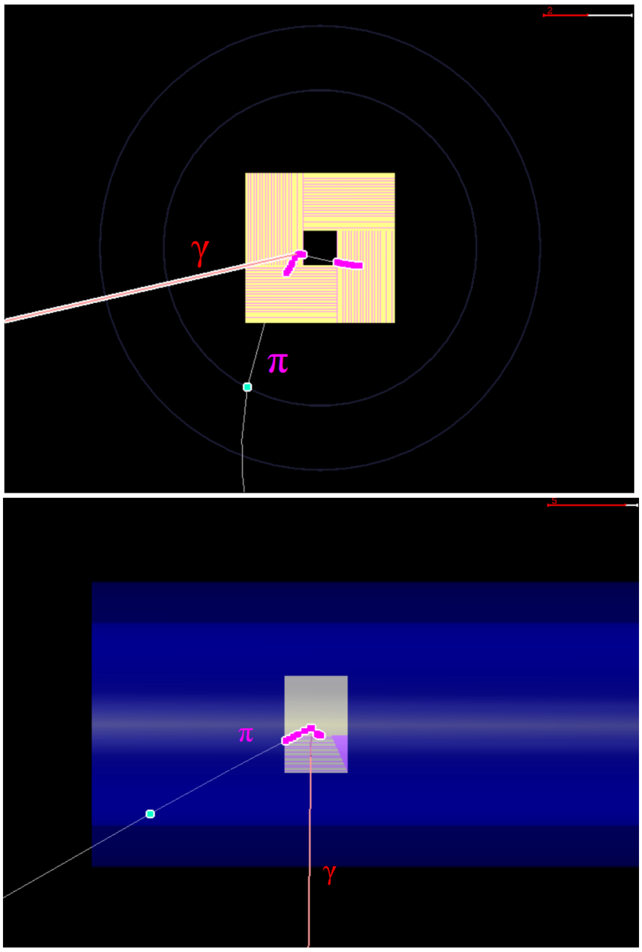

Figure 6.7: Event display of the ^{3}H + ${}^{10}_{\Lambda\Lambda}$Be production with its sequential mesonic decay. Both figures show the sequential mesonic decay of ${}^{10}_{\Lambda\Lambda}$Be. Pink squares symbols illustrate the trajectories of emitted pions within the secondary target. The red line represents the gamma emission of a double hypernuclear excited state. The green points represents hits on the scintillator fiber detector.

The two–stage procedure described above concerns the so–called signal generation, but a complete study of the experiment feasibility requires also to evaluate the contribution of background interactions, like the $\overline{p}+$ Nucleus process. Accordingly, the background influence will be studied in a dedicated section following the same simulation strategy as it was done for the signal.

On the other hand, one should remark that for simplicity the digitization, the reconstruction and analysis procedure will be applied considering the two stages of the hypernuclei generation separately. In the following the Monte Carlo information obtained from the two–steps of the hypernuclei simulation is transformed via the digitization process into reliable detector signals as they result from the readout detector electronics.

6.3 Digitization

During the digitization, the information extracted from the particle transport as a collection of hits, is processed to reproduce the signals in the front-end-electronics of the individual detectors, producing a digitized detector response. In this section, only the detectors involved in the production and detection of Hypernuclei are considered. Because their setup and their readout is still under investigation, a parametrized digitization was used for simplicity, which was derived from Monte Carlo calculations using a full digitization.

In the following, the digitization procedure of the secondary tracker, germanium detector array, and the time of flight system (Scintillator fibers and scintillator barrel detectors) will be explained.

Silicon Readout Electronics of the Secondary Active Target For simplicity, one of the digitization schemes of the Micro Vertex Detector (MVD) [187] has been also adopted for the secondary active target. This option of silicon detector types, consist of a readout performed by silicon strip detectors on both sides of the sensor.

The signal in the sensor (silicon layer) is formed by using the local trajectory within the layer material. The local trajectory is computed from the hit position at the entry and at the exit of the sensitive silicon layer at the sensor coordinates reference system. The channel number and the charge collected by the electronics are then determined by the position and the deposited energy of the hit. Then, the channel mapping of the trajectory is done on both sides of the sensor. That is accomplished, by calculating the number of digitized channels independently from the projection of the trajectory and its orientation on both sides of the sensor. After that, the charge signal is shared among all excited strips depending on the fraction of the local track.

In addition, the size of the readout structures are defined by the size of the spacing (pitch) of the strips. The channel is then assigned to a frontend and a common number of 128 channels per frontend is chosen. The reconstruction of the hit mean position is then calculated through the charge weighting between the strips of the clusters on the same sensor.

In the simulation, a smearing of the local hit position by $100\,\mu$m was considered to reproduce the cluster reconstruction on the sensor. The values of $100\,\mu$m and of 90 degree have been adopted for the strip pitch and the stereo angle respectively.

HPGe Detectors array response In the case of the germanium array detectors, the energy signal has been modelled as follows: For each cluster, the total energy deposit in each of the three germanium crystals has been summed up. The later is smeared with a Gaussian distribution, assuming a value of 3 keV for the standard deviation which coincides with the experimental energy resolution of the detectors.

To describe the response of these detectors, processes which are relevant for the interaction of the emitted photons with matter such as pair production, Compton scattering and the photoelectric effect have been taken into account.

Scintillator detectors response As described in Sect. 4.2.4, the readout electronics of scintillation barrel detector, commonly called Time–Of–Flight barrel in this work, will be arranged at both edges of its bars.

As a consequence, the detector will be sensitive to the position of ionizing particles interacting with its scintillating volume. On the other hand, one has to notice that scintillation light production on the time of flight barrel and on the fibers array detectors has not been implemented. Instead of that, the Monte Carlo hits information such as time and position have been used to parametrize the detector response. This parameterization procedure will be explained in the following paragraph.

The time information considered here corresponds to the time the particle takes to arrive to the detector volume from the interaction vertex. The parametrization adopted in the present work assumes that,

- the time resolution provided by the electronics device is about 100 ps[1].
- photons generated by the interaction of ionizing particles with the scintillator volume will travel without reflexions to the edges of each bar.

Knowing the Monte Carlo position information of the interacting particle and assuming that scintillation photons will move with a velocity given by the distance to the next readout device and the refraction index of the medium, the time difference between the both sides of the scintillator bar can be determined. The position of the scintillation source can be then reconstructed from the time

---

[1] achieved by others time of flight detectors of experiments such as the CDF experiment [185].

difference and the timing measurement is obtained by smearing the Monte Carlo timing information[2] with the time resolution of the electronic readout device.

The same procedure has been used to determine the response of the fiber array detector. Contrary to the scintillator Time–Of–Flight barrel the timing resolution achieved by them is about 450 ps. However, in order to study the background suppression capability by means of a time of flight measurement, further investigations have also been done, considering a start detector with a timing resolution comparable to the one of the TOF barrel detector (See discussion in Sec. 4.2.4 of chap. 4 and Sec. 6.5.3 in this chapter).

In the present work, the value for the time of flight is given by the difference between the timing measurement of the start detector (Scintillating fiber detector) and the one measured by the stop detector (scintillating barrel detector).

6.4 Reconstruction

As discussed in Sect. 4.1, the reconstruction of charged particles trajectories uses the hits information of the several detectors involved in the simulation after the digitization process. The reconstructed trajectories, denominated also tracks candidates, are parametrized with special algorithms provided by the selected track model to obtain information such as momentum, length of the trajectory, direction etc. In this section a particular emphasis will be given to the reconstruction of the low momentum charged particles resulting from the hypernuclei production mechanism. This procedure will mainly be accomplished by the secondary active target and eventually by the scintillation fibers array. Charged particles with moderated momenta emitted into the forward direction will be reconstructed making use of the time projection chamber as main tracker detector and of the time of flight system.

6.4.1 Momentum resolution and low momentum particles

The general aspects of the track reconstruction model within the $\overline{\mathsf{P}}\mathsf{ANDA}$ target spectrometer region have been reviewed in Appendix A.1. It has to be remarked that these algorithms have been mainly optimized for particles momenta above 500 MeV/c. As a consequence, low momentum particle, namely below 200 MeV/c, are reconstructed with a poor momentum resolution [187], and further improvements are required particularly in case of hypernuclei decay

---

[2] difference in the time of arrival of the particle at the scintillator with the collision time t0

charged products (See details in Sec. 5.2.3). The momenta of these particles ranges from 80 MeV/c to 200 MeV/c, where the energy loss and multiple scattering are quite important and have to be treated accurately. The momentum resolution of a particle depends mainly on the magnetic field strength, the radius of the trajectory and the radius of the tracking system or, in others words, on the total trajectory length. For a fixed value of the momentum p, and of the spectrometer radius, the resolution improves as the magnetic field increases. That means that the curvature of the particle trajectory (1/radius) increases leading to a better determination of the radius and for instance of the momentum. Of course, this statement is only valid as long as the diameter of the particle trajectory remains much larger than the spectrometer radius.

In addition, an improvement of the momentum determination, and for instance, of the momentum resolution is also achieved by increasing the number of detectors which contribute to the measurement of the particle trajectory. This behaviour is reported in ref. [187], where the resolution associated to the tracking algorithm achieved by the Micro Vertex Detector improves as soon as the tracklet information of Central Tracker system is added.

On the contrary, the amount of material the particle is passing through has also a negative influence on the resolution and must be carefully considered in the detector design. The expression which relates these magnitudes with the momentum resolution σ_p of a particle moving within a magnetic field B follows the relation $p = p_T \sin\theta$,

$$\left(\frac{\sigma_p}{p}\right)^2 = \left(\frac{\sigma_{p_T}}{p_T}\right)^2 + \left(\frac{\sigma_\theta}{\tan\theta}\right)^2 \tag{6.1}$$

where σ_{p_T} represents the resolution of the transversal momentum p_T on the rϕ-plane and σ_θ corresponds to the resolution in the beam direction. The emission angle is defined as θ. Each term on the rightened side of the formula can be expressed as a sum of the uncertainties caused by the multiple scattering and by the finite measurement resolution.

$$\frac{\sigma_{p_T}}{p_T} = \left(\frac{\sigma_{p_T}}{p_T}\right)^2_{\text{fit}} + \left(\frac{\sigma_{p_T}}{p_T}\right)^2_{\mathcal{MS}} \tag{6.2}$$

$$\begin{aligned} \left(\frac{\sigma_{p_T}}{p_T}\right)_{\text{fit}} &= \frac{p_T\epsilon}{0.3Bz\acute{L}^2}\sqrt{\frac{720}{N+5}} \\ \left(\frac{\sigma_{p_T}}{p_T}\right)_{\mathcal{MS}} &= \frac{p_T\theta_0}{0.3BzL\cos^2\lambda}\sqrt{1.43} \end{aligned} \tag{6.3}$$

where $\acute{L} = R\Delta\Phi$ is the projected length of the trajectory onto the bending plane. The position measurement error for each point, perpendicular to the trajectory is represented by ϵ. $N + 1$ is the number of points measured along the track. z is the particle charge. $\lambda = 90^0 - \theta$ and L is the total track length. Moreover, the mean scattering angle θ_0 is defined as follows,

$$\theta_0 = \frac{13.6z}{\beta cp}\sqrt{\frac{L}{X_0}}\left(1 + 0.030 \ln \frac{L}{X_0}\right)$$

where X_0 is the radiation length of the scattering medium and the kinematic variable $\beta = v/c$. The uncertainties associated to the θ are given as function of the number of hits N, the mean scattering angle θ_0 and the measurement uncertainty along the beam axis ϵ_z.

$$\frac{\sigma_\theta}{\tan\theta} = \frac{\epsilon_z}{L}\sqrt{\frac{12N}{(N+1)(N+2)}} + \frac{1}{\sqrt{3}}\theta_0 \tag{6.4}$$

Previous hypernuclei experiments denoted out that a good momentum resolution of particles with momenta below 200 MeV/c was affordable for magnetic field strengths in the range between 1 T and 0.5 T. The tracking of low momentum pions at the FINUDA experiment [188] is accomplished with a momentum resolution of 0.3% of FWHM. The magnetic field strength was optimized to 1.1 T to track pions with momentum around 250 MeV/c in a 1 m radius spectrometer.

On the other hand, the AGS-E906 [93] experiment achieved to reconstruct pions tracks with 0.4% (FWHM) at 100 MeV/c. The spectrometer with a radius of 30 cm was operated with a magnetic field of 0.5 T. Previous investigations on the Micro Vertex Detector tracking capabilities show that particle with momenta below 200 MeV/c and emitted in a wide angular range ($4^0 - 160^0$) are reconstructed with a momentum resolution of 2% (FWHM).

In comparison, the present setup of the secondary active target (See Fig. 6.1) has a radius of about 4 cm. Considering the scintillator fibers detector as eventual external tracker the value for the total radius accounts approximately 10 cm. This value is still very small to achieve a reliable momentum resolution for a magnetic field of 2 T. As a consequence, either the magnetic field is reduced to 1 T or the radius of the tracker is increased. However, with the present amount of material[3] (17% of the total radiation length X_0) it can result in an increase of the material effects due to energy loss and to the multiple scattering.

The present amount of material contributes already to deteriorate significantly the tracking resolution of low momentum particles traversing the detector. Here a compromise must be again found in order to have enough hyperons stopping vertexes within the secondary active target and at the same time not interfere much in the tracking resolution. Moreover, it has been shown that

---

[3] The amount of material is defined by the product of the detector thickness t and the material density ρ

with the present secondary active target design the most of the low momentum hyperons stop after traversing the two first absorber–silicon layers.

As a consequence, a further improvement of the detector geometry may be achieved by designing a new setup consisting of two absorber and silicon layers close to the interaction point and three silicon layers at outer radii. This solution corresponds already to an amount of material of 2.6% of the total radiation length. In addition, the dependence of the transverse momentum resolution for pion tracks has been calculated as a function of the magnetic field strength (2 T, 1 T and 0.5 T), the transversal momentum and the amount of material of the detector. Fig. 6.8 illustrates the results of these calculations.

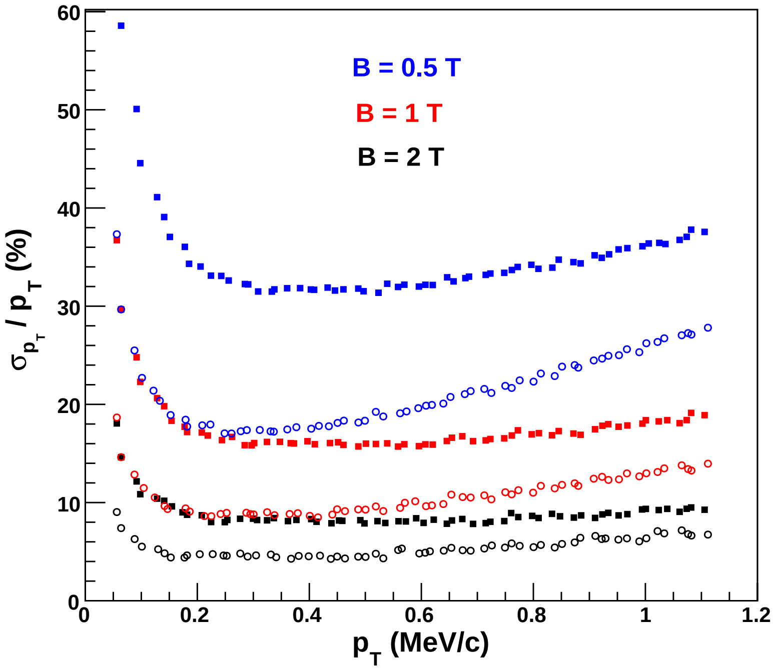

Figure 6.8: The dependence of the transversal momentum resolution for pions tracks calculated as a function of the magnetic field strength ((2 T (black), 1 T (red) and 0.5 T (blue)), the transversal momentum component and the amount of material of the detector. Filled squares represent the amount of material of 17% (present setup) and the empty circles regard the assumption of a material amount of the 2.6%.

The symbols denoted by empty circles correspond to an amount of material of 2.6% of a radiation length and the filled squares correspond to the present secondary target setup with a material amount of 17%. The resolution of the transverse momentum coordinate increases with the magnetic field and momentum. It reaches a minimum value around 200 MeV/c and decreases again in the low momentum region. This effect is due to the fact that low momentum pions will be strongly affected by the amount of material, losing energy rapidly.

In the present work the reconstruction of charged particles trajectories below 200 MeV/c has been performed without taking into account corrections for material effects. In contrast to the global tracking procedure, which uses the information of several detectors, the reconstruction of low momentum particles trajectories is treated via a local tracking process, namely by using only the reconstructed hits on the secondary active target and eventually on the scintillating fibers array detectors. The track finding is accomplished by an ideal pattern recognition algorithm based on the Monte Carlo information.

Due to the reduced dimensions of the tracking region surrounding the interaction point and to the material effects, the trajectories of low momentum particles within the secondary active target are more similar to parabolas than to helices. Therefore, a parabola track representation was chosen and the tracking algorithm employed for the fitting was the one described by the GENFIT [189] package. The GENFIT algorithm alone does not account for the material effects but, for the goal of this work it offers rather good results.

In addition, one can observe that most Ξ^- stop in the first few millimeters of the secondary target and therefore the efficiency for tracking pion pairs produced in the subsequent weak decays of double Λ hypernuclei is expected to be rather high. In fact, as it was mentioned before, these corrections will improve the resolution of the tracking algorithm. Further improvements concerning the use of more realistic algorithms for the patter recognition as well as for the tracking procedures, are foreseen in a near future.

6.4.2 Charged Particle Identification

Good particle identification (PID) for charged hadrons and leptons plays an essential role for $\overline{\mathsf{P}}$ANDA and must be guaranteed over a large momentum range from 200 MeV/*c* up to approximately 10 GeV/*c*. Several subdetectors provide useful PID information for specific particle species and momenta. While energy loss measurements within the trackers obtain good criteria for the distinction between the different particle types below 1 GeV/*c*, the DIRC detector is the most suitable device for the identification of particles with momenta above the Cerenkov threshold (700 MeV/c). Moreover, in combination with the tracking detectors, the EMC is the most powerful detector for an efficient and clean electron identification, and the Muon detector is designed for the separation of muons from the other particle species. The best PID performance however can be obtained by taking into consideration all available information of all subdetectors.

The PID procedure is divided in two different parts. In the first stage the recognition is done for each detector individually, so that finally probabilities

for all five particle hypothesis (e, μ, π, K and p) are provided. The probabilities are normalized uniquely by assuming same fluxes for each particle species.
In the second stage the global PID combines this information by applying a standard likelihood method. Based thereon, flexible tools can be used which allow an optimization of efficiency and purity, depending on the requirements of the particular physics channel. Based on the likelihoods obtained by each individual subdetector the probability for a track originating from a specific particle type $p(k)$ can be evaluated from the likelihoods as follows:

$$p(k) = \frac{\prod_i p_i(k)}{\sum_j \prod_i p_i(j)} \,, \tag{6.5}$$

where the product with index i runs over all considered subdetectors and the sum with index j over the five particle types e, μ, π, K and p.

In the following, special emphasis will be made to explain the particle identification techniques for the low and moderate momentum particles (pions, protons and kaons) emitted during the hypernuclei production. Basically the techniques here employed are the use of dE/dx and the timing measurements by the secondary active target and the TOF detector system respectively. Due to the readout electronics similarity between the secondary active target and the MVD readout electronics, the technique relative to dE/dx measurement performed by the latter will be also here adopted.

6.4.2.1 dE/dx Measurements

The energy loss of particles in thin layers of material directly provides an access to the dE/dx. As established from the Bethe-Bloch formula [190], particles of different types with a certain momentum have different specific energy losses, dE/dx. The mean energy loss dE/dx for moderate particle momenta is expressed as[4]

$$\frac{dE}{dx} = K\frac{\rho Z}{A}\frac{z^2}{\beta^2}\left(\ln\frac{2m_e c^2 W_{max}\beta^2\gamma^2}{I^2} - 2\beta^2 - \delta - 2\frac{C}{Z}\right) \tag{6.6}$$

This property can be used for particle identification, as illustrated in Fig. 6.9. This information is obtained by the detector readout electronics. The method however suffers from two limitations. First of all, at the bands overlapping points, there is no possibility to disentangle particles. Secondly, the distribution of the specific energy loss presents a long tail which makes difficult the separation, especially when large differences exist between the different particle yields. In $\overline{\text{P}}$ANDA, two detectors will provide access to a dE/dx measurement, the MVD detector, and the central spectrometer tracking system (Straw Tube Tracker or Time Projection Chamber).

---

[4] The constants definition can be found at ref. [190].

Detailed investigations performed for the Micro Vertex Detector points out that a good separation of the different particle species depends on one hand on the accuracy to measure the energy loss from the collected charge in the frontend electronics and on the other hand on a good knowledge of the track position with respect to the sensor surfaces.

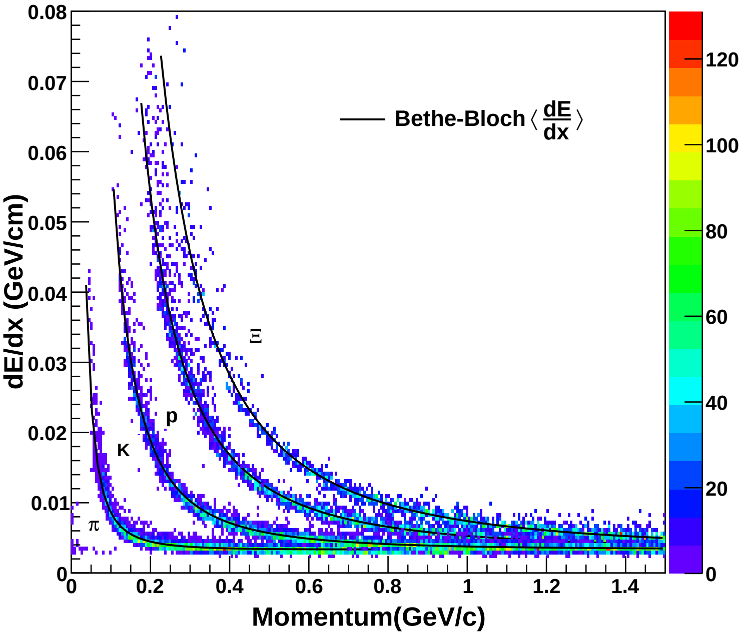

Figure 6.9: dE/dx information from the secondary active target versus track momentum for hyperons (upper band), protons/kaons (middle) and pions (lower).

Contrary to the usual truncated mean method consisting in summing the individual hit measurements dE_i/dx_i to an energy loss information

$$dE/dx = \sum_{i}^{n} dE_i/dx_i \tag{6.7}$$

and omitting the highest value, all hit measurements can be combined to a total quantity

$$\frac{dE}{dx} = \frac{\sum dE_i}{\sum dx_i}$$

The dE_i are the energy information from the reconstructed hit and the dx_i are obtained by calculating the length of the reconstructed track traversing the sensor material. This method gives a slightly smaller spread of the Landau-smeared energy loss compared to the truncated mean method.

The width of the individual bands depends on the energy-loss distribution which varies with momentum. The total error uncertainty contribution is parametrized by a single Gaussian distribution which is convoluted with the already Landau-distributed energy loss. The resulting distribution is calculated using numerical integration of the functional integral

$$w(s) = \int L(x)\, G(s - x) dx$$

with the parameters σ for the Gauss width, τ respectively for the Landau width and s, which is the most probable value of the Landau distribution. The used parametrizations for the distributions are

$$G_\sigma(x) = \frac{1}{\sqrt{2\pi}\sigma} e^{-x^2/\sigma^2}$$

for the Gauss distribution and

$$L_\tau(x) = \frac{1}{\pi\tau} \int_0^\infty e^{-t(\ln t - x/\tau)} \sin(\pi t) dt$$

for the scaled Landau distribution. For each particle type the parameters are then obtained independently by generating single particle events each over a wide momentum range. The energy loss distribution is then fitted to get the parameters $\hat{s}_i$, σ_i, τ_i for a given p_i. For all particle types the evolution of the parameters $\hat{s}(p)$, $\sigma(p)$ and $\tau(p)$ are parametrized with polynomials and can be used as a basis for the calculation of the particle hypothesis. An example of particle hypothesis calculated with this technique can be found in Ref. [187].

6.4.2.2 Timing measurement

Using the tracking (momentum, charge, track length) and the timing information particle identification may be performed. Indeed, a particle with mass m and momentum p has a velocity v which can be expressed in units of the light velocity c by $\beta = v/c$

$$\begin{aligned} \beta &= \frac{p}{\sqrt{p^2 + m^2}} \\ \gamma &= \frac{1}{\sqrt{1 - \beta^2}} \end{aligned} \tag{6.8}$$

Using the definition of γ and β, one gets the following expression $\frac{p}{m} = \beta\gamma$. For instance, Fig. 6.4.2.1 shows the value $\frac{p}{m}$ as a function of the particle momentum p and its charge q. For that, a data sample[5] of 200,000 $\Xi + \overline{\Xi}$ events have been

---

[5] Event generation has been accomplished by the UrQMD+Smm generator interface

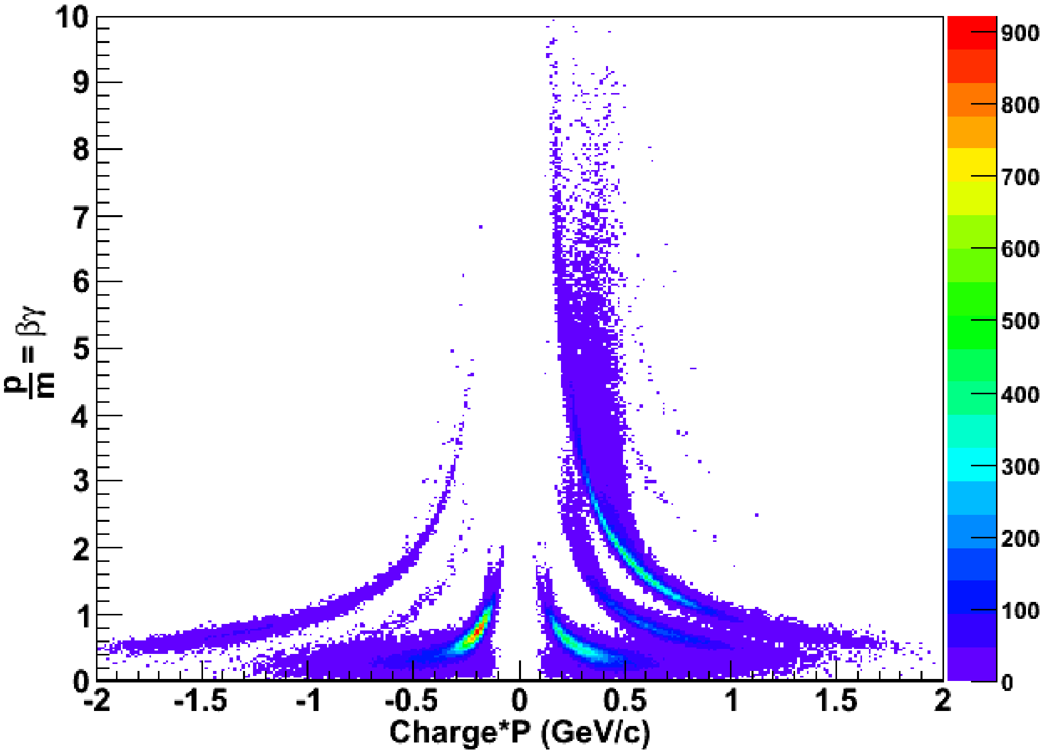

Figure 6.10: Particles separation using the timing and the track information. Particles resulting from the $\Xi + \overline{\Xi}$ with the UrQMD+SMM generator are separated according with their mass m, charge and momenta P.

generated at a magnetic field of 1 T. The bands on the negative region of this picture[6] represent the production of negative particles such as pions, kaons, and antiprotons[7]. The bands on the positive region of the picture correspond to positive charged particles such as pions, kaons, protons and light ions.

Based on this feature, different methods can be adopted for particle identification (PID). In the following, the so–called "contour method" and the "probability method" will be reviewed.

Contour method For this method all reconstructed primary particles are entered in a momentum versus mass plot as shown in Fig. 6.11. The mass m

---

[6] Defined as the product of the particle charge q and the momentum p

[7] $\overline{\Xi}$ free decay, $\overline{\Xi} \rightarrow \overline{\Lambda} + \overline{p}$

of the particle is then determined by the formula:

$$m = p\sqrt{\frac{t^2}{l^2} - 1}$$

being t the time of flight to travel a path length l.

Fig. 6.11 illustrates several clusters of points corresponding to pions, kaons and protons at a magnetic field $B = 1\,\mathrm{T}$ for a data sample of 200,000 $\Xi^- + \bar{\Xi}^+$ events. Additionally, mismatched tracks can leads to "wrong times" causing contamination, even in the low momentum region where the mass resolution ($\partial m/m$) is good. The mass resolution ($\partial m/m$) can be expressed as a function of the time, momentum and track length resolutions [8],

$$\begin{aligned} \partial m/m &= \sqrt{\gamma^4 \left(\partial l/l + \partial t/t\right)^2 + \left(\partial p/p\right)^2} \\ \gamma &= E/m \end{aligned} \tag{6.9}$$

where E represent the particle energy.

At larger momenta, the particle clusters become obviously wider because the mass resolution increases with the particle momentum even for practically constant time resolution ($\partial t/t$). Additionally, at small momenta, the particle clusters appear to be systematically distorted, i.e. curved towards larger masses. The reason is that the mass is calculated assuming that the particle momentum is constant, whereas it decreases due to energy loss when the particle travels all the way through the tracking and timing detectors. This effect can be reduced by using some effective momentum corresponding to the middle-point of the track, instead of the momentum at the vertex. The identification procedure is then accomplished by introducing specific contour cuts.

Probability method The probability method consists in assigning to each kind of particle a probability density function(p.d.f.) based on some separation parameter, for instance the mass, by fitting the appropriate Monte Carlo simulated distribution. Therefore, one can compute the probabilities for each track, measured with a given mass m, to be a pion, a kaon or a proton from the heights of the corresponding mass p.d.f's (f_k, f_π, f_p) at this m–value. Each p.d.f. should be normalized to the corresponding particle yield. The probability to be a particle of type i can be indeed defined as

$$P_i(m) = \frac{f_i}{f_\pi(m) + f_k(m) + f_p(m)} \tag{6.10}$$

Fig. 6.12 shows an example of the p.d.f, for $i = k, \pi, p$, obtained as Monte Carlo mass distributions. However, mass is not a very good separation parameter

---

[8] $\partial t/t$, $\partial p/p$ and $\partial l/l$ respectively

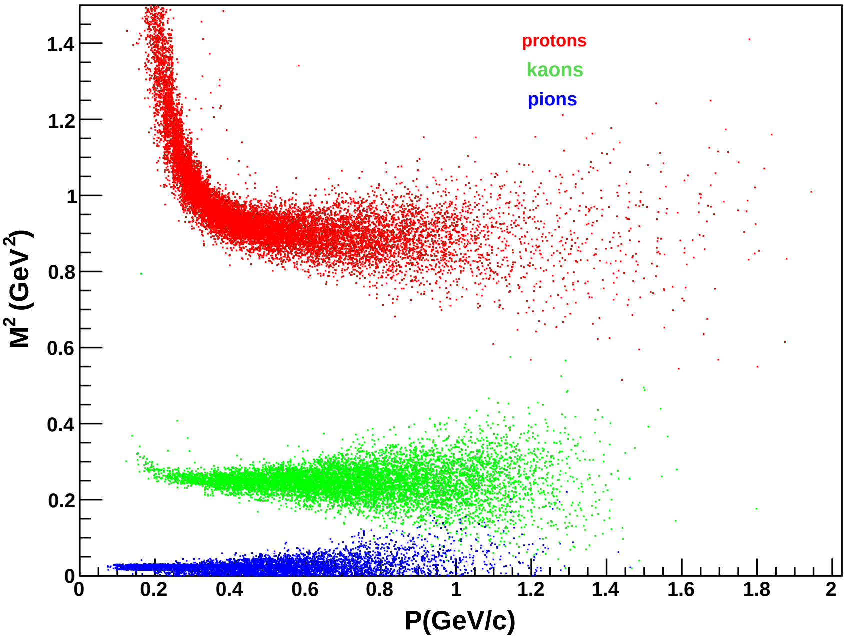

Figure 6.11: Mass separation with the TOF detector system(time resolution : 80 ps) as a function of the particle momentum for data sample of 200,000 $\Xi^- + \bar{\Xi}^+$ events with a magnetic field value of 1 T

because its probability density function has not a proper Gaussian shape as a consequence of the mass determination formula 6.9. Time–of–Flight is indeed gaussianly distributed and can be more conveniently used for probability calculations. For a track measured with a given flight–time t, the probability to have a mass m_i can be calculated for $i = k, \pi, p$ as

$$P_i(t) = \frac{g_i}{g_\pi(m) + g_k(m) + g_p(m)} \tag{6.11}$$

where $g(t_i)$ is the height of the Gaussian p.d.f. $g($ with mean value t and standard deviation $\sigma_t)$ at the time t_i derived from the track length l and momentum measurements with mass hypothesis m_i(see Fig. 6.13). Here a weighting procedure is applied to consider the different particle yields. The time–based probabilities obtained in this way are shown in Fig. 6.14 as functions of the mass derived according to formula 6.9. One can see the masses at which the probability for a particle to be a pion becomes equal to the probability to be a kaon($\equiv$ 0.3 GeV/c^2), and the probability to be a kaon becomes equal the probability to be a proton($\equiv$ 0.7 GeV/c^2) correspond to the crossing points of the π, K, p mass p.d.f's of Fig. 6.12.

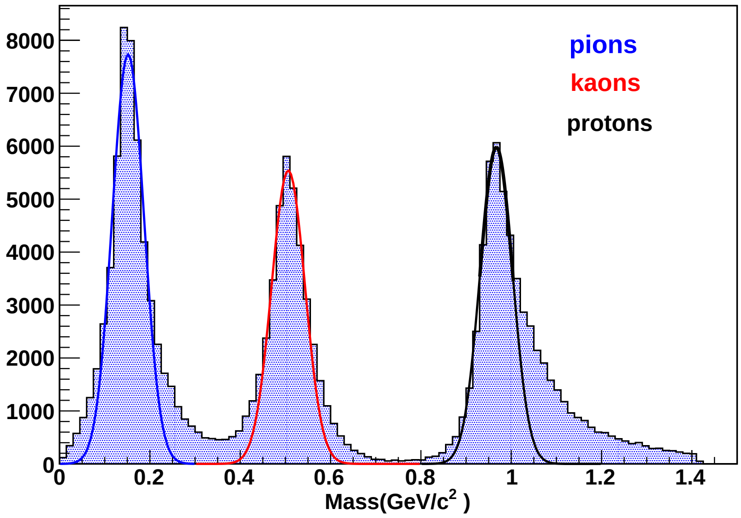

Figure 6.12: Mass probability density functions for pions, kaons and protons, obtained as mass spectra of unambiguously TPC–TOF matched tracks with a momentum ranging from a 200 MeV/c to 1.4 GeV/c (data sample contains 200,000 $\Xi^- + \bar{\Xi}^+$ events at B=1 T). Superimposed, some gaussian fits to guide the eye.

6.5 Analysis of a Hypernuclear Event

The analysis procedure in the present work is managed by tools provided by the Rho package [186]. For each event the information obtained after the reconstruction stage is associated to particle candidates (kaons, pions or photons) according to the particle hypothesis calculated during the particle identification process and are stored in particle lists. For the identification of complete decay chains selector applications can be applied to get access to the candidate lists and to extract information such as number of particles, total event energy or four vectors of each particle.

In the following, the analysis of a full hypernuclear event will be addressed. As discussed in Sec. 2.2.2 spectroscopic information on double hypernuclei will only be obtained via their decay products, namely γ–rays emitted from electromagnetic deexcitations and pions produced via the sequential mesonic decay. However, except for the case of very light hypernuclei, also neutral particles are emitted. Therefore, a unique identification of the double hypernuclei can only be reached via the emitted γ-rays from excited, particle stable states.

In the present work, an identification strategy will be introduced to uniquely assign observable transitions to the corresponding hypernuclei. This strategy is based on the coincidence detection of the deexcitation photons of produced double and single hypernuclei, and of pairs of decaying pions. On the other

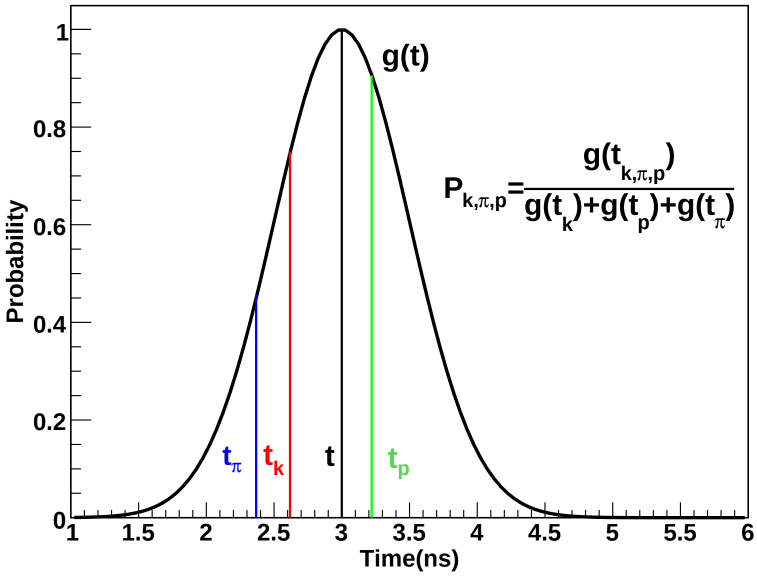

Figure 6.13: Example of time–of–flight probability density function. The standard deviation σ_t of this gaussian function, centered at the measured track time t, has been enlarged by an arbitrary factor for the sake of clarity.

hand, pions emitted via a two-body decay are monoenergetic and their momenta are strongly correlated. As a consequence one can use their coincident measurement as an effective method to tag the production of a double hypernucleus. Moreover, the momenta of the two pions provide information about the hypernucleus binding energy which is a unique signature of the hypernuclide.

In the following, the second stage of the multi–step production mechanism, will be analyzed according to the method explained above. As remarked before, this second step is the result of having simulated the statistical decay of the 7396 produced excited Ξ^- hypernuclei. The starting point of this analysis is the total energy spectrum measured by the germanium array detector and it is shown in Fig. 6.15. The main contributions to this spectra are electromagnetic deexcitations from excited particle stable states of double hypernuclei as well as excited states of conventional nuclei and single hypernuclei.

One can note, that the size of the bins (50 keV) in this plot is significantly larger than the resolution of the germanium detectors expected even for high data rates at normal conditions (3.4 keV at 110 kHz [191]). Even after 100 days of operation at $\overline{\text{P}}$ANDA and an integrated neutron fluency of about $6{\cdot}10^9$ neutrons/cm^2, one expects a degradation of the resolution by less than a factor of 3 to no more than 10 keV [192]. Several peaks seen in the spectrum around 1, 1.68 and 3 MeV are associated with γ-transitions in various hyper-

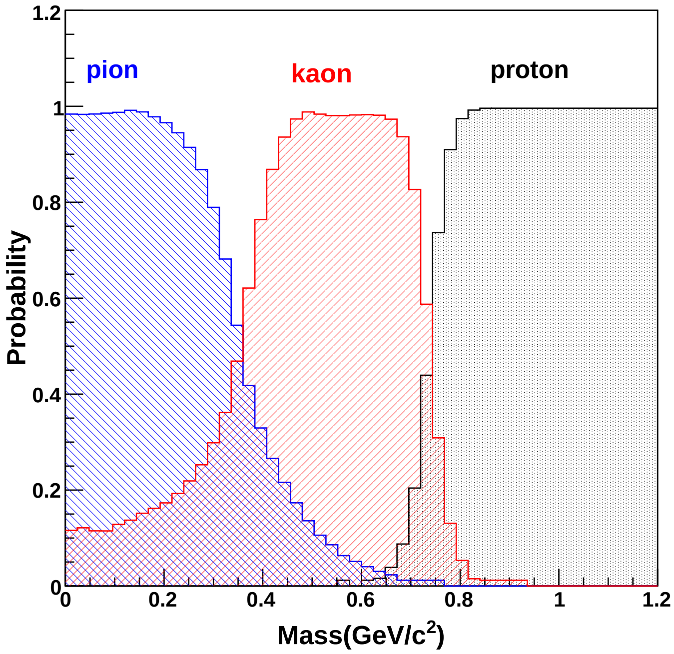

Figure 6.14: Time –based PID probability distributions as a function of the mass, for pions, kaons and protons, corresponding to unambiguously matched TPC–TOF tracks with a momentum range from 0.3 GeV/c to 1.4 GeV/c and a track length of approximately 1 meter at B=1 T

nuclei. However, for a clear assignment of these lines, additional experimental information will be needed. This additional information is the one related to the charged decay particles tracked in the secondary active target, and how to obtain it will be explained in the next paragraph.

After the tracking procedure which has been reported in Sec. 6.4, 14883 charged tracks candidates have been reconstructed. Additionally, with the application of the particle hypotheses, obtained via the dE/dx technique in combination with the tracking information, a number of 8133 tracks has been recognized as π^- candidates.

The next requirement is the selection of events containing two pion candidates since the sequential mesonic decay of a hypernuclei results in the emission of two negative pions. In case this requirement is fulfilled the pion candidates are ordered with respect to their momenta so that the pion with higher momentum is labeled as (p_H) and plotted against the one with the lower momentum (p_L). It can be noticed that due to this feature the coincident pion spectrum is folded about the line where $p_H = p_L$. The pion spectra of two–body decay from a double Λ hypernuclei at rest or nearly at rest, should exhibit a sharp

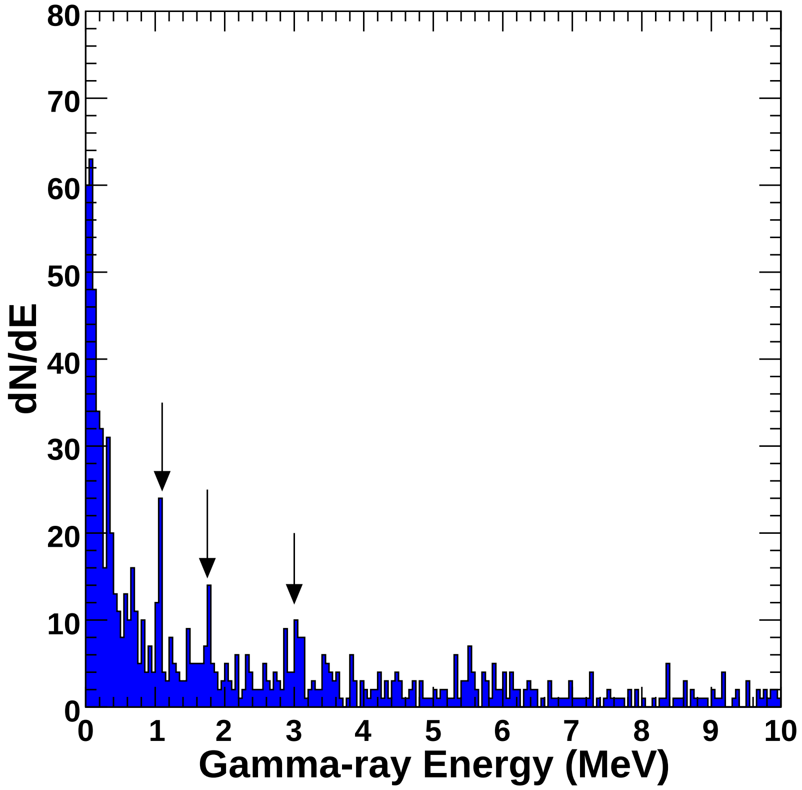

Figure 6.15: Total γ-ray spectrum resulting from the decay of double hypernuclei produced in a ^{12}C target and detected in the germanium array before additional cuts. The arrows illustrate some γ-transitions associated with various hypernuclei around 1, 1.68 and 3 MeV. The statistics of the simulations corresponds to a data taking time of about two weeks.

peak. A correlated signal with this feature can be interpreted as a pair of single–Λ hypernuclei if the momenta match known decays of single–Λ systems. On the contrary, it can be regarded as a double–Λ hypernucleus when only one of the lines matches a known decay momentum [87]. According to that, several regions of enhanced events, appear in the two–dimensional scatter plot of the pion pairs events (See Fig. 6.16). Fig. 6.16 shows the momentum correlation of all negative pion candidates from the secondary ^{12}C target. For the sake of clarity, the various bumps corresponding to different double hypernuclei are marked by different colors. The enhancement regions such as (98.8, 119) MeV/c, (99, 102) MeV/c, (74, 131) MeV/c, and (98.8, 133) MeV/c have been selected in the present analysis. In fact, these regions correspond to the most probable produced double Λ hypernuclei species in the case of a ^{12}C target (See chapter 5). One can then observe that the good separation of the different double hypernuclei provides an efficient selection criterion for their decays.

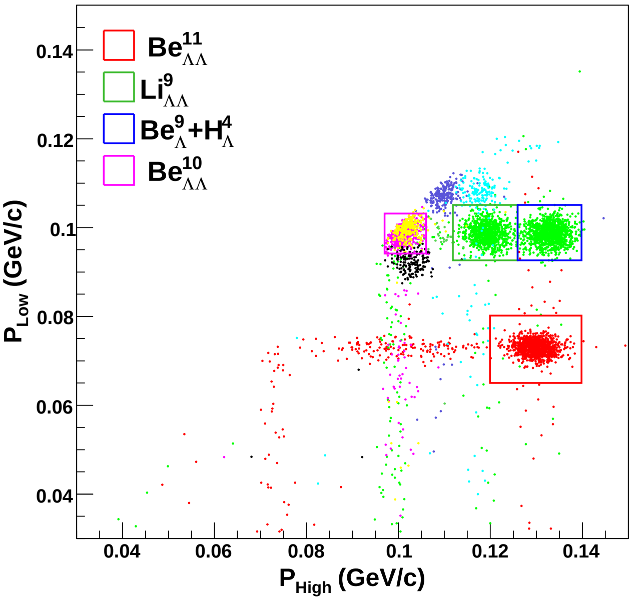

Figure 6.16: Momentum correlation of all negative pion candidates resulting from the decay of double hypernuclei in a secondary ^{12}C target.

In the following, the cited enhancement regions have been delimited by rectangular contours in the (p_{high}, p_{low})–plane. Events enclosed within these zones are used to gate the total energy spectra shown by Fig. 6.15 and obtain the corresponding energy spectra of the associated double–Λ hypernucleus. Fig. 6.17 shows the γ-ray spectra gated on the four regions indicated in the two-dimensional scatter plot. In the plots (a) and (d) the 1.684 MeV $\frac{1}{2}^+$ and the 2.86 MeV 2^+ states of $^{11}_{\Lambda\Lambda}$Be and $^{10}_{\Lambda\Lambda}$Be, respectively, can clearly be identified. Because of the limited statistics in the present simulations and the decreasing photopeak efficiency at high photon energies, the strongly populated high lying states in $^{9}_{\Lambda\Lambda}$Li at 4.55 and 5.96 MeV cannot be identified in (b). The two dominant peaks seen in part (c) result from the decays of excited single hyperfragments produced in the $\Xi^- + C \rightarrow^4_\Lambda H +^9_\Lambda Be$ reaction, i.e. $^4_\Lambda H$ at an excitation energy of 1.08 MeV [57, 58] and $^9_\Lambda Be$ at an excitation energy of 3.029 and 3.060 MeV [28, 193].

In the present simulation, several intermediate steps, which do not affect the kinematics and hence the detection of the decay products, have not been considered on an event-by-event basis. Obviously, these points are relevant for the final expected count rate:

- a capture and conversion probability of the Ξ^- of 5-10%.

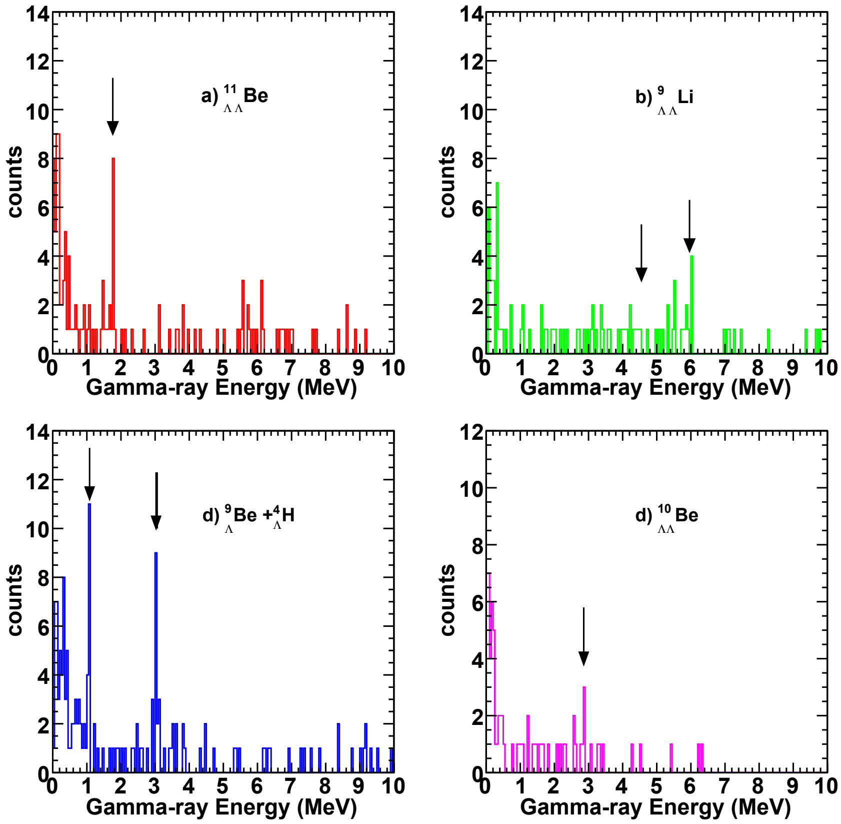

Figure 6.17: γ-spectrum detected in the Ge-array by cutting on the two pion momenta. The expected γ-transitions energies from single and double hypernuclei are marked by the arrows.

- typical probability of a double mesonic decay of 10% (c.f. Fig. 1.5).
- availability of data taking 50%.

With these additional factors taken into account, the spectra shown in Fig. 6.17 correspond to a running time at $\overline{\text{P}}$ANDA of about two weeks. It is also important to realize that gating on double non-mesonic weak decays or on mixed weak decays may significantly improve the final rate by up to a factor 10.

6.5.1 Background influence

The main background contribution to the coincident pion spectrum is expected to come from decays of quasi–free Ξ^-s, quasi–free Λs, and quasi–free Λs associated with hypernuclear decays. For instance, Ξ^- hyperons decays via the emission of a proton and two pions as shown below,

$$\begin{aligned} \Xi^- &\rightarrow \Lambda + \pi \\ \Lambda &\rightarrow p + \pi \end{aligned} \tag{6.12}$$

As a consequence, pions from these decay chains will populate the momentum bins below 140 MeV/c. The quasi–free pion spectrum does not have a so well defined structure as the one corresponding to the hypernuclei two–body decay, and it is approximately constant.

Another background source is the one corresponding with $\bar{p}+^{12}C$ reactions which does not lead to the production of $\Xi^- + \bar{\Xi}^+$ pairs. Even if the probability of generating particle with momenta below 140 MeV/c is very small, one should consider the fact that the cross section of this reaction mechanism is about 25000 times larger than the one corresponding to the production of $\Xi^- + \bar{\Xi}^+$ pairs. Therefore, the $\bar{p}+^{12}C$ process will also be studied as a possible background contribution.

In the present simulation, the main source of quasi–free Ξ^- decay is provided by the first step of the signal generation, which regards the production of $\Xi^- + \bar{\Xi}^+$ pairs. The events containing no stopping Ξ^- hyperons will be considered to be analyzed following the same procedure as before. The resulting coincident pion spectrum is shown by Fig. 6.18. The influence of this background signal affects also the energy spectra measurement of the several

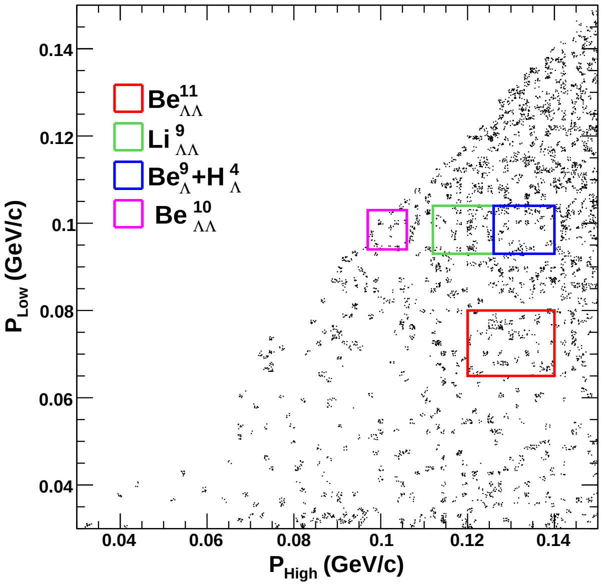

Figure 6.18: Momentum correlation of all negative pion candidates resulting from the quasi–free Ξ^- decay in a secondary ^{12}C target.

hypernuclear species treated before. Fig. 6.19 shows the contribution of the quasi–free background to the individual energy spectra of $^{9}_{\Lambda\Lambda}$, $^{10}_{\Lambda\Lambda}$Be $^{11}_{\Lambda\Lambda}$Be and the twin $^{4}_{\Lambda}H +^{9}_{\Lambda} Be$. These energy spectra have been obtained by applying the same momenta cuts (rectangular contours) as for the hypernuclear production. The lack of statistic in Fig. 6.19 allows only to make an approximated estimate of the signal–to–noise ratio, which is 3 to 1. Even though, this quantity seems to be too optimistic, and therefore a better estimation of the background signal due to the quasi–free decay of Ξ^- hyperons will need of an enhancement of the present statistic. In the next paragraph, the background contribution due to the inelastic $\overline{p} +^{12} C$ interaction will be estimated. For that, background reactions have been calculated by using the UrQMD+SMM [194] event Generator. At present, it is not possible to simulate the detector response for a sample of unspecific background events which is large enough to test background suppression in all details. The background suppression and signal detection capability can therefore only be estimated by using extrapolations based on

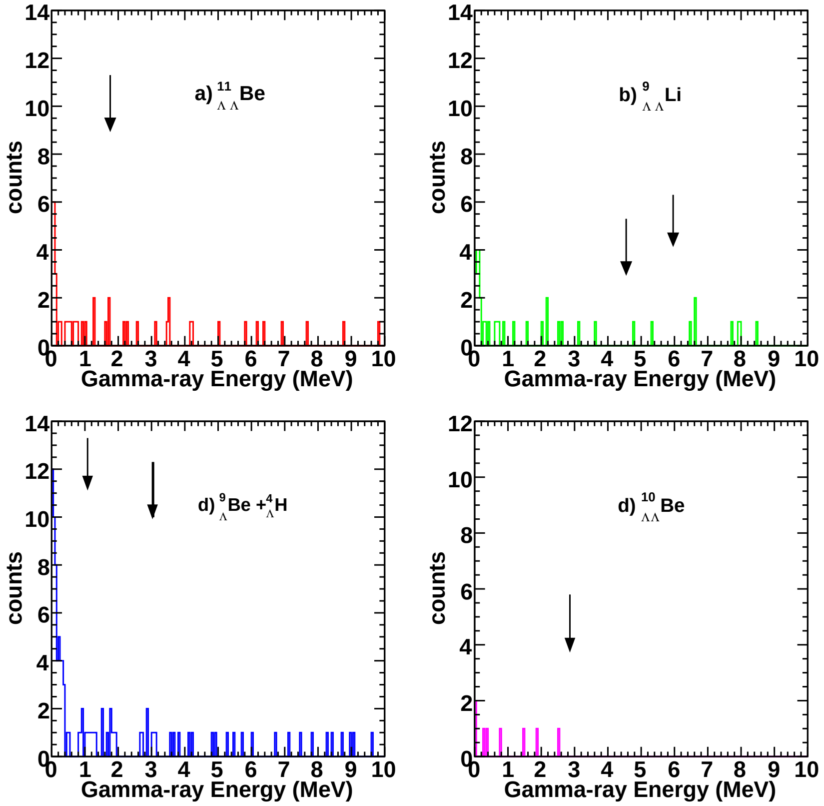

Figure 6.19: γ-spectrum associated with quasi–free Ξ^- decay events detected in the Ge-array by cutting on the two pion momenta. The expected γ-transitions energies from single and double hypernuclei are marked by the arrows.

simplified assumptions.

For the present analysis 100,000 $\overline{p} +^{12} C$ interactions at 3 GeV/c were generated. The total energy spectra resulting from the background simulation have been filtered by using the same technique as it was done for the signal events. Particularly the same cuts on correlated pion candidates have been applied to the background events, in order to obtain the corresponding background spectrum for each of the hypernuclei channels. For $^{11}_{\Lambda\Lambda}$Be as well as $^{10}_{\Lambda\Lambda}$Be only one single event survived the cuts. Both of these events had an energy deposition in the germanium detector exceeding 10 MeV significantly.

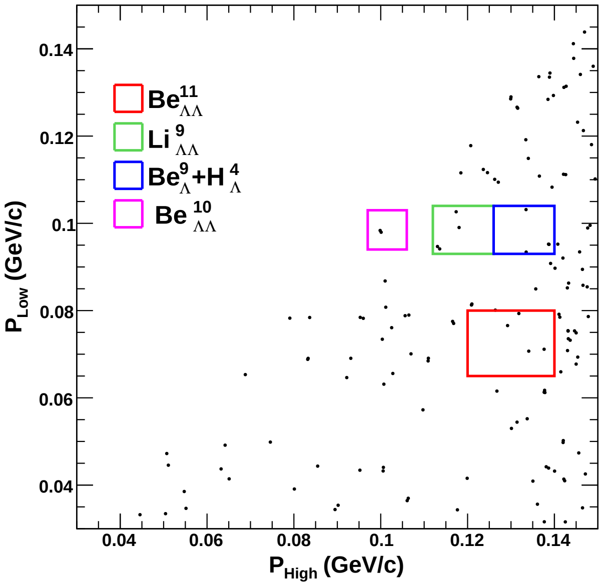

Figure 6.20: Momentum correlation of all negative pion candidates resulting from the $\overline{p}$+^{12}C reactions in a secondary ^{12}C target.

Several further improvements of the background suppression are expected by exploring the topology of the sequential weak decays. This includes the analysis of tracks not pointing to the primary target, multiplicity jumps in the detector planes and the energy deposition in the secondary target.

6.5.2 Comparison with UrQMD+SMM calculations

As previously discussed, the UrQMD+SMM generator can also be used for the generation of a hypernuclear event. In contrast to the INC generator, it can be used to obtain high statistics, and therefore, it can provide complementary information.

By using the UrQMD+SMM generator interface, a sample of 200,000 $\Xi^- + \overline{\Xi}^+$ events has been considered for the hypernuclei event generation at different

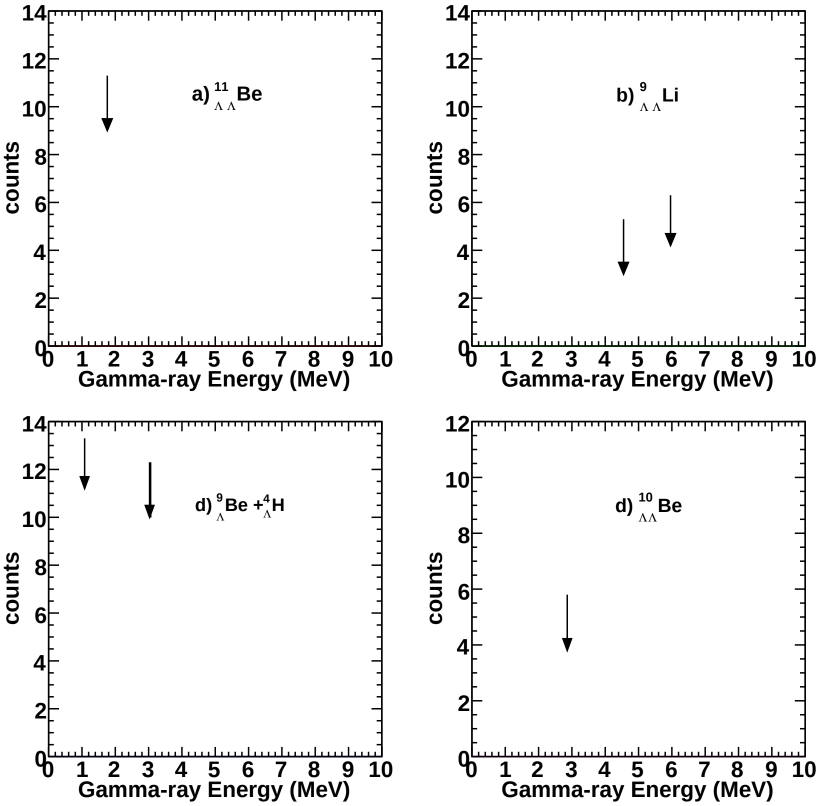

Figure 6.21: γ-spectrum associated with $\overline{p}$ + ^{12}C events detected in the Ge-array by cutting on the two pion momenta. The expected γ-transitions energies from single and double hypernuclei are marked by the arrows.

values of the magnetic strengths (2 T, 1 T and 0.5 T). This calculation has also had the purpose of studying the influence of the magnetic field on the number of stopped Ξ^-.

Nevertheless, no significant change has been observed, and the number of stopped Ξ^- within the absorber material was, for the three cases, almost the same ($\simeq$ 15,000). On the other hand, on can note that this number in comparison to the 7396 stopped Ξ^-, obtained by the INC calculations, is a factor of 2 larger. However, in the following the analysis results related to the UrQMD+SMM calculations at the magnetic field strength of 2 T will be presented.

Applying the same analysis procedure as in previous sections, the gamma spectra corresponding to the production of the double Λ hypernuclei $^{9}_{\Lambda\Lambda}$, $^{10}_{\Lambda\Lambda}$Be $^{11}_{\Lambda\Lambda}$Be and the twin hypernucleus $^{4}_{\Lambda}H +^{9}_{\Lambda} Be$ are shown in Fig. 6.22. One can observe in Fig. 6.22 that due to the enhancement of statistics, some of the γ-transitions not identified before, (such as the states in $^{9}_{\Lambda\Lambda}$Li at 4.55 and

5.96 MeV and the 2.86 MeV 2^+ states of $^{10}_{\Lambda\Lambda}$Be), can now be well distinguished (See panel (c) and (d) of Fig. 6.22).

In analogy to the results obtained before, it seems that the major valuable background source is due to the free decay of the Ξ^- hyperons. Taking as a reference the $^{9}_{\Lambda}Be$ γ-transition at 3.06 MeV in panel (d) of Fig. 6.22 and Fig. 6.23, the associated signal to noise ratio is 21 to 1. As a consequence, these results confirm the need for large statistics in order to make significant estimations of the capability to identify uniquely individual γ-transitions over the background.

6.5.3 Kaon identification based on timing measurements

As already mentioned, the production of low momentum Ξ^- via the $\overline{p}+p \rightarrow \Xi^-\overline{\Xi}^+$ reaction(See ref. [6]) seems mandatory for the performance of hypernuclei physics at the $\overline{\text{P}}$ANDA experiment. Because the value of this cross section is likely 4 orders of magnitude smaller than the one corresponding to the $\overline{p}+p$ annihilation process, the background suppression plays an important role in the unique identification of hypernuclei. Moreover, the major part (around 85%) of the associated $\overline{\Xi}^+$ annihilates inside the primary target nucleus releasing in most cases two positive kaons. Theses kaons are emitted particularly into the forward region, providing with its identification a possibility to tag the production of Ξ^- hyperons.

In the present work, a strategy will be introduced to identify low momentum kaons via the timing measurement of TOF (Time of flight system) in combination with the tracking performance of the TPC detector at $\overline{\text{P}}$ANDA. The efficiency of tagging the production of Ξ^- hyperons via the kaon identification will also be studied by considering different values for the timing resolution of the start detector. It is also important to note that the efficiency of the method will also depend on the geometrical acceptance of the detection system. The main difficulty of the proposed setup is to optimize the distance of the hypernuclear target to the central tracker of $\overline{\text{P}}$ANDA spectrometer. Due to the fact, that the backward region has been chosen for the placement of electronics readout of the central tracker detectors, the space left closed to the TPC detector is therefore limited (See Fig. 6.25).

The identification procedure consists of using the timing measurement, provided by the TOF detector system in combination with the tracking information given by the TPC (as discussed in Sec. 6.4.2.2), to separate different particles types. Moreover, the probability method, explained in Sec. 6.4.2.2 of this chapter, will be used to calculate the corresponding particle hypothese, through which kaons, pions or protons will be recognized. To enable the time of flight measurement, the produced particles must have enough momenta to cross the scintillator fibers array (start detector), the TPC and to arrive to the

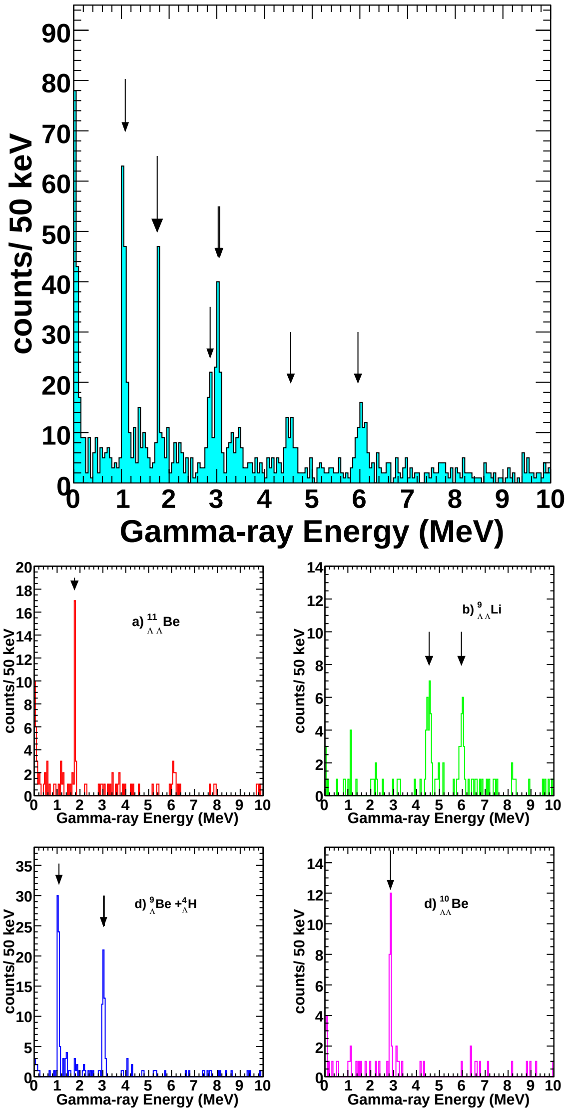

Figure 6.22: Calculations performed with the UrQMD+Smm generator. Top, Total γ-ray spectrum resulting from the decay of double hypernuclei produced in a ^{12}C target and detected in the germanium array before additional cuts. The arrows illustrate some γ-transitions associated with various hypernuclei. Bottom, γ-spectrum associated with events detected in the Ge-array by cutting on the two pion momenta. The expected γ-transitions energies from single and double hypernuclei are marked by the arrows.

time of flight barrel (stop detector). In other words, produced particles must be able to traverse the interior of the target spectrometer (radius R$\simeq$ 50 cm).

According to the expression $P_T = 0.3RBq$, positive charged kaons moving in a magnetic field B of 2 T must have a transverse momenta component P_T

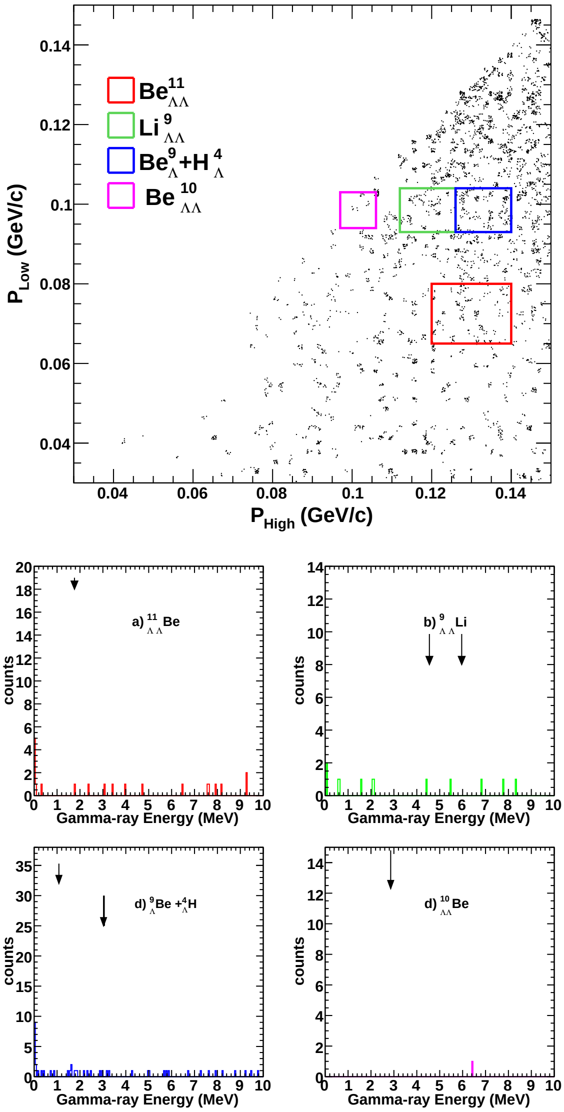

Figure 6.23: Calculations performed with the UrQMD+SMM generator. γ-spectra (right) associated with the quasi-free decay of Ξ^- events detected in the Ge-array by cutting on the two pion momenta (left). The expected γ-transitions energies from single and double hypernuclei are marked by the arrows.

above 150 MeV/c to fulfil this requirement. It is also important to note, that for a good suppression of the background signal, the detector acceptance for kaon detection has to be large. The reason for that, is that one should not only account for the probability of producing Ξ^-, but also one should consider the stopping probability and the conversion probability which represents 5% of the total rate. The enhancement in statistics can be easily achieved by reducing the magnetic field to 1 T. As a consequence, the number of positive

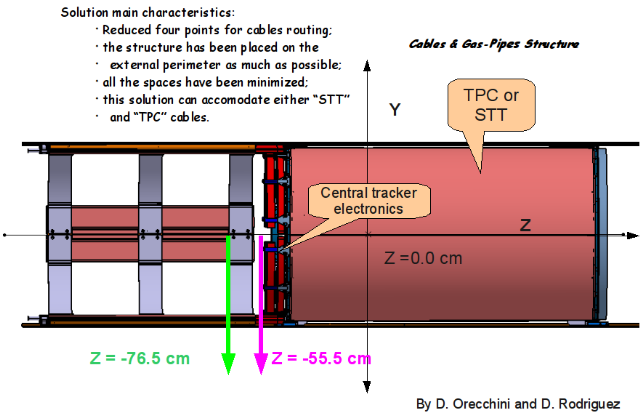

Figure 6.24: Side view of the interior of the $\overline{\text{P}}$ANDA detector. A compact structure has been suggested to root electronics cables from the central tracker region to the external part of the spectrometer [195]. The cylinder structure must be placed in the backward region of the $\overline{\text{P}}$ANDA spectrometer. For the sake of clarity, the possible placements of the hypernuclear interaction (IP) point have been labeled by green and pink arrows.

kaons fulfilling the above condition is then even larger, and the momentum threshold can be then placed below 100 MeV/c.

The starting point of the analysis begins with the production of 200,000 $\Xi^- + \bar{\Xi}^+$ pairs events at a magnetic field of 1 T by the extended UrQMD+SMM generator interface.

In the next stage, track candidates are built using the method introduced in Sec. 6.4. For that, hits produced in the scintillation fibers array, the TPC and scintillation barrel detector are considered. Particle tracks which do not fulfil this condition will not be accepted by the tracking procedure. Typically, the geometric acceptance of the scintillation barrel detector goes from 22° to 140° for an interaction point placed at center of the target spectrometer reference system. However, because the interaction point for the hypernuclear setup is placed at -76.5 cm from the target spectrometer center, the corresponding geometric acceptance will be from 14° to 90° (See Fig. 6.25).

For the present studies, the detector system acceptance for kaon identification is then of the order of 60% percent. Fig. 6.26 illustrates a typical kaon event traversing the volumes of scintillating fiber array detector, the TPC and the TOF barrel detector. The picture shows the kaon track from the front and side view.

In the next step, reconstructed tracks are assigned to kaon candidates according to the particle hypotheses obtained via the probability method as indicated in Sec. 6.4.2.2.

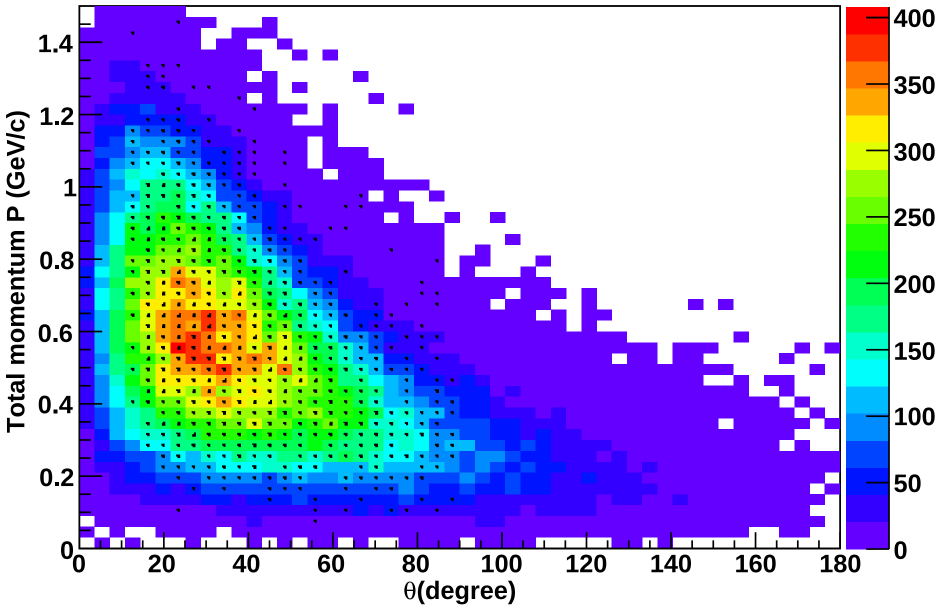

Figure 6.25: Scatter plot showing the transverse momentum distribution of generated kaons. Black boxes represent the geometric acceptance of the TOF barrel detector for kaons tracks which are accepted for analysis.

To study the kaon identification efficiency two detector options have been considered for the start detector. One corresponds to the use of the scintillator fibers detector (as discussed above) with a time resolution σ_t of 450 ps and the other possible option concerns the use of a detector with a time resolution comparable to the one of the scintillator Time–Of–Flight barrel (100 ps). Fig. 6.27 shows the reconstructed mass spectra assuming a start detector with a timing resolution of 450 ps (scintillating fibers array) and 100 ps (CVD detector). The particle mass spectrum has been calculated using the formula 6.9. One can see that for a start detector with a timing resolution comparable to the one of the TOF barrel (stop detector), particles such as pions, kaons and protons are well separated. On the contrary, the option of the scintillating fibers array detector must provide at least a timing resolution of about 400 ps to separate kaons from pions. From the tracking procedure, a momentum and the track length resolution of 1% and 3% respectively have been assumed for this analysis.

Furthermore, considering a scintillating fibers array as possible start detector, the kaon identification efficiency [9] [10] is around 50% and for the case of a time resolution of 100 ps the kaon identification efficiency is around the 95%.

---

[9] It is defined as the number of kaon identified by the PID system divided by the number of produced kaons

[10] assuming a kaon hypothesis larger than 0.4 (see Fig. 6.14)

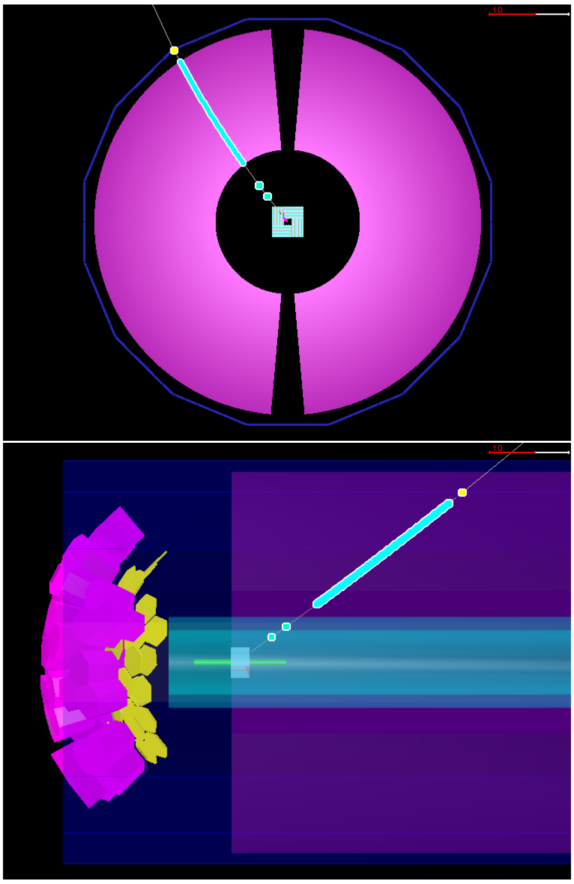

Figure 6.26: Upper and lower panel show respectively the X-Y and Y-Z view of the TOF system setup (for a IP placed at -55.cm). In both cases a kaon track is denoted by its hits on the fibers array, TPC and TOF barrel.

Accordingly, the $\Xi^- + \overline{\Xi}^+$ events which can be tagged based on the kaon identification strategy are of the order of 14% (450 ps) and 20% (100 ps) of the total production. Assuming a timing resolution of 100 ps for both, start and stop detectors, the number of stopped Ξ^- is around 3000, which represents a 20% of the total number of stopped Ξ^- achieved by using the UrQMD+SMM generator(See Fig. 4.3).

In addition to these calculations, the same simulation procedure has been calculated placing the hypernuclear detector setup at a distance of -55.5 cm from the center of the $\overline{\text{P}}$ANDA spectrometer. This is actually the closest distance to the central tracker the hypernuclear detector setup can be placed [195]. Nevertheless, under this condition the geometric acceptance of the TOF system should improve significantly. However, after having applied the same analysis procedure the efficiency to tag $\Xi^- + \overline{\Xi}^+$ events has a value of 28.3% considering a start detector with a time resolution of 100 ps. Assuming a start detector with a time resolution of 450 ps the efficiency is then about 20%.

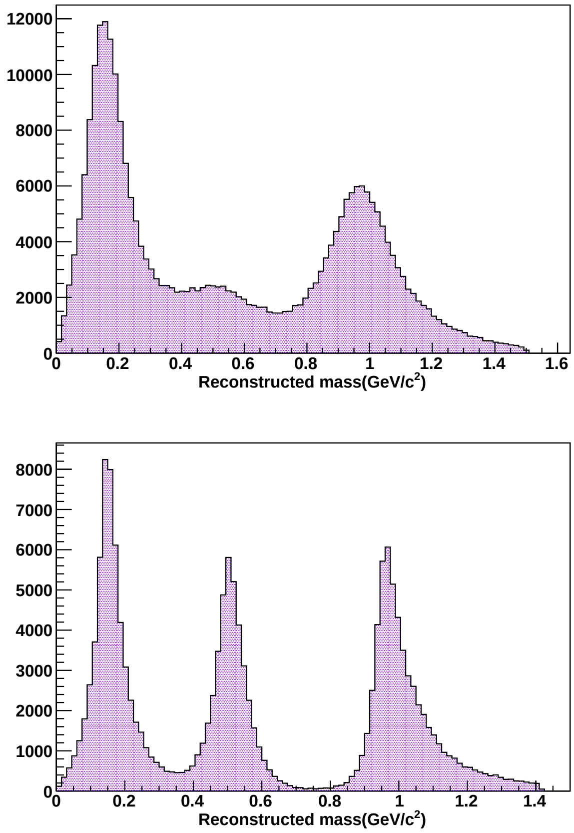

Figure 6.27: Mass reconstruction for positive charged pion, proton and kaons. The time resolution of TOF start detector options are 450 ps (top) and 100 ps (bottom) respectively. The resolution of the reconstructed momentum and length is 1% and 3% respectively. The magnetic field value was reduced to 1 T to increase the detector acceptance.

Furthermore, the contamination of events resulting from background ($\overline{p}$+^{12}C) reactions can also be estimated by applying the method explained above. Fig. 6.28 illustrates the reconstructed mass spectra of kaons, pions and protons particles generated as a result of $\overline{p}$+^{12}C reactions. Panels on the left and right side show the reconstructed mass spectrum assuming a start detector with time resolution of 450 ps and 100 ps, respectively. The particle separation is in the case of a start detector with a 100 ps resolution not well accomplished, maybe due to the small number of kaons in comparison to pions. The percentage of background events tagged considering the option of a start detector with a 100 ps time resolution is 7.7% and for the option of the scintillating fiber detector as start detector the contamination is 5.3%.

Table 8.1 gives an overview of the efficiency of the method, which has been suggested in this work, to tag the production $\Xi^- + \overline{\Xi}^+$ events over the

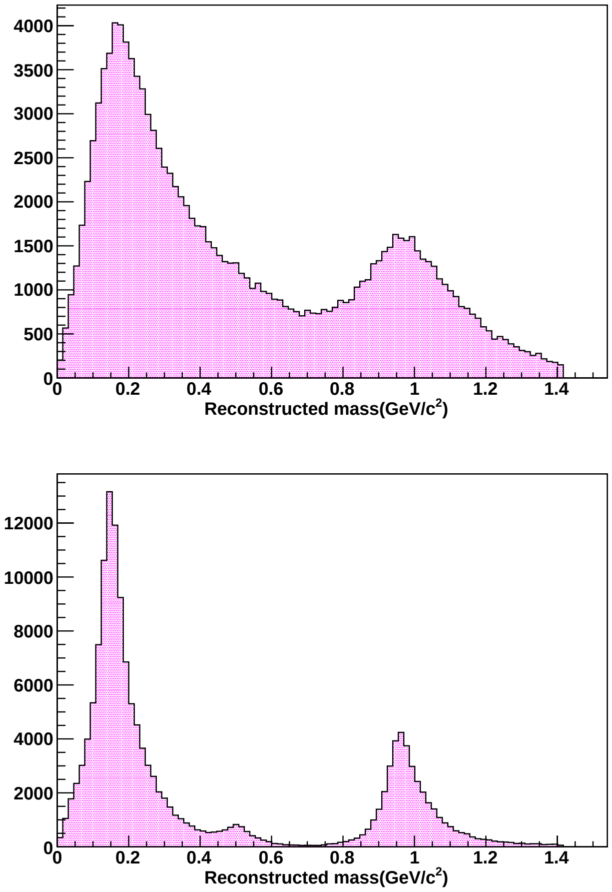

Figure 6.28: Mass reconstruction for positive charged pion, proton and kaons as a result of $\overline{p}$+^{12}C reactions. The time resolution of TOF start detector options are 450 (Top) and 100 ps (bottom), respectively. The resolution of the reconstructed momentum and length is 1% and 3% respectively. For this calculations a sample of 100,000 $\overline{p}$+^{12}C events have been considered.

Table 6.1: Efficiency of the proposed method for the tagging of $\Xi^- + \overline{\Xi}^+$ events over the background reactions ($\overline{p}$+^{12}C). The method is based on the identification of positive kaons produced as a result of the $\overline{\Xi}^+$ in the primary nuclear target

event	% at σ_t=450 ps	% at σ_t=80 ps
$\Xi^- + \overline{\Xi}^+$ (IP = -76.5 cm)	$\simeq$14.	$\simeq$19.
$\overline{p}$+^{12}C (IP = -76.5 cm)	5.3	7.7
$\Xi^- + \overline{\Xi}^+$ (IP = -55.5 cm)	$\simeq$20.	28.3

background resulting from the $\overline{p}$+^{12}C interactions. According to previous estimates [6], a reliable trigger efficiency based on the positive kaon identification would be approximately 40%.

Obviously, the value corresponding to the present setup is below the expected value. Furthermore, one should take into account that previous estimates have been done considering that the interaction point (IP) of the hypernuclear detector setup was placed at the center of the $\overline{\mathsf{P}}$ANDA spectrometer, where the geometrical acceptance is larger than the calculated with the present setup. Actually, due to the present $\overline{\mathsf{P}}$ANDA setup it will be impossible to place the hypernuclear setup so close to the center of the $\overline{\mathsf{P}}$ANDA spectrometer.

An alternative to the present setup for background discrimination could be the use of the energy measurement of the TPC without considering the TOF system.

In summary, one can conclude that a background suppression strategy with the present considerations would not be enough as stand-alone method, and therefore it must be combined with other techniques to improve the efficiency by a factor of two or more.

6.5.4 Radiation damage studies

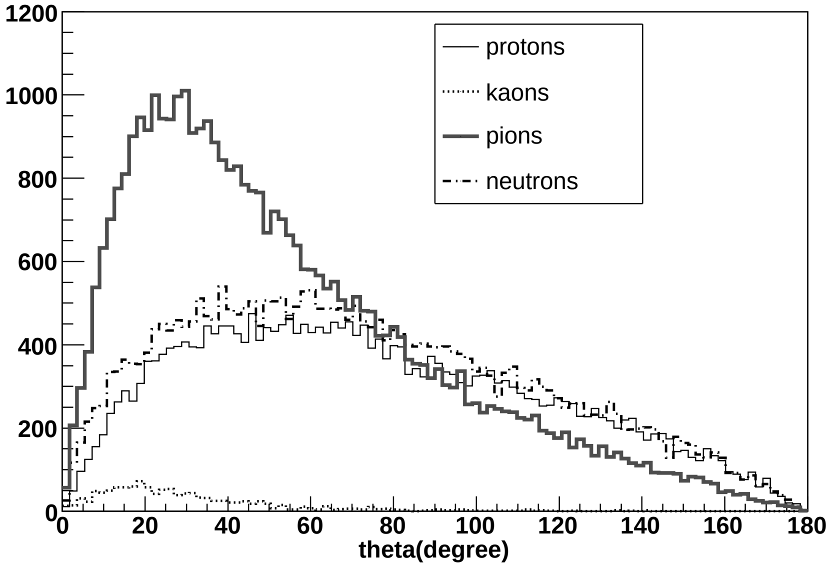

Figure 6.29: Distribution of produced particles from background reactions. The Germanium detectors will be affected mainly by particles emitted at backward axial angle.

In this section the possible radiation damages due the hadronic background reactions in the germanium detector array as well as in the scintillator fibers detectors will be evaluated.

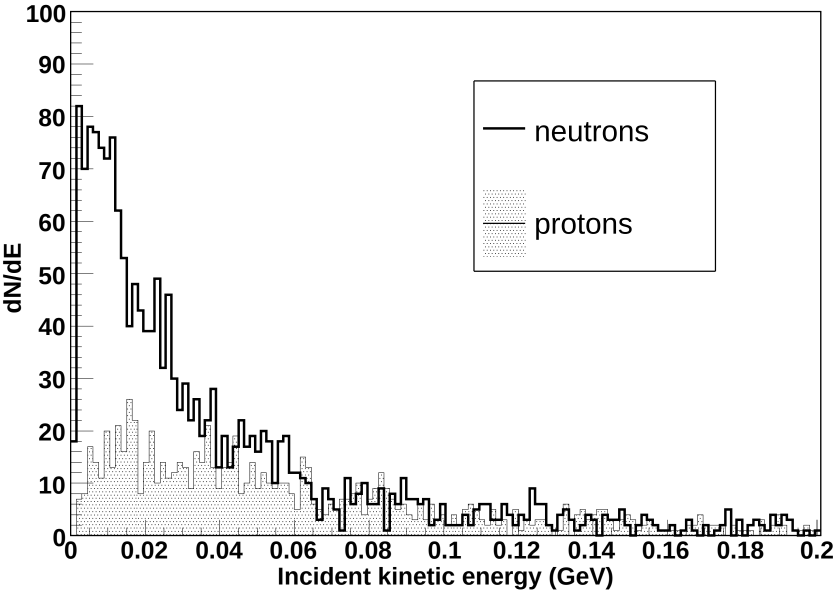

Figure 6.30: Incident kinetic energy of protons and neutrons entering the Germanium detector surface. The main contribution to a possible radiation damage of the detector is provided by neutrons.

Particles produced simultaneously with the double hypernuclei do not significantly disturb the γ-ray detection. The main limitation is the load of the Cluster–array by the high particles rate from uncorrelated background reactions. The $\overline{p}^{12}C \rightarrow \Xi^-\overline{\Xi}$ cross section of 2μb is about a factor 25000 smaller than the total $p\overline{p}$ cross section of 50 mb at 3 GeV/c. Charged particles and low energy neutrons which are emitted into the region covered by the Ge detectors will undergo electromagnetic and nuclear interactions and will thus contribute to the signal of the detector. The total energy spectra in the crystal has been obtained summing up event by event the energy contributions of the particles impinging on the Ge array.

Most of the produced charged and neutrals particles are emitted into the forward region not covered by the Germanium array (see Fig. 6.29). Charged particles emitted into backward axial angles are very low in kinetic energy, and will be absorbed to a large fraction in the material surrounding the primary target.

At an average interaction rate of $3 \cdot 10^6\,\mathrm{s}^{-1}$ UrQMD+SMM calculations of $\overline{\mathrm{p}}+^{12}\mathrm{C}$ interactions at 3 GeV/c momentum predict in the backward hemisphere a total charged and neutral particle rate of $2.3 \cdot 10^7\,\mathrm{s}^{-1}$. Since most of the charged particles emitted into backward axial angles are very low in kinetic energy, most of them will be absorbed in the beam pipe and in the signal cables coming from the silicon sensors of the secondary target.

More critical are neutrons emitted into the backward direction which also contribute to the radiation damage of the detector. Fig. 6.30 shows the kinetic energy distribution of protons and neutrons entering the surface of the Germanium detectors.

An n-type Germanium detector is expected to withstand a fast neutron fluence of about $4 \cdot 10^9/\mathrm{cm}^2$ without major degradation [215, 216, 214]. A reasonable operation may still be possible up to a neutron fluence of $10^{10}/\mathrm{cm}^2$. Assuming a distance of approximately 30 cm between the primary target and the Germanium detectors and an interaction rate of $3 \cdot 10^6\,\mathrm{s}^{-1}$ one finds a load of fast neutrons on the Germanium detectors of about $4\,000\,\mathrm{n}/\mathrm{cm}^2$. Taking no further precautions this would allow a continuous operation of about 30 days before an annealing procedure has to be performed.

In addition, the same simulation sample has been used to evaluate possible radiation damages on the scintillation fibers array readout electronics. Because of the forward peaked character of the proton and neutron background observed in Fig. 6.29, the arrangement of the readout electronics must be placed in the backward angle direction.

Accordingly, an integrated irradiation fluence at the SiPM location has been estimated to be around $2.3{\cdot}10^4$ neutrons + protons/s with an average nucleon kinetic energy of 25 MeV. Furthermore, radiation hardness studies have been performed [137] at the MAMI [42] accelerator facility, by exposing a sample of $1\,\mathrm{mm}^2$ SiPM manufactured by Photonique and composed of 500 APD to a beam of 14 MeV electrons.

Using the electron irradiation results radiation damage on the SiPM devices can be predicted by considering the non-ionizing energy loss (NIEL) of protons and neutrons distributed according to the simulated spectra. The resulting mean value of $7{\cdot}10^{-3}$ MeV·cm2/g (almost equal for both hadrons) has to be compared to $1.1{\cdot}10^{-4}\,\mathrm{MeV}{\cdot}\mathrm{cm}^2/\mathrm{g}$ for electrons implying that hadronic damage will be 64 times stronger. A fluence of $8{\cdot}10^7$ (12 days of operation at $5{\cdot}10^6$ collisions/s) will result in a degradation as shown in Fig 6.31.

Furthermore, annealing recovery was studied by heating the irradiated SiPM at 80^O C during two weeks. Only a partial recovery was observed. No further improvement was obtained by longer heating periods. In conclusion, the use of this specific type of SiPM is not recommended for an application in the $\overline{\mathsf{P}}\mathsf{ANDA}$ radiation environment.

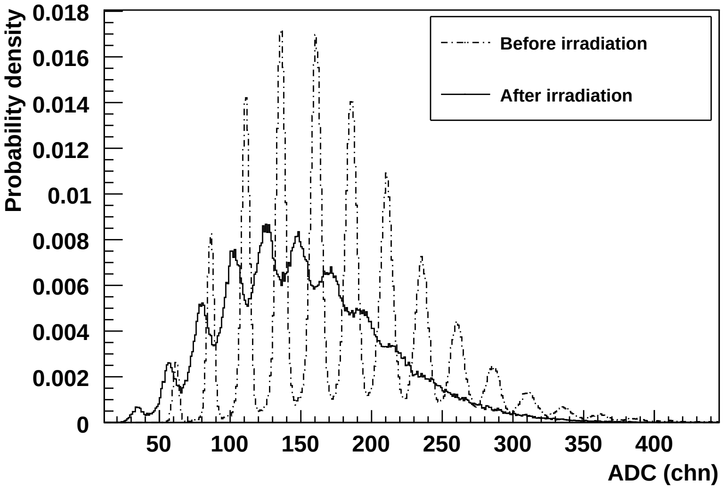

Figure 6.31: ADC spectra for low amplitude signals from green sensitive Photonique SiPM before and after irradiation with $3{\cdot}10^9$ electrons [137].

Chapter 7

HPGe Detector operating in magnetic field

High resolution γ-ray spectroscopy based on high-purity germanium (HPGe) detectors represents one of the most powerful experimental tools in nuclear physics. The introduction of this technique led to a significant progress in the knowledge of nuclear structure. It has been recently proven that also strangeness nuclear physics can benefit from the same advantages: the energy resolution of hypernuclear levels has been drastically improved from 1–2 MeV to a few keV in FWHM [196, 197].

The success of such a technique has encouraged other groups working on $\overline{\mathsf{P}}\mathsf{ANDA}$ at FAIR [199, 200] to investigate whether this technique could be extended and incorporated in their set-ups. The $\overline{\mathsf{P}}\mathsf{ANDA}$ magnetic spectrometer has a cylindrical geometry and is built around the target region covering a large solid angle ($\Omega \approx 4\pi\,\mathrm{sr}$). To maximize the detection efficiency HPGe a-rrays are to be mounted near the target region, implying the operation of these detectors in a strong magnetic field (up to $B \approx 1\,\mathrm{T}$).

The aim of the work described in this chapter is to study the feasibility of using HPGe detectors in high magnetic fields and to study the associated effects on their energy resolution as well as the study of eventual pulse shape distortions.

7.1 Germanium Detectors in magnetic fields

Germanium detectors which are typically used in low energy nuclear spectroscopy (see e.g. [203, 204]) are seldom operated in magnetic fields [206] and their behaviour under such conditions has been not well known in the past. Generally the deflection of the charge carriers in the magnetic field and the Penning effect in the vacuum surrounding the semiconductor can play a substantial role for the operation of large volume semiconductor devices in high magnetic fields.

For extended detector volumes and hence long drift paths the deflection of the charge carriers in the magnetic field may result in a larger rise-time of the signal due to longer drift paths or enhanced trapping and detrapping. By using standard shaping amplifiers the output signal reflects then the interplay between charge collection process and the transfer function of the amplifier. In practice an enhanced charge collection time will cause a reduction of the output signal even though the complete charge is collected eventually.

In case of trapping the timescales involved may be significantly larger than the typical time constants of the electronic network and this reduction is referred to as a ballistic deficit [207]. Sometimes this term is also used in a more general meaning [208, 209] for any decrease of the output signal due to an enhanced signal rise-time irrespective of its origin. In any case the associated larger fluctuations of the signal rise-time will deteriorate the energy resolution.

Trapping of charge carriers and losses due to recombination depend on the type of the germanium. In the case of n-type germanium detectors which are studied in the present work trapping is expected to be less significant than in p-type germanium detectors. Nonetheless, a reduction of the signal may be particularly important in the case of major radiation damages of the crystal lattice (see e.g. [205]).

The bending force of the magnetic field causes charged particles produced within the volume between the Ge crystal and the capsule to spiral around the field lines. The longer travel times of the rest gas ions may result in an enhanced Penning effect. The interaction of electrons with the residual gas within the capsule may cause secondary ionisation leading eventually to discharges.

The generation of an electric field perpendicular to the magnetic field lines and the direction of the current (Hall effect) may affect small electronic components carrying large currents. While the wide spread use of silicon detectors and their associated readout electronics in tracking systems demonstrates the feasibility to operate highly integrated electronic devices in high magnetic fields (see e.g. [210, 211, 212, 213]), the effect on the electronics of high resolution devices like HPGe detectors has not been studied yet.

7.2 Experimental Details

To verify that HPGe detectors can be safely and efficiently operated in a high magnetic field, two different kinds of detectors have been tested: the EUROBALL Cluster detector [214] and the VEGA detector [217].

7.2.1 The Euroball Cluster Detector

The EUROBALL Cluster detector consists of seven large hexagonal, n-type, closely packed, tapered Ge crystals housed in a common cryostat [214]. The crystals have a length of 78 mm and a diameter of 70 mm at the cylindrical back-end. To protect the sensitive intrinsic surface of the detectors and to improve the reliability each crystal is encapsulated. The capsules are made of aluminium with a thickness of 0.7 mm. The distance of the Ge surface to the inner wall of the capsule is only 0.7 mm which gives a distance of $3.0 - 3.5$ mm between the edges of two neighbouring detectors in a cluster. Each capsule is hermetically sealed by electron beam welding of the capsule lid.

The vacuum is maintained by a getter material which is active up to the temperature of 150^o C. The cold part of the preamplifier is mounted on the capsule lid. The detector has a typical energy resolution of 2.1 keV (FWHM) at 1.332 MeV for a ^{60}Co source using an AC coupled preamplifier. The AC coupling was chosen in order to operate the detector capsule on ground potential which facilitates the close packing and the cooling of several detectors in a common cryostat. Since the seven crystals in the cluster are identical, only three crystals were taken as a representative for the measurements.

7.2.2 The segmented clover detector, VEGA

The super-segmented-clover detector VEGA [217] consists of four large coaxial n-type Ge crystals which are four-fold electrically segmented. The crystals have a length of 140 mm and a diameter of 70 mm. They are arranged in the configuration of a "four-leaf" clover, and housed in a common cryostat. The core contact is AC coupled and the segments are DC coupled. The preamplifier used in the VEGA detector are similar to the one operated with the Cluster detector. Three crystals (B, C and D) and all four segments of one of the three (crystal B) were used in the present work. Prior to the studies in a magnetic field the energy resolution of the detectors was measured in the laboratory with a ^{60}Co source to be about 2.2 keV (FWHM) at 1.332 MeV.

7.2.3 Experimental set–up

Two series of measurements have been performed using the ALADiN dipole magnet [218]. For both series the HPGe detectors and a ^{60}Co γ-ray source, with an activity of 370 kBq, were positioned inside the magnet with the source placed in front of each detector. The ALADiN magnet aperture of $1.5 \times 0.5\,\mathrm{m}^2$ restricts to place a detector with its geometrical axis in the horizontal plane of the magnet. The direction of the magnetic field lines was perpendicular to the geometrical detector axis as shown in Fig. 7.1 (right). The magnetic field is maximal in the centre of the magnet and decreases along the z-direction as

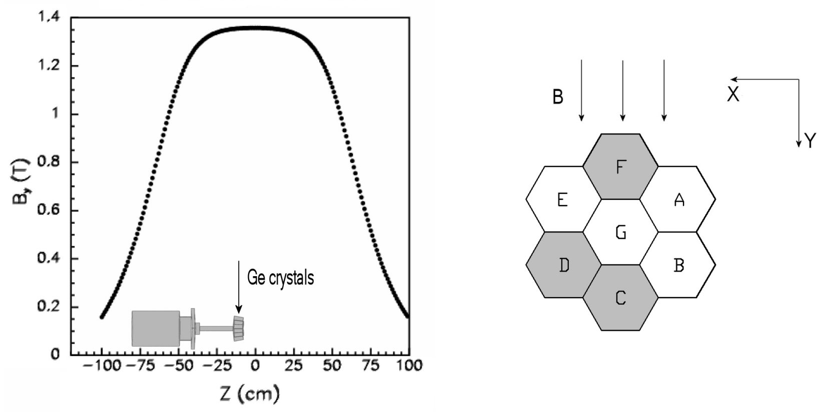

Figure 7.1: Illustration of the EUROBALL Cluster orientation inside the ALADiN magnet. The left panel shows the Cluster position inside the magnetic field and the calculated field map along the z-direction for 1800 A coil current. The right panel shows the end-cap of the Cluster, where the shaded crystals F, D, and C represent those which have been used during the measurements.

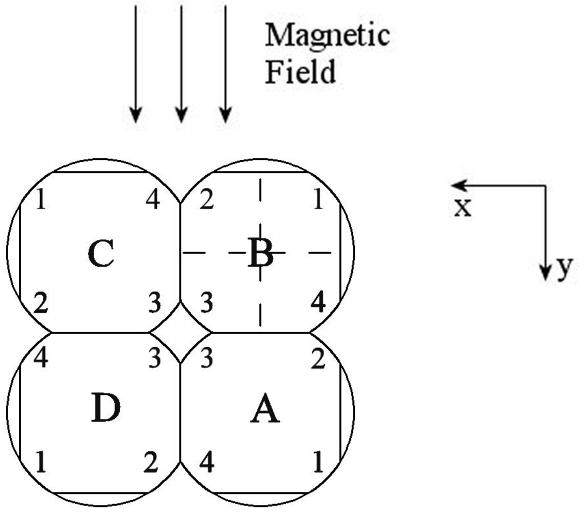

Figure 7.2: Illustration of the end-cap of the VEGA detector in clover geometry and its orientation inside of the ALADiN magnet. All four segments labelled by the numbers 1, 2, 3 and 4 of channel B were read out individually with a Flash-ADC.

illustrated in Fig. 7.1 (left). The detector end-caps have been placed as close as possible to the centre of the magnet in order to expose the germanium crystals to the highest magnetic field (about 7 cm from the centre as shown in Fig. 7.1).

The ^{60}Co source was placed at a distance of 27 cm and 20 cm away from the end-cap of the EUROBALL Cluster and VEGA detector, respectively. Fig. 7.1

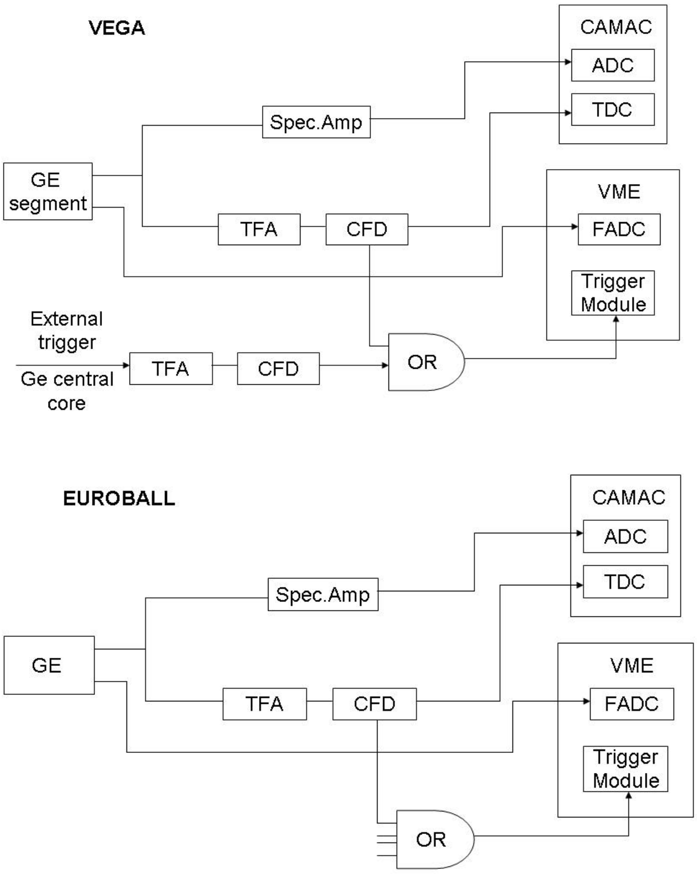

Figure 7.3: Scheme of the read-out electronics of VEGA (top) and Euroball cluster (bottom) detectors.

shows the scheme of the crystals inside the Cluster detector in the right panel. For the measurements with the EUROBALL Cluster three channels (C, D, F) out of the seven Ge crystals of the Cluster have been used. Channels C and D were fed with a voltage of 4000 V and channel F with 3500 V.

For the measurements with the VEGA detector data from three (B, C, D) of the four Ge crystals have been analysed. The geometry of the crystals of VEGA detector inside the magnet is shown in Fig. 7.2. They have been fed with voltages of 4000 V. The measurements can be divided in two groups: measurements done without magnetic field and those in which the magnetic field was tuned to 0.3 T, 0.6 T, 0.9 T, and 1.4 T for the EUROBALL Cluster detector and to 0.6 T, 1.1 T, 1.4 T, and 1.6 T for the VEGA detector.

For each EUROBALL Cluster channel (C, D, and F) one of the preamplifier outputs was split in two signals. One signal was fed to a spectroscopy amplifier (Ortec 572) with 3 μs shaping time, which output was digitised by an Analog-to-Digital converter (ADC Silena 4418/V, 8 channel, 12 bit resolution) and the second signal was fed to a VME 100 MHz Flash-ADC (FADC SIS3300, 8 channel, 12 bit resolution). The other output from the preamplifier was sent to a Timing-Filter-Amplifier (TFA Ortec 474), whose output was discriminated by a Constant-Fraction-Discriminator (Ortec CF 8000) to be used as a timing signal. The trigger was formed by a logic OR of the outputs from the three CFD channels. The ADC was read out via CAMAC bus.

Since the VEGA crystals are electrically segmented, the readout electronics differs from that corresponding to an EUROBALL Cluster in the trigger signal. One output of the preamplifier (core signal) for each channel was split in two branches as it was done for the EUROBALL Cluster set-up. Those preamplifier outputs corresponding to the the four segments of channel B were fed to the FADC. The trigger is formed from a coincidence of the logic OR of the CFD outputs of the four segments and an external trigger determined from the central core signal of channel B (see Fig. 7.3 for a detailed view).

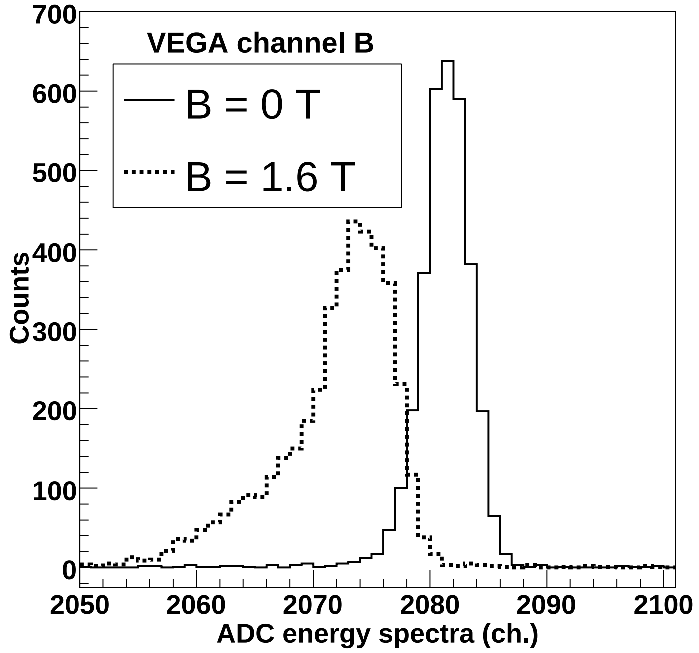

Figure 7.4: Pulse height spectra for the 1.332 MeV ^{60}Co γ-ray line measured with VEGA channel B at different values of the magnetic field. The continuous line presents the pulse height spectrum for the measurement without magnetic field and the dashed line the pulse height spectrum at a field of 1.6 T.

7.3 Data analysis

The analysis presented in this section is focused on the determination of the energy resolution from the pulse height spectra of both detectors by using conventional analogue electronics and on the study of the dependence of the pulse shape sampled by an FADC in magnetic fields. A detailed study on HPGe detectors operating with high rates in magnetic fields, based on the observation of pulse shapes, will be also discussed briefly.

Pulse height spectra taken with a shaping amplifier are presented in Fig. 7.4 for the 1.332 MeV ^{60}Co γ-ray line. Obviously, the line shape at $B = 1.6\,\mathrm{T}$ (dotted histogram) is significantly different from the line shape measured without field (solid histogram). The influence of the magnetic field causes a tail on the low-energy side.

Two different methods were used to extract the energy resolution of the detectors depending on whether the spectra were measured in a magnetic field or not. Since in absence of a magnetic field the line shape of all detectors is very close to a single Gaussian distribution, the pulse height spectra have been parametrised by Gaussian function.

In case the magnetic field was non-zero, the convolution of a Gaussian distribution and an exponential decay function was chosen to describe also the tail on the low-energy side of the peak. The observed line shape was fitted by a full absorption-peak superimposed on a quadratic background. The functional form used is

$$y_{a\otimes b} = c \cdot \exp(\frac{(x - x_0)}{\beta}) \cdot ERFC(\frac{(x - x_0)}{\sqrt{2} \cdot \sigma} + \frac{\sigma}{\sqrt{2} \cdot \beta}) \qquad (7.1)$$

, where $ERFC$ is the complement of the error function, x is the channel number, x_0 and σ are the centroid and the standard deviation of the Gaussian, β is the decay constant of the exponential and corresponds to the "skewness" of the skewed Gaussian.

The energy resolution was extracted from the pulse height spectra by parameterising the 1.332 MeV γ-ray full-absorption peak from a ^{60}Co source. From the parameterised line shape the value of Full-Width Half-Maximum (FWHM) was extracted. The dependence of the energy resolution (FWHM) on the strength of the magnetic field is shown for the EUROBALL Cluster as well as for the VEGA detector in Fig. 7.5. The energy resolution of one of the EUROBALL Cluster crystals is worse than the resolution of the two other crystals of the same detector because of pick-up noise in its electronic readout. In addition, the peak maximum of the γ-ray line shifts towards smaller energies with increasing field strength as shown in Fig. 7.6.

In order to clarify the question whether the shifts of the energy peak are due to a loss of charge carriers or whether this shift is caused by the interplay between an increased charge collection time in the germanium detector and the transfer function the FADC signals have been studied. For the sake of clarity, only results concerning the analysis of the VEGA detector FADC signals will be shown.

Fig. 7.7 shows the averaged pulse shape signals for 1.332 MeV γ-rays measured at zero magnetic field (solid line) and at $B = 1.6\,\mathrm{T}$ (dashed line). The two signals have been obtained by averaging over 5000 events each. Within the two time intervals of [0, 0.5 μs] and [3 μs, 4 μs] one finds mean amplitudes of 2056.7 (2065.7) and 1353.9 (1362.9) for $B = 0\,\mathrm{T}$ ($B = 1.6\,\mathrm{T}$), respectively.

Despite a very different shape of the rising edge, the difference between the initial baseline and the signal level at later times stays nearly constant at a value of about 702.8 . This indicates that the recombination or long-time trapping of charges cannot account for the reduced energy signals presented in Fig. 7.6.

As can be seen already in Fig. 7.7, the pulse shape is modified by the magnetic field. Fig. 7.8 shows the distribution of the rise time (defined as the time it takes for the pulse to rise from 10 % to 90 % of its full amplitude) for different values of the magnetic field for the VEGA detector. A significant change of its mean value by approximately 200 ns and a broadening of the distribution can be observed.

The ratio R between the mean rise time and the root mean square value decreases from values above 4 at low magnetic fields to 3.0 at $B = 1.6\,\mathrm{T}$. This behavior is opposite to what is expected for a purely diffusive motion of the charge carriers. In the latter case an increase of R proportional to the square root of the rise time would have been expected.

The simultaneous large shift and the broadening of the rise time distributions on one hand, and the rather similar asymptotic values of the pulses seen in Fig. 7.7 on the other hand suggest that the incomplete signal integration by the main amplifier is the main origin of the observed energy shift.

To verify the latter conjecture, the dependence of the amplifier transfer function on the variation of the rise time has been investigated with a pulse generator. This study confirmed that the rise-time variations due to the magnetic field influence are the main source of the energy shift seen in Fig. 7.6. An integration time of more than 3 μs could be needed to avoid an incomplete charge integration of the amplifier, however, the noise level may be increased in addition.

In order to explore the possibility to correct the shift of the pulse height by measuring the rise time event-by-event we show in Fig. 7.9 the correlation of the deduced γ-ray energy and the rise time for different magnetic fields. These distributions have been obtained event-by-event for the 1.332 MeV γ-line of one of the segments of VEGA channel B.

For all magnetic fields the low-energy tail of the γ-ray peak (see Fig. 7.4) is associated with an increased rise time. The strong correlations observed in Fig. 7.9 provides a characterisation of the amplifier at different values of the rise time.

The fit of a parabolic function to the correlation (see dark lines in Fig. 7.9) enables the correction of the energy spectra event-by-event for different magnetic fields. The correction functions are similar for all measurements at non-zero magnetic field, but they are shifted relative to that of the measurement at $B = 0\,\mathrm{T}$. Presently the origin of this strong shift is not understood.

Fig. 7.10 shows the corrected γ-ray energy spectra (dashed line) for VEGA channel B at 1.6 T in comparison to the one without correction (hashed). A significant improvement in the peak shape has been obtained. After applying this correction of the pulse height spectra, an improvement on the energy resolution for VEGA channel B as well as for EUROBALL Cluster channel C has been achieved as shown in Fig. 7.5. The open triangles in Fig. 7.5 represent the energy resolution for both detectors after this correction.

Furthemore, attempts regarding the analysis of the preamplifier signal alone has been also considered. The scope of this analysis is the extraction of the energy resolution from the preamplifier signal by using digital signal processing. However, the 2.2 keV of energy resolution could not be recovered under these circumstances (See more details in Appendix A.3). Indeed a longer FADC sampling would be needed in order to recover the standard value of the energy resolution for the VEGA detector.

7.3.1 High Rates measurements

The application of Germanium detectors is usually restricted to the low counting–rate environments as larger, high efficiency, crystals have longer charge collection times($\leq 1\,\mu$s). To achieve maximum energy resolution of germanium detectors from preamplifier is shaped to the Gaussian form with shaping time from 3 to 6 μs. The resulting total width of formed pulse is larger than 10 μs. This fact increases a probability of events piled up at rates per crystal higher than few tens of kHz, which is expected at $\overline{\mathsf{P}}\mathsf{ANDA}$. The pulse–shape analysis of the preamplifier signal was chosen to overcome this problem.

To study the influence of high rates on germanium detectors the following setup has been arranged. One representative crystal of the EUROBALL Cluster detector was exposed to ^{22}Na and $^{57,60}Co$ γ–ray sources in a sequence of measurements, achieving 1.5, 34, 110 kHz counting rate by changing the distance to the radiactive sources. The preamplifier signal was split into two separate branches. The first “analog” branch (A) consisted of timing filter and spectroscopic (SA) amplifiers, CAMAC peak–sensing ADC and constant–fraction discriminator. To achieve the best energy resolution the shaping time of SA was set to 3 μs. The second “digital” branch (D) consist of 100 MHz 14 bit flash ADC SIS3301. Flash ADC was used to store pulse traces which were later processed off–line. The length of the traces was chosen to be 1.3 ms and 100 μs for high and low rate measurements, respectively. The obtained traces were filtered by the moving window deconvolution (MWD) algorithm [219], what it has been described in Appendix A.3. However, MWD does not allow to measure the height of two neighbour pulses if they are closer in time as length of the filter. To overcome this limitation the digitalised signals were analysed by several filters with different length. Depending on the distance between neighbour pulses(*dt*) analyses program selected output value of the filter with maximum length but less than *dt* . The output of such analysis consists of energy, time and filter length information for each event. This allows to achieve maximum energy resolution in high–rate conditions as for each event shaping with optimal time constant is applied. Further in the text such analysis is referred as Multi–MWD (MMWD) [191]. Resulting energy resolutions (FWHM at 1332 keV, ^{60}Co) and fraction of rejected pulses measured for both branches are shown in table 8.3:

Counting rate (kHz)	Energy resolution keV		pulse rejection %	
brach:	A	D	A	D
1.5	2.4	2.4	0	0
34	2.5	3.0	21	9
110	2.7	3.4	71	18

The analog branch provided better energy resolution, however the probability of events piled up in analog branch drastically increases with counting rate. Figure 7.11 shows γ–ray spectra obtained at 110 kHz rate. Due to pile up resolving the D branch provided higher peak to background 11.7 in comparison to the 2.6 obtained with analog ADC (for 1332 keV ^{60}Co line).

The results of the test measurements show that the application of digital pulse shape analysis is very efficient for high counting rate environments.

7.3.2 Angular dependence

One could expect a dependence on the orientation of the detector with respect to the magnetic field. The energy resolution of the VEGA detector was also measured for different angles between the detector's axis and the magnetic field in order to investigate a possible angular dependence in the energy resolution. In particular, the energy resolution has been measured for the maximum magnetic field value (1.6 T) and without magnetic field. For technical reasons, the sensible part of the detector had to be placed at a distance of about one meter from the center of the magnet, corresponding to a lower field ~ 0.3 T, at an angle of 30°.

channel C (keV)	channel D (keV)	channel B (keV)	mag. field (T)
3.2	3.03	2.99	0.3
3.17	3.13	2.74	0

Table 8.2 summarises the results obtained. Differences are within the errors, indicating no deviation at 30° for a low magnetic field. Also for larger angles ($\sim 45°$) the magnetic field at the detector's position was too low to observe any dependence.

7.4 Discussion and Conclusion

Two important effects have been observed by operating HPGe detectors in high magnetic fields: a small degradation of the energy resolution and a change of the pulse shape of the preamplifier signal.

All crystals of both detectors show a similar behaviour in the magnetic field with an energy resolution degradation of about 1–2 keV. However, the resolution is still sufficient to perform γ-ray spectroscopy on hypernuclei. The asymmetry of the line shape appears as a low-energy tail in the pulse height spectra in Fig. 7.4. Moreover, the mean value of the energy spectrum exhibits a shift to low energies as shown in Fig. 7.6. The measurements have been performed over a period of two days without observing any problems in the electronics or sparking effects. After the measurements the original energy resolution was recovered.

A significant shift and broadening of the rise times distribution has been observed in the presence of a high magnetic field. This observation reflects the effect of the magnetic field on the charge collection process itself.

The observation of a strong correlation between the measured pulse height measured with analogue electronics and the rise time measured by a FADC for various magnetic field strengths reveals the change in rise time as the major contribution to the degradation of the energy resolution. Employing this correlation for a rise time correction of the energy allows to almost recover the original energy resolution. The remaining degradation at fields larger than 1 T amounts to approximately 0.5 keV.

One could expect a dependence on the orientation of the detector with respect to the magnetic field. In the present case a complete test of the orientation of the detector could not be carried out because of technical limitations: the aperture of the ALADiN magnet does not allow to freely rotate the axis of the detector. The set-up of the HPGe detectors in the future $\overline{\text{P}}$ANDA experiment requires a further test with the magnetic field orientation almost parallel the detector axis.

Finally, even though ALADIN being a resistive magnet it was not possible to reproduce a quencing situation, the behaviour of the VEGA detectors was monitored during a fast decrease of the current in the magnet from its maximum value (2400 A) to zero without observing any effect or detecting any damage.

The HPGe detectors were found to operate well in magnetic field conditions similar to those to be expected in future hypernuclear experiments at $\overline{\mathsf{P}}\mathsf{ANDA}$. However, the detectors used in the present work are coupled to huge dewars for their cooling with liquid nitrogen. These dewars have been the main obstacle for the study of the dependence of the energy resolution on the orientation of the detector in the magnetic field of ALADiN. Furthermore they affect the detector integration in $\overline{\mathsf{P}}\mathsf{ANDA}$ magnetic spectrometers. In order to circumvent these problems an electromechanical cooling system coupled to few encapsulated HPGe crystals is currently under development.

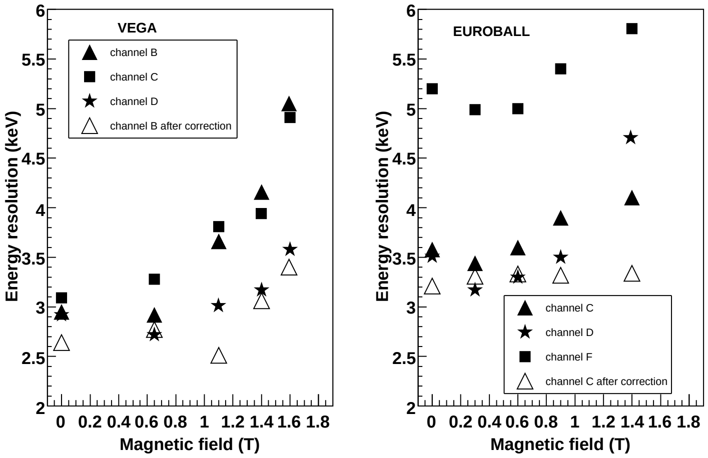

Figure 7.5: Measured energy resolution (FWHM) for the 1.332 MeV γ-line of VEGA and EUROBALL Cluster detectors in a magnetic field B. The resolution of EUROBALL channel F was worse because of noise pick-up. The empty symbols represent the improved energy resolution after the correction of the energy spectra for channel B and C, respectively(see text). Statistical errors for the values are smaller than the symbol size.

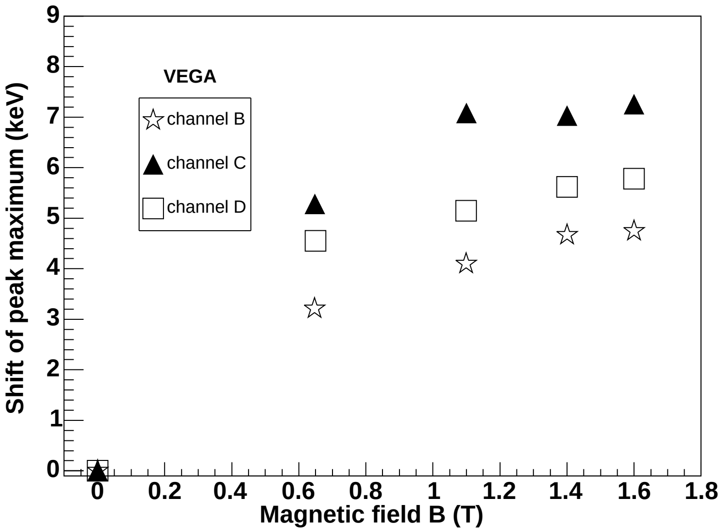

Figure 7.6: Shift to smaller energies of the 1.332 MeV γ-line peak maximum of the VEGA detector in a magnetic field B.

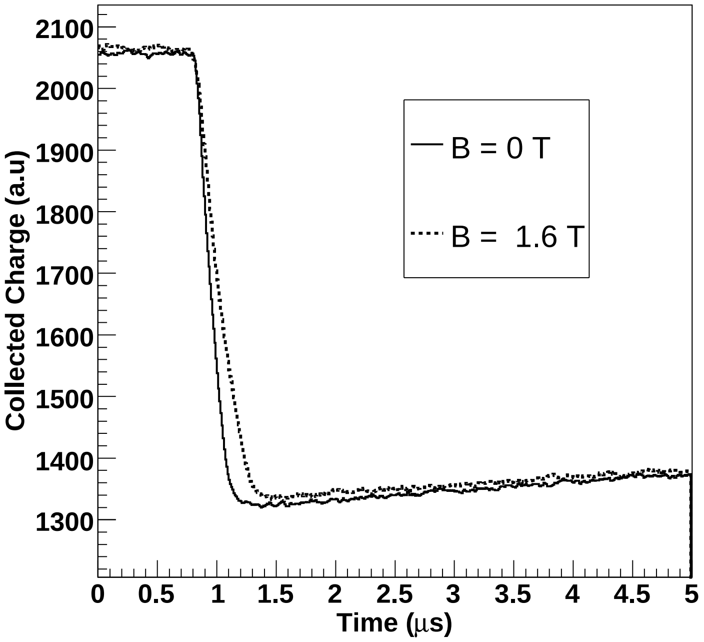

Figure 7.7: Averaged preamplifier outputs signals of VEGA channel B for the 1.332 MeV γ-ray measured at a magnetic field of $B = 0\,\mathrm{T}$ (solid line) and at $B = 1.6\,\mathrm{T}$ (dashed line). The two pulse shapes signals have been obtained by averaging over 5000 events each.

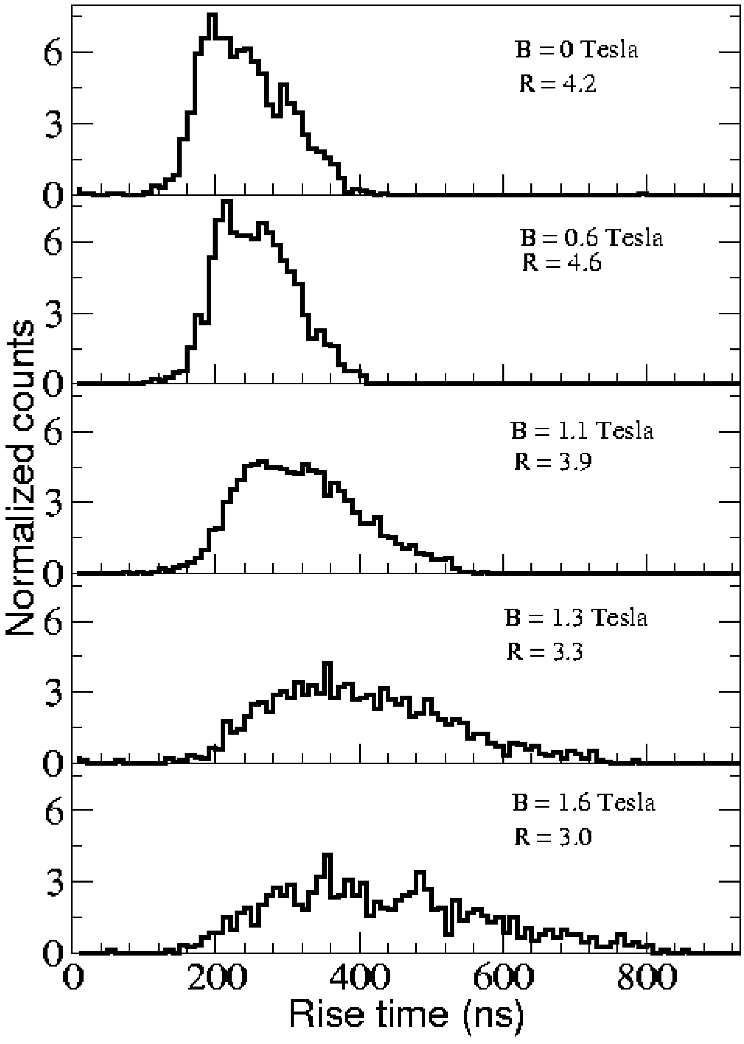

Figure 7.8: Measured rise time distribution for the 1.332 MeV γ-line of one of the segments of VEGA channel B in a magnetic field B. R gives the ratio between the mean value and the RMS value of the rise time distributions. Each distribution has been normalized by its integral.

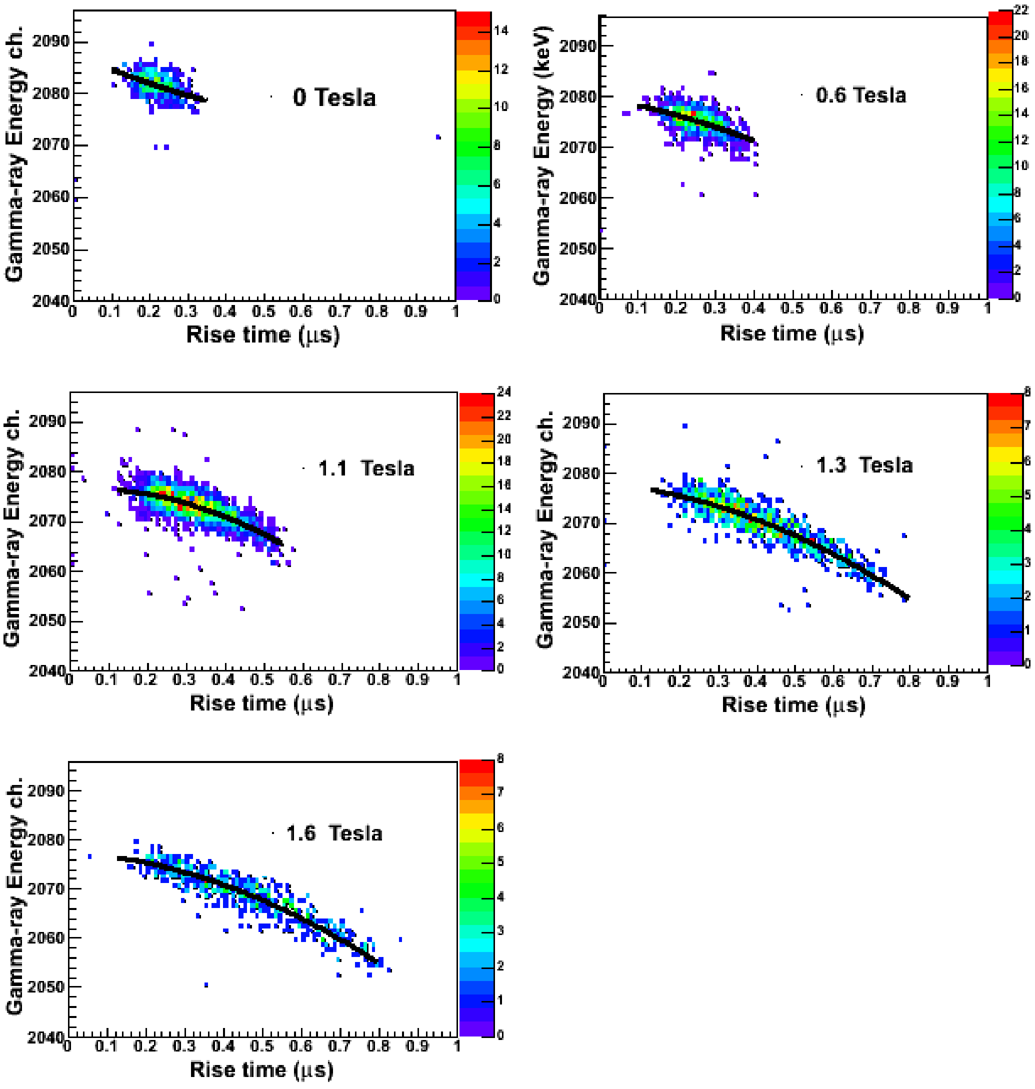

Figure 7.9: Correlation between the energy in channels and the rise time for the 1.332 MeV γ-rays of one of the segments of VEGA channel B in a magnetic field. The black line represents the parabolic fit function of each distribution at different values of the magnetic field.

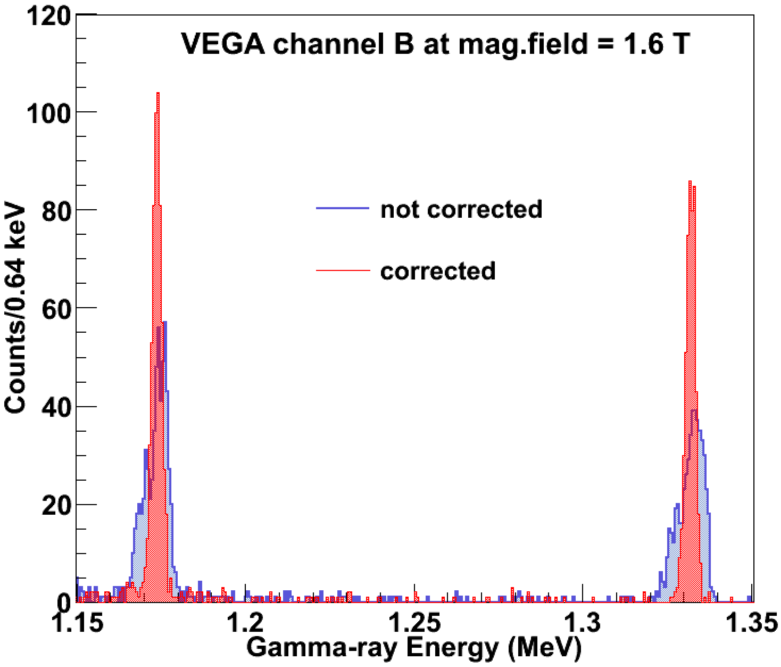

Figure 7.10: Two γ-ray energy spectra for ^{60}Co measured with VEGA channel B at maximum value of the magnetic field. The blue spectrum presents the pulse height spectrum for the measurement without correction and the red spectrum the corrected pulse height spectrum at a field of 1.6 T. Both spectra have been individually calibrated.

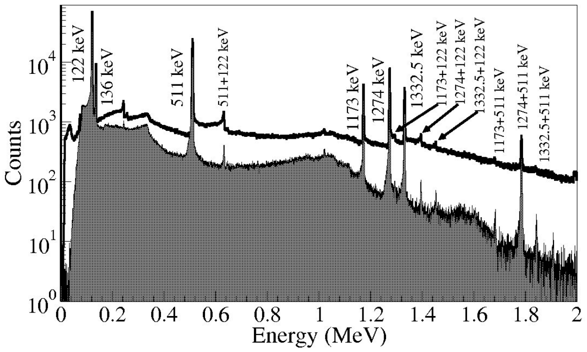

Figure 7.11: Gamma–ray spectrum of mixed calibration source of $^{57,60}Co$ and ^{22}Na obtained at 110 kHz counting rate by means of analog electronics (bold line histogram) and digital signal processing (shaded–area histogram). Spectra were normalised to the area of 1332.4 keV peak [191].

Chapter 8

Conclusions and Outlook

In summary, in the present work, the feasibility of performing high precision γ spectroscopy of double Λ hypernuclei at the PANDA experiment has been studied by means of a Monte Carlo simulation.

The simulation has to provide solutions to circumvent the problems due to the high hadronic environment and the space limitations in the backward beam direction of the $\overline{\mathsf{P}}$ANDA spectrometer. The main challenges for the hypernuclear project are,

- to produce enough statistics to perform gamma spectroscopy, in particular, the production of double hypernuclei in excited states must be significant.
- the reduced space in the backward beam direction of the $\overline{\mathsf{P}}$ANDA spectrometer to place the hypernuclear detector setup.
- radiation hard damages on the hypernuclear detectors, in particular the detectors dedicated for gamma spectroscopy.
- to provide reliable tracking algorithm for low momentum particles (charged decay products of hypernuclei).

For this issue, the designing and simulation of a devoted detector setup as well as of the mechanism to produce double Λ hypernuclei have been optimized together with the physics performance of the whole system.

The hypernuclei production mechanism has been performed by using two different event generators interfaces. The first stage of the production chain, the $\Xi^-\overline{\Xi}$generation, has been accomplished by the Intra Nuclear Cascade Model (INC) and an extension of the UrQMD code (UrQMD+SMM). Contrary to the INC, the UrQMD+SMM can generate high statistics, and the rate of Ξ^- is almost a factor of 10 larger.

For the second step, the statistical decay of a Ξ^--hypernuclei after the capture and the conversion into two Λ's is accomplished within a statistical decay model.

For the simulation, the PANDARoot software have been extended to enable the complete definition of the hypernuclei particles. Some assumptions have been done to implement the hypernuclei decay modes. In the case of the electromagnetic decay mode, it has been considered that all excited states decay to the ground state, and intermediate transitions are not taken into account. Also in case of the weak decay, only the pionic weak decay was considered. Further improvements of these calculations include a proper treatment of the hypernuclear decay modes.

Based on these simulations results, a micro ribbons made of ^{12}C target has been proposed as the best option for the primary target. The production rate achieved with this target is about $3 \cdot 10^6 \mathrm{s}^{-1}$.

In addition, the option selected for the geometry of the secondary active target is the one consisting of a compact structure of 26 mm thickness, with 20 layers of silicon strip detectors with alternating layers of absorber material. However, the simulation has shown that the present amount of material (17% of the total radiation length) can reduce the momentum resolution of low momentum particles. As a consequence, a future design could consist of only of 2 layers of absorber material and 5 layers of silicon (2.6% of the total radiation length). In addition, further improvements of this setup has to be evaluated together with realistic tracking algorithms. These improvements regard the energy losses and multiple scattering of the particles passing through the secondary active volume. Moreover, a reliable tracking algorithm have to be studied for the tracking of low momentum particles.

To perform gamma spectroscopy a germanium detector array has been suggested. The present setup of this detector has also been successfully tested within the simulation under the high hadronic environment of $\overline{\mathsf{P}}\mathsf{ANDA}$. Additionally, the energy resolution of the proposed germanium detectors (EUROBALL and VEGA) have been studied under the presence of the magnetic field. The results have shown no significant change for the energy resolution and any problem in the electronics or sparking effects was observed.

Moreover, a correlation between rise time and the pulse shape is used to correct almost completely the measured energy. Furthermore, a electromechanic cooling system coupled to few encapsulated HPGe crystals is currently under development. This option should help to circumvent the problems due to the limited space in the interior of the $\overline{\mathsf{P}}\mathsf{ANDA}$ spectrometer. In the present work, the electronic response of the germanium detectors have modeled by smearing with the expected energy resolution. Improvements regarding a complete simulation of the electronic signal in these detectors are also foreseen.

The production yields of hypernuclei in excited, particle stable states has been evaluated within the already statistical decay model for various nuclear

Table 8.1: Efficiency of the proposed method for the tagging of $\Xi^- + \overline{\Xi}^+$ events over the background reactions ($\overline{p}$+^{12}C). The method is based on the identification of positive kaons produced as a result of the $\overline{\Xi}^+$ in the primary nuclear target

event	% at σ_t=450 ps	% at σ_t=80 ps
$\Xi^- + \overline{\Xi}^+$ (IP = -76.5 cm)	$\simeq$14.	$\simeq$19.
$\overline{p}$+^{12}C (IP = -76.5 cm)	5.3	7.7
$\Xi^- + \overline{\Xi}^+$ (IP = -55.5 cm)	$\simeq$20.	28.3

targets. For different Ξ^- absorbing target nuclei, different produced double hypernuclei dominate. This feature can be combined with a weak decay model making possible more reliable estimates of the γ-ray yields for the double hypernucleus measurements envisaged by the $\overline{\text{P}}$ANDA collaboration. These calculations have been compared with the E906 data, but further improvements of the model are still to be done for a definite interpretation of the E906 data. Even though, these results suggest that the performance of γ-spectroscopy of double Λ seems possible.

In addition, from the point of view of the analysis, an efficient strategy has been implemented for the unique assignment of gamma–transitions to specific double hypernuclei. This technique combines the predicted energy spectra of each nuclear target with the measurement of two pion momenta from the subsequent weak decays of a double hypernuclei. As a result, some individual double hypernuclei species have been assigned to the gamma transitions measured by the germanium detector array.

For the background handling a method based on time measurement has also been implemented. A detector setup based on the combination of a scintillation fibers array detector, the $\overline{\text{P}}$ANDA TPC and TOF barrel detectors have been studied as possible detector setup option for this purpose.

The method uses the identification of positive kaons to tag the the production of $\Xi^- + \overline{\Xi}$ events. The efficiency of this method has been investigated as a function of the time resolution of the start detector and of distance to the central tracker. These investigations together with those corresponding to the contamination of background events are summarized in the following table 8.1. Nevertheless, further considerations have to be made to have a reliable statistics and therefore the efficiency has to be increased in a factor of 2 or more. The main technical difficulty of this study, was to generate a number of background reactions comparable with the signal, namely a factor 25000 larger. For a accurate evaluation of the background contribution an enhancement of the statistic is foreseen by using high performing computing machines.

Within the simulation, radiation damages have been evaluated on the scintillation fibers array readout electronics as wells on the HPGe cluster detector.

One one hand, it has been seen that the germanium detector will withstand the load of charged and neutral particles impinging on their surface. With the present production rate of $3{\cdot}10^6\,\mathrm{s}^{-1}$ a continuous operation of about 30 days before an annealing procedure seems achievable. On the other hand, it has been seen that the use of scintillator fiber detector as start detector will be not recommendable under such a interaction rate.

To conclude, the feasibility of performing γ spectroscopy of double Λ hypernuclei at the PANDA experiment seems possible. A further improvement of the statistic is needed for the background rejection studies. Moreover, a more realistic setup of the hypernuclear detectors has been suggested using the results of these studies to accomplish a better balance between the physical and the technical requirements.

Rate estimate Based on calculations, the various steps of the double hypernucleus production process have been quantified in order to derive an estimate of the final count rate.

According with these calculations, the rate estimate is based on an antiproton interaction rate of $3 \cdot 10^6\,\mathrm{s}^{-1}$. At a $\overline{\mathrm{p}}$ momentum of $3\,\mathrm{GeV}/c$ the $\overline{\mathrm{p}}\mathrm{p} \rightarrow \Xi^-\overline{\Xi}^+$ the production cross section is about $2\,\mu\mathrm{b}$ [81], to be compared to the elastic cross section $\sigma_e(\overline{\mathrm{p}}\mathrm{p} \rightarrow \overline{\mathrm{p}}\mathrm{p}) \approx 23.7\,\mathrm{mb}$ and the annihilation cross section of $\sigma_a(\overline{\mathrm{p}}\mathrm{p} \rightarrow X) \approx 26\,\mathrm{mb}$. Since no information on the mass dependence of the $\Xi^{-,0}\,\overline{\Xi}^+$ production cross section is available, we assume a $A^{2/3}$ dependence. This results in $\sigma(\Xi^{-,0}\,\overline{\Xi}^+)/\sigma_{tot} = 4 \cdot 10^{-5}$. With these assumptions we expect approximately 100 $\Xi^-\overline{\Xi}^+$ pairs per second or 11 million per day. For a target in the Carbon mass region the "production factor" (PF) is of the order $6{\cdot}10^{-3}$. This provides us with about 64 800 stopped Ξ^- per day.

Assuming a $\Xi^-\mathrm{p} \rightarrow \Lambda\Lambda$ conversion probability of only 5 %. This results in the production of about 3 240 double hypernuclei per day.

Individual excited states may be populated with up to 10 % of the total yield [184]. From the thickness of the secondary target and the neutron moderator we estimate for γ energies between 0.1 and 10 MeV an escape probability of a gamma ray from the target between 60 and 80 %. One cluster detector mounted at a distance of 30 cm covers 0.79 % of 4π. Since the decaying hypernuclei are at rest and assuming isotropic angular distributions, 15 cluster detectors will cover approximately 11.8 % of 4π corresponding to a full photopeak efficiency of 2.75 % for 1.33 MeV γ-rays.

The proposed trigger scheme assumes a detection of hadrons containing the associated anti-strange quarks. The cleanest tag will be a high momentum $\overline{\Xi}^+$ at small angles. However, the majority of $\overline{\Xi}^+$ will annihilate in the primary nucleus. Assuming the $\overline{\Xi}^+\mathrm{p}$ absorption cross section to be close to the $\overline{\mathrm{p}}\mathrm{p}$ annihilation cross section and averaging over the impact parameter we expect even in case of a carbon target a $\overline{\Xi}^+$ escape probability of only 20 %.

The expected reconstruction efficiency is about 50 %. While two kaons will be produced in the annihilation process, the trigger will be based on the detection of only one K^+ in the forward region $\theta \leq 40°$ not covered by the secondary target. In order to reduce the single K^+ rate of about $5 \cdot 10^5\,\mathrm{s}^{-1}$ to a rate acceptable by the DAQ, additional filters based, for example, on the vertex in the secondary target, the signals in the Germanium detectors or the missing energy in the forward region will be employed. In the present work, a kaon trigger efficiency between 20 % and 30 % has been achieved. However, an efficiency of about 40% would be a desirable aim.

In conclusion, the expected rate is of about 69 events per month for an individual transition (See Table 8.2). The total expected rate per month corresponding to the UrQMD+SMM calculations represents however a factor of 10 larger.

$\overline{\mathrm{p}}$ interaction rate	$3 \cdot 10^6\mathrm{s}^{-1}$
$\overline{\mathrm{p}}$ momentum	$3\,\mathrm{GeV}/c$
internal target	$Z \approx 6$
reactions of interest	$\overline{\mathrm{p}}\mathrm{p} \to \overline{\Xi}^+\Xi^-$
	$\overline{\mathrm{p}}\mathrm{n} \to \overline{\Xi}^+\Xi^0$
cross section ($\overline{\mathrm{p}}N$)	$2\,\mu\mathrm{b}$
rate	$100\,\mathrm{s}^{-1}$
Ξ^- PF	$7.5 \cdot 10^{-3}$
total stopped Ξ^-	64 800 per day
$\Xi^-\mathrm{p} \to \Lambda\Lambda$ conversion probability	5 %
produced $\Lambda\Lambda$ hypernuclei	3 240 per day
probability of individual transition	10 %
target escape probability ($E_\gamma = 1\,\mathrm{MeV}$)	70 %
full energy peak efficiency	2.75 %
trigger efficiency	20–30 %
detected individual transitions	69 per month

Table 8.2: Rate considerations for hypernuclear physics with γ-ray spectroscopy. The Intra nuclear Cascade Model has been used for the generation of $\overline{\mathrm{p}}\mathrm{p} \to \overline{\Xi}^+\Xi^-$ events.

It should be stressed that the present consideration leaves still room for numerous improvements. Experience gained during the first experiments and subsequent optimization of the experimental conditions may therefore allow to significantly increase the event rate.

$\bar{\mathrm{p}}$ interaction rate	$3 \cdot 10^6 \mathrm{s}^{-1}$
$\bar{\mathrm{p}}$ momentum	$3\,\mathrm{GeV}/c$
internal target	$Z \approx 6$
reactions of interest	$\bar{\mathrm{p}}\mathrm{p} \to \overline{\Xi}^+\Xi^-$
	$\bar{\mathrm{p}}\mathrm{n} \to \overline{\Xi}^+\Xi^0$
cross section ($\bar{\mathrm{p}}N$)	$2\,\mu\mathrm{b}$
rate	$100\,\mathrm{s}^{-1}$
Ξ^- PF	$7.5 \cdot 10^{-2}$
total stopped Ξ^-	648 000 per day
$\Xi^-\mathrm{p} \to \Lambda\Lambda$ conversion probability	5 %
produced $\Lambda\Lambda$ hypernuclei	32 400 per day
probability of individual transition	10 %
target escape probability ($E_\gamma = 1\,\mathrm{MeV}$)	70 %
full energy peak efficiency	2.75 %
trigger efficiency	20–30 %
detected individual transitions	690 per month

Table 8.3: Rate considerations for hypernuclear physics with γ-ray spectroscopy. The UrQMD+SMM event generator was used for $\bar{\mathrm{p}}\mathrm{p} \to \overline{\Xi}^+\Xi^-$ generation.

Appendix A

Appendix

A.1 The Track Model

The differential equation of motion of a particle with charge q and momentum $\vec{p}$ moving within a magnetic field $\vec{B}$ is given by the Lorentz force as follows,

$$\frac{d\mathbf{p}}{dt} = q \cdot \vec{v} \times \vec{B}$$

In the $\overline{\mathsf{P}}$ANDA target spectrometer the magnetic field $\vec{B} = (0.,0.,B_z)$ is assumed to be approximately homogeneous with $B_z = 2\,$Tesla and parallel to the z-axis, the particle trajectory can be then described by a helix. Reconstructed charged particles trajectories are then represented by a 5 parameter helix vector,

$$h = (d_0, \phi_0, \omega, z_0, \tan\lambda)$$

and a corresponding covariance matrix. The position $\vec{x}$ and the momentum $\vec{p}$ of the particle the helix trajectory are expressed as a function of these parameters, where d_0 is the distance of closest approach to the origin in the X-Y plane, signed by the angular momentum $\vec{r} \times \vec{p}$ at that point, ϕ_0 is the angle in the X-Y plane at closest approach, and z_0 the distance of closest approach to the origin in the z projection. The parameter $\omega = 1/r$ gives the curvature of the track in the X-Y plane, and $tan\lambda$ is the tangent of the track dip angle in the projection plane defined by the cylindrical coordinates r and z,

$$x = r\sin(\Phi) - (r + d_0)\sin(\Phi_0) \tag{A.1}$$

$$y = -r\cos(\Phi) + (r + d_0)\cos(\Phi_0) \tag{A.2}$$

$$z = z_0 + l\tan(\lambda) \tag{A.3}$$

$$p_x = p_t\cos(\Phi) \tag{A.4}$$

$$p_y = p_t\sin(\Phi) \tag{A.5}$$

$$p_z = p_t\tan(\lambda) \tag{A.6}$$

$$\tag{A.7}$$

Furthermore, l is the flight length in the X-Y plane, measured from the point of the helix closest to the z-axis, $\Phi = \Phi_0 + \omega l$ and the transversal coordinate of the particle momentum is related with the strength of the magnetic field $\vec{B}$, its charge and the curvature radius r as $p_t = -qrB_z$. In case of a inhomogeneous magnetic field $\vec{B}$, e.g forward spectrometer region, the differential equation of motion(A.1) has to be solved numerically. The kinematic information of the track is obtained by fitting the helix projection on the X-Y and the R-Φ plane respectively. This procedure leads to a Circle fit on the X-Y, from which the curvature ω, Φ_0, and d_0 are extracted, and to a linear fit on the R-Z plane, providing the dip angle $\tan(\lambda)$ and z_0. In the target spectrometer, a global track fit is performed using the information of the various tracking subdetectors. A track follower based on the well-tested GEANE package [127] combined with a generic Kalman filter (GENFIT [189]) is considered to optimize the momentum reconstruction for charged particles. Geane considers also the effect due to the energy loss and the multiple scattering along the particle trajectory within the material. Additionally to the helix parametrization, the GEANE package provides others track representations such as the parabola which is defined by means of position (x,y) and direction($\tan_x$,$\tan_y$) along the particle trajectory as

$$h \equiv (\frac{1}{p}, x, y, \tan_x, \tan_y) \tag{A.8}$$

$$\tan_x = \frac{dx}{dz} \tag{A.9}$$

$$\tan_y = \frac{dy}{dz} \tag{A.10}$$

$$\tag{A.11}$$

, and by a generic track representation defined by an orthonormal coordinates system to the track with axes u,v and w allowing to evaluate the track for a great variety of orientations.

$$h \equiv (\frac{1}{p}, u, v, \frac{du}{dw}, \frac{dv}{dw})$$

The three above representations are equivalent and one can go from one representation to the other by calculating the corresponding Jacobian.

A.2 Simulated Detector Setup

In the following the detector setup, which has been implemented in the simulation, will be described. The geometry elements of each subdetector will be listed as well as its materials composition. The definition of the geometry consists in declaring the volumes the particles are transported through. A volume is characterised by shape, dimensions, position and orientation with respect to a container or mother reference system. The materials of the volumes are defined in the simulation giving density, and constituting elements.

In the case of the hypernuclear detector, the corresponding layout can be divided into four regions: The interaction region($\theta = 40$–90) covered by a thin Carbon pipe and a secondary active target layout. The backward region($\theta =$ 130–150) which is devoted to the Gamma Spectroscopy arranged by the HPGe detector array. The external and forward region($\theta = 20$–40) dedicated to the background supression via a time of flight system. The $\overline{\mathsf{P}}$ANDA spectrometer is located at the origin of the mother or *Cave* reference system, namely at the (0,0,0) position. The beam direction is displaced along the Z axis of the *Cave* reference system.

Secondary Active Target The geometry layout implemented in the simulation is based on the already discussed concept design in section 4.2.2.

The beam pipe volume is described by a tube(TGeoBox) shape with a diameter of 14 mm, a thickness of 0.1 mm and a length of 200 mm. The pipe is made of Carbon.

A (TGeoBox) shape has been used to define the geometry of the Secondary Active target elements. It is displayed around the carbon pipe into four sectors, each of them forming a multi-layered structure of 1. mm thick absorber material alternated with 300 μm thick silicon layers. The width of each sector is 26 mm. The silicon and absorber layers have a maximum size of $41\times41\times0.3\,\mathrm{mm}^3$. In the present layout, the layers are so parametrized that the secondary target shape in the forward direction forms an angle of 40 degrees with the beam axis.

The whole layout is placed upstream at a distance of 70 cm from the center of *Cave* reference system. The 30 cm space left in the forward direction is covered by the Time Projection Chamber (TPC) readout electronics volume.

In the following, the material constituting the Active Secondary Target, the beam pipe and their properties will be listed in Table. A.1.

HPGe Array Detector The implementation of the HPGe Array Detector follows the description of section 4.2.3.

The volume which have been used to define the HPGe crystal and its capsule is the result of intersecting two solids: a cylinder and a hexagon. the solids dimensions for the crystal and the capsule as well as the material characteristics(Germanium and aluminum)are introduced at continuation.

- **Crystal**. The Germanium crystal is described by the intersection of a cylindrical volume and a hexagonal volume.

    1. Cylinder

Table A.1: Materials defined in the simulation of the Secondary Active Target. In the table, the atomic number is represented by Z and the mass number by A.

Material	Symbol	Density	constituent Elements	
		g/cm^3	A[g/ mole]	Z
Silicon	Si	2.33	28.0855	14.0
Carbon	C	2.265	12.011	6.0
Diamond	C	3.5	12.011	6.0
Beryllium	Be	1.848	9.01	4.0
Boron	B	2.460	10.811	5.0

Shape: *TGeoTube* class.

Dimensions : Inner radius, 0 mm; Outer radius,700 mm; Length, 780 mm.

Material : Germanium

2. Hexagone

   Shape: *TGeoPgon* class.

   Dimensions : Lower Phi Limit, 0 degree; Phi range, 360 degree; Number of sides, 6; Number of Z planes defining polygon sections, 2; Inner/Outer radius of the first Z plane, 0 and $3.50\times \cos(30^0)$ mm; Inner/Outer radius of the second Z plane, 0 and 3.50 mm; Length, 780 mm.

   Material : Germanium

3. **Capsule**. The Crystal capsule is described by the subtraction of two hexagonal shapes.

   Shape 1: *TGeoPgon* class.

   Dimensions : Lower Phi Limit, 0 degree; Phi range, 360 degree; Number of sides, 6; Number of Z planes defining polygon sections, 2; Inner/Outer radius of the first Z plane, 0 and 3.144; Inner/Outer radius of the second Z plane, 0 and 3.627 mm; Length, 840 mm.

   Material : Aluminum

   Shape 2: *TGeoPgon* class.

   Dimensions : Lower Phi Limit, 0 degree; Phi range, 360 degree; Number of sides, 6; Number of Z planes defining polygon sections, 2; Inner/Outer radius of the first Z plane, 0 and 3.078 mm; Inner/Outer radius of the second Z plane, 0 and 3.627 mm; Length, 790 mm.

   Material : Aluminum

Table A.2: Materials defined in the simulation of HPGe Detector array. In the table, the atomic number is represented by Z and the mass number by A or in the case of composes by the rate Z/A.

Material	Symbol	Density g/cm^3	constituent Elements A[g/ mole]	Z
Germanium	Ge	5.32	72.61	32.0
Aluminum	Al	2.70	26.98	13
Polypropylene	C_3H_6	0.074	..	..

- **Veto detector**

  Shape: *TGeoPgon* class.

  Dimensions : Lower Phi Limit, 0 degree; Phi range, 360 degree; Number of sides, 6; Number of Z planes defining polygon sections, 2; Inner/Outer radius of the first Z plane, 0 and 3.50$\times$ cos(30^0) mm; Inner/Outer radius of the second Z plane, 0 and 3.50$\times$ cos(30^0) mm; Length, 50 mm.

  Material : Polypropylene

The Germanium array is arranged in two rings at backwards axial angles. The placement of the individual triple clusters is performed over the surface of a half sphere of radius 30 cm. (For more details see Appendix B.)

In order to differentiate between charged and neutral particles impinging with the detector(crystal + capsule) surface, a veto detector has also been implemented. The veto detector consists of scintillator plates of 1 cm thickness with the same hexagonal shape than the capsule. They are placed at a distance of 0.5 cm from the detector capsule.

Due to the complexity of the structure, the whole layout is enveloped within a mother or containing volume(**TAssembly** , which facilitates its placement as a whole and the transport of particles within the different constituent volumes.

Time of Flight Scintillator Barrel To describe the layout of the cylindrical Time–of–Flight, a cylindrical volume containing 96 scintillator bars was arranged. The cylindrical volume consist of a polyhedral shape of 16 sides. Each of this side contains 6 bars, described by a TGeoBox class. The inner radius of the Polyhedron shape is 433.5 mm and the outer radius 438.5 mm.

The dimensions of each individual bars are 172.45×5×1860 mm^3. The whole layout is placed between the Time Projection Chamber(TPC) and the DIRC detectors. For the holding of the scintillator bars any supporting frame has been consider in the simulation.

The material of the Time of flight is BC408 or polyvinyltoluene.

Table A.3: Materials defined in the simulation of cylindrical Time of Flight. In the table, the atomic number is represented by Z and the mass number by A.

Material	Symbol $(CH)_n$	Density g/cm^3	constituent Elements Z/A
polyvinyltoluene	*BC408*	1.032	0.5415

Scintillator Fiber Detector The scintillator fiber detector consist of 1200 scintillating fibers placed parallel to the beam axis in two rings around the secondary active target. The first ring contains 500 fibers located at a distance of 70 mm from the primary interaction point. In the second ring, a number of 750 fibers are displaced at a distance of 99 mm from the primary interaction point. All the fibers have a diameter of 0.83 mm and a length of 1800 mm. The system is placed at the center of the *Cave* reference system. The scintillator material the fibers are made of is BC408.

A.3 Digital Pulse Shape Analysis

Attempts regarding the analysis of the preamplifier signal alone has been also considered. The scope of this analysis is the extraction of the energy resolution from the preamplifier signal by using digital signal processing. A typical preamplifier signal is illustrated in the upper part of Fig. A.1.

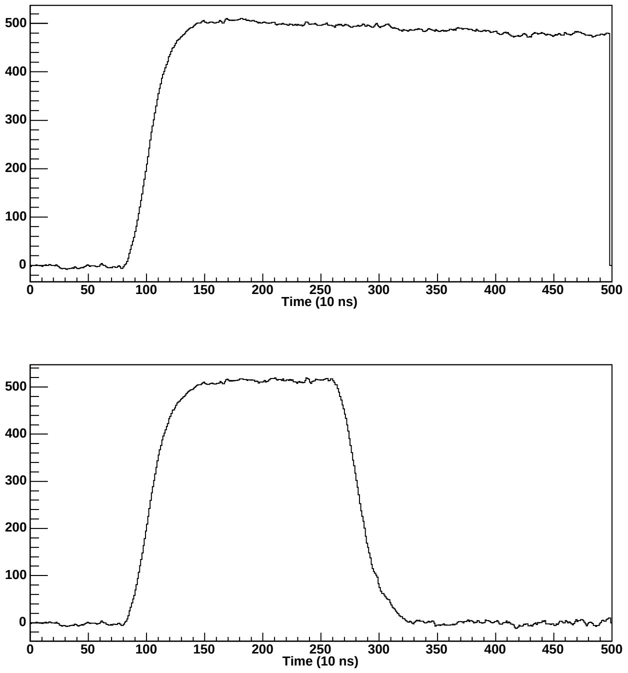

Figure A.1: Upper part corresponds to the preamplifier signal of the VEGA detector, which ideally follows an exponential decay. Lower part illustrates the step signal of length M=1.8 μs, after the application of MWD method.

The output signal of a charge integrating preamplier with continuous discharge consist of a fast rising step due to the charge collection, followed by an exponential tail due to the discharge of the capacitors over the resistor. The exponential tail reduces the final peak height depending on the rise time of the signal, therefore in order to extract the whole amplitude of the signal which corresponds to the energy of a gamma ray, the influence of the preamplifier has to be removed. This is accomplished by the moving window deconvolution algorithm (MWD) [219]. It consists of two parts:

1. the first part is a deconvolution, which transforms the continuous discharge preamplifier signal into a signal from a transistor reset preamplifier, which is a staircase signal.

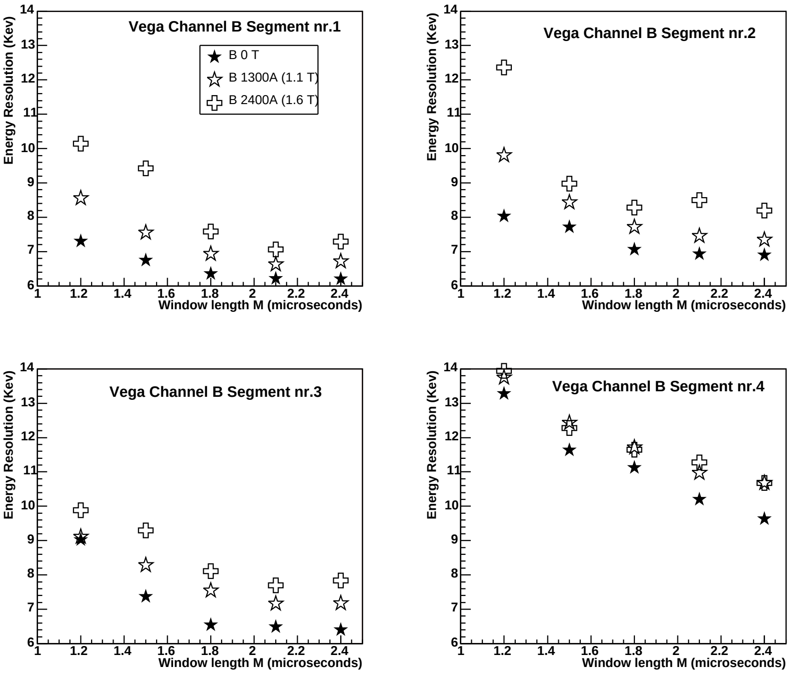

Figure A.2: Energy resolution for 4 segments of the Channel B at VEGA as a function of the length M of the deconvolution window and for different magnetic fields.

2. By applying numerical differentiation of such signal the moving window deconvolution equation is obtained. It converts an exponential signal into a step signal of length M, being M the width of the deconvolution window as shown in the lower part in Fig. A.1. Knowing the decay time and the start time of the signal, the initial amplitude can be determined from any data point of the decaying signal.

The decay time for VEGA is about $50\,\mu$s.
In Fig. A.2, the energy resolution of the 4 segments of the analysed channel at VEGA, extracted by using the method explained above, is shown as a function of the length M, for differents values of the magnetic field. Even though each segment shows a different character, all segments exhibit a common trend, i.e, the energy resolution improves by increasing M. For segments 1 and 2, it is observed that the resolution is recovered at high magnetic field with larger M value. One can expect that the larger M value the better the energy resolution arised from the MWD method. Due to the short length of the trace (see Fig. A.1), only $5\,\mu$s, specially to the short length of the baseline, the method could not be well optimized, and the reconstructed gamma-ray spectra present a worse energy resolution in comparison with those arised from the

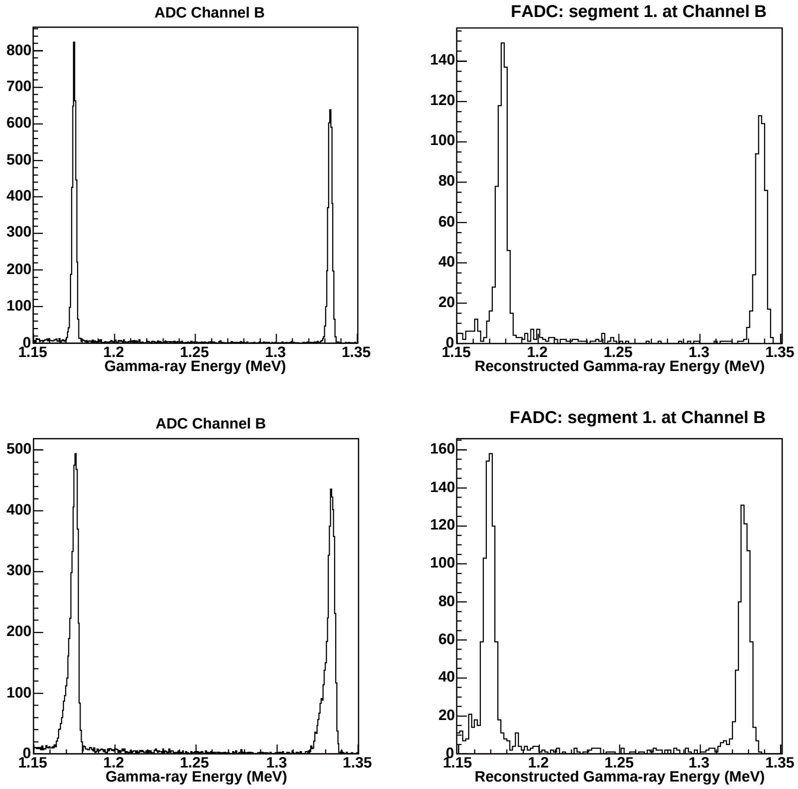

Figure A.3: Gamma-energy spectra of VEGA at different values of the magnetic field. The part on the left illustrates the ADC spectra of Channel B for the value of no magnetic field and at 1.6 T. The right part correspond to the reconstructed ADC spectra after pulse shape analysis at values of zero and 1.6 T for the magnetic field.

ADC spectra. the 2.2 keV of energy resolution could not be recovered under these circumstances by using the MWD algorithm(see Fig. A.3). Indeed a longer FADC sampling would be needed in order to recover the standard value of the energy resolution for the VEGA detector.

A.4 Single and Double hypernuclei spectroscopy

$$\begin{aligned}
\Lambda \qquad \text{Mass} &= 1115.684 \qquad \text{Mev}/c^2 \\
\text{isospin (I)} &= 0 \\
\text{Spin-Parity}(J^P) &= \frac{1^+}{2} \\
\text{Lifetime } (\tau_\Lambda) &= (2.63 \cdot 10^{-10})s
\end{aligned}$$

The single Λ hypernuclei masses m_{Hyp} have been calculated by using the binding energy of a Λ hyperon B_Λ at the ground state (obtained from experiments or from theoretical calculations) and the core nuclei m_{core}. The formula is the one introduced in Sec. 1.2,

$$m_{Hyp} = m_{core} + m_\Lambda - \mathrm{B}_\Lambda \tag{A.12}$$

Table A.4: Core Nuclei masses used for the calculation of the hypernuclei masses

Ion/Particle	Mass (MeV/c^2)	Ion/Particle	Mass (MeV/c^2)	Ion/Particle	Mass (MeV/c^2)
p	938.27945	$^{6}_{4}$Be	5605.3390	$^{11}_{5}$B	10252.6273
n	939.57287	$^{7}_{4}$Be	6534.2350	$^{12}_{7}$N	11191.
$\alpha(^{4}_{2}\mathrm{He})$	3727.40841	$^{8}_{4}$Be	7454.9088	$^{13}_{7}$N	12111.28
d($^{2}_{1}$H)	1875.627	$^{9}_{4}$Be	8392.0	$^{14}_{7}$N	13040.3051
t($^{3}_{1}$H)	2808.9432	$^{9}_{5}$B	8393.3725	$^{15}_{8}$O	13969.044
$^{3}_{2}$He	2808.4137	$^{7}_{5}$B	6545.		
$^{5}_{2}$He	4667.8719	$^{8}_{5}$B	7472.		
$^{7}_{2}$He	6545.5985	$^{10}_{5}$B	9324.5096		
$^{5}_{3}$Li	4667.6530	$^{9}_{6}$C	8407.91		
$^{6}_{3}$Li	5601.5625	$^{10}_{6}$C	9327.		
$^{7}_{3}$Li	6533.8845	$^{11}_{6}$C	10254.0988		
$^{8}_{3}$Li	7471.4245	$^{12}_{6}$C	11174.9506		
$^{9}_{3}$Li	8406.9337	$^{13}_{6}$C	12109.5771		

A.5 Production probability of ground and excited states of double hypernuclei for several target nuclei

Production probability of ground and excited states of accessible double hypernuclei after the capture of a Ξ^- in ^{9}Be, ^{10}B, ^{11}B and ^{13}C nuclei and the Ξ^- conversion into two Λ hyperons.

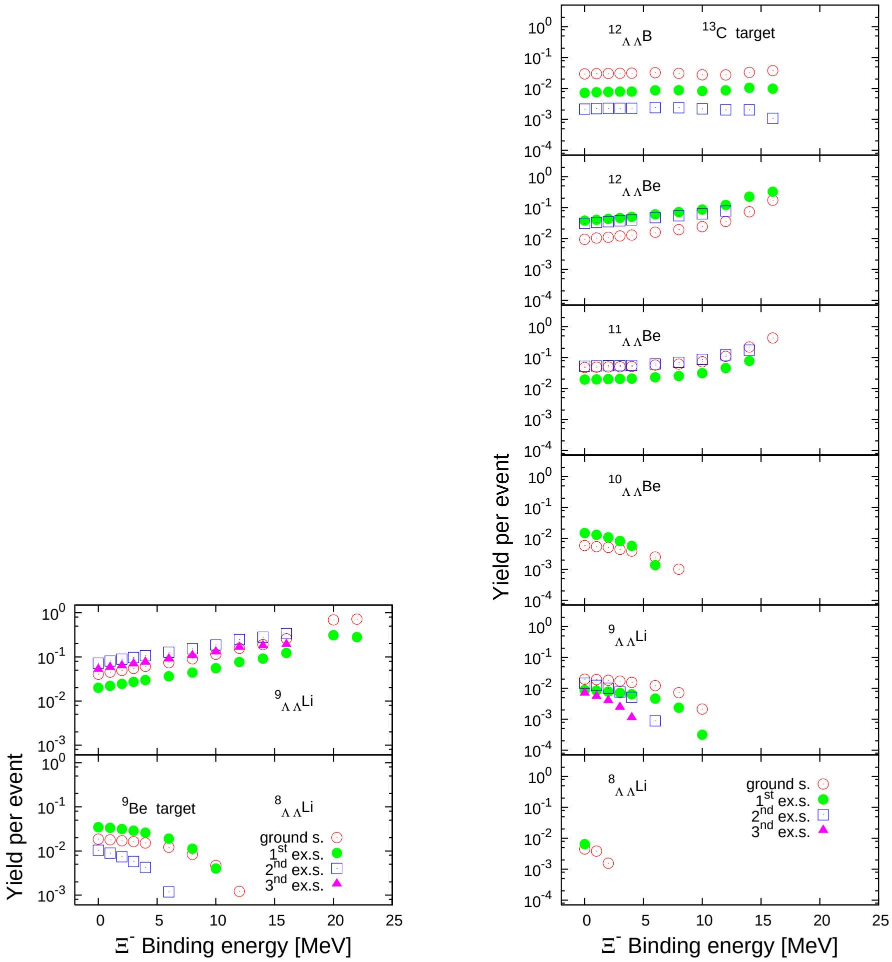

Figure A.4: Production probability of ground and excited states of accessible double hypernuclei after the capture of a Ξ^- in ^{9}Be and ^{13}C target nuclei and the Ξ^- conversion into two Λ hyperons.

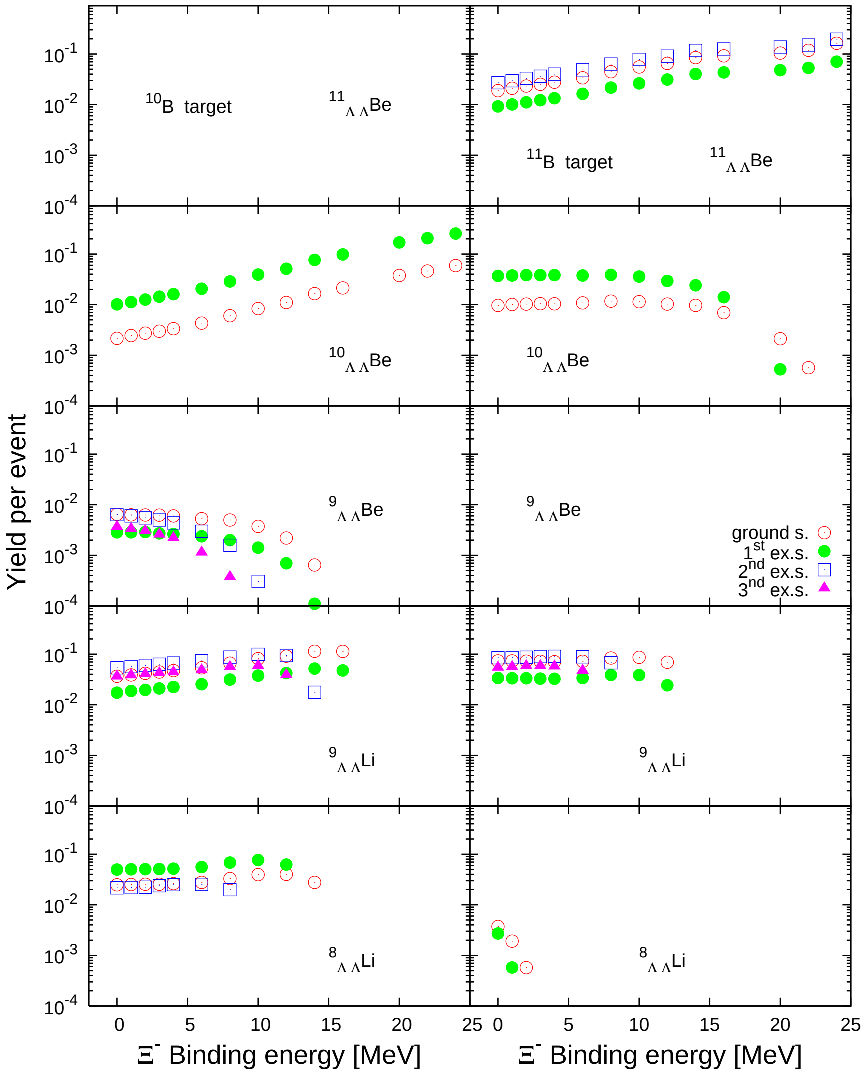

Figure A.5: Production probability of ground and excited states of accessible double hypernuclei after the capture of a Ξ^- in ^{10}B and ^{11}B target nuclei.

A.5.1 Hypernuclei definition

In order to define hypernuclei within the P ANDAROOT framework, the class FairParticle has been extended. A list of single, double hypernuclei with the corresponding decay modes are added to the database during the initialization procedure.

Table A.5: Decay modes of light single lambda hypernuclei (A<13). Here it is considered that the mesonic weak decay(two body decay) takes place from the ground state of the corresponding single hypernuclei.

single-hyp	# 1	# 2	# 3
${}^{3}_{\Lambda}$H	^{3}He	π^-	
${}^{4}_{\Lambda}$H	α	π^-	
${}^{4}_{\Lambda}$He	^{3}He	π^-	p
${}^{5}_{\Lambda}$He	α	π^-	p
${}^{6}_{\Lambda}$He	^{6}Li	π^-	
${}^{8}_{\Lambda}$He	^{8}Li	π^-	
${}^{6}_{\Lambda}$Li	α	π^-	2p
${}^{7}_{\Lambda}$Li	^{7}Be	π^-	
${}^{8}_{\Lambda}$Li	^{8}Be	π^-	
${}^{9}_{\Lambda}$Li	^{9}Be	π^-	
${}^{7}_{\Lambda}$Be	α	π^-	3p
${}^{8}_{\Lambda}$Be	^{8}B	π^-	
${}^{9}_{\Lambda}$Be	^{8}Be	π^-	p
${}^{10}_{\Lambda}$Be	^{10}B	π^-	
${}^{9}_{\Lambda}$B	${}^{9}C$	π^-	
${}^{10}_{\Lambda}$B	^{10}C	π^-	
${}^{11}_{\Lambda}$B	^{11}C	π^-	
${}^{12}_{\Lambda}$B	^{12}C	π^-	
${}^{12}_{\Lambda}$C	^{12}N	π^-	
${}^{13}_{\Lambda}$C	^{13}N	π^-	

Table A.6: Decay modes of double lambda hypernuclei (A<13). Here it is considered that the mesonic weak decay(two body decay) takes place sequentially for both Λ's from the ground state.

double-hyp	# 1	# 2	# 3
${}^{4}_{\Lambda\Lambda}\mathrm{H}$	${}^{3}\mathrm{He}$	π^{-}	p
${}^{5}_{\Lambda\Lambda}\mathrm{H}$	${}^{5}_{\Lambda}\mathrm{He}$	π^{-}	
${}^{5}_{\Lambda\Lambda}\mathrm{He}$	${}^{5}_{\Lambda}\mathrm{Li}$	π^{-}	p
${}^{6}_{\Lambda\Lambda}\mathrm{He}$	${}^{6}_{\Lambda}\mathrm{Li}$	π^{-}	
${}^{7}_{\Lambda\Lambda}\mathrm{He}$	${}^{7}_{\Lambda}\mathrm{Li}$	π^{-}	
${}^{7}_{\Lambda\Lambda}\mathrm{Li}$	${}^{7}_{\Lambda}\mathrm{Be}$	π^{-}	
${}^{8}_{\Lambda\Lambda}\mathrm{Li}$	${}^{8}_{\Lambda}\mathrm{Be}$	π^{-}	
${}^{9}_{\Lambda\Lambda}\mathrm{Li}$	${}^{9}_{\Lambda}\mathrm{Be}$	π^{-}	
${}^{9}_{\Lambda\Lambda}\mathrm{Be}$	${}^{8}_{\Lambda}\mathrm{Be}$	π^{-}	
${}^{10}_{\Lambda\Lambda}\mathrm{Be}$	${}^{10}_{\Lambda}\mathrm{B}$	π^{-}	
${}^{11}_{\Lambda\Lambda}\mathrm{Be}$	${}^{11}_{\Lambda}\mathrm{B}$	π^{-}	
${}^{12}_{\Lambda\Lambda}\mathrm{Be}$	${}^{12}_{\Lambda}\mathrm{B}$	π^{-}	
${}^{11}_{\Lambda\Lambda}\mathrm{B}$	${}^{10}_{\Lambda}\mathrm{B}$	π^{-}	p
${}^{12}_{\Lambda\Lambda}\mathrm{B}$	${}^{12}_{\Lambda}\mathrm{C}$	π^{-}	

Table A.7: Measured energy levels of single lambda hypernuclei from ${}^{3}_{\Lambda}H$ to ${}^{16}_{\Lambda}O$.

Nucleus	**Mass g.s**	Exc. Energy		lifetime
	MeV/c^2	MeV	J^P	τ(ps)
${}^{3}_{\Lambda}H$	2991.14	0.0	$\frac{1}{2}^+$	246
${}^{4}_{\Lambda}H$	3922.5	0.0	0^+	194
		1.05	1^+	
${}^{4}_{\Lambda}He$	3921.19	0.0	0^+	256
		1.15	1^+	
${}^{5}_{\Lambda}He$	4839.9	0.0	$\frac{1}{2}^-$	256
${}^{6}_{\Lambda}He$	5779.4	0.0	1^+	
${}^{8}_{\Lambda}He$	7654.2	0.0		
${}^{6}_{\Lambda}Li$	5778.7	0.0	1^+	
${}^{7}_{\Lambda}Li$	6711.53	0.0	$\frac{1}{2}^+$	
		0.692	$\frac{3}{2}^+$	
		2.050	$\frac{5}{2}^+$	
		2.521	$\frac{7}{2}^+$	
		3.88	$\frac{1}{2}^+$	
${}^{8}_{\Lambda}Li$	7641.8	0.0	1^+	
${}^{9}_{\Lambda}Li$	8578.7	0.0		
${}^{10}_{\Lambda}Li$	9510.25	0.0	1^-	
${}^{7}_{\Lambda}Be$	6715.9	0.0	$\frac{1}{2}^+$	
${}^{8}_{\Lambda}Be$	7643.15	0.0		
${}^{9}_{\Lambda}Be$	8564.49	0.0	$\frac{1}{2}^+$	201
		3.024	$\frac{5}{2}^+$	
		3.067	$\frac{3}{2}^+$	

Table A.8: Continuation of Tab. A.7

Nucleus	**Mass g.s** MeV/c^2	Exc. Energy MeV	J^P	lifetime τ(ps)
${}^{10}_{\Lambda}Be$	9499.32	0.0	0	
${}^{9}_{\Lambda}B$	8579.71	0.0	$\frac{3}{2}^+$	
${}^{10}_{\Lambda}B$	9499.69	0.0	1^-	
		0.1	2^-	
${}^{11}_{\Lambda}B$	10411.76	0.0	$\frac{5}{2}^+$	211
		not observed	$\frac{7}{2}^+$	
		1.482	$\frac{1}{2}^+$	
		not observed	$\frac{3}{2}^+$	
${}^{12}_{\Lambda}B$	11357.12	0.0	1^+	
${}^{12}_{\Lambda}C$	11358.71	0.0	1^-	231
		2.58	1^-	
		6.89	1^-	
		10.68	2^+	211
${}^{13}_{\Lambda}C$	12278.71	0.0	$\frac{1}{2}^+$	
${}^{14}_{\Lambda}C$	13213.32	0.0		
${}^{14}_{\Lambda}N$	13215.02	0.0		
${}^{15}_{\Lambda}N$	14127.41	0.0	$\frac{3}{2}^+$	
		2.268	$\frac{1}{2}^+$	
${}^{16}_{\Lambda}O$	15059.5	0.0	0^-	
		0.026	1^-	
		6.56	1^-	

Table A.9: Predicted energy levels of double hypernuclei. Ground and exited states of double hypernuclei used in the present calculation and the relevant references.

Nucleus	**Mass g.s** MeV/c^2	**Exc. Energy** MeV	J^P	ref./notes
$^{4}_{\Lambda\Lambda}H$	4107.47	0.0	1^+	[93, 87, 152, 153, 154, 151]
$^{5}_{\Lambda\Lambda}H$	5037.54	0.0	$\frac{1}{2}^+$	[71, 73, 149, 150, 151]
$^{5}_{\Lambda\Lambda}He$	5036.98	0.0	$\frac{1}{2}^+$	[71, 73, 149, 150, 151]
$^{6}_{\Lambda\Lambda}He$	5951.37	0.0	0^+	[94, 95]
$^{7}_{\Lambda\Lambda}He$	6889.82	0.0	$\frac{3}{2}^-$	[95]
$^{7}_{\Lambda\Lambda}Li$	6889.35	0.0	$\frac{3}{2}^-$	[95]
$^{8}_{\Lambda\Lambda}Li$	7821.27	0.0	1^+	[95]
		1.36	3^+	
		5.63	2^+	
$^{9}_{\Lambda\Lambda}Li$	8748.85	0.0	$\frac{3}{2}^-$	[95]
		0.73	$\frac{1}{2}^-$	
		4.55	$\frac{7}{2}^-$	
		5.96	$\frac{5}{2}^-$	
$^{9}_{\Lambda\Lambda}Be$	8751.04	0.0	$\frac{3}{2}^-$	[95]
		0.71	$\frac{1}{2}^-$	
		4.54	$\frac{7}{2}^-$	
		5.92	$\frac{5}{2}^-$	
$^{10}_{\Lambda\Lambda}Be$	9671.08	0.0	0^+	[95]
		2.86	2^+	
$^{11}_{\Lambda\Lambda}Be$	10603.35	0.0	$\frac{3}{2}^-$	[75, 95, 182]
		1.684	$\frac{1}{2}^+$	
		2.429	$\frac{5}{2}^-$	
		2.78	$\frac{1}{2}^-$	
		3.049	$\frac{5}{2}^+$	
		4.704	$\frac{3}{2}^+$	
		5.59	$\frac{3}{2}^-$	
		6.38	$\frac{7}{2}^-$	
		6.76	$\frac{9}{2}^+$	
		7.94	$\frac{5}{2}^-$	

Table A.10: continuation of Tab. A.9.

$^{12}_{\Lambda\Lambda}Be$	11534.05	0.0	0^+	[75, 95, 182]
		3.36	2^+	
		5.958	2^+	
		5.959	1^-	
		6.179	0^+	
		6.263	2^-	
		7.371	3^-	
		7.542	2^+	
$^{11}_{\Lambda\Lambda}B$	10603.71	0.0	$\frac{3}{2}^-$	[75, 95, 182]
		2.361	$\frac{5}{2}^-$	
		2.75	$\frac{1}{2}^-$	
		2.788	$\frac{5}{2}^+$	
$^{12}_{\Lambda\Lambda}B$	11532.52	0.0	3^+	[75, 95, 182]
		0.71835	1^+	
		1.74015	0^+	
		2.1543	1^+	
		3.5871	2^+	
		4.7740	3^+	
		5.1103	2^-	
		5.1639	2^+	
		5.180	1^+	
		5.9195	2^+	
		6.025	4^+	
		6.1272	3^-	
		6.56	4^-	
		6.873	1^-	
		7.003	3^+	
		7.430	1^-	
		7.469	2^+	
		7.480	2^-	
		7.5599	0^+	
		7.67	1^+	
		7.75	2^-	
		8.07	2^+	
		8.68	3^+	
		8.889	3^-	
		8.894	2^+	
$^{13}_{\Lambda\Lambda}B$	12456.59	0.0	$\frac{3}{2}^-$	[90]

List of Figures

List of Tables

Bibliography

[1] W. Greiner, Int. Journal of Modern Physics E **5**, 1 (1995).

[2] P. Haensel, A.Y.Potekhin, and D. Yakovlev, *Neutron Stars 1. Equation of state and structure*, Springer, 2007.

[3] J. Schaffner et al., Phys. Rev. Lett. **71** (1993), 1328.

[4] J. Schaffner-Bielich, Nucl. Phys. A **804** (2008), p. 309

[5] J. Pochodzalla, A. Botvina A. Sanchez Lorente, Proceedings Bormio, 2010.

[6] $\overline{\text{P}}$ANDA Collaboration, Technical Progress Report (GSI Darmstadt), pp. 1-383 (2005).

[7] I. Augustin, H.H. Gutbrod, D. Krämer, K. Langanke, H. Stöcker, Fourth International Conference on Fission and Properties of Neutron-Rich nuclei,Sanibel Island, Florida, 2007; arXiv:0804.0177v1 [hep-ph].

[8] N. Kaiser and W. Weise, Phys. Rev. C **71**, 015203 (2005).

[9] R. B. Wiringa and S. C. Pieper, Phys. Rev. Lett. **89**, 182501 (2002).

[10] S. C. Pieper, R. B. Wiringa, and J. Carlson, Phys. Rev. C **70**, 054325 (2004).

[11] S. C. Pieper, Quantum Monte Carlo Calculations of Light Nuclei, in *Lecture notes for Course CLXIX - "Nuclear Structure far from Stability: New Physics and new Technology"*, 2007, arXiv:0711.1500v1 [nucl-th].

[12] I. Stetcu, B. Barrett, and U. van Kolck, Phys. Rev. C **73**, 037307 (2006).

[13] C. Keil, F. Hofmann, and H. Lenske, Phys. Rev. C **61**, 06401 (2000).

[14] F. Hofmann, C. Keil, and H. Lenske, Phys. Rev. C **64**, 034314 (2001).

[15] S. Beane, P. Bedaque, A. Parreno, and M. Savage, Nucl. Phys. A **747**, 55 (2005).

[16] M. Savage, Baryon-baryon interactions from the lattice, in *Proc. of the IX International Conference on Hypernuclear and Strange Particle Physics*, edited by J. Pochodzalla and T. Walcher, page 301, SIF and Springer-Verlag Berlin Heidelberg, 2007, arXiv: 0612063 [nucl-th].

[17] A. G. Nicola and J. Pelaez, Phys. Rev. D **65**, 054009 (2002).

[18] H. Polinder, J. Haidenbauer, and U.-G. M. ner, Nucl. Phys. A **779**, 244 (2006).

[19] L. Tolos, A. Ramos, and E. Oset, Phys. Rev. C **74**, 015203 (2006).

[20] M. Lutz, C. Korpa, and M. Moeller, Nucl. Phys. A **808**, 124 (2008).

[21] I. Stetcu, B. Barrett, and U. van Kolck, Phys. Lett. B **653**, 358 (2007).

[22] B. Borasoy, E. Epelbaum, H. Krebs, D. Lee, and U.-G. Meißner, Eur. Phys. J. A **31**, 105 (2007).

[23] P. Navratil et al., Light nuclei from chiral EFT interactions, in *Proceedings of the 20th European Conference on Few-Body Problems in Physics (EFB20)*, 2007.

[24] D. Millener, C. Dover and A. Gal Phys. Rev. C **38**, 2700 (1988).

[25] B. Povh and M. Uhrmacher, Physik in unserer Zeit, 5(1981)138

[26] P. Achenbach *et al.*,(Private communication)

[27] R. Bertini, et al., Nucl. Phys. A 360 (1981) 315; R. Bertini, et al., Nucl. Phys. A 368 (1981) 365.

[28] M. May et al., Phys. Rev. Lett. **51**, 2085 (1983).

[29] W. Bruckner, et al., Phys. Lett. B 79 (1978) 157

[30] R. Grace, et al., Phys. Rev. Lett. 55 (1985) 1055.

[31] J.J. Szymanski, et al., Phys. Rev. C 43 (1991) 849.

[32] H. Outa, et al., Nucl. Phys. A 639 (1998) 251c.

[33] T. Yamazaki, et al., Nucl. Phys. 450 (1986) 1c.

[34] A. Sakaguchi, et al., Phys. Rev. C 43 (1991) 73.

[35] C. Milner, et al., Phys. Rev. Lett. 54 (1985) 1237.

[36] J.C. Peng, Nucl. Phys. A 450 (1986) 129c.

[37] H. Hotchi, et al., Phys. Rev. C 64 (2001) 044302.

[38] T. Hasegawa, et al., Phys. Rev. C 53 (1996) 1210.

[39] H. Noumi, et al., Phys. Rev. C 52 (1995) 2936.

[40] N. Nagae, Nucl. Phys. A 691 (2001) 76c.

[41] E.V. Hungerford, in: Il.-T. Cheon, S.W. Hong, T. Motoba (Eds.), Proceedings of the APCTP Workshop SNP99,World Scientic, Singapore, 2000, p. 356.

[42] P. Achenbach *et al.*,(A1 Collaboration), Strange Hadrons– strangeness in strongly interacting particles, in Biannual report 2002–3, p.244-258, Institut für Kernphysik, Joh. Gutenberg–Univ. Mainz

[43] A.K. Kerman and M. S. Weiss, Phys. Rev. C8(1973) 408

[44] A. U. Abdurakhimov *et al*, Nuovo cimento**A102**(1989)645.

[45] S. Avramenko, *et al.*, Nucl. Phys.**A547**(1992)95c

[46] T.A. Armstrong *et al*,Phys. Rev. C70 (2004)024902

[47] Conceptual Desigh Report, GSI,2001.

[48] F.J. Gillman, M.B. Wise, Phys. Rev. D 20 (1979) 2392.

[49] E.A. Paschos, T. Schneider, Y.L. Wu, Nucl. Phys. B 332 (1990) 285.

[50] J. Cohen, Prog. Part. Nucl. Phys. 25 (1990) 139

[51] E. Oset and A. Ramos., Prog. Part. Nucl. Phys. 41 (1998) 191.

[52] J. Dubach, G. B. Feldman, B. R. Holstein, and L. de la Torre, Ann. Phys. **249**, 146 (1996).

[53] M. DANVSZ and J. PNIEWSKI, Phil. Mag. **44**, 348 (1953).

[54] (D. ROCHESTER and C. C. BUTLER, Nature 160, 855 (1947).

[55] P. H. Pile, et al, Phys. Rev. Lett. 66 (1991) 2585

[56] O. Hashimoto and H. Tamura, Prog. Part. Nucl. Phys. **57**, 566 (2006).

[57] A. Bamberger et al., Nucl. Phys. B **60**, 1 (1973).

[58] M. Bedjidian et al., Phys. Lett. **62**, 467 (1976).

[59] R. E. Chrien, et al, Phys. Rev. C 41 (1990) 1062

[60] Y. Kondo et al., Nucl. Phys. A **676**, 371 (2000).

[61] J. Ahn et al., Phys. Lett. B **633**, 214 (2006).

[62] T. Motoba, Nucl. Phys. A **691**, 231c (2001).

[63] T. Rijken and Y. Yamamoto, arXiv:hep-ph/0207358v1.

[64] K. Tanida et al., Plan for the measurement of Ξ^--atomic X rays at J-PARC, in *Proc. of the IX International Conference on Hypernuclear and Strange Particle Physics*, edited by J. Pochodzalla and T. Walcher, page 145, SIF and Springer-Verlag Berlin Heidelberg, 2007.

[65] A. Buchmann, Z. Naturforschung **52**, 877 (1997).

[66] A. Buchmann and R. F. Lebed, Phys. Rev. D **67**, 016002 (2003).

[67] R. Jaffe, Phys. Rev. Lett. **38**, 195 (1977).

[68] R. Jaffe, Phys. Rev. Lett. **38**, 617E (1977).

[69] T. Sakai, K. Shimizu, and K. Yazaki, Prog. Theor. Phys. Suppl. **137**, 121 (2000).

[70] T. Yamada and C. Nakamoto, Phys. Rev. C **62**, 034319 (2000).

[71] K. S. Myint, S. Shinmura, and Y. Akaishi, Eur. Phys. J. A **16**, 21 (2003).

[72] I. Afnan and B. Gibson, Phys. Rev. C **67**, 017001 (2003).

[73] I. Filikhin, A. Gal, and V. Suslov, Phys. Rev. C **68**, 024002 (2003).

[74] A.S. Botvina and J. Pochodzalla, Phys. Rev. C **76**, 024909 (2007).

[75] Taiichi Yamada and Kiyomi Ikeda, Phys. Rev. C **56**, 3216 (1997).

[76] Yuichi Hirata, Yasushi Nara, Akira Ohnishi, Toru Harada and Jørgen Randrup, Nucl. Phys. A **639**, 389c (1998).

[77] Yuichi Hirata, Yasushi Nara, Akira Ohnishi, Toru Harada and Jørgen Randrup, Prog. Theor. Phys. **102**, 89 (1999).

[78] Y. Nara, A. Ohnishi and T. Harada and S. Shinmura, Proc. of the 25th INS International Symposium on Nuclear and Particle Physics with High-Intensity Proton Accelerators, Tokyo, Japan, Dec. 3-6, 1996, eds. T.K.Komatsubara, T.Shibata and T.Nomura (World Scientific, Singapore, 1998), pp 324-329.

[79] A. Ohnishi, Y. Hirata, Y. Nara, S. Shinmura and Y. Akaishi Nucl. Phys. A **684**, 595 (2001).

[80] C.J.Batty, E.Friedman, A.Gal, Phys. Rev. C **59**, 295-304(1999).

[81] H. N. Brown et al, Phys. Rev. Lett**8**, (1962) 255; 257 .

[82] Kaidalov and Volkovitsky, Physics with Secondary Beams,GSI, 1996

[83] K. Itonaga, T. Ueda, and T. Motoba, Nucl. Phys. A **691**, 197c (2001).

[84] A. Parreno, A. Ramos, and C. Bennhold, Nucl. Phys. A **65**, 015205 (2001).

[85] K. Sasaki, T. Inoue, and M. Oka, Nucl. Phys. A **726**, 349 (2003).

[86] Y. Sato and others, Nucl. Phys. A,**691**, 189c (2001)

[87] S. D. Randeniya and E. V. Hungerford, Phys. Rev. C **76**, 064308 (2007).

[88] M. Danysz, K. Garbowska, J. Pniewski, *et al.*, Nucl. Phys.**49**, 121 (1963).

[89] R.H. Dalitz, D.H. Davis, P.H. Fowler, A. Montwill, J. Pniewski, and J.A. Zakrzewski, Proc. R. Soc. Lond. A **426**, 1 (1989).

[90] C.B. Dover, D.J. Millener, A. Gal, D.H. Davis, Phys. Rev. C **44**, 1905 (1991).

[91] D.J. Prowse, Phys. Rev. Lett. **17**, 782 (1966).

[92] S. Aoki *et al.*, Prog. Theor. Phys. **85**, 1287 (1991).

[93] J.K. Ahn *et al.*, Phys. Rev. Lett. **87**, 132504-1 (2001).

[94] H. Takahashi, J.K. Ahn, H. Akikawa *et al.* Phys. Rev. Lett. **87**, 212501-1 (2001); A. Ichikawa, Ph.D. thesis, Kyoto University (2001).

[95] E. Hiyama *et al.*, Phys. Rev. C **66**, 024007 (2002).

[96] M. Büscher et al., The Moscow-Jülich Frozen-Pellet Target, in *Hadron Spectroscopy*, edited by A. Reis, C. Göbel, J. D. S. Borges, and J. Magnin, volume 814 of *American Institute of Physics Conference Series*, pages 614–620, 2006.

[97] C. Ekstroem et al., Nucl. Instrum. Meth. **A371**, 572 (1996).

[98] A. V. Boukharov et al., Phys. Rev. Lett. **100**, 174505 (2008).

[99] S. Barsov et al. ANKE, a new facility for medium energy hadron physics at COSY-J lich. Nuc. Ins. Meth. Phys. A, **462** , 364381, 2001.

[100] Technical report, ATLAS Technical Design Report 11, CERN/LHCC 98-13.

[101] Technical report, CMS Technical Design Report 5, CERN/LHCC 98-6.

[102] B. Ketzer, Q. Weitzel, S. Paul, F. Sauli, and L. Ropelewski, Nucl. Instrum. Meth. **A535**, 314 (2004).

[103] H. Staengle et al., Nucl. Instrum. Meth. **A397**, 261 (1997).

[104] K. Mengel et al., IEEE Trans. Nucl. Sci. **45**, 681 (1998).

[105] R. Novotny et al., IEEE Trans. Nucl. Sci. **47**, 1499 (2000).

[106] M. Hoek et al., Nucl. Instrum. Meth. **A486**, 136 (2002).

[107] Technical Proposal, CERN/LHC 9.71.

[108] Technical Proposal, 1994, CERN/LHCC 94-38, LHCC/P1.

[109] E.Auffray et al., Moscow, 1999.

[110] P. Abbon et al., Nucl. Instrum. Meth. **A577**, 455 (2007).

[111] N. Akopov et al.,Nucl. Instrum. Meth. **A479**, 511 (2002).

[112] G. S. Atoyan et al., Nucl. Instrum. Meth. **A320**, 144 (1992).

[113] G. David et al., Performance of the PHENIX EM calorimeter, Technical report, PHENIX Tech. Note 236, 1996.

[114] A. Golutvin, (1994), HERA-B Tech. Note 94-073.

[115] LHCb Technical Proposal CERN LHCC 98-4, LHCC/P4, 1998.

[116] I.-H. Chiang et al., (1999), KOPIO Proposal.

[117] H. Morii, (2004), Talk at NP04 Workshop at J-PARC.

[118] G. Atoyan et al., Test beam study of the KOPIO Shashlyk calorimeter prototype, in *Proceedings of "CALOR 2004"*, 2004.

[119] FairRoot, Simulation and Analysis Framework, http://fairroot.gsi.de.

[120] R. Brun and F. Rademakers, Phys. Res. **A389**, 81 (1996 1997).

[121] Virtual Monte Carlo, http://root.cern.ch/root/vmc.

[122] D. J. Lange, Nucl. Instrum. Meth. **A462**, 152 (2001).

[123] J. Catmor, R. Jones, and M. Smizanska, Development of the EvtGen package for the LHC and ATLAS, Proc. of CHEP2006, Mumbai, India, September 2006.

[124] A. Capella, U. Sukhatme, C.-I. Tan, and J. Tran Thanh Van, Phys. Rept. **236**, 225 (1994).

[125] M. Bleicher et al., J. Phys. **G25**, 1859 (1999).

[126] S. A. Bass et al., Prog. Part. Nucl. Phys. **41**, 225 (1998).

[127] CERN Program Library W5013 (1991).

[128] S. Agostinelli et al., Nucl. Instrum. Meth. **A506**, 250 (2003).

[129] FLUKA, http://www.fluka.org.

[130] P. Yepes, Nucl. Instr. and Meth. **A380**, 582 (1996).

[131] R. Frühwirth, A. Strandlie, and W. Waltenberger, Nucl. Instr. and Meth. in Phys. Res. **A490**, 366 (2002).

[132] F. Ferro, M. Agnello, F. Iazzi, and K. Szymanska, Nucl. Phys. A **789**, 209 (2007).

[133] W. R. Lozowski, D. Steski, H. Huang, and C. Naylor, Nucl. Instr. and Meth. in Physics Research A **590**, 157 (2008).

[134] D. Prahsun, Collaboration Meeting March 2010. Private communication.

[135] G. Gerl and H. Grawe and E. Roeckl http://www-gsi-vms.gsi.de/ eb/ html/ vegaproject.html, (1998)

[136] http://www.ortec-online.com/ detectors/ xcool.htm

[137] P. Achenbach , A. Sanchez Lorente, S. Sanchez Majos, J. Pochodzalla Nucl. Ins. Meth. Phys. A **610** (2009) 358361

[138] S. Sanchez Majos Phd Thesis, Private communication

[139] M. Pomorski, E. Bedermann et al. phys. stat. sol (a)**203**, 12, 3152 (2006)

[140] M. Danysz et al., Nucl. Phys. **49**, 121 (1963).

[141] A. Sanchez Lorente, A. Botvina, and J. Pochodzalla, (in preparation).

[142] J.P. Bondorf, A.S. Botvina, A.S. Iljinov, I.N. Mishustin and K. Sneppen, *Phys. Rep.* **257** (1995) 133.

[143] Y. Yamamoto, M. sano and M. Wakai, Prog. Theor. Phys. Supp. **117**, 265, (1994).

[144] M. Sano, M. Wakai and Y. Yamamoto, Prog. Theor. Phys. **87**, 957 (1992)

[145] E. Fermi, Progr. Theor. Phys. **5**, 570 (1950).

[146] F. Ajzenberg-Selove, *Nucl. Phys.* **A433**, 1 (1985).

[147] H. Bando, T. Motoba, and J. Zofka, *Int. J. Mod. Phys.* **A5**, 4021 (1990).

[148] E. Hiyama, Y. Yamamoto, T. Motoba and M. Kamimura, Phys. Rev. C. **80**, 054321 (2009).

[149] D. Lanskoy and Y. Yamamoto, Phys. Rev. C **69**, 014303 (2004).

[150] M. Shoeb, Phys. Rev. C **69**, 054003 (2004).

[151] H. Nemura, S. Shinmura, Y. Akaishi, and K. S. Myint, Phys. Rev. Lett. **94**, 202502 (2005).

[152] I. Filikhin and A. Gal, Phys. Rev. Lett. **89**, 172502 (2002).

[153] H. Nemura, Y. Akaishi, and K. S. Myint, Phys. Rev. C **67**, 051001(R) (2003).

[154] M. Shoeb, Phys. Rev. C **71**, 024004 (2005).

[155] C.B. Dover, A. Gal and D.J. Millener, Nucl. Phys. A **572**, 85 (1994).

[156] A.S. Botvina, A.S. Iljinov, I.N. Mishustin, J.P. Bondorf, R. Donangelo and K. Sneppen, Nucl. Phys. **A475**, 663 (1987).

[157] A.S. Botvina, Ye.S. Golubeva, and A.S. Iljinov. Statistical simulation of the break-up of light nuclei in hadron-nucleus reactions. INR, P-0657, 24 pages, Moscow, 1990.

[158] C. Dover and A. Gal, Ann. Phys. **147**, 309 (1983).

[159] E. Friedman and A. Gal, Phys, Report **452**, 89 (2007).

[160] S. Aoki et al., Phys. Lett. B **355**, 45 (1995).

[161] D. Millener, C. Dover, and A. Gal, Prog. Theor. Phys. Suppl. **117**, 307 (1994).

[162] K. Ikeda et al., Prog. Theor. Phys. **91**, 747 (1994).

[163] G. Kopylov, *Principles of resonance kinematics*, Moscow, 1970.

[164] J. Bondorf, A. Botvina, A. Iljinov, I. Mishustin, and K. Sneppen, Phys. Rep. **257**, 133 (1995).

[165] A. Botvina, Y. Golubeva, and A. Iljinov, INR, P-0657, Moscow (1990).

[166] A. Botvina et al., Z. Phys. A **345**, 413 (1993).

[167] A. Sudov et al., Nucl. Phys. A **554**, 223 (1993).

[168] D.H. Wilkinson et al., Phys. Rev. Lett. 3, 397 (1959).

[169] P.H. Steinberg and R.J. Prem, Phys. Rev. Lett. 11, 429 (1963).

[170] A. Bechdolff et al., Phys. Lett. 26B, 174 (1968).

[171] S. Aoki et al., Prog. Theor. Phys. 89, 493 (1993).

[172] A. Ichikawa et al., Phys. Lett. B 500, 37 (2001).

[173] S. Aoki et al., KEK E176 Collaboration, Nucl. Phys. A **828**, 191 (2009).

[174] K.Ahn et al.,in Hadrons and Nuclei,edited by Il-Tong Cheon et al.,AIP Conf. Proc. No.**594** AIP, Melville, NY, 2001, p.180.

[175] Yasuo Yamamoto, Masamichi Wakai, Toshio Motoba, Tomokazu Fukuda, Nucl. Phys. A **625**, 107 (1997)

[176] Izumi Kumagai-Fuse and Shigeto Okabe, Phys. Rev. C **66**, 014003 (2002).

[177] H. Kamada,J. Golak, K. Miyagawa, H. Witala, W. Glöckle, Phys. Rev. C **57**, 1595 (1998).

[178] H. Outa *et al.*, Nucl. Phys. A**639**, 251c (1998).

[179] Joe P. Nakano, *Study of Double-Lambda Hypernuclei by Using Cylindrical Detector System*, Ph.D. Thesis, Center for Nuclear Study, University of Tokyo, Report CNS-REP-28 (2000).

[180] A. Gal, Nucl.Phys.A **828**, 72 (2009).

[181] J. Pochodzalla, Nucl. Instr. Meth B **214**, 149 (2004).

[182] http://www.tunl.duke.edu/nucldata/

[183] Physik der Atomkerne : eine Einf. von Theo Mayer-Kuckuk, 2., berarb. Aufl. 1974

[184] T. Yamada and K. Ikeda, Nucl. Phys. **A585**, 79c, 1995.

[185] The CDFII Collaboration, R. Blair et al., The CDF II Detector Technical Design Report, FERMILAB-PUB-96/390-E

[186] Rho: A Set of Analysis Tools for ROOT, http://savannah.fzk.de/websites/hep/rho/.

[187] Resolution Studies for the Micro Vertex Detector of the $\overline{\mathsf{P}}\mathsf{ANDA}$ Experiment and the Reconstruction of Charmed Mesons for Specific Hadronic Channels, Rene Jaekel, Phd Thesis, 2009, private communication.

[188] M. Agnello *et al.*, (FINUDA collaboration), Phys. Lett. B622 (2005) 35.

[189] http://sourceforge.net/projects/genfit.

[190] Tech. Nuc. Part. Phys. Exp. W. R. Leo, Springer Verlag, Berlin, 1987.

[191] M. Kavatsyuk et al., GSI Annual report (2007).

[192] P. Leleux et al., Astronomy and Astrophysics **411**, L85 (2003).

[193] H. Akikawa et al., Phys. Rev. Lett. **88**, 082501 (2002).

[194] A. Galoyan, Private Comunication.

[195] A. Orecchini and D. Rodriguez,Panda Collaboration Meeting, Mechanical Integration, March. 2010 Private Comunication.

[196] H. Tamura *et al.*, Phys. Rev. Lett. 84 (26) (2000) 5963.

[197] O. Hashimoto and H. Tamura, Prog. Part. Nucl. Phys. 57 (2006) 564.

[198] T. Bressani, E. Botta, A. Feliciello, and V. Paticchio, Nucl. Phys. A754 (2005) 410c.

[199] $\overline{\text{P}}$ANDA collaboration, Strong interaction studies with antiprotons, GSI report, GSI, Darmstadt, Technical Progress Report (Jan. 2005).

[200] J. Pochodzalla, Nucl. Inst. & Meth. in Phys. Res B214 (2004) 149.

[201] E. Hiyama, M. Kamimura, T. Motoba, T. Yamada, and Y. Yamamoto, Phys. Rev. C 66(2002) 024007.

[202] A. Sanchez Lorente et al., Nucl. Inst. Meth A **573**, 410 (2007).

[203] P. T. Greenlees *et al.*, Eur. Phys. J. A20 (2004) 87.

[204] A.-P. Lepp?nen *et al.*, Eur. Phys. J. A28 (2006) 301.

[205] M. Descovich *et al.*, Nucl. Inst. & Meth. in Phys. Res A545 (2005) 199.

[206] Chr. Bargholtz *et al.*, Nucl. Inst. & Meth. in Phys. Res. A390 (1997) 160.

[207] G. F. Knoll, Radiation Detection and Measurement, John Wiley & Sons, Inc., New York, 1988.

[208] B.W. Loo, F.S. Goulding and D. Gao, IEEE Trans. Nucl. Sci. NS-35 (1988) 114.

[209] M. Moszyński and G. Duchêne, Nucl. Inst. & Meth. in Phys. Res. A308 (1991) 557.

[210] P. G Rancoita, Nucl. Phys. 10 (1984) 299.

[211] A. Castoldi, E. Gatti, V. Manzari and P. Rehak, Nucl. Inst. & Meth. in Phys. Res A399 (1997) 227.

[212] F. Albiol *et al.*, Nucl. Inst. & Meth. in Phys. Res A409 (1998) 236.

[213] M. Brigida *et al.*, Nucl. Inst. & Meth. in Phys. Res A564 (2006) 115.

[214] J. Eberth *et al.*, Nucl. Inst. & Meth. in Phys. Res. A369 (1996) 135.

[215] T.W. Raudorf and R. H. Pehl, Nucl. Instr. Meth., A255, 538, 1987

[216] R.H. Pehl and *et al.*, IEEE Trans. Nucl. Sci NS-26, 321, 1979

[217] J. Gerl *et al.*, in: Proc. Conf. on Physics from Large γ-ray Detector Arrays, Berkeley, USA, LBL Report 35687, 1994, p. 159.

[218] ALADiN Collaboration, Proposal for a forward spectrometer at the 4π detector, GSI Report 88-08, GSI, Darmstadt (1988).

[219] A. Georgiev, W. Gast and R.M. Lieder, An Analog-to-Digital Conversion Based on a Moving Window Deconvolution, IEEE Trans. Nucl. Sci. NS-41(4) (1994), 1116.

Acknownledgments